ABSTRACT

Title of Dissertation: DECOHERENCE AND DEFECTS IN COOPER-PAIR BOXES

Vitaley Zaretskey, Doctor of Philosophy, 2013

Directed by: Professor Frederick C. Wellstood
Department of Physics
Dr. Benjamin S. Palmer
Laboratory for Physical Sciences

This dissertation describes my detailed investigation of decoherence and defects in two Al/AlO_x/Al Cooper-pair box (CPB) charge qubits. Both devices were coupled to thin-film lumped-element superconducting aluminum LC resonators at a temperature of 25 mK. Device 1 was previously found to have an exceptionally long energy relaxation time of $T_1 = 205\,\mu$s and a strong correlation between the lifetime T_1 and the decoupling from the microwave drive line $dV_{g,\mathrm{rms}}/d\Omega_{R,0}$.

I determined the dephasing properties of this CPB though a series of experiments. I measured Ramsey fringes, extracted dephasing times T_φ in the range $200-500$ ns, and determined a corresponding bound of $S_q(f = 1\,\mathrm{Hz}) \leq \left(3\times10^{-3}\right)^2 e^2/\mathrm{Hz}$ on the amplitude of the $1/f$ charge noise affecting the qubit. I then carried out a spin echo experiment and found echo decay times T_{echo} in the $2.4-3.3\,\mu$s range, implying a high frequency $1/f$ charge noise cutoff of $\omega_c/2\pi \approx 0.2$ MHz.

I followed this up by fabricating and characterizing a nearly identical Device 2. This CPB had a reasonably long relaxation time $T_1 \approx 4-30\,\mu$s and again the lifetime T_1 and decoupling $dV_{g,\mathrm{rms}}/d\Omega_{R,0}$ were correlated. Although the lifetime of Device 2 was shorter

than that of Device 1, the results suggest that the exceptional relaxation time was somewhat reproducible and that this approach may lead to further improvements in qubit coherence.

During my initial characterization of Device 2, I discovered that it displayed an anomalously twinned transition spectrum. I studied this feature in detail in parallel with my decoherence experiments. I found that above the resonator resonance at $\omega_{res}/2\pi = 5.472\,\mathrm{GHz}$ the system spectrum was twinned but below it was quadrupled. This behavior was consistent with a pair of two-level systems (TLS) coupled non-resonantly to the CPB via both charge and critical current. I developed a model that matched this scenario and successfully fit the predicted spectrum to my data.

Both the coherent non-resonant interaction and joint charge and critical current CPB-TLS coupling are novel observations. From the fits I extracted microscopic parameters of the fluctuators including the well asymmetry, tunneling rate, and a minimum hopping distance of $0.2 - 0.45\,\text{Å}$. I also found a large fractional change of the Josephson energy $\Delta E_{J,k}/E_J \approx 30 - 40\%$, consistent with a non-uniform tunnel barrier containing a few dominant conduction channels and a defect that modulates one of them.

DECOHERENCE AND DEFECTS IN COOPER-PAIR BOXES

by

Vitaley Zaretskey

Dissertation submitted to the Faculty of the Graduate School of the
University of Maryland, College Park, in partial fulfillment
of the requirements for the degree of
Doctor of Philosophy
2013

Advisory Committee:
Professor Frederick C. Wellstood, Advisor / Chair
Dr. Benjamin S. Palmer, Advisor
Professor James R. Anderson
Professor Christopher J. Lobb
Professor John Cumings

Dedication

посвящается дедушке Мише

Acknowledgments

In the modern world, the research group, the peer group and the research environment have as much influence as the individual researcher in determining the fate of a scientific experiment. Every interaction, no matter how small or seemingly unrelated, contributes to progress and determines success. With this in mind I'd like to thank everyone who has helped or interacted with me. Thank you for sharing the burden and making the result possible. It's not my style to list everyone's name and a cute reason for their inclusion in this acknowledgment, instead I'd like to say a blanket thank you to everyone involved; you know who you are.

Contents

List of Tables viii

List of Figures ix

List of Symbols and Acronyms xii

1 Introduction 1

1.1 Quantum Computation . . . 1

1.2 Superconducting Qubits . . . 4

1.3 Circuit Quantum Electrodynamics . . . 9

1.4 Thesis Overview . . . 12

2 Circuit QED With the Cooper-Pair Box 14

2.1 Josephson Junction Basics . . . 14

2.2 Cooper-Pair Box Qubit . . . 16

2.3 Split Cooper-Pair Box . . . 18

2.3.1 Charge Staircase and Energy Levels . . . 21

2.3.2 Effect of Gate Voltage Perturbation . . . 22

2.4 Lumped Element LC Resonator . . . 24

2.5 Circuit QED . . . 32

2.5.1 Dispersive Limit . . . 33

2.5.2 Resonant Limit . . . 36

2.6 Qubit Readout . . . 36

2.6.1 Small Dispersive Shift Limit . . . 40

2.7 Purcell Effect . . . 42

2.8 AC Stark Effect . . . 43

3 Decoherence in the Cooper Pair Box 46
3.1 CPB as a Qubit . . . 46
3.1.1 Qubit Control . . . 48
3.2 Steady State Spectrum . . . 52
3.3 Relaxation . . . 53
3.3.1 Noise Sources Affecting the CPB . . . 55
3.4 Dephasing . . . 58
3.4.1 Ramsey Fringes . . . 61
3.4.2 Spin Echo . . . 65
3.4.3 Rabi Oscillations . . . 68
3.5 Qubit and Resonator Parameter Selection . . . 72
3.6 Transmon Limit of the CPB . . . 74

4 Experimental Details 78
4.1 Sample Fabrication . . . 78
4.1.1 Optical Lithography . . . 78
4.1.2 Material Deposition and Etching . . . 82
4.1.3 Electron Beam Lithography . . . 86
4.1.4 Junction Fabrication . . . 88
4.2 Cryogenics and Filtering . . . 92
4.2.1 Filtering and Thermalization . . . 94
4.2.2 Sample Box . . . 99
4.3 Qubit Control . . . 101
4.3.1 External Parameters . . . 101
4.3.2 Microwave Pulse Shaping . . . 102
4.4 Qubit State Readout . . . 107

5 Preliminary Qubit Characterization 113
5.1 Locating the Qubit . . . 113
5.1.1 Extracting Resonator Parameters . . . 113
5.1.2 Gate Bias Sweep . . . 116
5.1.3 Single Tone Spectroscopy . . . 118
5.2 Extracting Qubit Parameters . . . 120

5.2.1 Two-Tone Spectroscopy . . . 121
5.2.2 External Flux Dependence . . . 123
5.2.3 Single-Tone Spectroscopy With a Pump Tone . . . 126
5.3 Qubit Readout Optimization . . . 127
5.3.1 Dealing With Charge Noise . . . 127
5.3.2 Pulsed Probe Readout . . . 131
5.4 Qubit Performance Measurements . . . 134
5.4.1 Excited State Lifetime T_1 . . . 134
5.4.2 AC Stark Shift and Spectral Width . . . 136
5.4.3 Rabi Oscillations . . . 141

6 Decoherence and Reproducibility Experiments 144
6.1 Overview of Results for Device 1 . . . 144
6.1.1 Follow-up Decoupling Experiment . . . 148
6.2 Dephasing of Device 1 . . . 150
6.2.1 Pulsed Probe Rabi Oscillations . . . 150
6.2.2 State Tomography . . . 152
6.2.3 Ramsey Fringes . . . 155
6.2.4 Spin Echo . . . 158
6.2.5 Noise Bounds Considerations . . . 161
6.3 Reproducibility of the Lifetime and Decoupling Results . . . 162
6.3.1 Design Changes for Device 2 . . . 162
6.3.2 T_1 and Rabi Coupling in Device 2 . . . 163
6.3.3 Dephasing in Device 2 . . . 167

7 CPB-TLS Interaction Theory 168
7.1 The Physical Origin of Defects and Dissipation . . . 168
7.1.1 Two-Level Systems . . . 168
7.1.2 Qubit-TLS Interactions . . . 169
7.2 CPB Coupled to a TLS . . . 172
7.2.1 Resonant Qubit-TLS Interaction . . . 176
7.2.2 Non-resonant Qubit-TLS Interaction . . . 181
7.2.3 Extension to Multiple TLS's . . . 186

8 CPB-TLS Interaction Experiments 189
8.1 Non-resonant CPB-TLS Interaction . . . 189
8.1.1 System Spectrum . . . 189
8.1.2 Fits to the Single and Double TLS Models . . . 199
8.1.3 Discussion and Comparison to the Resonant Case . . . 205
8.2 Spectral Anomalies in Device 2 . . . 208
8.2.1 The Dead Zone . . . 208
8.2.2 Other Spectral Anomalies . . . 210

9 Conclusions 213
9.1 Overview of Main Results . . . 213
9.1.1 Dephasing and Reproducibility of Long Lifetime Qubits . . . 213
9.1.2 Critical Current and Charge Coupled Fluctuators . . . 215
9.2 Future Outlook . . . 216

Appendix A Fabrication Recipes 219
A.1 Resonator Fabrication Recipe for Device 2 . . . 219
A.2 CPB Fabrication Recipe . . . 221

Bibliography 223

List of Tables

1.1 Summary of the key parameters of Devices 1 and 2. 12

6.1 Summary of the decoherence and noise bounds of Devices 1 and 2. 160

8.1 Optimal fit parameters for the single TLS model. 203

8.2 Optimal fit parameters for the double TLS model. 203

List of Figures

1.1 Schematic of a Josephson junction 4

1.2 The main types of superconducting qubits 6

1.3 Typical cavity QED setup 11

2.1 Schematics of basic and split Cooper-Pair boxes. 16

2.2 Expectation value of the charge of the CPB. 22

2.3 Energy levels and transition spectrum of the CPB. 23

2.4 Schematics of the superconducting LC resonator and CPB qubit. 25

2.5 Electric field and current simulation of the lumped element resonator. . . . 26

2.6 Theoretical resonator S_{21} amplitude and phase. 30

2.7 System spectrum in the dispersive limit. 35

2.8 System spectrum containing a resonant avoided crossing. 37

2.9 Dispersive shift in the strong dispersive limit. 39

2.10 Dispersive shift in the weak dispersive limit. 41

3.1 Bloch sphere representation of a qubit state. 47

3.2 Qubit operations viewed as rotations on the Bloch sphere. 51

3.3 Ramsey fringes pulse sequence and filter function. 62

3.4 Types of $1/f$ noise spectra. 64

3.5 Spin echo pulse sequence and filter function. 66

3.6 Rabi oscillations pulse sequence and filter function. 69

3.7 Rotating frame used to analyze Rabi oscillations. 70

3.8 Charge dispersion in the transmon. 75

3.9 Relative anharmonicity of the transmon. 76

4.1 Microfabrication process flow. 79

4.2 Double-angle evaporation process flow. . . . 89
4.3 Photograph of the dilution refrigerator. . . . 93
4.4 Dilution refrigerator setup. . . . 95
4.5 Photograph of the sample box. . . . 99
4.6 Time trace of a representative qubit control pulse. . . . 103
4.7 Pulse shaping setup schematic and photograph. . . . 105
4.8 Coherent heterodyne readout schematic. . . . 110

5.1 Transmission parameter S_{21} of the resonator of Device 2. . . . 114
5.2 Gate voltage sweeps of Device 2. . . . 117
5.3 Single-tone spectroscopy of Device 2. . . . 119
5.4 Two-tone spectroscopy of Device 1. . . . 120
5.5 Preliminary two-tone spectroscopy of Device 2. . . . 122
5.6 E_J versus external magnetic field for Device 2. . . . 124
5.7 Single tone spectroscopy with a pump tone for Device 2. . . . 125
5.8 Examples of charge noise in Device 2. . . . 128
5.9 Pulsed probe spectral amplitude versus third tone power. . . . 133
5.10 Pulsed probe T_1 curve with fit of Device 2. . . . 135
5.11 AC Stark shift and spectral broadening in Device 2. . . . 138
5.12 Pulsed probe spectral peak and spectral width scaling in Device 2. . . . 140
5.13 Rabi oscillations in Device 2. . . . 142

6.1 Microscope images of Devices 1 and 2. . . . 145
6.2 SEM images of Devices 1 and 2. . . . 146
6.3 Lifetime, decoupling, and line transmission of Device 1. . . . 147
6.4 History of the system transmission amplitude $|S_{21}|$. . . . 149
6.5 Pulsed probe Rabi oscillations in Device 2. . . . 151
6.6 State tomography of Device 1. . . . 153
6.7 Theoretical state tomography for Device 1. . . . 154
6.8 Ramsey fringes in Device 1. . . . 156
6.9 Spin echo in Device 1. . . . 159
6.10 Lifetime and decoupling of Device 2. . . . 164
6.11 Comparison of lifetime and decoupling between Devices 1 and 2. . . . 165

7.1 Diagram of the position and potential energy of a charged TLS. 172
7.2 Resonant CPB-TLS system spectrum. 178
7.3 Effects of $E_{R,1}$ and $E_{int,1}$ on the resonant system spectrum. 179
7.4 Effects of $\Delta E_{J,1}$ and $T_{LR,1}$ on the resonant system spectrum. 180
7.5 Non-resonant CPB-TLS system spectrum. 182
7.6 Effects of $E_{R,1}$ and $E_{int,1}$ on the non-resonant system spectrum. 184
7.7 Effects of $\Delta E_{J,1}$ and $T_{LR,1}$ on the non-resonant system spectrum. 185

8.1 The 7.06 GHz and 6.65 GHz two tone spectra. 191
8.2 The ≈ 6.50 GHz and 5.52 GHz two tone spectra. 192
8.3 The 5.20 GHz spectrum. 194
8.4 The 5.05 GHz spectrum. 195
8.5 The 4.85 GHz spectrum. 196
8.6 The 4.45 GHz and 3.95 GHz two tone spectra. 198
8.7 Fits of spectra above the resonator to the single TLS model. 201
8.8 Fits of spectra below the resonator to the single TLS model. 202
8.9 Fits to the double TLS model. 204
8.10 Single-tone spectroscopy in the dead zone. 209
8.11 Two-tone spectroscopy of TLS ghosts. 211

List of Symbols and Acronyms

Acronyms

CPB	Cooper-pair box
CPW	coplanar waveguide
QED	quantum electrodynamics
RIE	reactive-ion etch
SET	single electron transistor
SMA	subminiature version A
TLS	two-level system

Physical constants

$\hbar$	reduced Planck's constant ($1.054 \times 10^{-34}\,\mathrm{J \cdot s}$)
Φ_0	magnetic flux quantum ($h/2e = 2.068{\times}10^{-15}\,\mathrm{T \cdot m^2}$)
e	magnitude of the charge of an electron ($1.602 \times 10^{-19}\,\mathrm{C}$)
h	Planck's constant ($6.626 \times 10^{-34}\,\mathrm{J \cdot s}$)
k_B	Boltzmann's constant ($1.381 \times 10^{-23}\,\mathrm{J/K}$)

Cooper-pair box parameters

α_r	relative anharmonicity
Δ	superconducting energy gap
ϵ_m	charge dispersion

γ	gauge-invariant phase difference
$\omega_{01}/2\pi$	transition frequency between the ground and first excited state
$\omega_{\mu w}/2\pi$	microwave pump tone frequency
$\omega_{CPB}/2\pi$	transition frequency between the ground and first excited state of a CPB
Φ	magnetic flux bias
σ^+, σ^-	raising, lowering operators for the CPB
C_Σ	total capacitance of the CPB island to ground, $C_\Sigma = C_j + C_g$
C_g	capacitance between the voltage gate and the CPB island
C_j	capacitance of a Josephson junction
$D_{\lambda,\perp}$	sensitivity to quantum λ parameter noise
$D_{\lambda,z}$	sensitivity to low frequency λ parameter noise
$D_{\lambda 2,z}$	second order sensitivity to low frequency λ parameter noise
$D_{\Phi,z}$	sensitivity to low frequency flux (Φ) noise
$D_{n_g,\perp}$	sensitivity to quantum n_g noise
$D_{n_g,z}$	sensitivity to low frequency charge (n_g) noise
$D_{n_g 2,z}$	second order sensitivity to low frequency charge (n_g) noise
$D_{q,\perp}$	sensitivity to quantum charge noise
$D_{V,\perp}$	sensitivity to quantum voltage noise
E_c	Cooper-pair box charging energy, $E_c = e^2/2C_\Sigma$
E_J	Josephson energy
E_J^{sum}	maximum Josephson energy, $E_J = \Phi_0 I_0/2\pi$
I_0	junction critical current
I_J	supercurrent flowing through a Josephson junction

J_0	junction critical current density
N	excess number of Cooper-pair on the island of a CPB
n_g	reduced gate bias voltage, $n_g = C_g V_g / e$
P_{ox}	junction oxidation pressure
P_p	pump tone power
R_n	junction normal state resistance
T	temperature
t	time
t_{ox}	junction oxidation time
T_c	superconducting transition temperature
V_g	gate bias voltage
V_J	voltage across a Josephson junction

Qubit performance parameters

$\Delta\nu_{\mathrm{R}}$	Ramsey frequency
η	Rabi rotation axis angle with the z-axis, $\cos\eta = \Delta\nu_{\mathrm{R}}/\Omega_R$
Γ_1	longitudinal relaxation (depolarization) rate, $\Gamma_1 = 1/T_1 = \gamma_\parallel + \gamma_\perp$
Γ_2	transverse relaxation (decoherence) rate, $\Gamma_2 = 1/T_2$
Γ_ν	pure dephasing due to noise at $\omega = 2\pi\Omega_R$
Γ_φ	pure dephasing rate, $\Gamma_\varphi = 1/T_\varphi$
λ	control parameter of the qubit Hamiltonian
ω_{avg}	angular cutoff frequency corresponding to the averaging time
ω_{uv}	angular upper cutoff frequency
ω_c	$1/f$ noise cutoff or transition angular frequency

$\Omega_{R,0}$	resonant Rabi frequency
Ω_R	Rabi frequency
$\tilde{\Gamma}_1$	relaxation rate in the rotating frame, $\tilde{\Gamma}_1 = 1/\tilde{T}_1$
$\tilde{\Gamma}_2$	decoherence rate in the rotating frame, $\tilde{\Gamma}_2 = 1/\tilde{T}_2$
$\tilde{\Gamma}_\varphi$	pure dephasing rate in the rotating frame
$\tilde{T}_1$	energy relaxation time in the rotating frame
$\tilde{T}_2$	unbroadened coherence time in the rotating frame
A_λ^2	amplitude of classical $1/f$ noise of parameter λ at $f = 1\,\mathrm{Hz}$
$f_{z,\mathrm{echo}}(t)$	spin echo decay function
$f_{z,\mathrm{exp}}(t)$	measurement dependent decay function
$f_{z,\mathrm{Rabi}}(t)$	Rabi oscillations decay function
$f_{z,\mathrm{Ram}}(t)$	Ramsey fringes decay function
$S_{\lambda,\mathrm{c}}(\omega)$	classical spectral density of noise of parameter λ
$S_{\lambda^2}(\omega)$	quantum spectral density of noise of parameter λ^2
$S_\lambda(\omega)$	quantum spectral density of noise of parameter λ
$S_{\Phi,1/f}(f)$	low frequency classical $1/f$ flux noise
$S_{q,1/f}(f)$	low frequency classical $1/f$ charge noise
$S_q(\omega)$	quantum spectral density of charge noise
$S_V(\omega)$	quantum spectral density of voltage noise
T'	Rabi oscillation decay time
T_1	energy relaxation time, $T_1 = 1/\gamma = \Gamma_1$
T_2	unbroadened coherence time, Ramsey fringes decay time
T_2^*	spectroscopic coherence time

T_{echo} decay time of the spin echo envelope

T_{φ} pure dephasing time

$W_{\text{echo}}(\omega,t)$ spin echo filter function

$W_{\text{exp}}(\omega,t)$ measurement dependent filter function

$W_{\text{Rabi}}(\omega,t)$ Rabi oscillations filter function

$W_{\text{Ram}}(\omega,t)$ Ramsey fringes filter function

Resonator parameters

$\bar{n}$ average number of photons in the resonator

κ photon decay rate, $\kappa = \omega_{res}/Q_L$

$\omega_{res}/2\pi$ resonator transition frequency

$a^{\dagger}, a$ creation, annihilation operators for photons in the resonator

C lumped element capacitance

C_c effective coupling capacitance of the resonator to the transmission line

L lumped element inductance

Q_e external quality factor

Q_i internal quality factor

Q_L loaded quality factor

Circuit QED parameters

χ dispersive shift of the resonator or qubit angular frequency, $\chi = g^2/\Delta$

Δ detuning between the qubit and the resonator, $\Delta = \omega_{CPB} - \omega_{res}$

$\gamma_{\perp}$ decay rate of the qubit into all non-cavity modes (non-radiative)

$\gamma_{\parallel}$ decay rate of the qubit into cavity modes (radiative)

$g/2\pi$ qubit-resonator coupling strength

n_{crit} critical photon number, for $n > n_{\mathrm{crit}}$ the dispersive approximation fails

Two-level system parameters

$\Delta E_{J,k}$ Josephson coupling energy between the CPB and the k-th TLS

$\Gamma_{1,TLS}$ TLS longitudinal relaxation (depolarization) rate, $\Gamma_{1,TLS} = 1/T_{1,TLS}$

$\Gamma_{2,TLS}$ TLS transverse relaxation (dephasing) rate, $\Gamma_{2,TLS} = 1/T_{2,TLS}$

$\omega_{TLS,k}/2\pi$ transition frequency of the k-th TLS

$E_{int,k}$ charge coupling energy between the CPB and the k-th TLS

$E_{R,k}$ well asymmetry energy of the k-th TLS

$g_{TLS}/2\pi$ qubit-TLS coupling strength

$T_{1,TLS}$ TLS energy relaxation time, $T_{1,TLS} = 1/\Gamma_{1,TLS}$

T_{12} direct TLS-TLS coupling energy

$T_{2,TLS}$ TLS unbroadened coherence time, $T_{2,TLS} = 1/\Gamma_{2,TLS}$

$T_{LR,k}$ tunneling energy of the k-th TLS

1 Introduction

1.1 Quantum Computation

Quantum information processing involves using quantum superposition and entanglement, along with classical state information, to perform computation. At the time of this writing the idea of quantum computing is over 30 years old. Although Feynman is often credited as the spiritual father of the field [1], others had proposed similar ideas and had even begun extending the theory of computation to the quantum world [2, 3]. Despite this early work, the field lay nearly dormant for a decade until Shor's factoring algorithm [4] and Grover's search algorithm [5] sparked renewed interest in the theory. The first experimental attempts were based on trapped ions [6] and nuclear magnetic resonance (NMR) [7, 8]. The examination of many other quantum systems soon followed. Additionally, theoretical work began to include more practical aspects of quantum computing. Shor and Steane both developed quantum error correction protocols [9, 10] while DiVincenzo identified the necessary criteria for creating a quantum computer [11]. The field has been very fruitful and is rapidly growing at this time. Today, candidate quantum computing platforms include trapped atoms and ions [6, 12], quantum dots [13], confined 2D electron gasses [14], superconducting circuits [15, 16, 17], donors in silicon [18], nitrogen impurities in diamond [19, 20] and optical systems [21]. Great progress has also been made in the theoretical understanding of both fundamental quantum information theory and practical obstacles to physical implementation. These advances include a deeper understanding of decoherence processes and how to ameliorate them [22, 23] as well as novel error reduction schemes such as topological protection [24]. Finally the field of quantum computing itself has advanced enough to begin cross-pollinating with other fields and sprouting new areas of research. For example, circuit quantum electrodynamics (cQED) [25] has emerged as an interesting area because it allows access to previously inaccessi-

ble regimes of cavity quantum electrodynamics (QED). Other examples include quantum noise limited amplifiers [26], which have promising applications both within and outside quantum computing, and hybrid systems in which nanomechanical resonators coupled to qubits [27] present novel and unexplored physical systems. With both incremental progress and disruptive developments occurring at a rapid pace, quantum computing is a vibrant field with a very bright future.

Motivations for pursuing quantum computing research may be placed into two broad categories: pure and applied. Pure goals include exploration of novel quantum systems or new regimes of existing quantum systems. Applied goals are typically more long term and mainly comprise the research, development and production of a quantum computer. Such a device would have one significant advantage over a classical computer, namely algorithmic speedup of some key functions. The time complexity of an algorithm describes the scaling of the computation time of that algorithm with the size of the input N. For instance, Shor's factoring algorithm [4] is exponentially faster than its classical counterpart while Grover's search algorithm [5] offers a quadratic speedup. Exponential speedup would mean that as the size N of the input grows, a problem that would take centuries to solve on a classical computer could be solved in minutes on a quantum computer. Once a quantum computer of a sufficiently large size is built, the currently known algorithms—Grover's search, Shor's factoring and others—could have significant impact on fields such as cryptography and potentially bioinformatics. Ultimately, the biggest impact of quantum computing may be in the area of practical quantum simulation of physical systems. As the size of an interacting quantum system grows, the time necessary to model the behavior of such a system on a classical computer grows exponentially. On the other hand, a quantum computer would be able to simulate any other quantum system with at most a polynomial slowdown. Many systems that are of interest to industry and academia consist of hundreds to hundreds of thousands of interacting atoms, a number too large to be examined analytically and too small for the application of statistical mechanics. One can imagine a future where, rather than relying on brute force trial and error or slow classical supercomputers to perform drug design, biochemists utilize quantum computers to design and test new cures with the same efficiency and throughput as modern industrial projects employing computer-aided engineering. Although early computers such as the Colossus [28] and the ENIAC [29] were used for narrow applications such as wartime code break-

ing and calculating artillery firing tables, modern computers have revolutionized every aspect of human life. While it's very difficult to predict the impact that quantum computing will have on society, it's safe to say that eventually it will be significant.

A key short term goal in quantum computing involves the physical realization of a small scale quantum computer. This requires development of single qubits and their corresponding readout and control, reducing single qubit errors and defects and implementing architectures to scale the system to many qubits.

Qubits are the basic building blocks of a quantum computer, the quantum version of bits in a classical computer. A qubit is a quantum two-level system that can be manipulated and measured and whose physical state is used to encode information. In principle, any quantum two-level system could be used as a qubit and in practice many candidate systems have been considered. Each approach has it's own set of advantages and drawbacks, usually involving trade-offs between coherence, scalability and readout. The difficulty in choosing a qubit is due to the inherently contradictory nature of the requirements of a quantum computer. Control and readout, and to a lesser extent scalability, require active manipulation of the qubit and coupling to other qubits, readout circuitry and the environment. Unfortunately the information stored in a qubit is very fragile—the state of a single atom or electron is quite easy to perturb—and unwanted or uncontrolled interactions very easily destroy a quantum state. This destruction or loss of information about a quantum state is called decoherence.

Some systems, such as trapped atoms or ions, are very well isolated from their environment and other undesired interactions. Such systems can have coherence times on the order of seconds [30]. This performance comes at the cost of physical size and difficulty scaling to multiple qubits for the simple reason that atom traps are large objects and building multiple qubits takes additional resources. Miniaturized atom trap chips [31] have been developed to address some of these issues, but these systems still face limitations in performance. At the other end of the spectrum are superconducting circuits, quantum dots and other solid-state implementations. Made with standard microfabrication techniques, these systems are significantly easier to scale, tune and couple. This comes at the cost of lower coherence times, typically in the $1-10\,\mu$s range for superconducting qubits, due to lossy materials in the immediate environment and strong coupling to noise sources. In an interesting parallel, as atom and ion trap researchers have worked

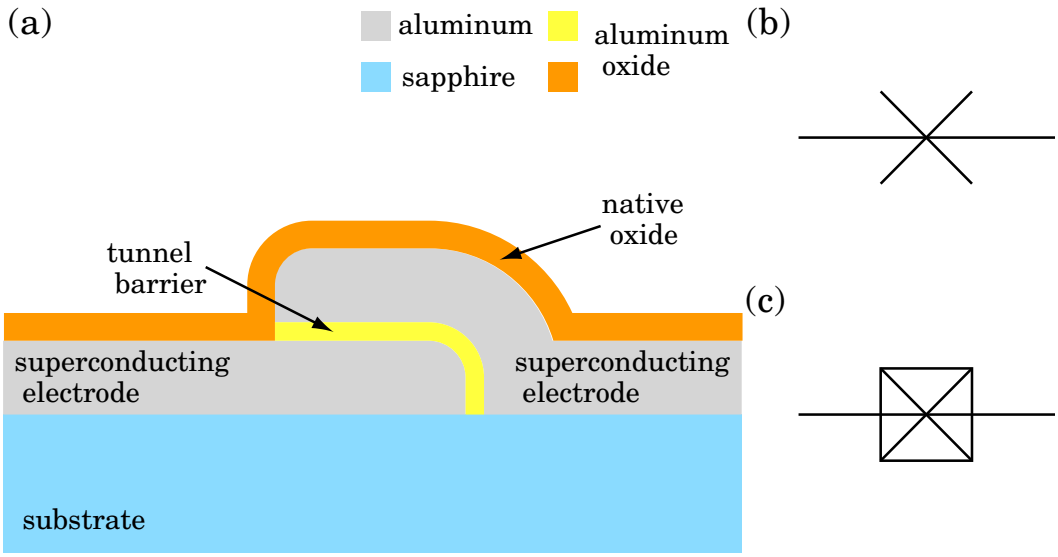

Figure 1.1: (a) Cross section of a Josephson junction. The color legend identifies materials commonly used in superconducting qubits. (b) Circuit symbol for a pure Josephson element or a large area Josephson junction. (c) Circuit symbol for a Josephson junction with non-negligible charging effects, i.e. an ultrasmall junction.

to shrink their systems, researchers working on superconducting qubits have been making their systems larger while decoupling the qubit from the environment [32], producing systems that more closely resemble an artificial atom in a cavity.

1.2 Superconducting Qubits

Superconducting qubits may be thought of as quantized electrical circuits. Nevertheless, the conceptual framework of classical electrical engineering provides insight into their operation. The fundamental building block of all superconducting qubits is the Josephson junction [33]. In the language of electrical circuits, a Josephson junction is a lossless, nonlinear inductor. Physically it consists of two superconducting electrodes separated by a thin insulating barrier (typical thickness $\approx 1\,\mathrm{nm}$) [see Fig. 1.1(a)]. The barrier coherently couples the superconducting wavefunctions in the two electrodes and allows tunneling of Cooper-pairs (the carriers in a superconductor) between them.

While an ideal Josephson element is a pure nonlinear inductance [see Fig. 1.1(b)], a real Josephson junction also has an associated shunting capacitance and resistance. The capacitance arises from the geometrical configuration of a typical junction, namely two conductors separated by a dielectric. The energy scale associated with current flowing in the Josephson inductance [33] is called the Josephson energy E_J while the energy scale

associated with charging of the junction capacitance is the charging energy E_c. The combination of Josephson inductance and junction capacitance bears a strong resemblance to one of the simplest circuits—the LC oscillator—but with an important difference. The nonlinearity of the Josephson inductance guarantees that the oscillator will be anharmonic, that is the level spacing isn't uniform and it's possible to address individual levels. If the level spacing were uniform a control pulse could cause transitions to higher excited states and it wouldn't be possible to use Josephson junctions as qubits.

Josephson junction circuits also meet the two conditions necessary to quantize a circuit [34]. First, in order for discrete energy levels to be resolvable, the widths of the spectral lines must be smaller than their spacing which in turn implies that the quality factor Q must obey $Q \gg 1$. This is readily achieved with isolated superconducting circuits as their residual resistance is typically very small. Second, thermal fluctuations will tend to wash out quantum coherent behavior unless $k_B T \ll \hbar\omega$, where T is the temperature and $\hbar\omega$ is the transition energy of the oscillator. The transition frequency ω of Josephson circuits can be tuned to the GHz range. This is both experimentally convenient and corresponds to temperatures of several 100 mK, significantly larger than typical dilution refrigerator temperatures of ≈ 25 mK.

Josephson junctions are in other ways conducive to use as qubits. Their nature as circuit elements lends itself well to integration with other circuitry needed for qubit readout and control and their parameters are easily adjusted during design and fabrication, leading to many options for qubit type and optimization.

There are three basic qubit types based on Josephson junctions: phase, flux and charge. The difference among them is the choice of quantization variable and consequently the corresponding dominant physical quantity and energy scale. The phase qubit [17] consists of a dc current biased Josephson junction and is called so because the phase of the superconducting wavefunction across the tunnel barrier is the quantized quantity [see Fig. 1.2(a)]. Varying dc current varies the anharmonicity of the qubit and also tunes the transition frequency ω_{01} between the ground and first excited state. In a phase qubit the Josephson energy $E_J = \Phi_0 I_0/2\pi$ is much larger than the charging energy $E_c = e^2/2C_j$ and consequently the phase across the junction is well-defined while the total charge that has tunneled across is not. Here I_0 is the junction critical current and C_j is the capacitance shunting the junction.

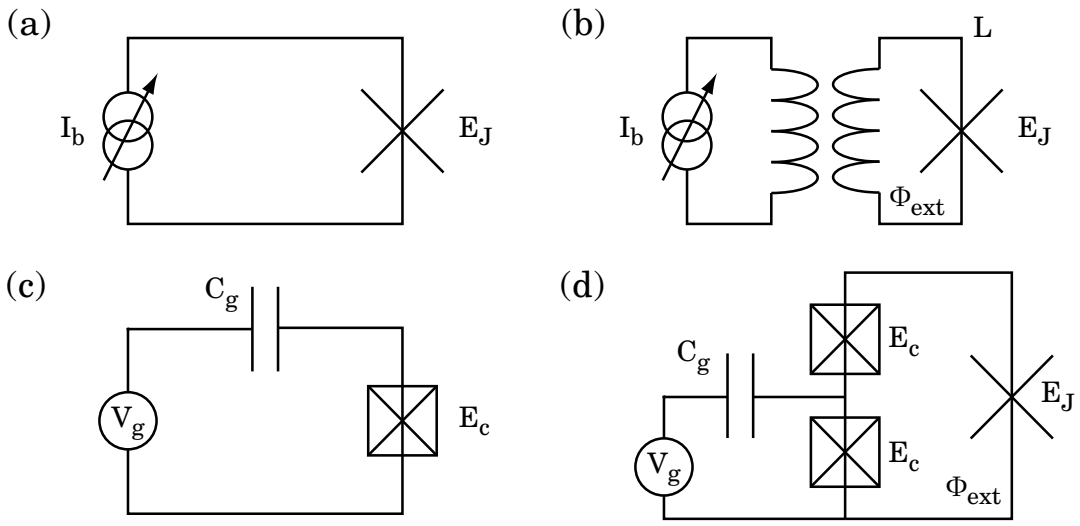

Figure 1.2: Simplified schematics of the various superconducting qubit types. (a) Phase qubit. (b) Flux qubit. (c) Charge qubit. (d) A hybrid design.

A flux qubit [16] consists of a superconducting loop interrupted by one or more Josephson junctions [see Fig. 1.2(b)]. Its basic operating principle utilizes Josephson junction anharmonicity along with the fact that the flux passing through a superconducting loop is quantized in integer multiples of the magnetic flux quantum Φ_0. The circulating current around the loop can flow either clockwise, counter-clockwise, or both and is used as the qubit state variable. An external flux bias is used to tune the transition frequency ω_{01} between the ground and first excited state. Similar to a phase qubit, the Josephson energy E_J of a flux qubit is larger, but not much larger, than the charging energy E_c. Therefore the circulating current, which is a function of the phase across the tunnel barrier, is a relatively well-defined quantity.

A charge qubit, also called a Cooper-pair box (CPB) [15, 35, 36], consists of one or two Josephson junctions connected to a superconducting island [see Fig. 1.2(c)]. A CPB differs from the other two qubit types in that $E_c \gg E_J$, i.e. the charging energy dominates the Josephson energy. This limit can be reached by using an ultrasmall area ($\approx 100 \times 100\,\mathrm{nm}^2$) junction. The small area yields a small junction capacitance C_j and the charging energy $E_c \propto 1/C_j$ is large [see Fig. 1.1(c)]. As a consequence of this the phase across the junction isn't well defined while the charge that has tunneled across is a good quantum number. In effect, the junction behaves as a highly nonlinear capacitor instead of an inductor [37]. In a charge qubit the qubit states are the number of excess Cooper-pairs on a superconducting island and the transition frequency is controlled by an applied gate

voltage.

Numerous variations and hybrid superconducting qubits have been developed in addition to the three basic types [see Fig. 1.2(d)]. Most have been derived from the CPB or phase qubit and involve the addition of shunting capacitors or inductors. They usually operate in the $E_c \lessapprox E_J$ range where charging effects are weakly dominant. Examples of such qubits include quantronium, which is a CPB shunted by a single large Josephson junction [38], transmon, which is a capacitively shunted CPB or an unbiased phase qubit [39], and fluxonium, [40] which is an inductively shunted CPB. The benefits of such hybrid designs include different readout capabilities and improved performance via reduced sensitivity to noise and junction defects.

The same properties that offer superconducting qubits their advantages over other approaches also lead to their drawbacks. In a Josephson junction, the phase is a macroscopic degree of freedom, akin to the center of mass of a physical object, representing the collective behavior of a large number of Cooper-pairs. The macroscopic nature facilitates strong coupling to the environment or other systems and allows simple integration with control and readout circuits and coupling between multiple qubits. In contrast, the degrees of freedom of trapped atoms or ions are microscopic and are very weakly coupled to their surroundings. The strong coupling capabilities of superconducting qubits can readily lead to undesirable coupling to environmental noise sources or spurious degrees of freedom. Such uncontrolled coupling leads to energy relaxation and dephasing, the two principal effects that produce decoherence. Relaxation is energy loss to the environment and results from coupling to lossy materials or electromagnetic modes. Energy loss is characterized by the relaxation time T_1 and limits the time available for qubit state measurement. Pure dephasing is loss of information about the quantum mechanical phase of superpositions of states of the system and limits the time available for computation. It may be caused by unwanted entanglement, interaction with other quantum mechanical systems such as individual material defects, or by external noise.

The tunability of superconducting qubits brings with it some additional drawbacks. If the transition frequency ω_{01} is set by an external control parameter, then noise in that control parameter will translate into fluctuations of ω_{01} which in turn lead to an uncertainty in the phase and dephasing. Variations during fabrication of a qubit carries with it its own set of consequences. Statistical variation during production means nominally

identical qubits may turn out to be different, which poses challenges to scaling. Even more detrimental are material defects that are present in all physical devices. Josephson junction qubits are particularly susceptible to individual atomic-scale charged defects in or near the tunnel barrier. Individual defects behave as quantum mechanical systems and may couple strongly to the qubit, acting both as sources of relaxation and dephasing. Again there is an interesting contrast with trapped atoms or ions for which the properties are set by nature and don't have the flexibility nor the uncontrolled variability of superconducting qubits.

Unlike undesired coupling to noise sources, coupling to control and readout circuitry is necessary for proper qubit operation. For superconducting qubits this is readily achieved—they are circuit elements after all—by wiring up the qubit to control and readout elements. Quantum control involves sending pulses to the qubit, typically at or near the transition frequency, to deterministically change the state of the qubit. The tunability of superconducting qubits allows the transition frequency to be placed in the low microwave bands where relatively cheap and convenient sources, detectors and other equipment are available. Unfortunately this coupling carries with it a set of drawbacks, some due to system non-ideality and some due to fundamental constraints of quantum mechanics. Even with adequate filtering, control lines act as channels for noise and a balance must be maintained between sufficient coupling to operate the qubit and excessive coupling leading to short coherence times. Part of the difficulty lies in the fact that it's impossible to construct a perfect filter that functions from radio frequency to infrared and beyond. This is an issue because even a single stray infrared photon propagating down a control line has the energy necessary to break many Cooper-pairs into high energy quasiparticles (electrons) which then proceed to generate a cascade of additional quasiparticles and other excitations. The resultant population is above the expected thermal level based on the physical temperature of the setup and can cause decoherence and other issues with qubit control [41, 42].

Qubit readout is the process of determining the state of a qubit. This is done by projecting the qubit state onto the state of another system and subsequently measuring that state with a classical apparatus. This readout system is ideally more robust and easier to detect than the qubit itself and typically the measurement is of a semiclassical variable such as a voltage or a phase of a microwave signal. Occasionally, such as with phase

qubits or optical photons, this system is the same physical element as the qubit itself. More often it's a coupled element such as a resonator [25] or SQUID [43], that acts as a detector such that the transition probability between its states depends on the state of the qubit.

The simple picture of qubits as circuit elements breaks down when discussing readout. The qubit and readout components are intimately connected and the act of determining the qubit state simultaneously and unavoidably affects that state. This quantum measurement back-action is a consequence of one of the fundamental rules of quantum mechanics: the act of measurement projects the system being measured to one of the eigenstates of the operator corresponding to the measured observable, commonly known as wavefunction collapse. Depending on the choice of readout scheme, it's possible to mitigate [44] or even exploit this effect [45]. Here again, the strong coupling possible in superconducting qubits confers potential advantages by allowing many options for readout schemes and granting access to regimes not accessible in other systems.

1.3 Circuit Quantum Electrodynamics

While there are many readout schemes, one in particular is both exceptionally elegant and versatile. Circuit quantum electrodynamics (cQED) involves coupling a qubit to a high quality factor resonator [25]. As a consequence of the coupling, changes in the qubit state shift the resonance frequency of the resonator which is subsequently measured, typically by recording the transmission through the resonator circuit. Heuristically, if the resonator is imagined as an LC oscillator circuit, then in the case of weak coupling the qubit can be considered as an additional state-dependent capacitance which loads the oscillator and shifts the resonance frequency. The cQED readout method possesses several key advantages. Under ideal circumstances the fraction of the probe signal that is not transmitted through the resonator is reflected back; no power is dissipated in the circuit. The lack of on-chip energy dissipation during readout eliminates a potentially significant noise source and improves qubit performance. Second, the readout does not measure the phase, flux or charge of the corresponding qubit but projects to the qubit energy eigenbasis. Furthermore, this coupling is via a second order (dispersive) quantity such as the electric or magnetic susceptibility, and consequently minimizes energy decay

via the readout.

In the case of a CPB, the coupling to a resonator is due to an effective electric dipole moment of the qubit rather than simply the charge. By avoiding direct charge coupling, the readout can be arranged so that relaxation and dephasing via the readout channel is reduced. Additionally, it's possible to operate a CPB qubit at the charge degeneracy point, a region not amenable to charge readout but possessing reduced sensitivity to charge noise. Finally, as a consequence of embedding the qubit in a resonator circuit, the resonator can serve a dual role, as a detector and also as a narrow-band filter, blocking some noise from reaching the qubit. In practice, by detuning the qubit transition from the resonance frequency of the resonator, the spontaneous decay rate of the qubit from electromagnetically radiating is reduced by the Purcell effect [46, 47].

The theory of quantum measurement imposes constraints on the readout process that aren't present when determining the state of a classical variable. One such limitation—wavefunction collapse—has already been mentioned in section 1.2. Due to its simplicity and flexibility, circuit QED is an exemplary system for elucidating the nature of quantum measurements. In a simplified picture of the readout process, a photon enters the resonator and probes the joint qubit-resonator state, in the process becoming entangled with the qubit. It then leaves the resonator, carrying with it information about the qubit state. When a classical amplifier detects this quantum photon and converts it to a more robust classical signal, it simultaneously measures and influences the qubit state. This is an example of what Einstein termed "spooky action at a distance" [48].

The quantum measurement process may further be classified as strong or weak [49]. Elaborating on the picture outlined above, the strength of a readout indicates how many photons it takes to fully determine the qubit state. In a strong measurement a single photon carries with it all the information about the qubit state whereas in a weak measurement it takes many such photons to determine the state of the qubit. This strength is set by the strength g of the qubit-resonator coupling and the degree of the subsequent qubit-photon entanglement. At first glance it might seem a strong readout is preferable to a weak one as it allows information to be acquired quickly. However in the quantum world, a weak measurement also implies a partial collapse of the wavefunction, a property that is very advantageous if one wants to avoid significantly perturbing the qubit. Additionally, weak readout is useful in situations where it's not possible to strongly cou-

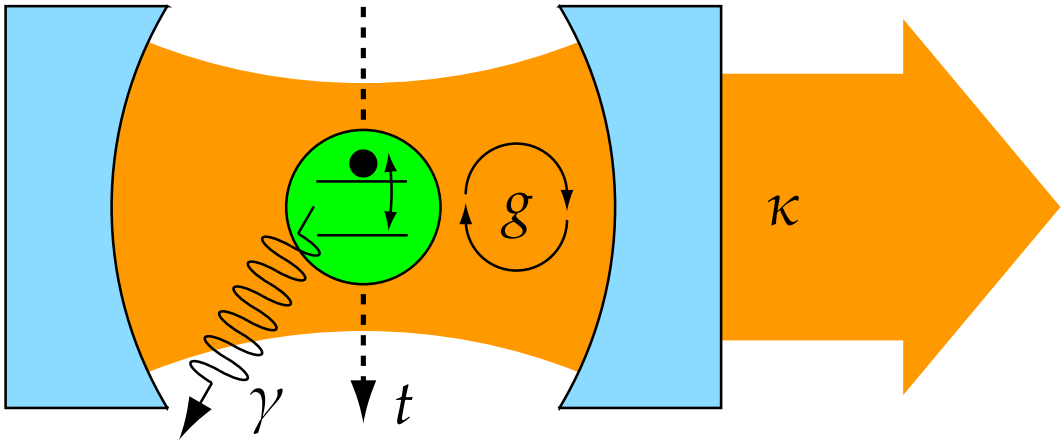

Figure 1.3: Schematic of a typical optical cavity QED setup. An atom with two energy levels (green) interacts with a single photon mode (orange) confined by mirrors (blue) to form a cavity. The black dot is an electron occupying one of the atom's energy levels. g is the atom-photon interaction strength, κ is the photon decay rate, γ is the atom decay rate and t is the atom transit time through the cavity. Adapted from Jeff Kimble's group at Caltech [51].

ple the qubit to the resonator or when the presence of noise necessitates a long signal integration time.

In addition to measurement induced wavefunction collapse, measurement back-action is another consequence of coupling the qubit to a readout system. Just as the state of the qubit modulates the resonance frequency of the resonator, photons in the resonator shift the qubit transition frequency ω_{01}. This AC Stark shift [50] may produce qubit dephasing. This behavior emphasizes that the qubit and the readout are intimately connected and are no longer completely separate physical systems.

While up to this point circuit QED has been discussed in the context of qubit readout, there's much more to it than that. It's a rich system for studying the interaction of light and matter on a fundamental level. In particular, circuit QED was initially inspired by cavity QED [52, 53], which involves atoms and 3D optical cavities [see Fig. 1.3]. While the interaction between an atom and a single photon in free space is too weak to study quantum coherent behavior in detail, the confinement of photons in a small optical cavity can increase this interaction strength by several orders of magnitude. This permits the observation and manipulation of effects involving individual atoms and photons.

Circuit QED expands on this idea by leveraging the strengths of superconducting qubits

Table 1.1: Summary of the key qubit and resonator parameters for the two devices that were studied in detail. See Ch. 2 and Ch. 3 for definitions of these parameters.

device	Device 1	Device 2
resonator parameters		
$\omega_{res}/2\pi$	5.446 GHz	5.472 GHz
Q_L	22,000	35,000
Q_i	32,000	147,000
Q_e	70,000	47,000
CPB parameters		
E_J^{sum}	19 GHz	7.33 GHz
E_c	6.24 GHz	4.3 GHz
C_g	4.5 aF	19.1 aF
g	5 MHz	15 MHz
qubit performance		
T_1	$30-200\,\mu$s	$4-30\,\mu$s
T_2	$200-500$ ns	$\gtrsim 60$ ns
T_{echo}	$2.4-3.3\,\mu$s	—
T'	$1-2\,\mu$s	$0.2-1.8\,\mu$s

as tunable artificial atoms to further increase the coupling strength and enable exploration of previously inaccessible coupling regimes. Along with greater understanding of basic physics, this may lead to new approaches for single microwave photon generation and detection. When applied to quantum information processing, circuit QED has applications beyond readout. The exceptional control available to superconducting qubits and resonators allows resonators to be used as a quantum bus or quantum memory [54, 55, 56]. The initial success of circuit QED with charge qubits has led to its widespread adoption for use with other types of superconducting qubits [57, 56] and even other solid state quantum computing implementations [58]. This approach continues to yield impressive and impactful results and shows great promise for use in reaching the ultimate goal of creating a scalable quantum computer.

1.4 Thesis Overview

One of the goals of experimental quantum computing research is understanding and minimizing the impact of environmental noise and other deleterious interactions. My research consisted of quantifying the decoherence of two charge qubits (Device 1 and Device 2) that were weakly coupled to on-chip LC resonators [see Table 1.1]. The characterization of Device 1 was initiated by another group member, Z. Kim, who observed a strong correlation

between the exceptionally long energy relaxation time T_1 and the Rabi coupling strength, which was determined from the dependence of the Rabi frequency on drive voltage [59]. I continued that work by quantifying the dephasing properties of that sample. I review CPB and circuit QED basics in Chapter 2 and go over the theory of decoherence in a CPB in Chapter 3. The experimental setup I used for my work is described in Chapter 4. As detailed in Chapter 6, I performed Ramsey fringe and spin echo experiments and extracted the Ramsey fringe decay time T_2 and spin echoes envelope decay time T_{echo}. While the relaxation time T_1 placed bounds on the high frequency noise affecting the qubit, I used my dephasing measurements to calculate bounds on the low frequency components of the noise. Together with the previous data, this provided a more complete picture of the spectrum of noise coupled to the qubit.

The fabrication details of Device 2 may be found in Chapter 4 while Chapter 5 contains a description of the preliminary characterization of that sample. In Chapter 6, I discuss how I confirmed the reproducibility of the correlation between T_1 and Rabi coupling by performing a similar characterization of the second CPB qubit. Although the results were not as clear cut as those of Device 1, I did observe a similar correlation in Device 2. In the course of acquiring that data, I observed anomalous features in the transition spectrum of Device 2. As discussed in Chapter 8, I took detailed measurements of these features and afterward developed a theoretical model, derived in Chapter 7, to explain them. My model expanded on an earlier model developed by F. C. Wellstood [60] to explain anomalous splittings observed by Z. Kim in the spectrum of a CPB qubit with an RF-SET readout [61]. By fitting the spectrum predicted by my model to the experimentally determined spectrum, I extracted the microscopic physical parameters of the two-level system (TLS) responsible for the anomalies. In Chapter 9 I review my results and propose possible follow up experiments.

2 Circuit QED With the Cooper-Pair Box

2.1 Josephson Junction Basics

The fundamental building block of all superconducting qubits is the Josephson tunnel junction [33]. The most common implementation used in quantum computing bears a strong resemblance to a parallel plate capacitor in that it consists of two superconducting electrodes separated by a thin ($\approx 1\,\mathrm{nm}$) dielectric barrier. The barrier is sufficiently thin so that the phase of the superconducting condensate in the two electrodes is linked by tunneling of Cooper-pairs. The classical dynamics of a junction are governed by the two Josephson relations [33]

$$I_J = I_0 \sin\gamma \tag{2.1}$$

$$\frac{d\gamma}{dt} = \frac{2\pi}{\Phi_0} V_J. \tag{2.2}$$

I_J is the supercurrent flowing through the junction, V_J is the voltage difference across the two electrodes, γ is the gauge-invariant difference of the phases of the superconducting wavefunctions in the two electrodes, I_0 is the critical current of the Josephson junction, $\Phi_0 = h/2e$ is the magnetic flux quantum, t is time, and $e = 1.602 \times 10^{-19}\,\mathrm{C}$ is the magnitude of the charge of an electron. At zero voltage, a supercurrent I_J can flow across the junction, up to a maximum value of I_0. If there is a constant voltage drop across the junction, then the phase difference across it will evolve at a rate proportional to V_J leading to an ac current of amplitude I_0 and frequency $2\pi V_J/\Phi_0$. These two behaviors are known, respectively, as the dc and ac Josephson effects.

We may obtain an effective junction inductance by taking the time derivative of Eq.

2.1, combining with Eq. 2.2 and eliminating γ in favor of I_J. The resultant relation is

$$V_J = \frac{\Phi_0}{2\pi I_0} \frac{1}{\sqrt{1-(I_J/I_0)^2}} \frac{dI_J}{dt}. \tag{2.3}$$

Comparing with the current voltage relationship for an inductor, $V = LdI/dt$, we see that we can define the Josephson inductance as

$$L_J = \frac{\Phi_0}{2\pi I_0} \frac{1}{\sqrt{1-(I_J/I_0)^2}}. \tag{2.4}$$

Notice that $L_J \approx \Phi_0/2\pi I_0$ for $I_J \ll I_0$ and L_J increases with increasing $I_J < I_0$. From Eqs. 2.3 and 2.4 we see that an ideal Josephson junction behaves as a lossless, nonlinear inductor.

In the discussion so far we have neglected the energy stored in the geometric capacitance C_j due to the junction leads. To help understand the effect of this capacitance, we first consider the energy accumulated in the Josephson junction when a supercurrent flows through it. The electrical work done on the junction by an external source supplying current to the junction is given by $\int I_J V_J dt$ with I_J and V_J given by Eq. 2.1 and 2.2. Integrating we obtain an expression for the potential energy:

$$U = -\frac{\Phi_0 I_0}{2\pi}\cos\gamma = -E_J\cos\gamma \tag{2.5}$$

with the Josephson energy $E_J = \Phi_0 I_0/2\pi$. Combining Eq. 2.5 with the charging energy of the junction, the total energy of an isolated junction is then given by

$$\begin{aligned} E &= -E_J\cos\gamma + \frac{1}{2}C_j V_J^2 \\ &= -E_J\cos\gamma + \frac{1}{2}C_j\left(\frac{\Phi_0}{2\pi}\right)^2\left(\frac{d\gamma}{dt}\right)^2. \end{aligned} \tag{2.6}$$

In this form, we can easily identify potential energy and kinetic energy terms. Furthermore, for $\gamma \ll 1$, $\cos\gamma \approx 1-\gamma^2/2$, and this reduces to the energy of a simple harmonic oscillator. Analogous to the development of a quantum simple harmonic oscillator [62], we note that γ and $i\frac{\partial}{\partial\gamma}$ are conjugate variables. Using $Q = CV = C(\Phi_0/2\pi)d\gamma/dt$ we make the operator replacement $-Q/2e = N \rightarrow i\frac{\partial}{\partial\gamma}$ and obtain the Hamiltonian for an isolated Josephson junction:

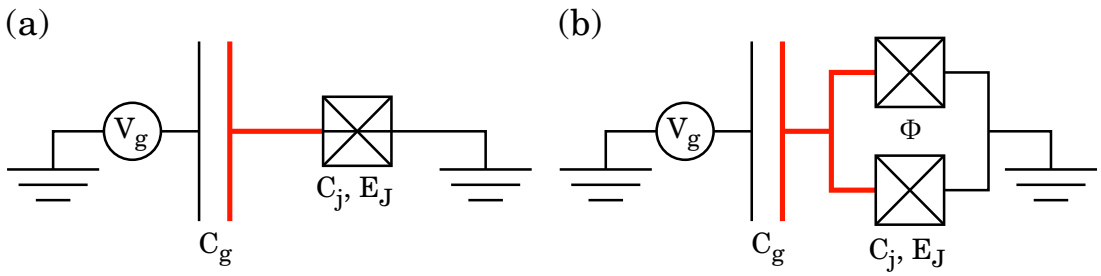

Figure 2.1: Schematics of basic and split Cooper-Pair boxes. (a) A basic CPB with a single Josephson junction of capacitance C_j and Josephson energy E_J. (b) A split CPB with two Josephson junctions each with junction capacitance $C_j/2$ and Josephson energy $E_J/2$. In both diagrams the CPB island is marked in red and is capacitively coupled to a voltage bias V_g with capacitance C_g. Applying flux Φ to the loop formed by the two junctions modulates E_j.

$$H = -E_J \cos\gamma - 4E_c \frac{\partial^2}{\partial\gamma^2} \tag{2.7}$$

or:

$$\hat{H} = -E_J \cos\hat{\gamma} + 4E_c \hat{N}^2 \tag{2.8}$$

where $E_c = e^2/2C_j$ is the charging energy and N is the number of Cooper-pairs that have tunneled across the junction. From Eq. 2.8 we see that E_J and E_c form two competing energy scales that determine the optimal quantization basis, either the phase γ or the charge N. For large area junctions, often found in phase qubits [63], C_j is large and hence E_c is small and the phase is well defined. Junctions used in superconducting charge qubits are in the opposite limit, as discussed in detail in the following section.

2.2 Cooper-Pair Box Qubit

In the limit $E_c \gg E_J$ the charging energy dominates and charge, rather than phase, is the well defined quantum variable. We consider a typical experimental Cooper-pair box (CPB) qubit [15, 35, 36] consisting of a superconducting island coupled to a voltage bias V_g with capacitance C_g and connected to a grounded superconducting reservoir by one or two Josephson junctions with charging energy $E_c \gg E_J$ [see Fig. 2.1(a)]. To simplify the analysis, quasiparticle states will be neglected.

The potential of the island V_i is given by

$$V_i = \frac{C_g V_g - 2ne}{C_\Sigma} \tag{2.9}$$

where $C_\Sigma = C_j + C_g$ is the total island capacitance to ground and n is the number of excess Cooper-pairs on the island. The total electrostatic energy of the system is then

$$U_{el} = \frac{1}{2} C_g \left(V_g - V_i\right)^2 + \frac{1}{2} C_j (0 - V_i)^2 \tag{2.10}$$

which upon substituting Eq. 2.9 into Eq. 2.10 reduces to

$$U_{el} = \frac{C_g C_j V_g^2}{2C_\Sigma} + \frac{(2ne)^2}{2C_\Sigma}. \tag{2.11}$$

The work done by the voltage source when a Cooper-pair tunnels on or off the island is

$$W_{el} = 2eV_g \frac{C_g}{C_\Sigma} \tag{2.12}$$

which when subtracted from Eq. 2.11 gives the electrostatic free energy

$$\begin{aligned} E_{el} &= \frac{e^2}{2C_\Sigma} \left(2n - n_g\right)^2 + \frac{e^2}{2C_\Sigma} \left(\frac{C_j}{C_g} - 1\right) n_g^2 \\ &= E_c \left(2n - n_g\right)^2 + E_c \left(\frac{C_j}{C_g} - 1\right) n_g^2 \end{aligned} \tag{2.13}$$

where $E_c = e^2/2C_\Sigma$ and $n_g = C_g V_g / e$ is the reduced gate voltage. The second term in the expression is a constant with respect to n and may be discarded since it won't influence junction dynamics.

Combining the electrostatic free energy (Eq. 2.13) and the Josephson energy (Eq. 2.5) the Hamiltonian of a CPB is

$$\hat{H}_{CPB}\left(n_g\right) = E_c \left(2\hat{N} - n_g\right)^2 - E_J \cos\hat{\gamma}. \tag{2.14}$$

We may express the entire Hamiltonian in the charge basis by writing $\cos\hat{\gamma} = \frac{1}{2}\left(e^{i\hat{\gamma}} + e^{-i\hat{\gamma}}\right)$ and using $e^{\pm i\hat{\gamma}} |n\rangle = |n \pm 1\rangle$ [33]:

$$\hat{H}_{CPB}\left(n_g\right) = E_c \sum_n \left(2n - n_g\right)^2 |n\rangle\langle n| - \frac{E_J}{2} \sum_n \left(|n+1\rangle\langle n| + |n\rangle\langle n+1|\right) \tag{2.15}$$

where the summation is over all possible number of excess Cooper-pairs on the island. It's also possible to express the CPB Hamiltonian entirely in the phase basis. Using $N \rightarrow i\frac{\partial}{\partial\gamma}$ the Hamiltonian becomes

$$\hat{H}_{CPB}(n_g) = \int_0^{2\pi} E_c\left(2i\frac{\partial}{\partial\gamma} - n_g\right)^2 - E_J\cos\gamma\,|\gamma\rangle\langle\gamma|\,d\gamma. \tag{2.16}$$

The charge basis is preferred in most cases due to charge being the more sharply defined variable and because most interactions of the CPB with its environment or other systems occur via the charge degree of freedom. The wavefunctions in the phase representation may be obtained analytically using Mathieu functions [64] and become useful when the charging energy no longer dominates the Josephson energy.

In the limit $E_c \gg E_J$ the charging energy dominates and Eq. 2.13 describes the energy of a CPB. Minimizing the energy at a given n_g with respect to n we obtain $n = n_g/2$. However, for the eigenstates the number of Cooper-pairs must be a whole number, and the minimum in energy occurs at the integer closest to $n_g/2$. As the gate bias is increased from 0, the number of Cooper-pairs on the island remains the same until n_g is an odd integer value, at which point a single additional Cooper-pair tunnels onto the island [see Fig. 2.2]. This charge versus voltage bias relation is known as the Coulomb staircase. The corresponding energy curves consist of a family of parabolas with minima at odd integer values of n_g. Nearest neighbor parabolas intersect at odd n_g values at the energy E_c [see Fig. 2.3(a)]. As will be discussed in detail in Sec. 2.3.1, E_J acts to smooth out the corners of the Coulomb staircase and create avoided crossings where the electrostatic energy curves of different n intersect.

More discussion of the basic physics of the CPB is available in the textbook by M. Tinkham [33].

2.3 Split Cooper-Pair Box

The basic Cooper-pair box has a single charge degree of freedom and a single external bias V_g. This reduces its sensitivity to other types of noise such as flux but also restricts its operation. The more commonly employed design is that of the split Cooper-pair box. In this variation the superconducting island is connected to the grounded reservoir by two parallel Josephson junctions [see Fig. 2.1(b)] in a SQUID-like geometry. This allows

an externally applied flux to tune the effective Josephson energy E_J and opens up flux as another degree of freedom.

The electrostatic energy of a split CPB is the same as that of the basic CPB [see Eq. 2.13] but with $C_\Sigma = C_{j,1} + C_{j,2} + C_g$ where the indices 1 and 2 refer to the two Josephson tunnel junctions. The Josephson energy is the sum of the two individual Josephson energies

$$E_J = -E_{J,1}\cos\gamma_1 - E_{J,2}\cos\gamma_2 \tag{2.17}$$

where again the indices refer to the individual junctions. Defining two new variables θ and γ as

$$\begin{aligned} \theta &= \gamma_1 - \gamma_2 = 2\pi\Phi/\Phi_0 \\ \gamma &= \frac{\gamma_1+\gamma_2}{2}, \end{aligned}$$

allows the phase difference θ to be expressed in terms of the applied flux Φ using flux quantization. Substituting the new variables into Eq. 2.17 and using trigonometric identities leads to

$$\begin{aligned} E_J(\Phi) &= -\left(E_{J,1}+E_{J,2}\right)\cos\left(\pi\frac{\Phi}{\Phi_0}\right)\cos\gamma + \left(E_{J,1}-E_{J,2}\right)\sin\left(\pi\frac{\Phi}{\Phi_0}\right)\sin\gamma \\ &= -E_J^{\text{sum}}\cos\left(\pi\frac{\Phi}{\Phi_0}\right)\cos\gamma + d\times E_J^{\text{sum}}\sin\left(\pi\frac{\Phi}{\Phi_0}\right)\sin\gamma \end{aligned} \tag{2.18}$$

where $E_J^{\text{sum}} = E_{J,1} + E_{J,2}$ and $d = \left(E_{J,1} - E_{J,2}\right)/E_J^{\text{sum}}$. If we assume the ideal case of identical junctions, Eq. 2.18 simplifies to

$$\begin{aligned} E_J(\Phi) &= -E_J^{\text{sum}}\cos\left(\pi\frac{\Phi}{\Phi_0}\right)\cos\gamma \\ &= -E_J^{\text{eff}}\cos\gamma \end{aligned} \tag{2.19}$$

where $E_J^{\text{eff}} = E_J^{\text{sum}}\cos(\pi\Phi/\Phi_0)$. In other words the ideal split CPB behaves exactly as the basic CPB but with a flux tunable Josephson energy E_J^{eff}. In practice we found that our devices had $d \lessapprox 0.1$ and this required small corrections to be made to the CPB energy spectrum, as will be discussed at the end of this section. For the remainder of this dissertation, and unless specified, I will use CPB to refer to the split CPB and E_J to refer to E_J^{eff}.

As long as $E_c \gtrsim E_J$, the energy levels of the CPB are sufficiently anharmonic such that the ground $|g\rangle$ and first excited $|e\rangle$ states may be addressed independently of the higher levels and the CPB may be operated as a qubit. In this case in most situations of interest, we may safely ignore the higher lying levels and simplify analysis of the dynamics by approximating the CPB as a two-level system.

The eigenstates and energies of the CPB Hamiltonian may be calculated in either the charge or phase basis. When $E_c \gtrsim E_J$ the charge basis is the optimal choice for this calculation. Furthermore, if $E_c \gg E_J$ only two charge states are needed to accurately model the behavior at a given value of n_g. Keeping only $n = \{0,1\}$, as is appropriate for $0 \leq n_g \leq 1$, Eq. 2.15 truncates to

$$\mathbb{H}_{CPB}\left(n_g,\Phi\right) = \begin{pmatrix} E_c\left(0-n_g\right)^2 & -E_J/2 \\ -E_J/2 & E_c\left(2-n_g\right)^2 \end{pmatrix} \tag{2.20}$$

where the Φ dependence of E_J is given by Eq. 2.19. If $E_c \approx E_J$, additional charge states, typically $n = \{-1,0,1,2\}$, are kept in the truncation to improve the accuracy of the approximation. The simplification to a 2×2 matrix elucidates the roles of E_c and E_J: E_c determines the scale of the electrostatic energy parabolas associated with the charge states while E_J is a perturbation that serves to couple the charge states. Without E_J it would not be possible to change the charge state of the box at a fixed n_g.

The truncated CPB Hamiltonian is a 2×2 matrix and is readily diagonalized to yield the energies and eigenstates. The energy difference between the ground and excited state is given by

$$\hbar\omega_{CPB}\left(n_g,\Phi\right) = \sqrt{\left(4E_c\left(1-n_g\right)\right)^2 + E_J^2} \tag{2.21}$$

which at the avoided crossing at $n_g = 1$ is equal to E_J, the coupling strength between the two states. We can conveniently express the eigenstates of the Hamiltonian in terms of the $|0\rangle$ and $|1\rangle$ charge states by introducing the mixing angle

$$\theta_{\mathrm{m}} = \arctan\left(\frac{E_J}{4E_c\left(1-n_g\right)}\right) \tag{2.22}$$

which characterizes the relative rotation between the two basis. Using this notation the

eigenstates of the Hamiltonian are

$$\begin{aligned} |g\rangle &= \cos(\theta_{\rm m}/2)|0\rangle + \sin(\theta_{\rm m}/2)|1\rangle \\ |e\rangle &= -\sin(\theta_{\rm m}/2)|0\rangle + \cos(\theta_{\rm m}/2)|1\rangle\,. \end{aligned} \tag{2.23}$$

At the degeneracy point $n_g = 1$ the charge states are maximally coupled and the eigenstates are equal superpositions of the two charge states while at $n_g = 0$ or $n_g = 2$ the eigenstates are nearly pure charge states.

Following a similar construction, if $d \neq 0$ the energy difference between the ground and excited state is found to be

$$\hbar\omega_{CPB}\left(n_g,\Phi\right) = \sqrt{\left(4E_c\left(1-n_g\right)\right)^2 + E_J^{\rm sum\,2}\left(\cos^2\left(\pi\frac{\Phi}{\Phi_0}\right) + d^2\sin^2\left(\pi\frac{\Phi}{\Phi_0}\right)\right)}. \tag{2.24}$$

Comparing with Eq. 2.21, we see that the effect of the junction asymmetry is small, except as $\Phi/\Phi_0 \to 1/2$, even for values as large as $d \approx 0.2$.

A more in-depth discussion of the split CPB is available in the dissertation by A. Cottet [64].

2.3.1 Charge Staircase and Energy Levels

As derived in Section 2.2, the charge versus voltage relation of a CPB is the Coulomb staircase [see Fig. 2.2]. When $E_J = 0$ the charge states are uncoupled and the charge state closest to $n_g/2$ minimizes the energy. Exactly at $n_g = 1$ the system is in a superposition of charge states. The effect of E_J is to couple the charge states and round the steps of the staircase. For $E_J \ll E_c$ only two charge states contribute significantly to the ground state, but as E_J increases the contribution from additional charge states becomes increasingly important. More charge states must also be included to find higher level states or accurately describe the system outside of the region $0 \leq n_g \leq 1$.

The uncoupled $E_J = 0$ electrostatic energy curves are a series of parabolas that are centered at even values of n_g and have degenerate crossings at the odd values of n_g [see Fig. 2.3(a)]. E_J is a perturbation which lifts this degeneracy and produces an avoided crossing of, to first order, size E_J. The interplay of the two energy scales is visible in the transition spectrum [see Fig. 2.3(b)] given by the difference in energies between the

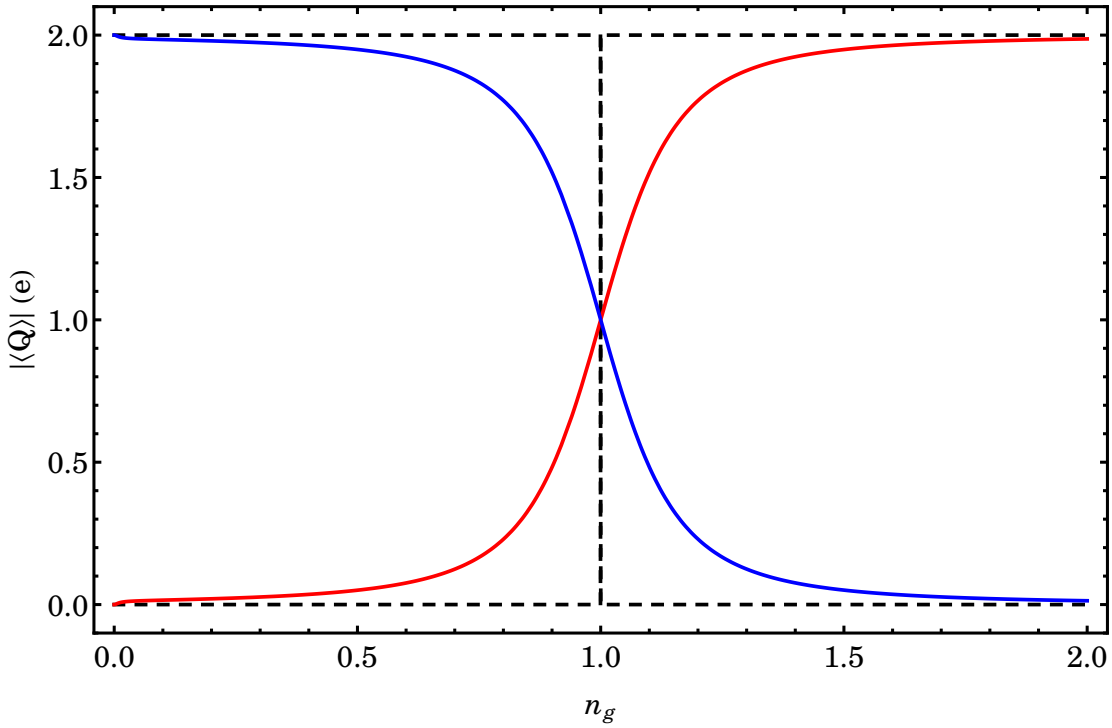

Figure 2.2: Expected value of the magnitude of the charge $|\langle Q\rangle|$ on the island of the CPB for the ground (red) and excited (blue) states for $E_J/E_c = 2/3$. The dashed black curves are the corresponding plots with $E_J = 0$, demonstrating the effect of E_J.

two states. At the degeneracy point $n_g = 1$ the minimum energy difference is E_J and the curve closely resembles a parabola with curvature $8E_c^2/E_J$. Away from $n_g = 1$ the transition energy varies approximately linearly with n_g reaching a maximum of $4E_c$.

2.3.2 Effect of Gate Voltage Perturbation

The CPB is a charge qubit and consequently its dominant interaction with control systems or the environment is typically via the charge degree of freedom. The interaction energy corresponding to a gate voltage perturbation δn_g—either due to an applied voltage or movement of nearby charges—and is given by $\left(\partial\hat{H}/\partial n_g\right)\delta n_g$. In the two-level charge representation we can write $\partial\hat{H}/\partial n_g$ as [see Eq. 2.14 or 2.20]

$$\begin{aligned}\frac{\partial\hat{H}}{\partial n_g} &= -2E_c\begin{pmatrix}(0-n_g) & 0\\ 0 & (2-n_g)\end{pmatrix}\\ &= -4E_c\hat{N}.\end{aligned} \tag{2.25}$$

The same unitary transformation that diagonalizes the two-state Hamiltonian trans-

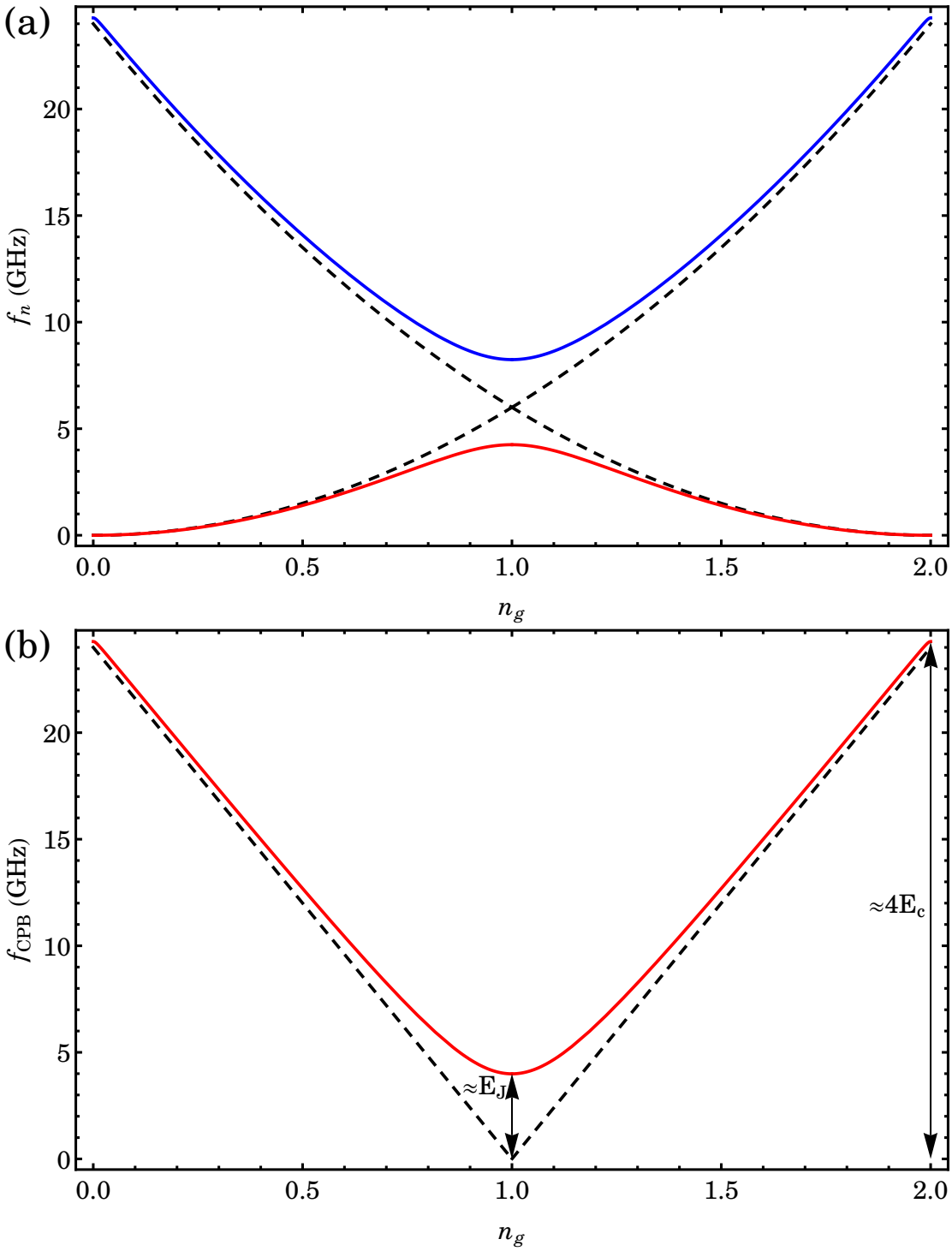

Figure 2.3: Plot of (a) the calculated energies $f_n = E_n/h$ of the ground (red) and excited (blue) states of the CPB and (b) the calculated transition spectrum $f_{CPB} = E_{CPB}/h = (E_1 - E_0)/h$ of the CPB versus n_g. The values of $E_c = 6\,\mathrm{GHz}$ and $E_J = 4\,\mathrm{GHz}$ are representative of the devices measured for this dissertation. The dashed black curves are the corresponding plots with $E_J = 0$, demonstrating the effect of E_J.

forms the above into

$$\begin{aligned}\frac{\partial \hat{H}}{\partial n_g} &= 4E_c\left(-\sin\theta_{\mathrm{m}}\frac{\hat{\sigma}_x}{2}+\cos\theta_{\mathrm{m}}\frac{\hat{\sigma}_z}{2}\right)\\ &= \frac{4E_c}{\hbar\omega_{CPB}}\left(-E_J\frac{\hat{\sigma}_x}{2}+\left(4E_c\left(1-n_g\right)\right)\frac{\hat{\sigma}_z}{2}\right)\end{aligned} \tag{2.26}$$

where σ_x and σ_z are Pauli spin operators and the second equality is obtained using Eq. 2.22. From Eq. 2.26 we can see that a static gate voltage perturbation δn_g shifts the transition frequency (the σ_z term) and mixes the levels only to second order (the σ_x term). At the charge degeneracy point $n_g = 1$ this simplifies to

$$\begin{aligned}\frac{\partial \hat{H}}{\partial n_g} &= -\frac{2E_cE_J}{\hbar\omega_{CPB}}\hat{\sigma}_x\\ &= -2E_c\hat{\sigma}_x.\end{aligned} \tag{2.27}$$

At this operating point a resonant gate perturbation may be used to manipulate the qubit but also resonant charge or voltage noise will induce transitions between the two states.

2.4 Lumped Element LC Resonator

Circuit QED [25] involves the physics of a resonator and a qubit that are coupled together. The CPB qubit has already been described in the previous section [see Sec. 2.3]. Here we discuss the physics of the other component, the lumped element superconducting resonator.

High frequency components are most commonly characterized in terms of their S-parameters or ABCD-parameters [65]. For a 2-port device the S-parameters characterize the reflection and transmission coefficients of the device and are defined by

$$\begin{pmatrix}V_1^-\\V_2^-\end{pmatrix}=\begin{pmatrix}S_{11}&S_{12}\\S_{21}&S_{22}\end{pmatrix}\begin{pmatrix}V_1^+\\V_2^+\end{pmatrix} \tag{2.28}$$

where $V^+_{\{1,2\}}$ are the incident voltage waves on ports $\{1,2\}$ and $V^-_{\{1,2\}}$ are the respective reflected voltage waves. S-parameters are more useful in practice as they can be directly measured by a vector network analyzer. The ABCD-parameters relate the total input and

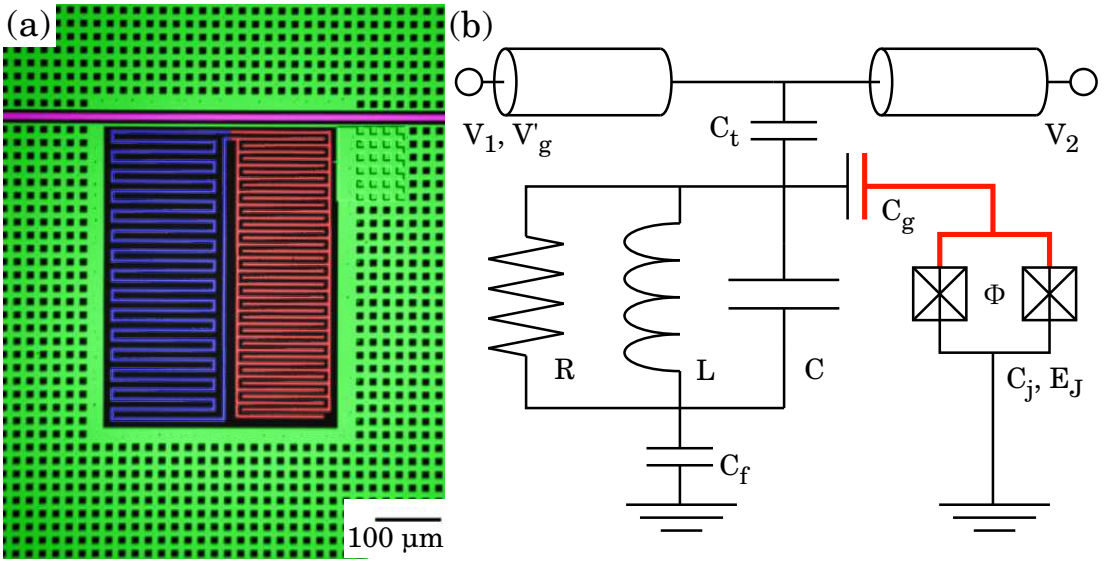

Figure 2.4: Schematics of the superconducting LC resonator and CPB qubit. (a) Colorized microscope image of the lumped element resonator showing the meander inductor L (blue), interdigital capacitor C (red), center conductor of the CPW (purple) and the surrounding ground plane (green). (b) Full circuit schematic including the LC resonator and CPB qubit. The inductor L and capacitor C are in parallel with each other and an effective resistance R representing the internal resonator losses. The resonator is capacitively coupled to a CPB of parameters C_j, E_J (the CPB island is marked in red) with coupling capacitance C_g. The entire structure is floated by two capacitors C_t and C_f. It is driven by input voltage V_1 and measured via output voltage V_2 while the CPB is biased by source dc voltage V_g'.

total output voltages and currents and are defined by

$$\begin{pmatrix} V_1 \\ I_1 \end{pmatrix} = \begin{pmatrix} A & B \\ C & D \end{pmatrix} \begin{pmatrix} V_2 \\ I_2 \end{pmatrix} \tag{2.29}$$

where $V_{\{1,2\}}$ and $I_{\{1,2\}}$ are the total voltages and currents at ports $\{1,2\}$. The ABCD-parameters are useful for calculating the total ABCD-parameters of a cascade of 2-port networks as the total ABCD-parameters are given by the matrix product of the ABCD-parameters of the individual components.

Each of the lumped element resonators we used in our work consisted of an interdigital capacitor C in parallel with a meander inductor L [66] [see Fig. 2.4(a)]. One side of the resonator was capacitively coupled to the center pin of a coplanar waveguide (CPW) transmission line [66] with coupling capacitance C_t and the other side was weakly coupled to the surrounding ground plane with capacitance C_f [see Fig. 2.4(b)]. The floating resonator design allowed us to bias the CPB which was capacitively coupled to the resonator

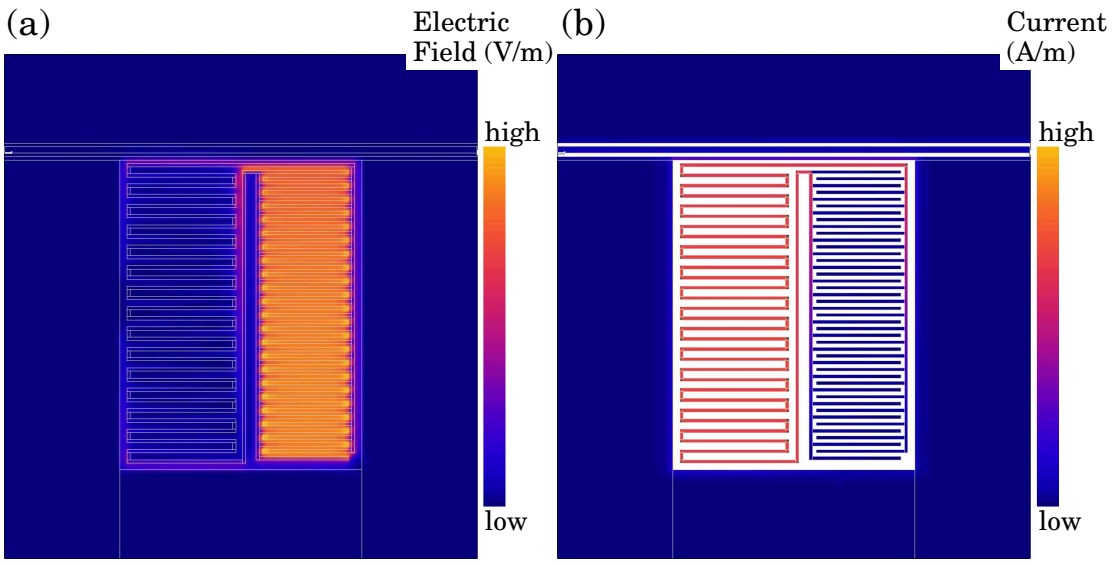

Figure 2.5: Microwave Office simulation of a lumped element resonator driven on resonance. Density plots of (a) the electric field and (b) the current in the resonator. Note that the electric field is concentrated and uniformly distributed mainly in the interdigital capacitor while the current is concentrated and uniformly distributed mainly in the meander inductor. See Fig. 2.4(a) for an identification of the resonator components. Simulation results courtesy of B. Suri.

[see Sec. 2.5]. While the actual coupling between the resonator and the transmission line had both capacitive and inductive character, we chose to simplify the analysis by treating it as purely capacitive.

Our lumped element resonator has two main advantages over the more common $\lambda/2$ or $\lambda/4$ CPW resonators. It's physically more compact than the $\lambda/2$ or $\lambda/4$ resonators and has no higher modes up to 28 GHz, reducing qubit relaxation due to the multimode Purcell effect [67] [see Sec. 2.7]. However the more complicated geometry of lumped element systems makes analytically predicting resonator properties more difficult. Instead we modeled our resonator's behavior using Microwave Office [68], a 2D finite element electromagnetic simulation software. From the simulation results we found that on resonance the electric field is concentrated and uniformly distributed mainly over the interdigital capacitor [see Fig. 2.5(a)] while the current is concentrated and uniformly distributed mainly in the meander inductor [see Fig. 2.5(b)]. This is the expected behavior for a lumped element circuit.

The impedance Z_L of a lumped element resonator is given by the series combination of

the two coupling capacitors C_t and C_f and the unloaded parallel RLC resonator:

$$\begin{aligned} Z_L &= \frac{1}{i\omega C_t} + \frac{1}{i\omega C_f} + \frac{1}{\frac{1}{i\omega C} + i\omega L + \frac{1}{R}} \\ &= \frac{1}{i\omega C_c} + \frac{1}{\frac{1}{i\omega C} + i\omega L + \frac{1}{R}} \end{aligned} \tag{2.30}$$

where R represents any internal losses in the bare resonator and $1/C_c = 1/C_t + 1/C_f$ is the effective coupling capacitance.

It's useful to heuristically motivate the large amount of algebra which is to follow. Resonance in a circuit occurs when the imaginary part of the impedance $\mathrm{Im}\, Z = 0$ vanishes [65]. In the case of the unloaded parallel RLC resonator it's easy to see that this occurs when $\omega^2 = 1/LC$. The width of an unloaded resonator is determined by its internal losses, in this case represented by R. Coupling a resonator to a transmission line loads it, shifting the resonance frequency and broadening the linewidth by creating an additional loss channel. The loaded resonator impedance has a more complicated dependence on the frequency. By first locating the exact (or approximate) frequency such that $\mathrm{Im}\, Z(\omega_{res}) = 0$ and then making a linear approximation to the impedance around ω_{res} it's possible to obtain approximate analytic solutions for the resonator S-parameters. If the resonator quality factor is high (and hence the linewidth is narrow), this method will produce good results since any realistic impedance may be approximated by the first two terms of its Taylor series in a narrow interval [69].

We may write the ABCD matrix for the lumped element resonator as [65]

$$\begin{pmatrix} A & B \\ C & D \end{pmatrix} = \begin{pmatrix} 1 & 0 \\ 1/Z_L & 1 \end{pmatrix} \tag{2.31}$$

and consequently the S-parameters for the entire circuit are

$$S_{22} = \frac{-Z_0}{2Z_L + Z_0} \tag{2.32}$$

$$S_{21} = \frac{2Z_L}{2Z_L + Z_0} \tag{2.33}$$

where $Z_0 = 50\,\Omega$ is the characteristic impedance of the transmission line. Note that $S_{21} =$

$1+S_{11}$. Substituting Z_L into S_{22} gives

$$S_{22} = -\frac{\zeta}{\frac{1}{i\omega(C+C_c)} + i\omega L + \frac{1}{R} + \zeta} \tag{2.34}$$

where

$$\zeta = i\omega C_c \left(\frac{1}{i\omega L} + i\omega C + \frac{1}{R}\right)\frac{Z_0}{2}. \tag{2.35}$$

We define the loaded resonance frequency $\omega_{res}^2 = 1/L(C+C_c)$ and the detuning $\Delta = \omega - \omega_{res}$. This allows us to rewrite $i\omega(C+C_c) = i(\omega_{res}+\Delta)/\omega_{res}^2 L$ and approximate

$$\begin{aligned} \frac{1}{\omega} &= \frac{1}{\omega_{res}}\frac{1}{(1+\Delta/\omega_{res})} \\ &\approx \frac{1}{\omega_{res}}(1-\Delta/\omega_{res}) \end{aligned} \tag{2.36}$$

for $\Delta \ll \omega_{res}$. From Eq. 2.36 we can approximate the imaginary part of the S_{22} denominator as

$$\frac{1}{i\omega(C+C_c)} + i\omega L \approx i\frac{2\Delta}{\omega_{res}^2 L}, \tag{2.37}$$

i.e. a linear approximation around $\omega = \omega_{res}$. We also make a series of approximations to simplify ζ:

$$\begin{aligned} \zeta &= \left(\frac{C_c}{L} - \omega^2 C_c C + i\frac{\omega C_c}{R}\right)\frac{Z_0}{2} \\ &\approx \left(\frac{C_c}{L} - \omega^2 C_c C\right)\frac{Z_0}{2} \\ &\approx \left(\frac{C_c}{L} - \omega_{res}^2 C_c C\right)\frac{Z_0}{2} \\ &= (\omega_{res} C_c)^2 \frac{Z_0}{2}. \end{aligned} \tag{2.38}$$

The first approximation uses typical values of $\omega_{res} \approx 2\pi \times 5\,\mathrm{GHz}$ and $C_c \approx 5\,\mathrm{fF}$ to discard the third term $\frac{\omega C_c}{R} \ll 1$ while the second assumes that $\omega \approx \omega_{res}$.

Identifying $1/\zeta = R_e$ as the external impedance we rewrite S_{22} [see Eq. 2.34] as

$$S_{22} = -\frac{1/R_e}{i\frac{2\Delta}{\omega_{res}^2 L} + \frac{1}{R} + \frac{1}{R_e}}, \tag{2.39}$$

a form which makes transparent the increase in linewidth due to the external coupling. Defining the corresponding quality factors $Q_i = R/\omega_{res}L$, $Q_e = R_e/\omega_{res}L$ and $1/Q_L = 1/Q_i +$

$1/Q_e$ Eq. 2.39 becomes

$$S_{22} = -\frac{Q_L/Q_e}{1 + iQ_L \frac{2(\omega-\omega_{res})}{\omega_{res}}} \tag{2.40}$$

and S_{21} is given by

$$\begin{aligned} S_{21} &= 1 + S_{22} \\ &= 1 - \frac{Q_L/Q_e}{1 + iQ_L \frac{2(\omega-\omega_{res})}{\omega_{res}}}. \end{aligned} \tag{2.41}$$

Hence the loaded resonator has the same line shape as the bare resonator but is shifted and broadened by the coupling to the transmission line.

Two-port microwave circuits can be characterized with a vector network analyzer which drives the device under test with a pure tone at a given frequency and measures the reflected and transmitted voltage signals. The frequency of the drive tone is stepped through a range of values around the resonance while the data at each frequency is accumulated into a plot. The S-parameters are found from the ratio of reflected or transmitted voltage to the input voltage. In general S_{21} is a complex quantity and the data is most commonly represented by two curves—the amplitude ($|S_{21}|$) [see Fig. 2.6(a)] and phase ($\arg S_{21}$) [see Fig. 2.6(b)]. The S_{21} amplitude dB scale plot may also be interpreted as the ratio of transmitted power to the input power ($|S_{21}|^2$) without any additional conversion due to a factor of 2 difference between the definitions of dB for voltage and power. However, one needs to be careful with such plots to make sure it's $20\log|S_{21}|$ that's being plotted, and not $10\log|S_{21}|$.

In addition to the transmitted and reflected power characterized by the S-parameters, energy is stored in the resonator when it's driven on or near its resonant frequency. On resonance the steady state stored energy is $U = \left(2Q_L^2/Q_e\right)(P_{in}/\omega_{res})$ where P_{in} is the input power [70]. This may also be expressed as the number of photons stored in the resonator by dividing the stored energy by the energy per photon $n = U/\hbar\omega_{res}$. A signature of this stored energy may be observed by recording the transient ring-up or ring-down of the resonator. If the output power of the resonator is monitored while the input power is abruptly switched off, the output power will decay from the steady state value to zero on a time scale given by the cavity energy decay time $1/\kappa = Q_L/\omega_{res}$. A similar ring-up behavior is observed if the input power to the resonator is abruptly turned on. The

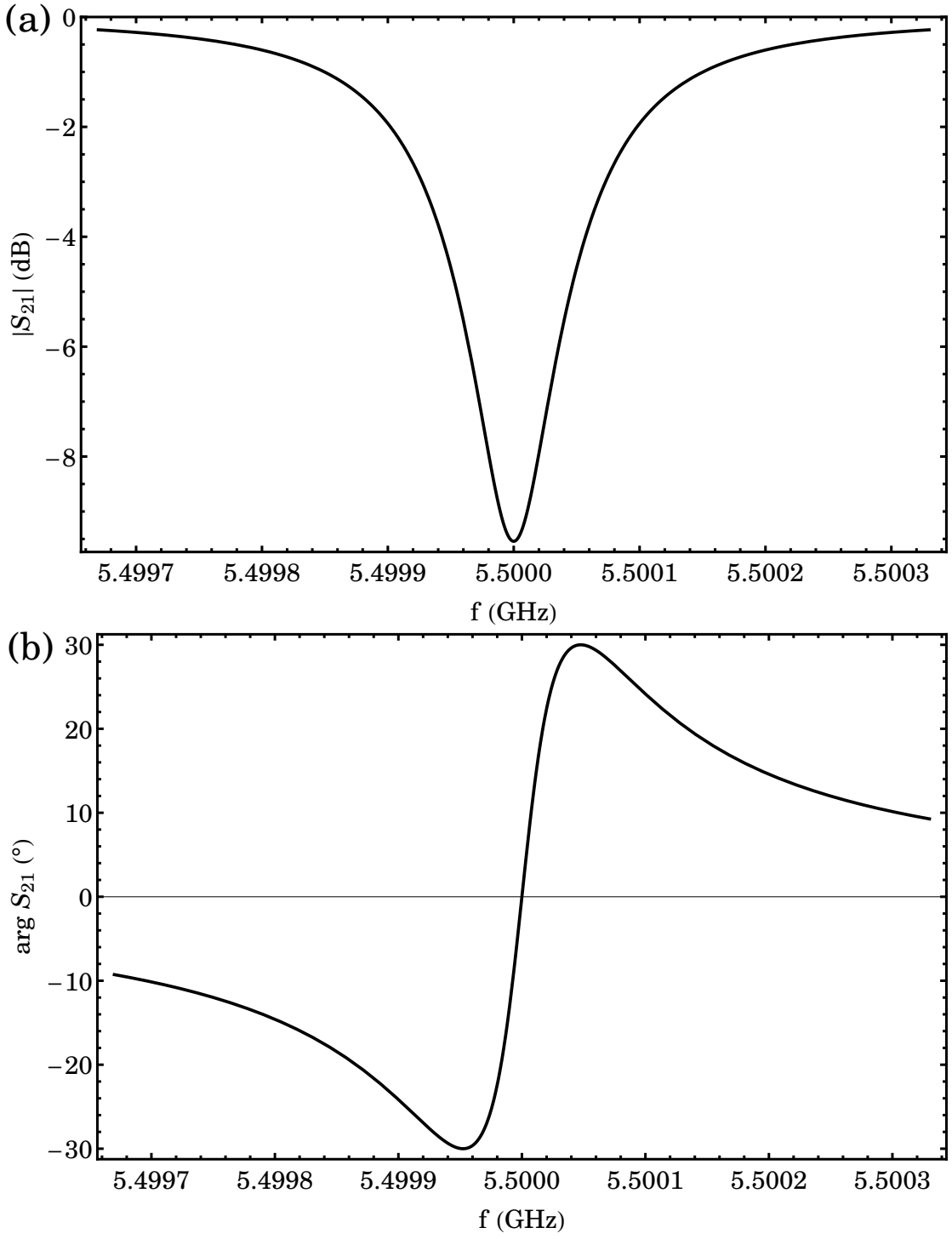

Figure 2.6: (a) Plot of resonator S_{21} amplitude ($20\log|S_{21}|$) versus frequency and (b) phase ($\arg S_{21}$) versus frequency. The values of $\omega_{res} = 5.5\,\text{GHz}$, $Q_L = 33,300$, $Q_i = 100,000$ and $Q_e = 50,000$ are representative of those used in this dissertation.

response time of the resonator, that is the time to reach the steady state, after changes in its properties is also given by the decay rate κ. For example, if a resonator is used to readout the state of a qubit coupled to it, information on changes of the qubit state on time scales faster than $1/\kappa$ would be obscured. Rather than faithfully representing the qubit state, the transmitted signal would be a convolution of the fast qubit dynamics and the slow resonator response.

The treatment of the resonator so far has been classical. To develop a quantum description of the lumped element resonator we follow the canonical harmonic oscillator quantization prescription [62]. We begin by writing the LC resonator Hamiltonian

$$\hat{H}_{\mathrm{LC}} = \frac{\hat{q}^2}{2C} + \frac{\hat{\varphi}^2}{2L} \tag{2.42}$$

where $\hat{q}$ is the operator for charge stored on the capacitor and $\hat{\varphi}$ is the operator for flux stored in the inductor. This form is analogous to the Hamiltonian of a simple harmonic oscillator $H_{\mathrm{SHO}} = p^2/2m + \frac{1}{2}m\omega^2 x^2$ and we will quantize it by introducing operators a and $a^\dagger$ such that

$$\begin{aligned} \hat{q} &= \sqrt{\frac{\hbar}{2Z_c}}\left(a^\dagger + a\right) \\ \hat{\varphi} &= i\sqrt{\frac{\hbar Z_c}{2}}\left(a^\dagger - a\right) \end{aligned} \tag{2.43}$$

where $Z_c = \sqrt{L/C}$ is the characteristic impedance of the resonator. The creation and annihilation operators $a^\dagger$ and a satisfy the commutation relation $\left[a, a^\dagger\right] = 1$. In this notation the cavity Hamiltonian is given by

$$H_{\mathrm{LC}} = \hbar\omega_{res}\left(a^\dagger a + \frac{1}{2}\right). \tag{2.44}$$

A more in-depth discussion of the lumped element LC resonator is available in the dissertation by Z. Kim [71].

2.5 Circuit QED

Coherent interaction between a cavity and a two-level system such as a qubit can be described by the Jaynes-Cummings Hamiltonian [72]

$$H_{\text{J-C}} = \hbar\omega_{res}\left(a^{\dagger}a + \frac{1}{2}\right) + \frac{\hbar\omega_{CPB}}{2}\sigma_z + \hbar g\left(a^{\dagger}\sigma^{-} + a\sigma^{+}\right) \tag{2.45}$$

where σ^{+}, σ^{-} are qubit raising and lowering operators and σ_z is a Pauli matrix. The first term describes a harmonic oscillator while the second describes a two level system. The last term is the dipole interaction between the two and describes the coherent emission ($a^{\dagger}\sigma^{-}$) or absorption ($a\sigma^{+}$) of one quanta of energy by the qubit from the resonator at rate g when the two systems are resonant with one another.

Competing with the coherent dynamics of the Jaynes-Cummings Hamiltonian are incoherent energy decay processes. We will define the decay rate of photons in the resonator by κ, which is related to the loaded quality factor by $\kappa = \omega_{res}/Q_L$, while the energy decay of the qubit into non-cavity modes is given by $\gamma_{\perp}$. These two processes reduce the time available for coherent cavity-qubit interaction and broaden the respective spectral lines, obscuring the effects of the cavity-qubit coupling.

We assume the CPB-resonator interaction is electrostatic in nature. The CPB Hamiltonian depends on the reduced gate voltage $n_g = C_g V_g/e$. When the qubit is embedded in or near the lumped element capacitor [see Figs. 2.4 and 6.1], in addition to the classical bias V_g, there will be a contribution from the quantum voltage across the resonator capacitor. The reduced gate bias n_g transforms into the operator $\hat{n}_g$ given by

$$\hat{n}_g = \frac{C_g\left(V_g + \hat{V}\right)}{e} \tag{2.46}$$

where $\hat{V} = \alpha\hat{q}/C$ is the operator for voltage across the resonator capacitor including the scaling α due to the mode structure of the resonator and the position of the CPB. Plugging this into the electrostatic term of the CPB Hamiltonian [see Eq. 2.14] and expanding the square gives

$$\hat{H}'_{CPB,\text{el}} = E_c\left(2\hat{N} - \hat{n}_g\right)^2 + \frac{4E_c C_g\hat{V}\left(2V_g + \hat{V}\right)}{e} - \frac{4E_c C_g\hat{V}\hat{N}}{e}. \tag{2.47}$$

The first term is the original CPB electrostatic Hamiltonian. The second term is not qubit state dependent and hence can be ignored as it will not affect qubit-resonator dynamics. The last term is the qubit-resonator coupling $\hat{H}_c$.

Expressing $\hat{V}$ in terms of $\hat{q}$, and then in terms of a and $a^\dagger$ using Eq. 2.43, gives

$$\hat{H}_c = 2\hbar g\left(a^\dagger + a\right)\hat{N} \tag{2.48}$$

where $g = eV_0\beta/\hbar$ is the qubit-resonator coupling strength, $V_0 = \sqrt{\hbar\omega_{res}/2C}$ is the rms vacuum voltage fluctuations in the resonator and $\beta = \alpha C_g/C_\Sigma$ accounts for the voltage division ratio of the CPB and the position of the CPB in the lumped element resonator. At $n_g = 1$, $\hat{N} = \hat{\sigma}_x/2$ and the coupling term becomes

$$\hat{H}_c = \hbar g\left(a^\dagger + a\right)\hat{\sigma}_x. \tag{2.49}$$

Writing $\sigma_x = \sigma^+ + \sigma^-$ and substituting into the interaction Hamiltonian we find

$$\hat{H}_c = \hbar g\left(a^\dagger + a\right)\left(\sigma^+ + \sigma^-\right). \tag{2.50}$$

We further simplify the expression by making the rotating wave approximation (RWA) [73]:

$$\hat{H}_c \approx \hbar g\left(a^\dagger\sigma^- + a\sigma^+\right). \tag{2.51}$$

This approximation discards terms which describe a change in the energy of the system (such as a join excitation $a^\dagger\sigma^+$ or joint relaxation $a\sigma^-$) and is valid when $\omega_{res} + \omega_{CPB} \gg g$ and $\omega_{res} + \omega_{CPB} \gg |\omega_{res} - \omega_{CPB}|$. This interaction term now has the Jaynes-Cummings form [see Eq. 2.45].

A more in-depth discussion of circuit QED is available in the dissertations by D. Schuster [74] and L. Bishop [75].

2.5.1 Dispersive Limit

In the Jaynes-Cummings Hamiltonian the qubit-resonator interaction term couples pure qubit and resonator states. If the coupling term $\hat{H}_c$ is weak, the eigenstates of the system

are nearly pure states. Specifically if the detuning between the qubit and the resonator $\Delta = \omega_{CPB} - \omega_{res}$ is much larger than the coupling strength g, we can apply non-degenerate perturbation theory to simplify the Hamiltonian. Keeping terms to second order in g/Δ yields the approximate Hamiltonian [25]

$$H_{\text{J-C}} = \hbar\left(\omega_{res} + \frac{g^2}{\Delta}\sigma_z\right)\left(a^\dagger a + \frac{1}{2}\right) + \frac{\hbar\omega_{CPB}}{2}\sigma_z. \tag{2.52}$$

The limit $g \ll \Delta$ is called the dispersive limit. The qubit and cavity don't directly share excitations but instead the resonance frequency of the resonator is dispersively shifted by $\chi = \pm g^2/\Delta$ due to the state of the qubit. A closer look shows that this approximation is only valid when $\sqrt{n}g \ll \Delta$, i.e. the coupling effectively scales with the number of photons n in the resonator [25]. Thus the dispersive limit fails when a large number of photon are stored in the resonator. This threshold is given by [25]

$$n_{\text{crit}} = \frac{\Delta^2}{4g^2} \tag{2.53}$$

where $\bar{n} = \langle \hat{N} \rangle = \langle a^\dagger a \rangle$ is the average number of photons in the resonator. If the photon number exceeds this value, the approximation no longer accurately describes the system and nonlinear effects become significant.

Typical values of $g/2\pi$ for CPBs studied in this dissertation were in the $5-10\,\text{MHz}$ range with detunings $\Delta/2\pi$ of 100s of MHz or more. This placed the system in the dispersive limit provided less than about 25 photons are stored in the resonator. As the CPB transition frequency ω_{CPB} can be tuned over a wide range with either an external flux or a gate voltage, we were able to exploit this to characterize our system and extract key parameters such as g and ω_{res}. By using an external flux to tune the Josephson energy above the resonance frequency $E_J > \omega_{res}$, the qubit transition energy ω_{CPB} can be made to lie above the resonator for all values of the gate bias n_g [see Fig. 2.7(a)]. The detuning Δ is smallest at $n_g = 1$ and hence the dispersive shift $\chi = g^2/\Delta$ is largest there. As n_g is changed away from $n_g = 1$, both the detuning increases and the dipole coupling strength decreases (note that $\hat{N} = \sin\theta_{\text{m}}\hat{\sigma}_x/2 + \cos\theta_{\text{m}}\hat{\sigma}_z/2$ as can be seen by combining Eq. 2.25 and 2.26) and at $n_g = 0$ or $n_g = 2$ the dispersive shift is negligible. This change in the dispersive shift is most easily observed by recording the resonator resonance frequency as a function of n_g near $n_g = 1$ [see Fig. 2.7(b)]. At $n_g = 1$ the resonator is pushed by

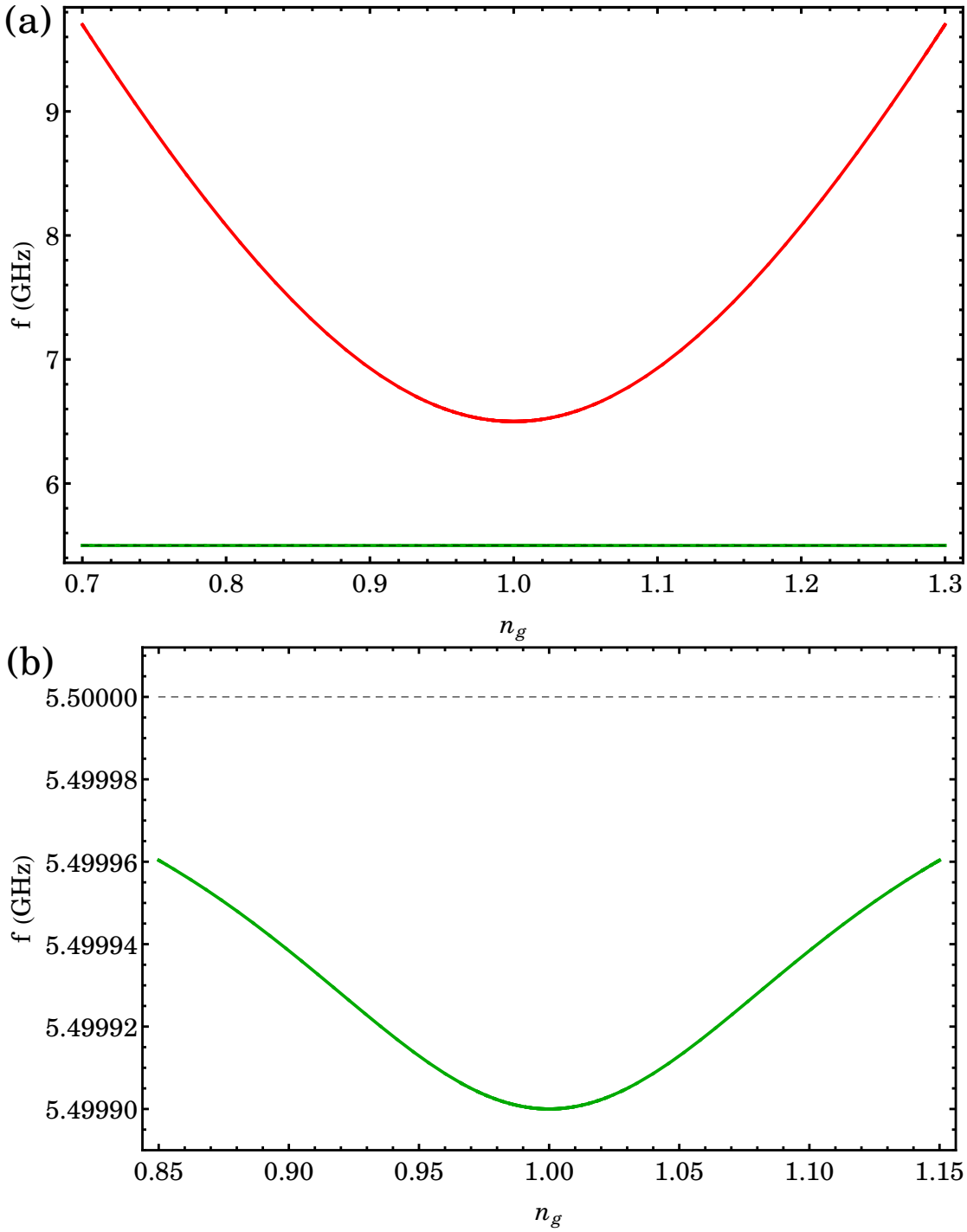

Figure 2.7: System spectrum in the dispersive limit. (a) Transition spectrum of the qubit (red) and resonator (green) with $E_J > \hbar\omega_{res}$. The values used to generate the theory plot are $E_c/h = 6\,\text{GHz}$, $E_J/h = 6.5\,\text{GHz}$, $\omega_{res}/2\pi = 5.5\,\text{GHz}$ and $g/2\pi = 10\,\text{MHz}$. The black dashed line is the bare resonator spectrum. (b) Zoom in of the resonator spectrum near $n_g = 1$ focusing on the ground state dispersive shift.

the maximum amount but approaches the bare resonance frequency as we move toward $n_g = 0$ or $n_g = 2$. This measurement, in combination with spectroscopic determination of the qubit transition energy ω_{CPB} , allows us to extract the dipole coupling strength g and the bare resonator frequency.

2.5.2 Resonant Limit

The opposite limit to the dispersive limit is the resonant limit of the Jaynes-Cummings Hamiltonian. In this case the detuning Δ approaches 0 and the coupling becomes a dominant energy scale. Rather than crossing, the degeneracy is lifted by the coupling and the levels form an avoided crossing of size $2g$, called the vacuum Rabi splitting [76]. At this point the eigenstates are equal superposition of pure qubit and resonator states and a single excitation quanta in the system will coherently oscillate between the qubit and the cavity modes at rate $g/2\pi$.

This effect can be observed in a CPB by tuning the Josephson energy with an external flux such that $E_J = \hbar\omega_{res}$. In particular, when by biasing the CPB $\hbar\omega_{CPB}\left(n_g = 1\right) = E_J$, a vacuum Rabi splitting would be present at $n_g = 1$. However a more practical and common approach is to tune the Josephson energy below the resonance frequency, i.e. $E_J < \hbar\omega_{res}$. As the gate bias is moved away from $n_g = 1$, the qubit transition energy will increase and at points $n_g = 1 \pm \Delta n_g$ cross the resonator and form an avoided crossing [see Fig. 2.8]. As we continue moving the gate bias toward $n_g = 0$ or $n_g = 2$, the CPB energy will move far above the resonator and we may use the same characterization technique as described in Sec. 2.5.1. One notable difference is that when the qubit is tuned below the resonator, the sign of the detuning is Δ negative and the resonator frequency is pushed up in the range between $1 - \Delta n_g < n_g < 1 + \Delta n_g$.

2.6 Qubit Readout

Quantum measurement [77, 49] can be thought of as a process of projecting the state of one system onto another. Typically the state of a small and fragile system, such as a qubit, is projected onto a larger and more robust system, the meter system. To perform this the two systems need to be coupled. The simplest coupling is of the form $\chi\hat{A}\hat{M}$ where $\hat{A}$ operates on the qubit, $\hat{M}$ operates on the meter system and χ is a measure of the

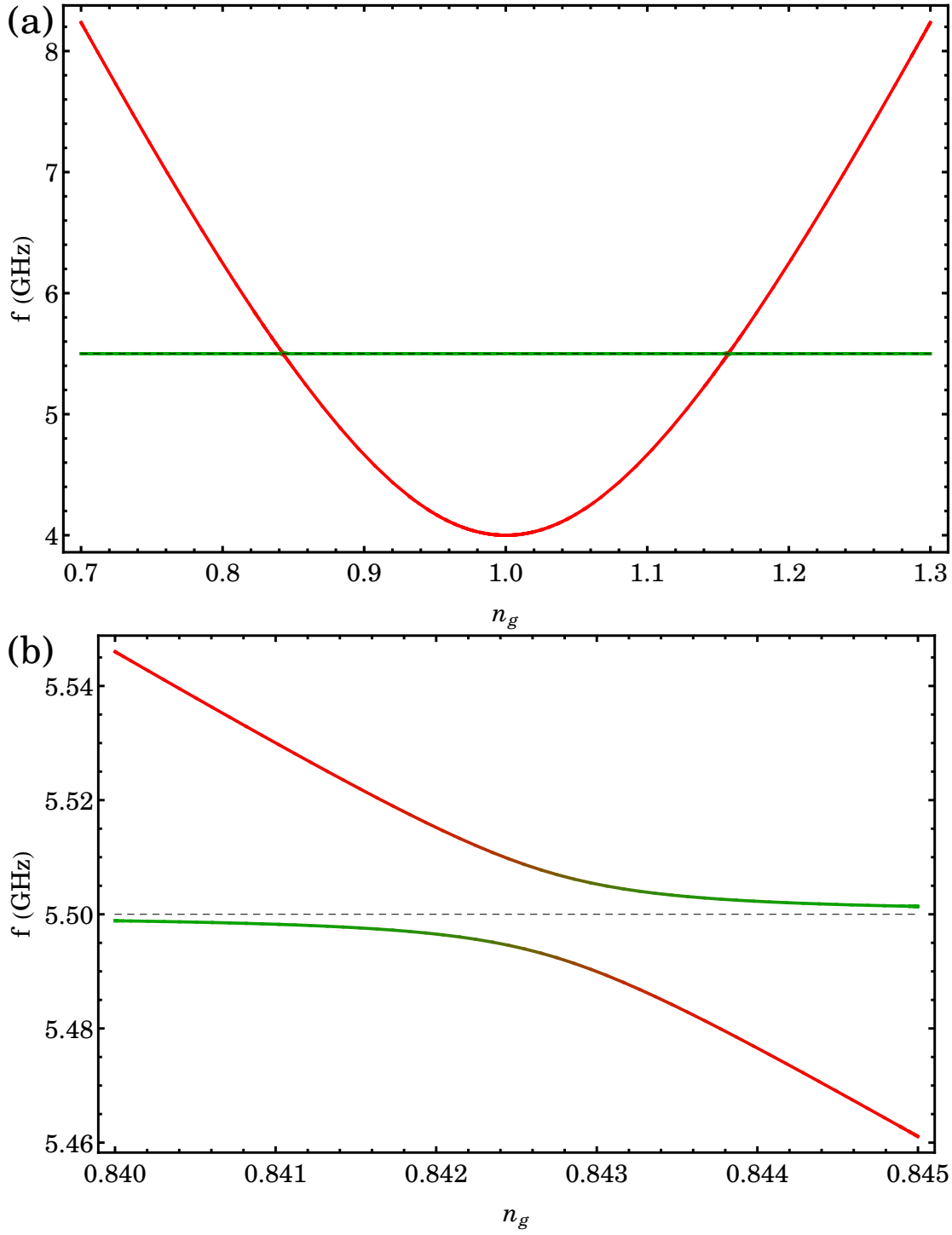

Figure 2.8: Transition spectrum of a CPB coupled to a resonator, plotted versus gate bias n_g, containing a resonant avoided crossing. (a) Transition spectrum of the qubit (red) and resonator (green) with $E_J < \hbar\omega_{res}$. The values used to generate the theory plot are $E_c/h = 6\,\mathrm{GHz}$, $E_J/h = 4\,\mathrm{GHz}$, $\omega_{res}/2\pi = 5.5\,\mathrm{GHz}$ and $g/2\pi = 10\,\mathrm{MHz}$. The black dashed line is the bare resonator spectrum. (b) Zoom in of the resonant avoided crossing near $n_g = 0.84$ with blended colors indicating superposition states. The two states are split by $2g\left(n_g\right)$.

coupling strength. The dispersive limit Jaynes-Cummings interaction term has this form $\left(g^2/\Delta\right)\sigma_z\hat{N}$ and this suggests we can view the resonator as a tool to measure the state of the qubit. Since it will take us some time to record and determine the state of the resonator, it's important that we are able to perform repeated measurements of the state of the qubit without causing random changes in the qubit state. Mathematically this can only happen if the measurement perturbation commutes with the system Hamiltonian. This is expressed as

$$\begin{aligned} \frac{d}{dt}\hat{A}\hat{M} &= 0 \\ &= \frac{1}{i\hbar}\left[\hat{A}\hat{M},\hat{H}_{CPB}\right] \end{aligned} \tag{2.54}$$

which states that the measurement operator (or state property) does not change during the measurement process and we may relate this time derivative to commutation with the CPB Hamiltonian. Since $\hat{A}=\sigma_z$ commutes with $\hat{H}_{CPB}$, $\left[\sigma_z,\hat{H}_{CPB}\right]=0$, the resonator readout of the CPB state satisfies this property. This is known as a quantum non-demolition (QND) measurement. In addition to allowing repeated measurements of the state, this property reduces the measurement system back-action [77, 49].

The interaction between the qubit and the resonator is used to map the qubit state onto the phase or amplitude of the resonator photons. Due to the QND nature of the readout, the qubit state may be repeatedly mapped to many photons, making the signal stronger and allowing it to be averaged, improving the signal to noise ratio. It's easiest to see how the qubit state is mapped to the resonator photons and then readout by considering the dispersive limit Jaynes-Cummings Hamiltonian [see Eq. 2.52]

$$H_{\text{J-C}} = \hbar\left(\omega_{res}+\chi\sigma_z\right)\left(a^\dagger a+\frac{1}{2}\right)+\frac{\hbar\omega_{CPB}}{2}\sigma_z. \tag{2.55}$$

The resonance frequency of the coupled cavity is $\omega_{res}-\chi$ for the qubit in the ground state and $\omega_{res}+\chi$ for the qubit in the excited state (assuming positive detuning $\Delta>0$, the sign of χ is reversed otherwise) [see Fig. 2.9(a)]. The process of determining the qubit state is now mapped to the problem of determining the resonance frequency of the resonator. In electrical engineering language, the CPB acts as a state dependent lossless capacitor [37] coupled to the resonator. This additional reactance loads the resonator and shifts its

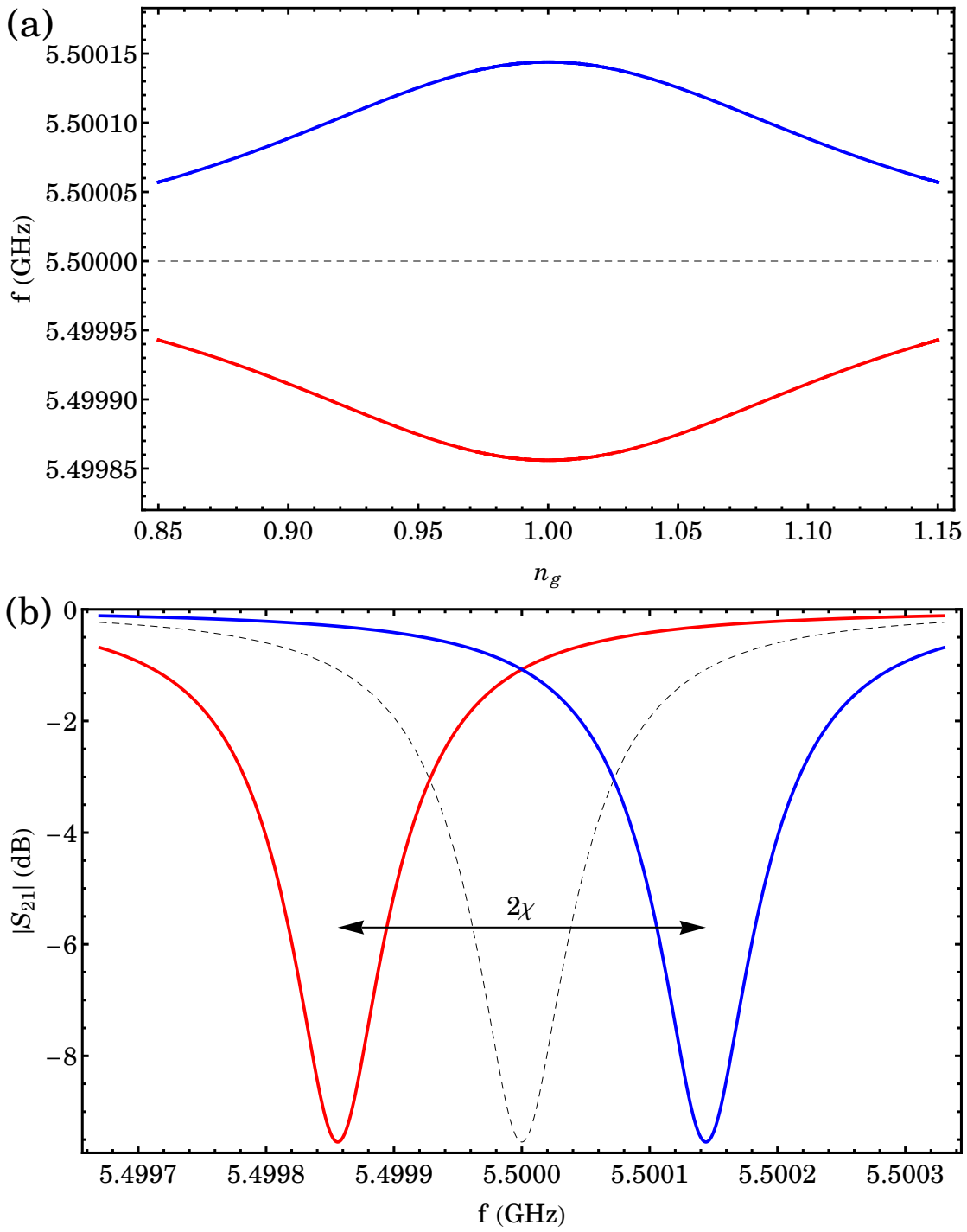

Figure 2.9: Qubit state dependent resonance of the cavity. (a) Resonator spectrum with the qubit in the ground state (red) and excited state (blue) with $E_J > \hbar\omega_{res}$. The values used to generate the theory plots are $E_c/h = 6.0\,\text{GHz}$, $E_J/h = 6.5\,\text{GHz}$, $\omega_{res}/2\pi = 5.5\,\text{GHz}$ and $g/2\pi = 12\,\text{MHz}$. The black dashed line is the bare resonator spectrum. (b) Resonator dispersive shift in the strong dispersive limit. S_{21} amplitude for the qubit in the ground (red) and excited (blue) states at $n_g = 1$. The two peaks are offset by 2χ.

resonance frequency.

The protocol to determine the resonance frequency depends on the relative sizes of the dispersive shift χ and the resonator linewidth $\kappa = \omega_{res}/Q_L$. If the dispersive shift is greater than the resonator linewidth $\chi > \kappa$ then the two qubit state dependent peaks are individually resolvable [see Fig. 2.9(b)]. If the dispersive shift is also greater than the qubit linewidth $\chi > 1/T_2^*$ this is called the strong dispersive limit. In this limit it's possible to resolve the effects of an individual excitation quanta. In the case of the resonator this means being able to resolve both resonator peaks while for the qubit this enables the observation of photon number splitting [78]. When both resonator peaks are resolvable, readout is performed by probing the resonator at one of the two dispersively shifted resonance peaks, for instance $\omega_{res} - \chi$ corresponding to the qubit in the ground state. In the case of our notch filter design, the transmission of the cavity will be minimal when the qubit is in the ground state and nearly unity when the qubit is in the excited state [79, 80, 25]. If we perform an ensemble average with the qubit in the mixed state then the excited state probability will be proportional to the transmitted voltage $P_e \propto \langle V_{\text{out}} \rangle$. The complete measurement protocol involves calibrating the transmitted voltage based on measurements when the qubit is in the ground and excited states to account for effects of the transmission line. Finally the integration time of the resonator signal is limited by the qubit lifetime $T_1 = 1/\gamma$. The specifics of our experimental qubit readout calibration and protocol is detailed in Secs. 4.4 and 5.3.2.

2.6.1 Small Dispersive Shift Limit

When the dispersive shift is less than the resonator linewidth $\chi < \kappa$ the two qubit state dependent peaks are not individually resolvable [see Fig. 2.10(a)]. If the dispersive shift is also less than the qubit linewidth $\chi < 1/T_2^*$ this is called the weak dispersive limit. In this limit the effects of a single excitation quanta are not resolvable. However, in this limit we can instead determine the relative phase shift of the output voltage. As the phase shift within a resonance peak is nearly linear in the detuning, the phase shift between the two resonator states is $\theta_{\text{out}} = 2g^2/\Delta\kappa$ [see Fig. 2.10(b)] [25, 81]. This simplifies the readout procedure as the excited state probability is proportional to the phase of the transmitted voltage $P_e \propto \langle \theta_{\text{out}} \rangle$. The calibration procedure to remove effects of the transmission line is also easier to perform. Biasing the CPB at $n_g = 1$ and $n_g = 0$, respectively,

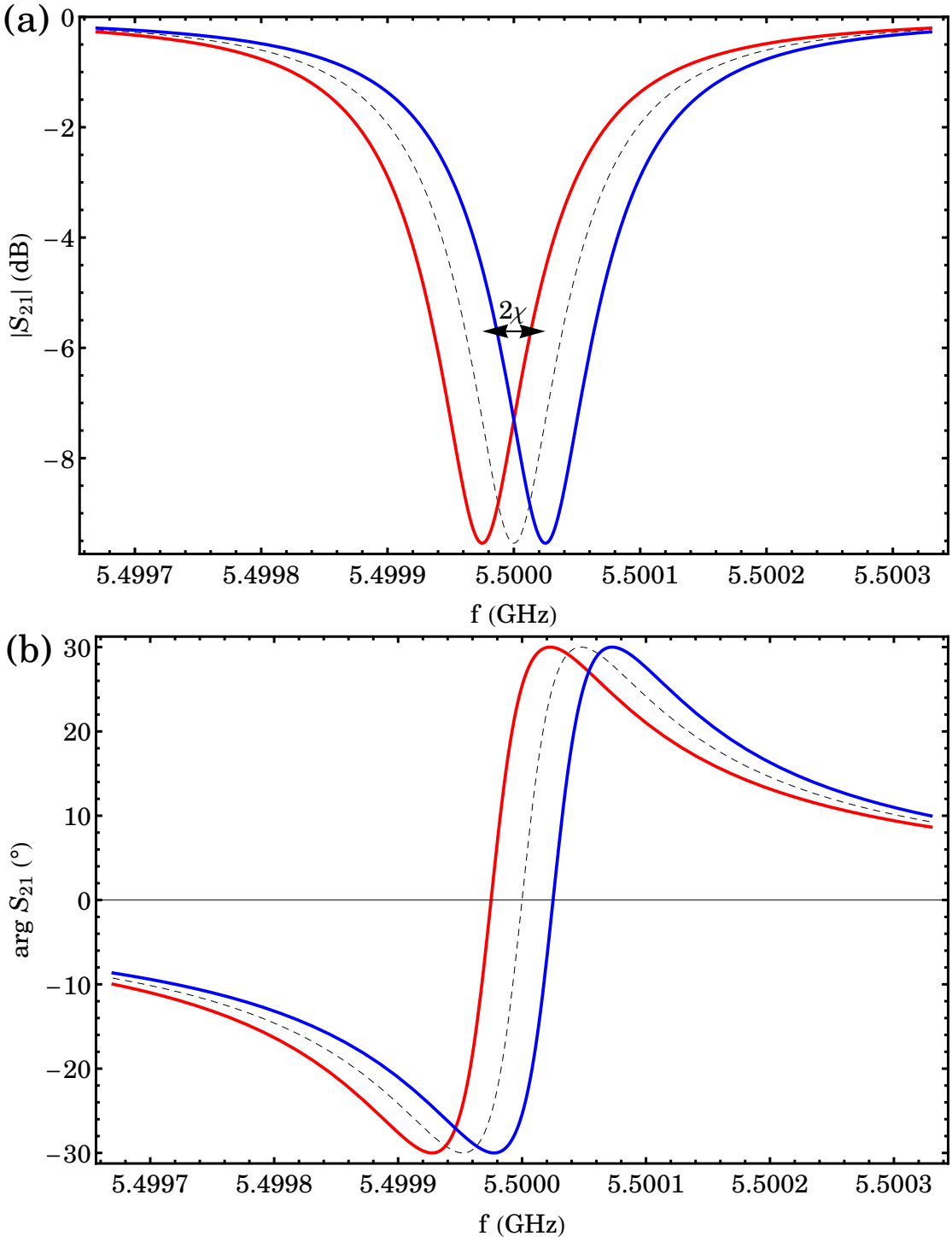

Figure 2.10: Dispersive shift in the weak dispersive limit. (a) S_{21} amplitude and (b) phase for the qubit in the ground state (red) and excited state (blue) at $n_g = 1$. The values used to generate the theory plot are $E_c/h = 6.0\,\text{GHz}$, $E_J/h = 6.5\,\text{GHz}$, $\omega_{res}/2\pi = 5.5\,\text{GHz}$ and $g/2\pi = 5\,\text{MHz}$. The black dashed line is the bare resonator spectrum. The frequencies of the two peaks differ by 2χ.

one finds the output phase corresponding to the qubit in the ground state and the bare resonator. Since we expect the bare resonator frequency to be midway between the two qubit state dependent resonator frequencies [see Fig. 2.10(b)], it also corresponds to the phase of a $P_e = 50\%$ state. These two measurements are sufficient to calibrate the readout for all possible mixed states. The remaining details of our experimental qubit readout calibration and protocol is detailed in Secs. 4.4 and 5.3.2.

2.7 Purcell Effect

The coupled qubit-resonator system of circuit QED allows the qubit to alter the resonator state properties but it also works in reverse, with the resonator state affecting qubit properties and dynamics. Several of these effects were relevant to our work on characterizing the CPB qubit. The first of these is the Purcell effect [46, 47]. The Purcell effect is a change in the decay rate of the qubit $\gamma_\parallel$ due to the coupling to the resonator. In the resonant coupling limit ($\omega_{CPB} = \omega_{res}$) the total qubit decay rate Γ_1 is given by

$$\Gamma_1 = \frac{\gamma_\perp}{2} + \frac{\kappa}{2} \tag{2.56}$$

where $\gamma_\perp$ is the decay rate of the qubit into non-cavity modes. The factors of 1/2 occur because in this limit the eigenstates are equal superpositions of qubit and photon states and excitations are shared equally between the two, leading to a qubit decay rate that is the average of the two rates. In the dispersive limit the total qubit decay rate is approximately

$$\Gamma_1 = \gamma_\perp + \left(\frac{g}{\Delta}\right)^2 \kappa \tag{2.57}$$

where $(g/\Delta)^2$ maybe be interpreted as the fraction of the qubit state residing in the photon state.

The Purcell effect radiative decay rate of the qubit $\gamma_\parallel$ may either be enhanced or suppressed relative to that of the free space decay rate. This is elucidated by an electrical engineering picture of the qubit environment. In the dispersive limit the impedance seen by the qubit is that of a parallel RLC combination at frequency ω_{CPB}. The real part of

this effective impedance determines the decay rate into the cavity mode [82]

$$\begin{aligned} \mathrm{Re}\, Z_{\mathrm{eff}}(\omega_{CPB}) &= \frac{Z_c}{1+\frac{\Delta^2}{(\kappa/2)^2}} \\ &\approx Z_c \frac{(\kappa/2)^2}{\Delta^2} \end{aligned} \tag{2.58}$$

where $Z_c = \sqrt{L/C}$ is the characteristic impedance of the resonator and the approximation is valid for large detuning $\Delta \gg \kappa$. The typical resonator characteristic impedance $Z_c \approx 100\,\Omega$ is of the same order of magnitude as the impedance $Z_0 = 50\,\Omega$ of a transmission line or $Z_0 = 377\,\Omega$ of free space [83]. Consequently for large detuning $\mathrm{Re}\, Z_{\mathrm{eff}}(\omega_{CPB}) \ll Z_c \approx Z_0$ and the decay rate is significantly suppressed relative to the free space rate. Alternatively, in the resonant limit $\gamma_\parallel = \kappa/2$ which depends on the cavity decay rate and may be enhanced as compared to the free space rate.

Purcell effect considerations are important when choosing a resonator design and the detuning Δ at which to operate the qubit. If the detuning is too small, the Purcell effect may suppress the CPB lifetime and degrade its performance as a qubit. Resonator design is a significant factor because the Purcell effect occurs for coupling to any cavity mode, not just the lowest one. In $\lambda/2$ or $\lambda/4$ CPW resonators the higher lying modes are periodically spaced in frequency and lie relatively close to the fundamental mode. Although the detuning to each such mode is large, their quantity and typically lower quality factor still degrade qubit performance in an effect called the multimode Purcell effect [67]. It is for this reason that we chose a lumped element resonator design which has no higher modes up to 28 GHz.

2.8 AC Stark Effect

The AC Stark effect [84, 50] is a shift in the transition energy of the qubit due to photons stored in the resonator. It is the analog of the dispersive shift of the resonator due to the state of the qubit and is an example of measurement back-action. We may readily observe its origin by simply rearranging the terms in the dispersive limit Jaynes-Cummings Hamiltonian. Starting from Eq. 2.52 and regrouping the product terms, we can write

$$H_{\text{J-C}} = \hbar\omega_{res}\left(a^\dagger a + \frac{1}{2}\right) + \frac{\hbar}{2}\left(\omega_{CPB} + 2\chi a^\dagger a + \chi\right)\sigma_z. \tag{2.59}$$

The AC Stark shift is produced by the second term in the parenthesis ($2\chi a^\dagger a$) while the last term (χ) is responsible for the Lamb shift [84, 85, 86, 87]. Here we see that the AC Stark effect produces a linear change in the qubit transition frequency as a function of photon number with a shift of 2χ per photon in the cavity. The Lamb shift is due to coupling to the vacuum fluctuations and is equal to the AC Stark shift for half a photon. As the Lamb shift is independent of photon number, it doesn't affect qubit operation or readout.

The AC Stark shift affects qubit operation in two ways. First, we can write the qubit transition frequency as a function of $\bar{n} = \langle \hat{N} \rangle = \langle a^\dagger a \rangle$ the average number of photons in the resonator

$$\omega_{CPB}(\bar{n}) = \omega_{CPB,0} + 2\chi\bar{n} \tag{2.60}$$

where $\omega_{CPB,0}$ is the transition frequency without any photons in the resonator but including the Lamb shift. Consequently the qubit spectrum will depend on the resonator probe power and we need to account for this. For our devices $2\chi < 1/T_2^*$, where T_2^* is the qubit spectroscopic width, and we performed spectroscopy and other dephasing insensitive measurements by continuously probing the resonator at a low probe power corresponding to $\bar{n} \approx 10 - 25$. At this probe power the AC Stark shift was not enough to significantly change the qubit spectrum. Additionally, we were able to calibrate the number of photons in the resonator by measuring the qubit transition frequency versus probe power and, along with an independent measurement of χ, fit the data to a line [see Sec. 5.4.2].

Our probe signal is produced by a microwave source which generates an effectively pure tone at the probe frequency. In quantum optics this corresponds to a coherent signal and creates a Poisson distribution of the number of photons in the resonator. The Poisson distribution has fluctuations about the mean of order $\sqrt{\bar{n}}$ that broaden the qubit spectral line. If dephasing due to the AC Stark shift dominates the bare qubit spectral width $1/T_2^*$, the resulting qubit spectral line has a Gaussian profile with standard deviation [80]

$$\sigma = \sqrt{\bar{n}}2\chi. \tag{2.61}$$

In this limit the qubit dephasing occurs on a time scale faster than the cavity response time, leading to inhomogeneous broadening. To avoid this additional dephasing during

experiments to characterize qubit coherence we implemented a pulsed probe scheme [81] in which the resonator was populated with photons only at the end of any qubit pulse sequence. The specifics of our experimental qubit readout procedure are described in detail in Sec. 5.3.2.

3 Decoherence in the Cooper Pair Box

3.1 CPB as a Qubit

A physical implementation of a general-purpose or universal quantum computer must satisfy the DiVincenzo criteria [11]. We can state the criteria succinctly as follows:

1. The system must possess scalable, well-defined qubits.
2. It must be possible to initialize the system to a pure state.
3. A universal set of one and two qubit quantum gates must be available to perform computation.
4. It must be possible to perform qubit-specific measurements of the system's state.
5. The system needs coherence times sufficiently long to perform computation.

The circuit QED architecture, consisting of a CPB box and a superconducting resonator, meets all these requirements. Due to its anharmonicity the CPB may be treated as a well-defined two-level system. In the limit $E_c \gtrapprox E_J$, the minimum transition frequency between the two lowest levels is $\omega_{01}\left(n_g = 1\right) \approx E_J/\hbar$ while the transition frequency between the first and second excited states is $\omega_{12}\left(n_g = 1\right) \approx 8E_c/\hbar$. This means it's possible to address the ground-to-excited state transition without populating higher states. Sufficient cooling of the qubit further ensures that higher lying states are not thermally populated. The relative occupation probability of the ground and first excited state is given by [88]

$$\begin{aligned} P_1/P_0 &= e^{-\hbar\omega_{01}/k_B T} \\ &\approx 10^{-5} \end{aligned} \tag{3.1}$$

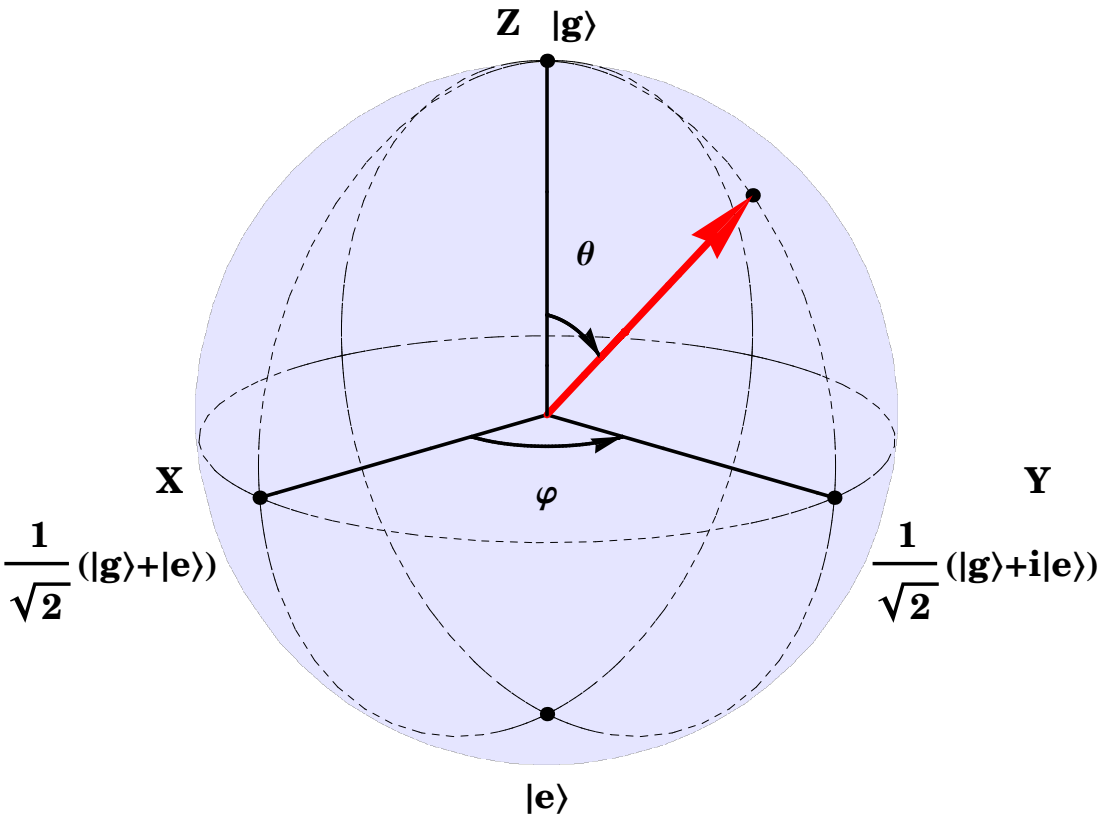

Figure 3.1: Bloch sphere representation of a qubit state. An arbitrary qubit state $|s\rangle = \alpha|g\rangle + \beta|e\rangle$ is mapped to a Bloch vector by writing α and β in terms of angular variables θ and φ. These are then assigned to a point on the surface of a unit sphere in $\mathbb{R}^3$ by interpreting them as the angles of spherical coordinates.

assuming the system is thermalized at typical dilution refrigerator temperatures of $T \approx 25\,\mathrm{mK}$ and $\omega_{01}/2\pi \approx 6\,\mathrm{GHz} \approx 300 \times k_B/h\,\mathrm{mK}$. Relaxation [see Sec. 3.3] acts as a natural reset, bringing the qubit to the ground state if one waits for several excited state lifetimes.

While a universal set of quantum gates and a multi-qubit system weren't implemented for this work, such control is possible for charge qubits [89]. A set of basic qubit manipulations via ac resonant pulses was used in our work to study the coupling and coherence of two CPBs and is described in detail in Sec. 3.1.1. Qubit state readout has already been described in Sec. 2.6. Decoherence in solid-state qubits remains a major challenge to their use in a practical quantum computer. An experimental study of the decoherence in CPB qubits is one of the two main topics of this dissertation [see Ch. 6].

An arbitrary qubit state $|s\rangle$ can be written as a linear superposition of the ground state $|g\rangle$ and excited state $|e\rangle$:

$$\begin{aligned} |s\rangle &= \alpha|g\rangle + \beta|e\rangle \\ &= \cos(\theta/2)|g\rangle + e^{i\varphi}\sin(\theta/2)|e\rangle \end{aligned} \tag{3.2}$$

where in general α and β are complex and satisfy $|\alpha|^2 + \left|\beta\right|^2 = 1$. Using this constraint and the fact that only the relative phase between the two states is meaningful, the superposition may be written in terms of two angular variables θ and φ where $P_e = \sin^2(\theta/2)$ and φ is the relative phase between the two states. These two angles may be interpreted as the angles of spherical coordinates and hence any qubit state may be mapped to a point on the unit sphere in $\mathbb{R}^3$ [see Fig. 3.1]. This is known as the Bloch sphere representation [90]. In this dissertation, $|g\rangle$ maps to the North pole while $|e\rangle$ maps to the South pole and points on the equator represent an equal superposition of $|g\rangle$ and $|e\rangle$. Single qubit operations are represented by rotations of the Bloch vector on the Bloch sphere.

3.1.1 Qubit Control

Qubit operations are implemented by modulating an external parameter of the CPB Hamiltonian. For charge qubits this is typically the gate voltage n_g and involves applying non-adiabatic dc pulses with rise time much shorter than the characteristic time of the Josephson coupling [15] or resonant microwave pulses with rise times slow enough (and hence with a narrow enough frequency bandwidth) not to cause transitions between higher lying states [91] [see Sec. 4.3.2].

Consider a nearly resonant ac perturbation of the gate voltage n_g at $n_g = 1$ of the form

$$\delta n_g(t) = \Delta n_g \cos\left(\omega_{\mu w} t + \phi\right) \tag{3.3}$$

with $\omega_{\mu w} \approx \omega_{CPB}$. We will limit the discussion to the sweet spot $n_g = 1$ because at that point the transition frequency is insensitive to first order to small variations of n_g and this suppresses dephasing induced by fluctuations of the control parameter n_g [see Sec. 3.4]. The effect of the perturbation $\delta n_g(t)$ is to add a time-dependent perturbation term

to the bare Hamiltonian [see Eq. 2.14]

$$\begin{aligned}\hat{H}_{\mu w} &= -2E_c\Delta n_g \cos\left(\omega_{\mu w}t+\phi\right)\hat{N} \\ &= -2E_c\Delta n_g \cos\left(\omega_{\mu w}t+\phi\right)\frac{\hat{\sigma}_x}{2} \\ &= -h\Omega_{R,0}\cos\left(\omega_{\mu w}t+\phi\right)\hat{\sigma}_x \end{aligned} \tag{3.4}$$

where $\Omega_{R,0} = E_c\Delta n_g/h$ is the Rabi frequency on resonance. In general a qubit operator corresponding to a perturbation may be written as [62]

$$\hat{D} = D_x\hat{\sigma}_x + D_y\hat{\sigma}_y + D_z\hat{\sigma}_z + D_I\hat{I} \tag{3.5}$$

where $D_x = \mathrm{Re}\langle g|\hat{D}|e\rangle$ and $D_y = \mathrm{Im}\langle g|\hat{D}|e\rangle$ and $\hat{I}$ is the 2×2 identity matrix. The $\hat{\sigma}_x$ and $\hat{\sigma}_y$ terms will couple the $|g\rangle$ and $|e\rangle$ states while the $\hat{\sigma}_z$ term will shift the energy levels. In the general case the Rabi frequency is given by $\Omega_{R,0} = \Delta d\sqrt{D_x^2+D_y^2}/h$ where Δd is the amplitude of the perturbation. Note that if $n_g \neq 1$ then $\hat{N}$ also has a $\hat{\sigma}_z$ component [see Sec. 2.3.2]. However in the typical range of $0.85 < n_g < 1.15$ accessed in this dissertation this was not a significant contribution.

By performing a series of manipulations, we can simplify and elucidate the effect of the perturbation term. We begin by adding and subtracting $\sin\left(\omega_{\mu w}t+\phi\right)\hat{\sigma}_y$ and rearranging Eq. 3.4 into rotating and counter-rotating terms

$$\begin{aligned}\hat{H}_{\mu w} &= -h\Omega_{R,0}\cos\left(\omega_{\mu w}t+\phi\right)\hat{\sigma}_x \\ &= -\frac{h\Omega_{R,0}}{2}\left[\left\{\cos\left(\omega_{\mu w}t+\phi\right)\hat{\sigma}_x + \sin\left(\omega_{\mu w}t+\phi\right)\hat{\sigma}_y\right\}\right. \\ &\quad \left.+\left\{\cos\left(\omega_{\mu w}t+\phi\right)\hat{\sigma}_x - \sin\left(\omega_{\mu w}t+\phi\right)\hat{\sigma}_y\right\}\right]. \end{aligned} \tag{3.6}$$

We now change to a frame that rotates with the drive frequency using the unitary transformation $U = e^{i\omega_{\mu w}t\hat{\sigma}_z/2}$. In this frame the Hamiltonian transforms as [92, 93]

$$H_{\mathrm{rot}} = UHU^\dagger - i\hbar U\frac{\partial U^\dagger}{\partial t}. \tag{3.7}$$

Using the Baker-Hausdorff lemma [62] we find the transformed Pauli matrices

$$\begin{aligned} U\hat{\sigma}_x U^\dagger &= \cos\left(\omega_{\mu w} t\right)\hat{\sigma}_x - \sin\left(\omega_{\mu w} t\right)\hat{\sigma}_y \\ U\hat{\sigma}_y U^\dagger &= \sin\left(\omega_{\mu w} t\right)\hat{\sigma}_x + \cos\left(\omega_{\mu w} t\right)\hat{\sigma}_y \\ U\hat{\sigma}_z U^\dagger &= \hat{\sigma}_z. \end{aligned} \tag{3.8}$$

Substituting the transformed Pauli matrices into Eq. 3.6 and using trigonometric identities we find

$$\begin{aligned} \hat{H}_{\mu w,\mathrm{rot}} &= -\frac{h\Omega_{R,0}}{2}\left[\left\{\cos\left[\left(\omega_{\mu w}-\omega_{\mu w}\right)t+\phi\right]\hat{\sigma}_x + \sin\left[\left(\omega_{\mu w}-\omega_{\mu w}\right)t+\phi\right]\hat{\sigma}_y\right\}\right. \\ &\quad \left. + \left\{\cos\left[\left(\omega_{\mu w}+\omega_{\mu w}\right)t+\phi\right]\hat{\sigma}_x - \sin\left[\left(\omega_{\mu w}+\omega_{\mu w}\right)t+\phi\right]\hat{\sigma}_y\right\}\right] \\ &\approx -\frac{h\Omega_{R,0}}{2}\left(\cos\phi\hat{\sigma}_x + \sin\phi\hat{\sigma}_y\right) \end{aligned}$$

where the last line is obtained by making the rotating wave approximation (RWA) [73] and discarding the fast counter-rotating terms. Additionally, if $\omega_{\mu w} \neq \omega_{CPB}$ the bare qubit Hamiltonian $\hat{H}_{CPB} = \hbar\omega_{CPB}\hat{\sigma}_z/2$ transforms to yield a detuning term [see Eq. 3.7]

$$\hat{H}_{CPB,\mathrm{rot}} = \frac{h\Delta\nu_{\mathrm{R}}}{2}\hat{\sigma}_z \tag{3.9}$$

where $\Delta\nu_{\mathrm{R}} = \left(\omega_{CPB}-\omega_{\mu w}\right)/2\pi$ is the Ramsey frequency. Hence the total effective Hamiltonian in the rotating frame is

$$\hat{H}_{\mathrm{rot}} = \frac{h\Delta\nu_{\mathrm{R}}}{2}\hat{\sigma}_z - \frac{h\Omega_{R,0}}{2}\left(\cos\phi\hat{\sigma}_x + \sin\phi\hat{\sigma}_y\right). \tag{3.10}$$

The dynamics of a qubit subject to a near-resonant ac perturbation are analogous to that of an electron in an effective static magnetic field

$$\vec{b} = \Omega_{R,0}\cos\phi\hat{x} + \Omega_{R,0}\sin\phi\hat{y} - \Delta\nu_{\mathrm{R}}\hat{z} \tag{3.11}$$

where $\hat{x}$, $\hat{y}$ and $\hat{z}$ are the Cartesian coordinates unit vectors. During driven evolution, the spin of the electron, and by analogy the Bloch state vector, precesses according to [83, 62]

$$\frac{d\vec{s}}{dt} = \vec{b}\times\vec{s}. \tag{3.12}$$

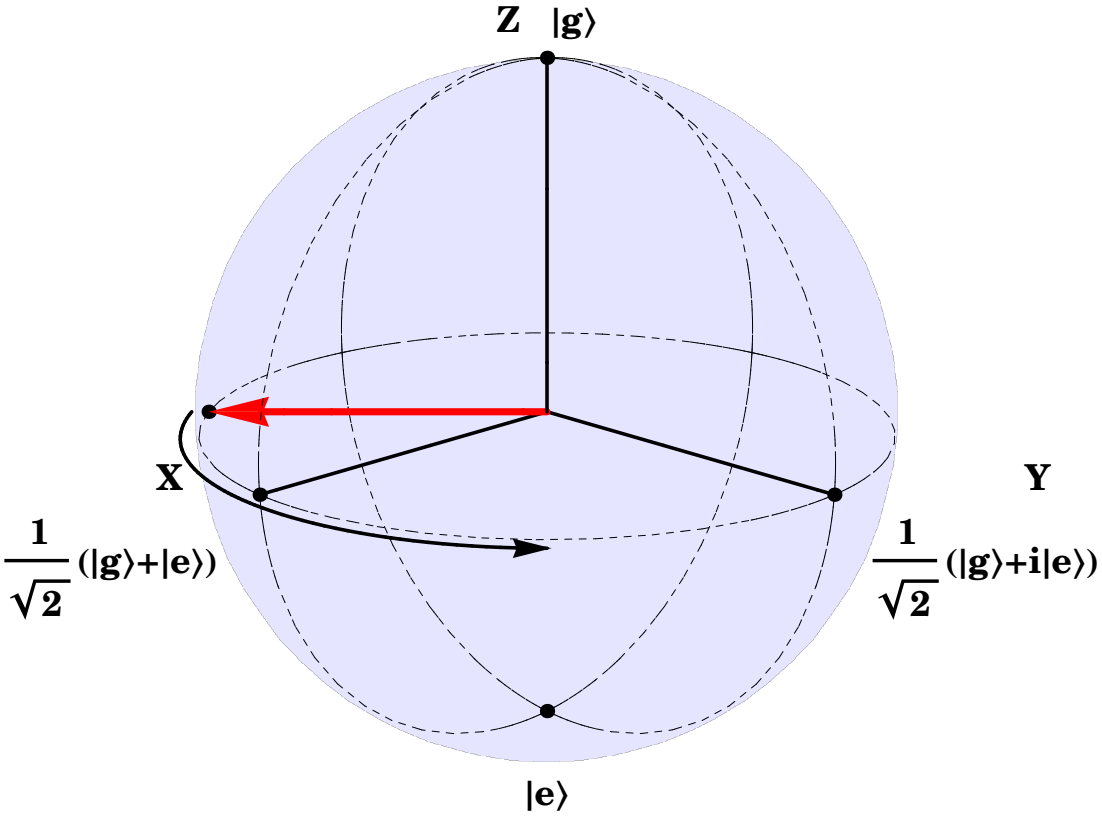

Figure 3.2: Qubit operations may be viewed as rotations on the Bloch sphere. For example, free evolution of the qubit, present during the Ramsey fringes sequence, may be viewed as rotation about the z-axis at rate $\Delta\nu_{\mathrm{R}}$ in the co-rotating frame.

Hence we see that the qubit may be manipulated into an arbitrary superposition state by the application of a proper sequence of pulses. An individual pulse is equivalent to a rotation operation on the Bloch sphere, rotating around the axis given by $\hat{b} = \vec{b}/\left\|\vec{b}\right\|$ at the rate [see Fig. 3.2]

$$\Omega_R = \sqrt{\Omega_{R,0}^2 + \Delta\nu_{\mathrm{R}}^2} \tag{3.13}$$

called the Rabi frequency. Free evolution constitutes rotation around the detuning field $\vec{b} = -\Delta\nu_{\mathrm{R}}\hat{z}$ at the Ramsey frequency $\Delta\nu_{\mathrm{R}}$.

3.2 Steady State Spectrum

In the limit of weak coupling between the qubit and the environment, Bloch-Redfield theory [94, 95] offers a phenomenological model of two-level system behavior. The coherent quantum evolution of a qubit is disrupted by two incoherent decay processes, longitudinal relaxation (depolarization) described by rate $\Gamma_1 = 1/T_1$ and transverse relaxation (decoherence) described by rate $\Gamma_2 = 1/T_2$. The theoretical derivation of these rates from the noise sources affecting the qubit is described in Sec. 3.3 and 3.4. The decoherence rate may further be decomposed into two components, one due to relaxation and the other due to pure dephasing $\Gamma_\varphi = 1/T_\varphi$ and related by

$$\begin{aligned} \Gamma_2 &= \Gamma_1/2 + \Gamma_\varphi \\ 1/T_2 &= 1/2T_1 + 1/T_\varphi \end{aligned} \tag{3.14}$$

where the 1/2 arises because Γ_1 describes probability decay but Γ_φ describes amplitude decay. Pure dephasing is due to polarization-preserving variation of the transition frequency.

If the spectral densities of all the noises affecting the qubit are uncorrelated, the decay is exponential and the longitudinal and transverse relaxations can be separated [96]. In this limit, the qubit free evolution from an initial state $|s\rangle = \alpha|g\rangle + \beta|e\rangle$ at time $t = 0$ to time t is described by the density matrix

$$\rho = \begin{pmatrix} 1 + \left(|\alpha|^2 - 1\right) e^{-t/T_1} & \alpha^*\beta e^{-t/2T_1} e^{-t/T_\varphi} e^{-i\Delta\nu_{\mathrm{R}}t} \\ \alpha\beta^* e^{-t/2T_1} e^{-t/T_\varphi} e^{i\Delta\nu_{\mathrm{R}}t} & \left|\beta\right|^2 e^{-t/T_1} \end{pmatrix}. \tag{3.15}$$

In general if the low frequency noise responsible for dephasing is correlated the simple exponential decay e^{-t/T_φ} is replaced by a more complicated and measurement dependent decay function $f_{z,\mathrm{exp}}(t)$ where the subscript "exp" denotes the experiment performed [see Sec.3.4].

The effects of decoherence on qubit performance are most easily observed by examining the width and saturation level of the spectroscopic lineshape. The lineshape is determined by continuously driving the qubit with pump power P_p, at a set frequency $\omega_{\mu w}$ with all other control parameters fixed, and recording the steady-state excited state probability P_e. The pump frequency $\omega_{\mu w}$ is then stepped through a range of values near ω_{CPB} to obtain the spectroscopic lineshape. The excited state probability as a function of pump power is found from the steady state solution of the Bloch equations [97] and has a Lorentzian lineshape given by

$$P_e = \frac{1}{2}\frac{(2\pi\Omega_R)^2 T_1 T_2}{1+(2\pi\Delta\nu_{\mathrm{R}}T_2)^2+(2\pi\Omega_R)^2 T_1 T_2}. \tag{3.16}$$

where $\Omega_R = \Omega_R(P_p) \propto \sqrt{P_p}$ as described in Sec. 3.1.1. At low pump power the excited state probability is linear in pump power while at high pump power it saturates at 1/2. We may also determine the half width at half max (HWHM) of the spectroscopic Lorentzian using Eq. 3.16 and find that it follows

$$2\pi\nu_{\mathrm{HWHM}} = \frac{1}{T_2^*} = \frac{1}{T_2}\sqrt{1+(2\pi\Omega_R)^2 T_1 T_2}. \tag{3.17}$$

At low pump power $\Omega_R \to 0$ and the spectroscopic coherence time T_2^* is equal to the coherence time T_2 given by Ramsey fringes decay time [see Sec. 3.4.1] while at high pump power the width is proportional to pump amplitude.

3.3 Relaxation

In the previous section we treated the relaxation time $T_1$and dephasing time T_φ as empirical quantities. Here we review their theoretical derivation from the spectral densities of the noise sources affecting the qubit and the qubit parameters. Each control parameter λ of the qubit Hamiltonian, such as the reduced gate voltage n_g or external flux bias Φ of the CPB, is coupled to uncontrolled or noisy environmental degrees of freedom. This

coupling causes the control parameters to introduce stochastic modulations of the qubit Hamiltonian. In a manner analogous to a harmonic n_g perturbation [see Sec. 2.3.2], each noisy control parameter results in a corresponding perturbation term to the qubit Hamiltonian.

If the control parameter is $\lambda(t) = \lambda_0 + \delta\lambda(t)$ where λ_0 is the average value and $\delta\lambda(t)$ is a small random fluctuation, we may expand the qubit Hamiltonian as

$$\begin{aligned} \hat{H}(\lambda(t)) &= \hat{H}(\lambda_0) + \delta\lambda(t)\frac{\partial\hat{H}(\lambda)}{\partial\lambda} + \delta\lambda^2(t)\frac{1}{2}\frac{\partial^2\hat{H}(\lambda)}{\partial\lambda^2} + \ldots \\ &= \hat{H}(\lambda_0) + \delta\lambda(t)\left[H_{x,1}\hat{\sigma}_x + H_{y,1}\hat{\sigma}_y + H_{z,1}\hat{\sigma}_z\right] + \ldots \end{aligned} \tag{3.18}$$

where we have written $\partial\hat{H}(\lambda)/\partial\lambda$ in terms of the Pauli spin matrices and discarded the term proportional to $\hat{I}$. This calculation is more easily carried out in the basis which has no λ dependence and afterwards transforming to the energy eigenbasis. Terms containing $\delta\lambda(t)$ describe linear coupling while terms containing $\delta\lambda^2(t)$ describe quadratic coupling of the qubit to the corresponding fluctuations of λ. Combining the transverse terms we write the lowest order perturbation responsible for transitions between the ground and excited state as

$$\hat{H}_\perp(\delta\lambda(t)) = \delta\lambda(t) D_{\lambda,\perp}\hat{\sigma}_\perp \tag{3.19}$$

where $D_{\lambda,\perp} = \sqrt{H_{x,1}^2 + H_{y,1}^2}$, $\hat{\sigma}_\perp = e^{i\theta}\hat{\sigma}_+ + e^{-i\theta}\hat{\sigma}_-$, and $\theta = \arg\left(H_{x,1} - iH_{y,1}\right)$. Using second order perturbation theory [62] we write the energy as

$$\omega_{01}(\lambda(t)) = \omega_{01}(\lambda_0) + \frac{\partial\omega_{01}}{\partial\lambda}\delta\lambda(t) + \left(\frac{\partial^2\omega_{01}}{\partial\lambda^2} - \frac{D_{\lambda,\perp}^2}{\omega_{01}}\right)\delta\lambda^2(t). \tag{3.20}$$

A noise source can be described by a corresponding quantum spectral density [49, 82] of noise

$$S_\lambda(\omega) = \int_{-\infty}^{\infty}\left\langle\delta\hat{\lambda}(0)\delta\hat{\lambda}(t)\right\rangle e^{i\omega t}dt \tag{3.21}$$

where $\hat{\lambda}$ is an environmental operator whose noise $\delta\hat{\lambda}(t)$ we are interested in. We also define the corresponding classical limit $k_BT \gg \hbar\omega$ of the spectral density of noise

$$S_{\lambda,\mathrm{c}}(\omega) = \int_{-\infty}^{\infty}\langle\delta\lambda(0)\delta\lambda(t)\rangle e^{i\omega t}dt. \tag{3.22}$$

The classical spectral density of noise is symmetric in frequency and its low frequency

components $S_{\lambda,c}(\omega \ll \omega_{01})$ are responsible for dephasing by inducing adiabatic variations of the transition frequency ω_{01} [see Sec. 3.4]. Decoherence due to depolarization involves energy exchange with a noise source and requires the quantum spectral density for a proper theoretical description.

The $S_\lambda(\omega > 0)$ component of the quantum noise describes absorption of energy by the environment and is responsible for relaxation of the qubit while the $S_\lambda(\omega < 0)$ component describes emission and is responsible for excitation of the qubit. If we assume a short correlated and weakly coupled noise source the depolarization rate is [82]

$$1/T_1 = \Gamma_1 = \Gamma_{exc} + \Gamma_{rel} \tag{3.23}$$

where Γ_{exc} is the excitation rate and Γ_{rel} is the relaxation rate. Fermi's golden rule [62] gives the rates as

$$\begin{aligned} \Gamma_{exc} &= \frac{1}{\hbar^2} D^2_{\lambda,\perp} S_\lambda(-\omega_{01}) \\ \Gamma_{rel} &= \frac{1}{\hbar^2} D^2_{\lambda,\perp} S_\lambda(\omega_{01}). \end{aligned} \tag{3.24}$$

If we assume our qubit environment is in thermal equilibrium at $k_B T \ll \hbar\omega_{01}$, the number of available modes at the transition frequency of the qubit is exponentially suppressed and $\Gamma_{exc} \to 0$ and $\Gamma_1 \to \Gamma_{rel}$. In practice non-equilibrium noise can cause excitation of the qubit but we found that this effect is not significant in our experimental setup, except for generating non-equilibrium quasiparticles. We observed that the excited state probability P_e when the CPB is prepared in the ground state is below our P_e measurement resolution, which implies $P_e < 0.01$.

3.3.1 Noise Sources Affecting the CPB

The noise sources affecting a qubit may be broadly categorized as having macroscopic sources such as control and readout circuitry or microscopic sources such as charge fluctuators or quasiparticles. The CPB is a charge qubit and is only weakly sensitive to noise that doesn't couple to the charge degree of freedom or the critical current. Here we will focus the discussion only on noise sources that couple via charge. The effect of a gate voltage perturbation has already been derived in Sec. 2.3.2 and from Eq. 2.27 we see that

the sensitivity to a gate voltage perturbation at $n_g = 1$ is

$$D_{n_g,\perp} = -2E_c. \tag{3.25}$$

As n_g is not a directly measured physical quantity it's useful to define the corresponding sensitivities to a voltage perturbation on the gate electrode

$$D_{V,\perp} = -2E_c C_g/e \tag{3.26}$$

and a charge perturbation

$$D_{q,\perp} = -2E_c/e. \tag{3.27}$$

The CPB gate is controlled by an external voltage, and fluctuations in that voltage translate into fluctuations in n_g. If this gate is coupled to an electrical environment with impedance $Z(\omega)$ then the spectral density of voltage noise associated with that impedance is given by the Johnson-Nyquist formula [82]

$$S_V(f) = \frac{2hf\,\mathrm{Re}[Z(f)]}{e^{hf/k_BT} - 1} \tag{3.28}$$

where the spectrum extends to both positive and negative frequencies. Qubit lifetime is enhanced by ensuring that the real part of the gate impedance is as small as possible. In our experiments the qubit is imbedded in a superconducting resonator used for readout. If the coupling between the qubit and the resonator is weak, we may treat the resonator as an effective impedance seen by the qubit. The real part of the impedance is given by the impedance of the parallel RLC circuit

$$\mathrm{Re}[Z(\omega)] = \frac{Z_c}{1 + (\omega - \omega_{res})^2/(\kappa/2)^2} \tag{3.29}$$

for $|\omega - \omega_{res}| \gg g$ where Z_c is the characteristic impedance and κ is the decay rate [see Sec. 2.4]. This can be viewed as an electrical engineering description of the Purcell effect [see Sec. 2.7]. For large detuning, weak coupling, and small κ this effective impedance is a very small quantity and doesn't inhibit qubit performance. However it's important to note that lossy parasitic modes of the sample box, the device chip or the control and readout wiring may also couple to the qubit in this fashion and suppress the lifetime [see

Sec. 6.1.1]. For this reason it's important to monitor for such spurious resonances during the assembly of the experimental setup and remove them if possible.

Lossy materials in or near to the qubit open other channels for qubit decoherence. The most important example of this is dielectric loss in the dielectrics in which the qubit's electric fields reside. Since the qubit has a complex geometry the field distribution is not simple nor confined to a single material and, in addition to the material properties, it's important to consider the participation ratio of field energy in each dielectric near the qubit. If we assume the simple case that the qubit lifetime is limited by dissipation in the junction capacitance then the spectral density of charge noise for $\hbar\omega \gg k_B T$ is [59]

$$S_q(\omega) = 2\hbar C_\Sigma \tan\delta \tag{3.30}$$

where $\tan\delta$ is the loss tangent of the junction oxide. While the loss tangents of nanoscale dielectrics at cryogenic temperatures are not well known, the loss tangent of amorphous AlO_x is commonly estimated to be $\tan\delta \approx 10^{-3}$ [98] and our own results suggest it may be as low as $\tan\delta \approx 10^{-8}$ in the small volumes formed by a junction oxide barrier [59].

Non-equilibrium quasiparticles are another potential source of energy loss [99, 100]. The qubit can decay by exchanging energy with a quasiparticle that tunnels from the island to the reservoir. Due to the charge sensitivity of the CPB, the presence of quasiparticles manifests itself as a breakdown of $2e$ periodicity of the qubit spectrum versus the reduced gate bias n_g. A single electron tunneling between the CPB island and the reservoir changes the gate bias by $1e$. A large density of quasiparticles may randomly tunnel on a time scale faster than the measurement time and lead to apparent $1e$ periodicity of the qubit spectrum. We observed such a breakdown of $2e$ periodicity in our earlier CPB designs with dissipative readout [61] but not in our current dispersive readout design.

In addition to quantum noise responsible for relaxation, the CPB is also affected by classical low frequency noise which causes dephasing. The origin of this low frequency noise isn't fully understood but its spectral density is known to follow a $1/f$ type power law for a large variety of physical systems. In the case of the CPB this consists of $1/f$ charge noise, due to charges moving in the vicinity of the qubit, with spectral density

$$S_{q,1/f}(f) = A_q^2/|f| \tag{3.31}$$

with typical values of $A_q \approx 10^{-3} - 10^{-4}\,\mathrm{e}/\sqrt{\mathrm{Hz}}$ [101, 43, 38, 81]. The CPB is also affected by $1/f$ flux noise, possibly due to spins on the surface of the metal films [102]. While charge noise is typically the dominant dephasing mechanism, flux noise may contribute if the qubit is operated away from the flux sweet spots at $\Phi/\Phi_0 = 0$ or $\Phi/\Phi_0 = 1/2$ and the sensitivity to charge noise has been sufficiently reduced by choice of qubit parameters [see Sec. 3.5 and 3.6]. The $1/f$ flux noise has spectral density

$$S_{\Phi,1/f}(f) = A_\Phi^2/|f|^\alpha \tag{3.32}$$

with α typically near 1 and $A_\Phi \approx 1 - 10\,\mu\Phi_0/\sqrt{\mathrm{Hz}}$ [103] with the lower end of that range most applicable to the types and sizes of Josephson junctions used in CPBs [104, 105].

3.4 Dephasing

Pure dephasing describes the decay of the off-diagonal elements of the density matrix

$$\rho = \begin{pmatrix} |\alpha|^2 & \alpha^*\beta f_{z,\exp}(t) e^{-i\Delta\nu_R t} \\ \alpha\beta^* f^*_{z,\exp}(t) e^{i\Delta\nu_R t} & |\beta|^2 \end{pmatrix} \tag{3.33}$$

where $f_{z,\exp}(t)$ is the experiment specific generalized decay function, the lifetime T_1 has been assumed to be infinite and the coupling to the noise sources is weak. It's caused by adiabatic fluctuations of the transition frequency ω_{CPB} and may be categorized into two types. Faster fluctuations will affect a single evolution of the qubit (one decay lifetime) while slower fluctuations, called inhomogeneous broadening, will affect the ensemble averaging performed during a typical experiment. Due to the random fluctuations of the transition frequency ω_{CPB}, the accumulated phase $\phi_{01}(t) = \int_0^t \omega_{CPB}(t')\,dt'$ between the ground state $|g\rangle$ and excited state $|e\rangle$ diffuses around the average value $\langle\phi_{01}\rangle(t) = \langle\omega_{CPB}\rangle t$. The phase is now a stochastic variable

$$\phi_{01}(t) = \langle\omega_{CPB}\rangle t + \Delta\phi(t) \tag{3.34}$$

with deterministic average value $\langle\omega_{CPB}\rangle t$ and random spread $\Delta\phi(t)$ [106]. An initial state $|s\rangle = \alpha|g\rangle + \beta|e\rangle$ at time $t = 0$ evolves at time t into a mixture of states given by

$$|s(t)\rangle = \alpha|g\rangle + \beta e^{i\langle\omega_{CPB}\rangle t} e^{i\Delta\phi(t)}|e\rangle \tag{3.35}$$

and the corresponding decay function is [22, 23]

$$f_{z,\exp}(t) = \left\langle e^{i\Delta\phi(t)} \right\rangle. \tag{3.36}$$

The decay function $f_{z,\exp}(t)$ can be expressed in terms of physical quantities such as the qubit sensitivity to noise and the spectral density of noise by first writing the Taylor expansion of $\omega_{CPB}(\lambda_0 + \delta\lambda(t))$ due to fluctuations $\delta\lambda(t)$ around the mean λ_0

$$\begin{aligned} \omega_{CPB}(\lambda_0 + \delta\lambda(t)) &= \langle\omega_{CPB}\rangle(\lambda_0) + \Delta\omega_{CPB}(t) \\ &= \langle\omega_{CPB}\rangle(\lambda_0) + \frac{\partial\omega_{CPB}}{\partial\lambda}\delta\lambda(t) + \frac{1}{2}\frac{\partial^2\omega_{CPB}}{\partial\lambda^2}\delta\lambda^2(t) \\ &= \langle\omega_{CPB}\rangle(\lambda_0) + D_{\lambda,z}\delta\lambda(t) + D_{\lambda 2,z}\delta\lambda^2(t) \end{aligned} \tag{3.37}$$

where $D_{\lambda,z} = \partial\omega_{CPB}/\partial\lambda$ and $D_{\lambda 2,z} = \partial^2\omega_{CPB}/\partial\lambda^2/2$. We can then write $\Delta\phi(t)$ as

$$\Delta\phi(t) = \int_0^t D_{\lambda,z}\delta\lambda\left(t'\right)dt' \tag{3.38}$$

or

$$\Delta\phi(t) = \int_0^t D_{\lambda 2,z}\delta\lambda^2\left(t'\right)dt' \tag{3.39}$$

depending on whether the coupling is linear or quadratic. The case of quadratic coupling arises when $D_{\lambda,z} = 0$ due to choice of the qubit operating parameters, for example when $D_{n_g,z}\big|_{n_g=1} = 0$ for the CPB. In this case the qubit is insensitive to parameter fluctuations to first order and the coherence time is enhanced.

We next assume that $\Delta\phi(t)$ is Gaussian distributed in which case $\left\langle e^{i\Delta\phi(t)}\right\rangle$ is the characteristic function for the Gaussian distribution [106]

$$f_{z,\exp}(t) = e^{-\frac{1}{2}\langle\Delta\phi^2(t)\rangle}. \tag{3.40}$$

If the spectral density of $\delta\lambda$ noise and $\delta\lambda^2$ noise is $S_\lambda(\omega)$ and $S_{\lambda^2}(\omega)$ respectively then we

can further simplify expressions Eqs. 3.38 and 3.39 and write [22, 23]

$$\ln f_{z,\exp}(t) = -\frac{1}{2} D_{\lambda,z}^2 2 \int_{\omega_{\text{avg}}}^{\omega_{\text{uv}}} S_\lambda(\omega) W_{\exp}(\omega,t) d\omega \tag{3.41}$$

for the case of linear coupling and

$$\ln f_{z,\exp}(t) = -\frac{1}{2} D_{\lambda 2,z}^2 2 \int_{\omega_{\text{avg}}}^{\omega_{\text{uv}}} S_{\lambda^2}(\omega) W_{\exp}(\omega,t) d\omega \tag{3.42}$$

for the case of quadratic coupling and where $W_{\exp}(\omega,t)$ is the filter function corresponding to the experiment performed, $\omega_{\text{avg}} = 2\pi/t_{\text{avg}}$ is set by the total time of ensemble measurements t_{avg}, ω_{uv} is an upper cutoff frequency, typically chosen to be ω_{CPB}, and the factor of 2 is due to the spectral density of noise being even at low frequencies.

$D_{\lambda,z}$ and $D_{\lambda 2,z}$ can be found by taking the corresponding derivatives. Starting with $\hbar\omega_{CPB}(n_g,\Phi)$ given by Eq. 2.21 we find the charge noise sensitivities

$$D_{n_g,z} = -\frac{16E_c^2(1-n_g)}{\hbar\omega_{CPB}(n_g,\Phi)} \tag{3.43}$$

and

$$D_{n_g 2,z} = \frac{1}{2}\frac{16E_c^2}{\hbar\omega_{CPB}(n_g,\Phi)} - \frac{1}{2}\frac{\left(16E_c^2(1-n_g)\right)^2}{\hbar^3\omega_{CPB}^3(n_g,\Phi)}. \tag{3.44}$$

At $n_g = 1$ $D_{n_g,z}\big|_{n_g=1} = 0$ and the CPB is insensitive to charge noise to first order. At this operating point $D_{n_g 2,z}$ simplifies to

$$D_{n_g 2,z}\big|_{n_g=1} = \frac{1}{2}\frac{16E_c}{E_J}. \tag{3.45}$$

Similarly the flux noise sensitivity can be found by starting with Eq. 2.24 and taking the derivative with respect to Φ. We find

$$D_{\Phi,z} = \frac{\pi}{2\Phi_0}\left(\frac{E_{J,max}}{\hbar}\right)^2 \frac{(d^2-1)\sin\left(2\pi\frac{\Phi}{\Phi_0}\right)}{\omega_{CPB}(n_g,\Phi)} \tag{3.46}$$

where we have taken care to use the form of $\hbar\omega_{CPB}(n_g,\Phi)$ containing the full junction asymmetry d dependence. From Eq. 3.46 we see that the flux sweet spot is at $\Phi/\Phi_0 = 0$ or $\Phi/\Phi_0 = 1/2$ at which points $D_{\Phi,z} = 0$.

Further analytic evaluation of $f_{z,\exp}(t)$ depends on the experiment performed and as-

sumptions about the spectral density of noise and is discussed in the following sections. A more in-depth discussion of decoherence is available in the dissertation by G. Ithier [107].

3.4.1 Ramsey Fringes

A Ramsey fringes experiment measures coherence during free evolution of the qubit state. A pulse detuned by $\Delta\nu$ from the qubit transition frequency acts as a $\pi/2$ rotation around, for instance, the x-axis to prepare the qubit in an equal superposition state. The qubit is then allowed to freely evolve for a time t, is again rotated by $\pi/2$ in the same manner and finally the excited state probability is measured [see Fig. 3.3(a)]. The filter function for this experiment is [107]

$$W_{\mathrm{Ram}}(\omega,t) = t^2 \,\mathrm{sinc}^2\left(\frac{\omega t}{2}\right) \tag{3.47}$$

where ω is the noise frequency being integrated over and t is the time at which the qubit state is measured [see Fig. 3.3(b)]. The duration of the control pulses is assumed to be negligible. This function may be viewed as the Fourier transform of a time domain boxcar filter. The filter function describes the sensitivity of a particular experiment to noise at various frequencies. The Ramsey fringes filter function $W_{\mathrm{Ram}}(\omega,t)$ is similar to a low pass filter with maximum sensitivity to low frequency noise and a minimum at $\omega = 2\pi/t$ with a series of rapidly shrinking lobes at higher frequencies. Unlike a standard low pass filter, the frequency cutoff of the Ramsey fringes filter function $W_{\mathrm{Ram}}(\omega,t)$ changes with the measurement time t, concentrating more of its area and becoming more sensitive to low frequency noise as the experiment progresses.

The final ingredient needed to evaluate the decay function $f_{z,\mathrm{exp}}(t)$ is the spectral density of noise $S_\lambda(\omega)$. If we assume the simple case of white noise $S_\lambda(\omega) = S_\lambda(0)$ the decay function is [107]

$$f_{z,\mathrm{Ram}}(t) = \exp\left[-\pi D_{\lambda,z}^2 t S_\lambda(0)\right]. \tag{3.48}$$

Since pure dephasing is due to fluctuations of the transition frequency during the experiment, a direct measurement of the spectrum should be consistent with the inferred spread of the transition frequency. This is indeed the case and is best illustrated by an exponential decay function of the form $f_{z,\mathrm{Ram}}(t) = \exp(-t/T_2)$ where T_2 is the Ramsey fringe decay time when there is no inhomogeneous broadening. In this case the spectral

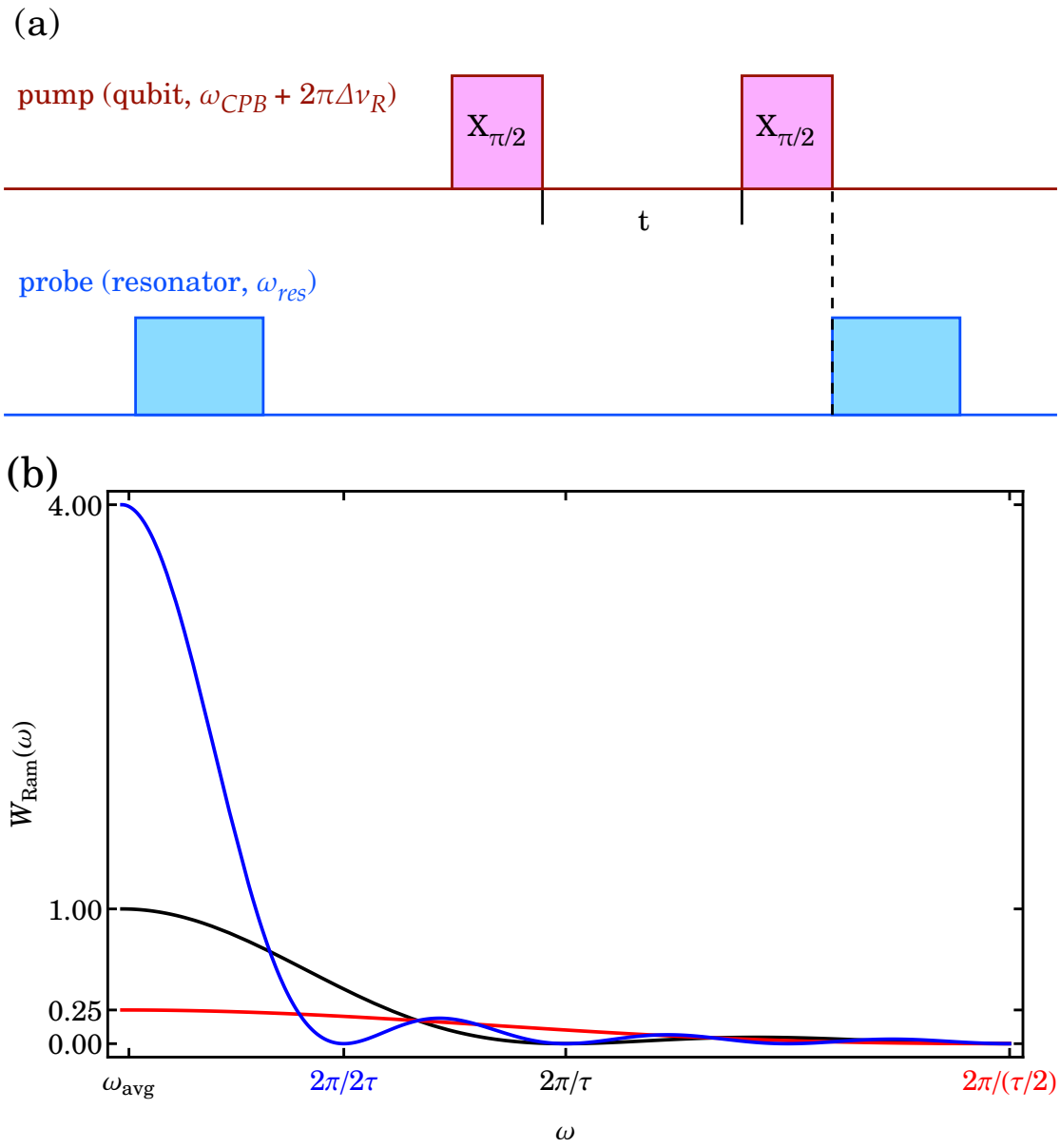

Figure 3.3: (a) The control pulse sequence for Ramsey fringes consists of a $\pi/2$ rotation, free evolution for time t, and another $\pi/2$ rotation, typically about the same axis. Synchronized with the end of the qubit manipulation is a readout pulse which projects the qubit state to $|g\rangle$ or $|e\rangle$. (b) The Ramsey fringes filter function resembles a low pass filter. At short measurement time $t = \tau/2$ (red) the function is low and wide. As the measurement time advances, the function narrows and grows in height (measurement time $t = \tau$, black and measurement time $t = 2\tau$, blue), concentrating near $\omega = 0$.

width is related to the dephasing time by

$$T_2 = \frac{1}{2\pi\nu_{\mathrm{HWHM}}} \tag{3.49}$$

where ν_{HWHM} is the spectroscopic half width at half maximum in units of Hz of a Lorentzian resonance peak. Similar relationships exist between more complex decay functions and spectral lineshapes [107].

In practice a charge qubit is affected by $1/f$ charge noise [see Sec. 3.3.1]. For our purposes, $1/f$ noise spectra may be broadly categorized into three types. A wideband $1/f$ noise spectrum extends to all frequencies [see Fig. 3.4(a)]. A static $1/f$ noise spectrum has a hard cutoff at ω_c and is assumed to be 0 afterward [see Fig. 3.4(b)]. Such a spectrum approximates that due to fluctuations that are slow or constant on the time scale of a single pump and probe sequence (typically on the order of $1\,\mu$s) but varies between the many such sequences comprising an ensemble average (typically on the order of 1 s). A quasi-static $1/f$ noise spectrum is a more realistic model than static $1/f$ noise. It has a soft cutoff at ω_c at which it crosses over into a more rapidly decaying noise spectrum, such as $1/f^2$ [see Fig. 3.4(c)].

Analytic solutions for the Ramsey decay function $f_{z,\mathrm{Ram}}(t)$ may be derived assuming various noise spectral densities and qubit coupling strengths. If the qubit is linearly coupled to wideband $1/f$ noise [see Eq. 3.31], the decay function is [64]

$$f_{z,\mathrm{Ram}}(t) = \exp\left[-t^2 D_{\lambda,z}^2 A_\lambda^2 \ln\left(1/\omega_{\mathrm{avg}} t\right)\right]. \tag{3.50}$$

If the noise spectrum is $1/f$ static with cutoff at ω_c the decay function is very similar [108, 109, 110]

$$f_{z,\mathrm{Ram}}(t) = \exp\left[-t^2 D_{\lambda,z}^2 A_\lambda^2 \ln\left(\omega_c/\omega_{\mathrm{avg}}\right)\right]. \tag{3.51}$$

Note that $\sigma_\lambda^2 = 2A_\lambda^2 \ln\left(1/\omega_{\mathrm{avg}} t\right)$ is the variance of wideband $1/f$ noise and, in contrast to white noise, increases with time. Additionally the decay is non-exponential, in this case following a Gaussian profile. In cases of non-exponential decay, it's not possible to define a decay rate and instead the dephasing time is defined by $\left|f_{z,\mathrm{exp}}\left(T_{\mathrm{exp}}\right)\right| = 1/e$. Finally if the decay function is complex valued the phase of $f_{z,\mathrm{Ram}}(t)$ shifts the phase of the Ramsey oscillations.

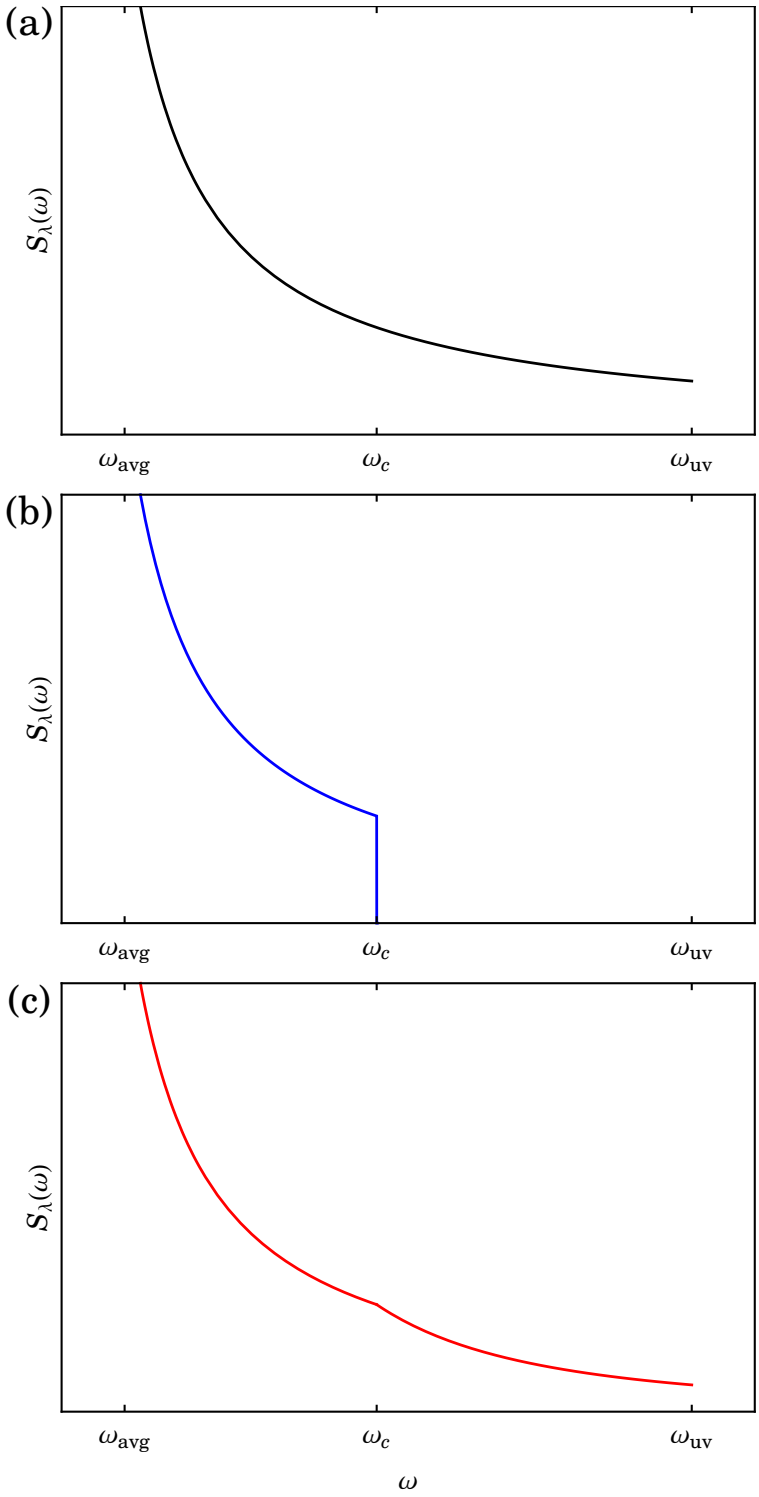

Figure 3.4: Possible $1/f$ noise spectra. (a) A wideband spectrum extends to all frequencies while (b) a static spectrum has a hard cutoff at ω_c. (c) A quasi-static spectrum has a soft cutoff at ω_c after which it transitions to a faster falloff, such as $1/f^2$.

Quadratic coupling of the qubit to the noise source is mathematically handled similarly to linear coupling but requires one additional simplifying assumption. It's necessary to make assumptions regarding or derive the spectral density $S_{\lambda^2}(\omega)$ and probability distribution of $\delta\lambda^2$. The probability distribution of $\delta\lambda^2$ may be assumed to be Gaussian or $\delta\lambda$ may be assumed to be the Gaussian variable with $\delta\lambda^2$ consequently having a non-Gaussian distribution. However, both approaches lead to very similar results and will be used as convenient. The spectral density of $\delta\lambda^2$ is approximately given by [109]

$$S_{\lambda^2}(\omega) = \frac{1}{\pi}\int_{-\infty}^{\infty} S_\lambda(\omega') S_\lambda(\omega-\omega')\, d\omega' \tag{3.52}$$

where $S_\lambda(\omega)$ is the assumed spectral density of $\delta\lambda$. For $1/f$ charge noise [see Eq. 3.31] this gives

$$S_{q^2,1/f}(f) = \frac{4}{\pi}A_q^2 \frac{\ln|\omega/\omega_{\text{avg}}|}{|\omega|}. \tag{3.53}$$

If we assume quadratic coupling to wideband $1/f$ noise with Gaussian $\delta\lambda^2$ distribution the decay function is [109]

$$f_{z,\text{Ram}}(t) = \exp\left[-\left(\frac{1}{2}D_{\lambda 2,z}\frac{A_\lambda^2}{\pi}t\ln(\omega_{\text{avg}}t)\right)^2\right]. \tag{3.54}$$

Alternatively if the $1/f$ noise is quasi-static with a soft cutoff at ω_c and the distribution of $\delta\lambda$ assumed Gaussian then the decay function for short times $t < t_c = 2/\left(D_{\lambda 2,z}A_\lambda^2\right)$ is [108, 109, 110]

$$f_{z,\text{Ram}}(t) = 1/\sqrt{1-2iD_{\lambda 2,z}A_\lambda^2 t\ln\left(1/\omega_{\text{avg}}t\right)} \tag{3.55}$$

and transitions to an exponential decay for long times.

3.4.2 Spin Echo

A spin echo measurement can be thought of as a form of open loop control to reduce dephasing due low frequency noise at the expense of increased sensitivity to the higher frequency noise components. In the language of NMR, the spin echo technique [111] counters the effects of inhomogeneous broadening, producing linewidth limited only by homogeneous broadening. Similar to Ramsey fringes, the pulse sequence begins with a $\pi/2$ rotation around, for instance, the x-axis to prepare the qubit in a state with an equal superposition of $|g\rangle$ and $|e\rangle$. The qubit evolves freely for a time $t/2$ after which another

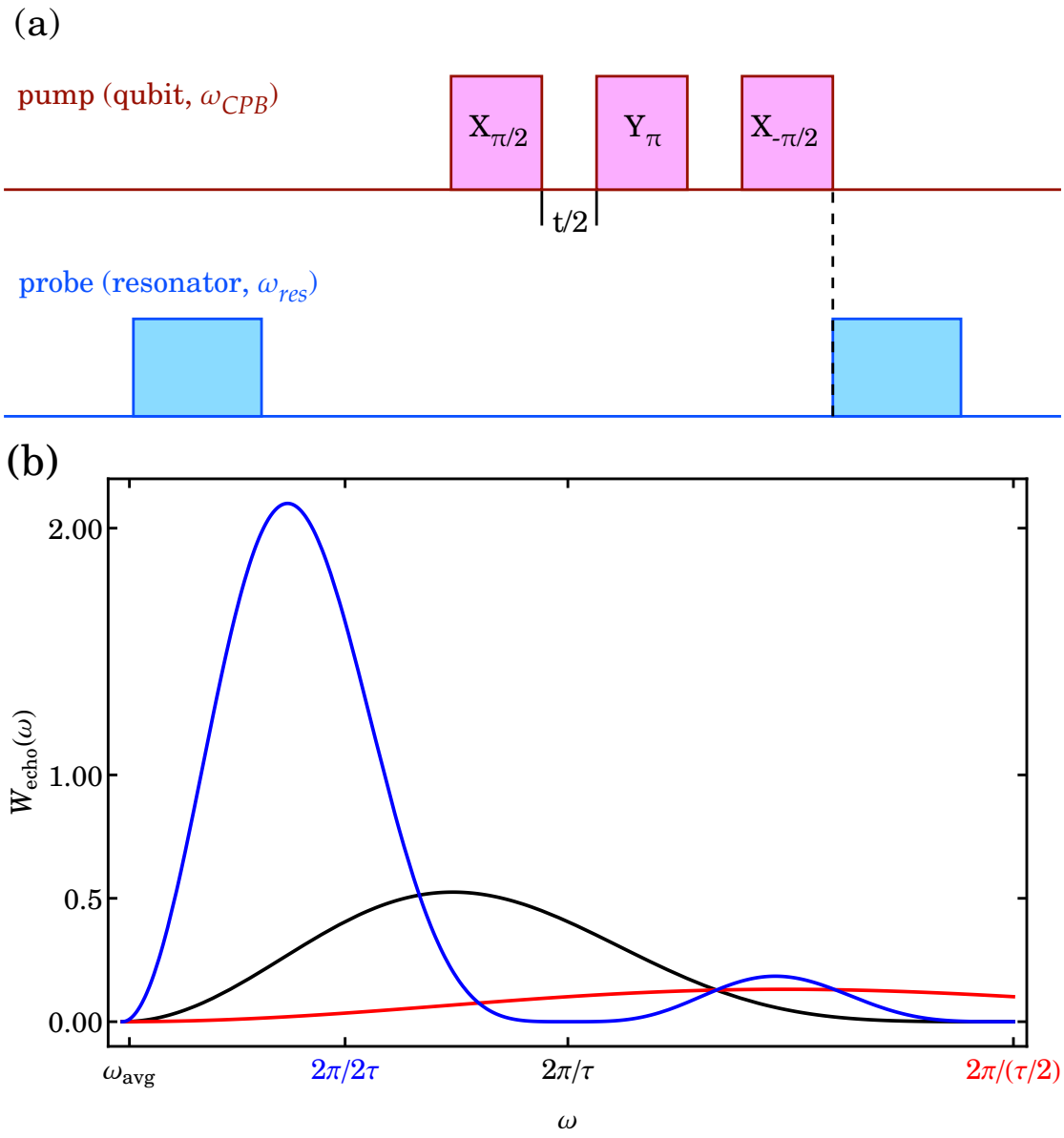

Figure 3.5: (a) The control pulse sequence for spin echo consists of a $\pi/2$ rotation, free evolution for time $t/2$, a π rotation, typically about the orthogonal axis, a second free evolution for time $t/2$, and another $\pi/2$ rotation about the original axis. Synchronized with the end of the qubit manipulation is a readout pulse which projects the qubit state to $|g\rangle$ or $|e\rangle$. (b) The spin echo filter function closely resembles a bandpass filter with pass band near $2\pi/t$. As the measurement time advances, the passband narrows, grows in height and moves to lower frequencies but always remains 0 at $\omega = 0$. Plotted is the evolution of the filter function with measurement time t, starting with $t = \tau/2$ (red) to time $t = \tau$ (black) and finally to time $t = 2\tau$ (blue).

pulse is used to rotate the qubit by π around either the same axis as the first time or the orthogonal axis, in this example the y-axis. The qubit then continues with another free evolution for time $t/2$, is rotated by $\pi/2$ around the same as axis as the first rotation and the excited state probability is measured after the last qubit manipulation pulse [see Fig. 3.5(a)]. The effect of the intervening π rotation is to refocus the transverse component of the Bloch vector that is along the axis of the refocusing pulse. Visualized on the Bloch sphere, the effect of the refocusing pulse on a set of precessing Bloch vectors is to swap the positions of the fast and slow vectors such that the slow ones are given a boost while the fast ones are set back by exactly the amount needed so as to refocus at the echo time t.

The filter function for this experiment is [107]

$$W_{\text{echo}}(\omega, t) = t^2 \sin^2\left(\frac{\omega t}{4}\right) \text{sinc}^2\left(\frac{\omega t}{4}\right) \tag{3.56}$$

where ω is the noise frequency being integrated over and t is the time at which the qubit state is measured [see Fig. 3.5(b)]. The spin echo filter function is similar to a bandpass filter with a passband at center frequency $\omega \approx 2\pi/t$. As the measurement time t increases the passband moves to lower frequencies but it remains insensitive to low frequency noise as $W_{\text{echo}}(0, t) = 0$. Additionally the area of the spin echo filter function is equal to the area of the Ramsey fringes filter function. Consequently the spin echo sequence doesn't reduce the dephasing rate for white noise and the decay function is given by

$$f_{z,\text{echo}}(t) = \exp\left[-\pi D_{\lambda,z}^2 t S_\lambda(0)\right]. \tag{3.57}$$

We may analytically evaluate the spin echo decay function based on various assumptions about the noise spectrum and the coupling. Assuming linear coupling to wideband $1/f$ noise [see Eq. 3.31], the decay function is [112, 113]

$$f_{z,\text{echo}}(t) = \exp\left[-t^2 D_{\lambda,z}^2 A_\lambda^2 \ln 2\right]. \tag{3.58}$$

If we define the enhancement factor as the increase in the dephasing time due to spin

echo as compared to the Ramsey fringes decay time we find

$$T_{\text{echo}}/T_2 = \sqrt{\left|\ln\left(\omega_{\text{avg}}t\right)\right|/\ln 2} \tag{3.59}$$

which is approximately $T_{\text{echo}}/T_2 \approx 4.5$ for typical values $t = 1\,\mu\text{s}$ and $\omega_{\text{avg}} = 1\,\text{Hz}$. The spin echo sequence does improve upon the Ramsey sequence but it's also limited by the high frequency tail of the $1/f$ noise. If the qubit is coupled linearly to $1/f$ noise with a high frequency cutoff ω_c, the detailed form of the spin echo decay function depends on the form of the cutoff. The decay function in the case of static $1/f$ noise is given by [108, 109, 110]

$$f_{z,\text{echo}}(t) = \exp\left[-\frac{1}{32}D_{\lambda,z}^2 A_\lambda^2 \omega_c^2 t^4\right] \tag{3.60}$$

while the case of quasi-static $1/f$ noise is given by

$$f_{z,\text{echo}}(t) = \exp\left[-\frac{1}{12}D_{\lambda,z}^2 A_\lambda^2 \omega_c t^3\right]. \tag{3.61}$$

In both cases the enhancement factor is greater than for the wideband case with the exact value depending on both ω_c and the shape of the high frequency noise cutoff.

Quadratic noise coupling leads to more complicated polynomial decay functions. Assuming static $1/f$ noise with cutoff at ω_c and a Gaussian distribution of $\delta\lambda$ the decay function is given by [114]

$$f_{z,\text{echo}}(t) = 1/\sqrt{1 + \frac{1}{8}D_{\lambda 2,z}^2 \omega_c^2 t^4 A_\lambda^4 \ln\left(1/\omega_{\text{avg}}t\right)}. \tag{3.62}$$

In general the spin echo decay function strongly depends on the exact shape of the cutoff.

3.4.3 Rabi Oscillations

Decoherence during driven evolution is measured by recording the decay of Rabi oscillations. Rabi oscillations [62] are the cyclic absorption and stimulated emission of photons by a qubit driven by a resonant or near-resonant harmonic drive. The qubit is excited by a pulse of duration t and the excited state probability is measured immediately after [see Fig. 3.6(a)]. The excited state probability has a sinusoidal dependence on the pulse length t which, for a resonant drive, is used to calibrate the π and $\pi/2$ pulses. The π pulse

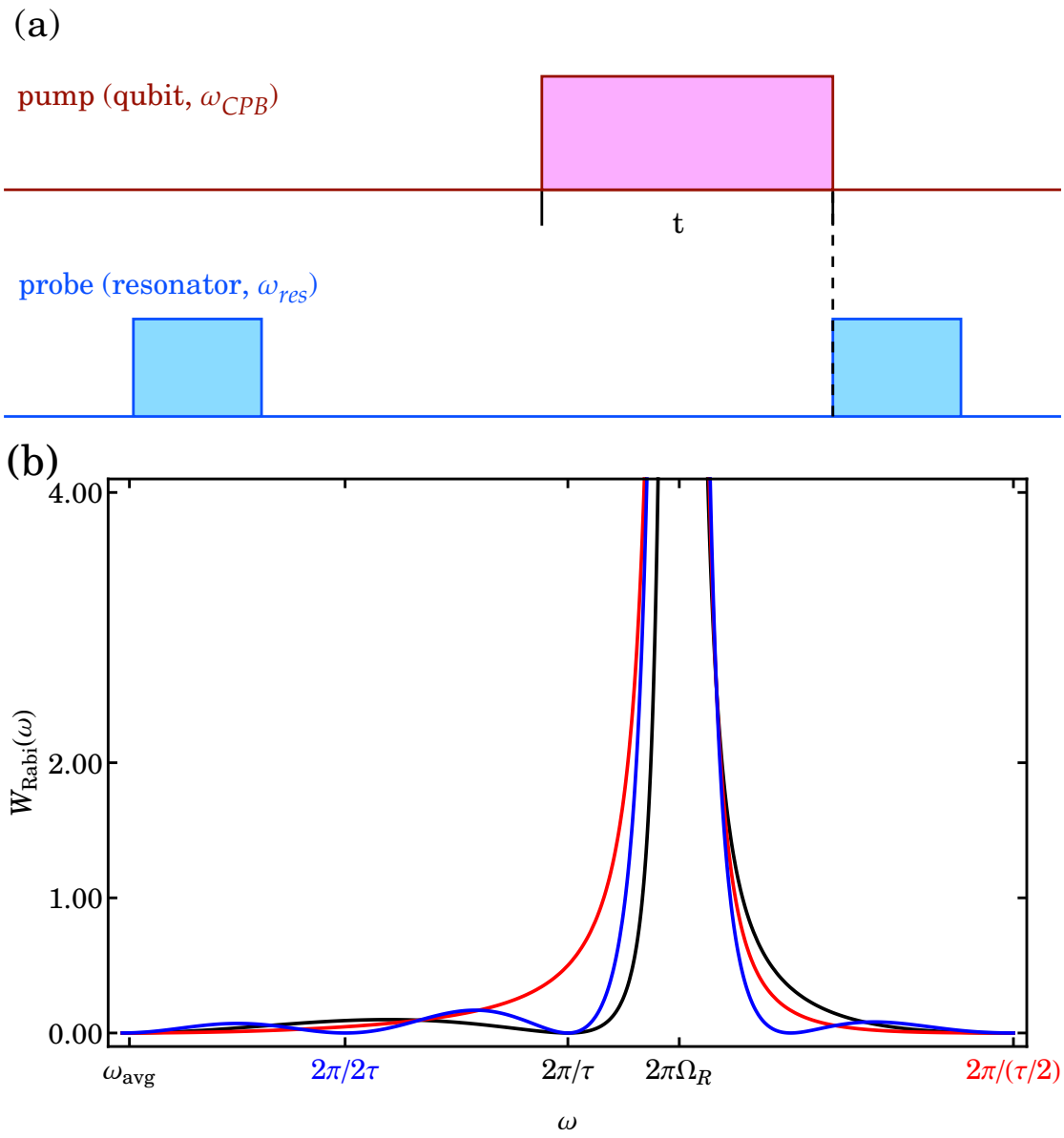

Figure 3.6: (a) The control pulse sequence for Rabi oscillations consists of an excitation pulse of duration t immediately followed by a readout pulse which projects the qubit state to $|g\rangle$ or $|e\rangle$. (b) The Rabi oscillations filter function closely resembles a bandpass filter with pass band at $2\pi\Omega_R$. The sharpness of the filter function is set by the measurement time t but the filter shape doesn't significantly change as the measurement time advances. The filter function is plotted at measurement times $t = \tau/2$ (red curve), $t = \tau$ (black curve), and $t = 2\tau$ (blue curve) and is seen to remain nearly the same.

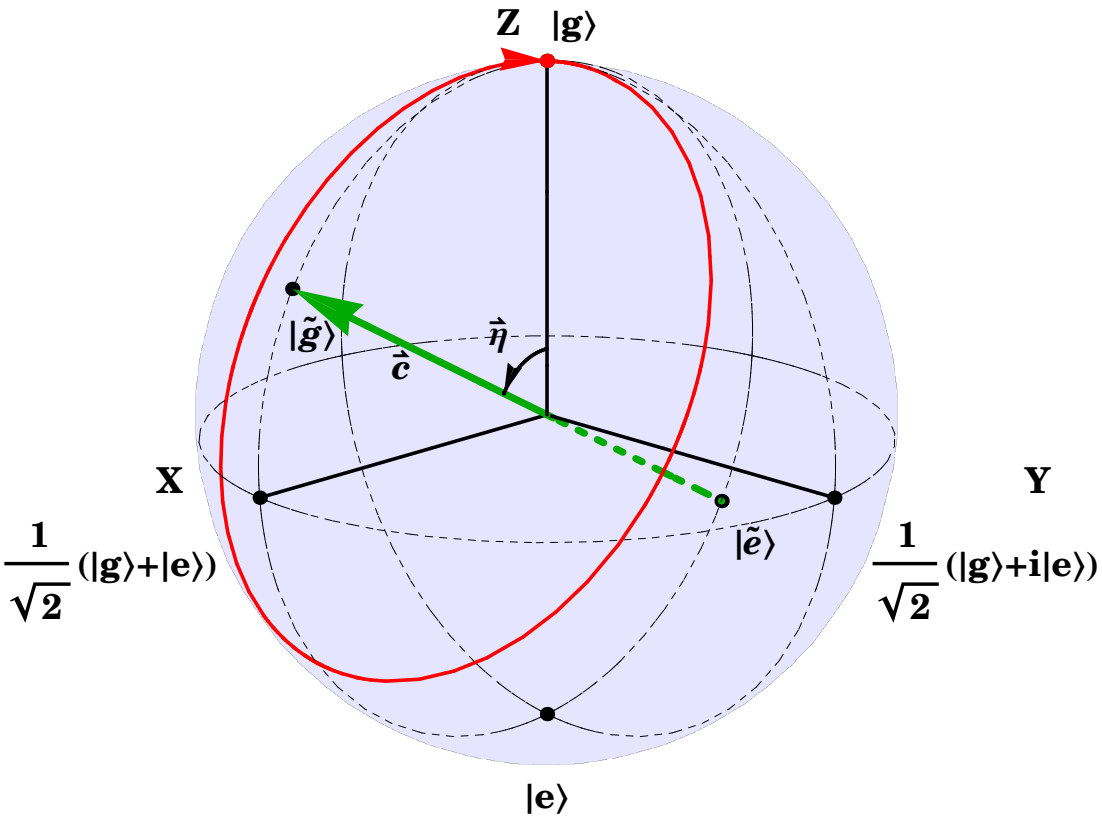

Figure 3.7: Rotating frame used to analyze Rabi oscillations. The frame rotates at the drive frequency $\omega_{\mu w}$ around the axis $\vec{c} = \left(\Omega_{R,0}, 0, \Delta\nu_{\mathrm{R}}\right)$ (green). The qubit state is expressed in the new eigenbasis $\{|\tilde{g}\rangle, |\tilde{e}\rangle\}$ and its driven evolution is a rotation around the axis $\vec{c}$ (red) at the Rabi frequency $\Omega_R = \sqrt{\Omega_{R,0}^2 + \Delta\nu_{\mathrm{R}}^2}$.

length is often conveniently chosen as the duration corresponding to the first excited state probability maximum while the $\pi/2$ pulse length is half of the π pulse length.

To analyze Rabi oscillations, it's convenient introduce a new eigenbasis $\{|\tilde{g}\rangle, |\tilde{e}\rangle\}$ in a rotating frame. The frame rotates around a fixed axis $\vec{c}$ on the Bloch sphere at the drive frequency $\omega_{\mu w}$ [see Fig. 3.7]. The horizontal component of the axis of rotation $\vec{c}$ has magnitude $\Omega_{R,0}$ and lies in the equatorial plane. Its exact direction depends on the phase of the drive but we may, without loss of generality, chose it to be along the x-axis. The vertical component of the axis $\vec{c}$ is $\Delta\nu_{\mathrm{R}} = \left(\omega_{CPB} - \omega_{\mu w}\right)/2\pi$, leading to an angle η with the z-axis defined by $\cos\eta = \Delta\nu_{\mathrm{R}}/\Omega_R$ or $\sin\eta = \Omega_{R,0}/\Omega_R$. The evolution of the qubit state is a rotation around the axis $\vec{c}$ at the Rabi frequency Ω_R. Analogous to T_1 and T_2, we define a relaxation time $\tilde{T}_1$ and a coherence time $\tilde{T}_2$ which correspond to the decay of the longitudinal and of the transverse parts of the density matrix in the rotating eigenbasis.

Assuming a white noise spectrum and taking into account the frequency shifts due to the transformation to the rotating frame, the relaxation rate in the rotating frame is

found to be [115]

$$\tilde{\Gamma}_1 = \sin^2\eta\Gamma_\nu + \frac{1+\cos^2\eta}{2}\Gamma_1 \tag{3.63}$$

where $\Gamma_\nu = \pi D^2_{\lambda,z} S_\lambda(2\pi\Omega_R)$. Decoherence in the rotating frame satisfies an equation similar to Eq. 3.14 of the form [115]

$$\tilde{\Gamma}_2 = \tilde{\Gamma}_1/2 + \tilde{\Gamma}_\varphi \tag{3.64}$$

where

$$\tilde{\Gamma}_\varphi = \frac{3-\cos^2\eta}{4}\Gamma_1 + \Gamma_\varphi\cos^2\eta + \frac{1}{2}\Gamma_\nu\sin^2\eta \tag{3.65}$$

is the pure dephasing in the rotating frame. At zero detuning $\cos\eta = 0$ and Eqs. 3.63 and 3.65 reduce to

$$\begin{aligned} \tilde{\Gamma}_1 &= \Gamma_\nu + \frac{1}{2}\Gamma_1 \\ \tilde{\Gamma}_\varphi &= \frac{3}{4}\Gamma_1 + \frac{1}{2}\Gamma_\nu. \end{aligned} \tag{3.66}$$

Unlike Ramsey fringes, which are most sensitive to noise at $\omega = 0$, Rabi oscillations are most sensitive to a narrow band of noise centered around $\omega = 2\pi\Omega_R$. Thus by studying the decay time of Rabi oscillations, one can access the spectral density of noise for frequencies that typically range from 1 MHz to 200 MHz. From Fig. 3.6(b) we see that the effect of low frequency noise is suppressed to first order in Rabi oscillations. Fluctuations of the transition frequency manifest themselves as fluctuations of the Rabi frequency Ω_R and couple to second order, as may be seen by performing a Taylor expansion of Ω_R in the detuning $\Delta\nu_\mathrm{R}$

$$\begin{aligned} \Omega_R &= \sqrt{\Omega^2_{R,0} + \Delta\nu^2_\mathrm{R}} \\ &\approx \Omega_{R,0} + \frac{\Delta\nu^2_\mathrm{R}}{2\Omega_{R,0}}. \end{aligned} \tag{3.67}$$

If the noise spectrum isn't white, such as the case of $1/f$ noise, then the decay due to low frequency noise is no longer exponential. In this case the exponential decays associated with the rates Γ_1 and Γ_ν combine with the non-exponential decay from the low frequency

noise and the Rabi decay function is given by [107]

$$f_{z,\mathrm{Rabi}}(t) = f_{z,\cos\eta}(t) \times \exp\left[-\left(\frac{3-\cos^2\eta}{4}\Gamma_1 + \frac{1}{2}\Gamma_\nu \sin^2\eta\right)t\right] \tag{3.68}$$

where the exponential decay factor is due to Γ_1 and Γ_ν from Eq. 3.65. $f_{z,\cos\eta}(t)$ is the Ramsey decay function appropriate to the assumed coupling and noise spectrum but with the noise scaled by $\cos\eta$, specifically via the substitution $D_{\lambda,z} \to D_{\lambda,z}\cos\eta$ and $D_{\lambda 2,z} \to D_{\lambda 2,z}\cos\eta$ as appropriate.

Alternatively, we could directly solve for the Rabi decay function starting with Eq. 3.41 or 3.42 and then assuming a specific noise spectrum and using the Rabi filter function [23]

$$W_{\mathrm{Rabi}}(\omega,t) = t^2\left(\frac{\Omega_R\omega/2\pi}{\Omega_R^2-(\omega/2\pi)^2}\right)^2 \mathrm{sinc}^2\left(\frac{\omega t}{2}\right). \tag{3.69}$$

This filter function has a shape comparable to the spin echo filter function but has smaller harmonic weight and a passband centered around frequencies Ω_R [see Fig. 3.6(b)]. This may be understood by considering that Rabi oscillations are most sensitive to noise near $\omega_{\mathrm{rot}} = 0$ in the frame rotating at Ω_R which appears as noise near Ω_R in the laboratory frame.

3.5 Qubit and Resonator Parameter Selection

The choice of qubit parameters E_J, E_c, and C_g is determined by factors such as fabrication feasibility, availability of compatible experimental equipment and the desired qubit coherence. The CPB is a charge qubit and consequently is most sensitive to charge noise. To minimize this sensitivity we characterized the qubit coherence at the charge sweet spot $n_g = 1$. At this point the transition frequency is given by $\hbar\omega_{CPB} = E_J$ [see Eq. 2.21]. Our microwave qubit control electronics are limited to the range $1-20\,\mathrm{GHz}$ while optimal performance and noise filtering lies in the range $4-8\,\mathrm{GHz}$. This constrains our operational E_J to the $4-8\,\mathrm{GHz}$ range. We found a large variance in our fabricated E_J^{sum}, about $\pm 50\%$ for nanoscale Josephson junctions, so that in practice if E_J^{sum} is found to be above the optimal range, it can be tuned down using an applied external flux Φ [see Eq. 2.19]. Ideally E_J^{sum} is in the $4-8\,\mathrm{GHz}$ range so as to enable operation of the qubit at the double sweet spot at $n_g = 1$ and $\Phi/\Phi_0 = 0$. However, since the CPB sensitivity to flux noise is

much lower than its sensitivity to charge noise, operation away from the flux sweet spot is not necessarily detrimental to qubit performance and we have used qubits with E_J^{sum} as large as 20 GHz without any apparent issues.

The choice of E_c is bounded above and below by two criteria. E_c/E_J must be sufficiently large so that the device behaves as a charge qubit. This is typically achieved by having $E_c \gg E_J$. If $E_c \gtrsim E_J$ the charging energy is still the dominant energy scale but more than two charge states are needed to accurately model qubit dynamics. On the other hand, at the sweet spot the charge sensitivity $D_{n_g 2,z} = 8E_c^2/E_J$ [see Eq. 3.45] and it's advantageous to reduce E_c/E_J to improve qubit performance. We chose to optimize E_c for longer qubit coherence times and used $E_c/E_J \approx 1$ which corresponds to E_c in the $4-8$ GHz range.

Our ability to tune E_J and E_c independently relies on the fact that, while both are functions of the construction of the junction, they depend on different factors. Specifically, $E_c = e^2/2C_\Sigma$ where $C_\Sigma = C_j + C_g$ and $E_J = \Phi_0 I_0/2\pi$ [see Sec. 2.1]. Since $C_j \gg C_g$ the two relations may be approximated as $E_c \propto 1/C_j$ and $E_J \propto I_0$. C_j is the junction capacitance and scales as $C_j \propto A/d$ where A is the junction area and d the thickness of the dielectric whereas the critical current I_0 scales as $I_0 \propto A \times e^{-\xi d}$ where ξ is a constant. In practice, we use our choice of E_c to constrain the area A. The approximate thickness d_0 is fixed at about $1-2$ nm. As $E_c \propto d_0$, a small change in $d_0 \pm \Delta d$ induces a correspondingly small change in E_c. However, since $E_J \propto e^{-\xi d_0}$ and $\xi d_0 \gg 1$, a small change in d_0 results in a large change in E_J. This allows us to effectively independently tune E_J during junction fabrication after selecting an E_c value.

In addition to the set of qubit parameters, the resonator parameters ω_{res}, Q_L, Q_e, Q_i and the qubit-resonator coupling capacitance C_g need to be selected. ω_{res} is limited to the $4-8$ GHz range for the same reason as E_J. Additionally ω_{res} shouldn't be placed too far or too near to the qubit transition frequency ω_{CPB}. If the detuning is too small, the Purcell effect [see Sec. 2.7] will degrade the qubit excited state lifetime. If the detuning is too large, the dispersive shift χ [see Sec. 2.6] may be too small and require long averaging times during readout. For the lumped element resonators we chose to use $\omega_{res} = 5.5$ GHz.

Q_L affects the CPB in a similar fashion. If the quality factor Q_L is too low, the Purcell effect will degrade the qubit excited state lifetime. Additionally a low Q_L may decrease the signal-to-noise ratio if the system is in the small dispersive shift limit [see Sec. 2.6.1]. On the other hand, a very large Q_L will increase the rise time of the resonator, given by

$\tau_{res} = 1/\kappa = Q_L/\omega_{res}$. The readout signal is approximately the average value of the excited state probability during the integration time [see Sec. 2.6]. Increasing the integration time improves the signal-to-noise ratio but decreases the average value of the excited state probability because that decays at a rate T_1 during the integration window. Fortunately this loss of visibility is well understood and may be accounted for theoretically during post-processing. Our Q_L values are typically in the $20,000-40,000$ range and are set by Q_i, which is in the $30,000-150,000$ range and varies from to sample to sample, and Q_e, which is in the $50,000-70,000$ range and is determined by resonator layout. These loaded quality factor Q_L values correspond to resonator ring up times of the order of $\approx 1\,\mu$s.

Finally C_g sets the strength of the qubit-resonator coupling g and hence the dispersive shift χ [see Sec. 2.5]. We used C_g on the order of $\approx 10\,$aF, which puts our system in the dispersive limit with a dispersive shift large compared to the resonator linewidth.

3.6 Transmon Limit of the CPB

As discussed in the preceding section, reducing E_c/E_J decreases the CPB sensitivity to charge noise. If we continue decreasing the charging energy E_c so that $E_J \gg E_c$, we encounter the transmon [116] and phase qubit limits. We can reduce E_c by adding shunting capacitance across the existing CPB design. This additional capacitance increases C_Σ and consequently lowers E_c without changing the critical current I_0 of the junction or requiring larger qubit areas which would be more likely to contain material defects.

As E_c/E_J is decreased below one, the qubit energy levels lose their dependence on gate bias and become flatter, eventually becoming independent of charge [see Fig. 3.8]. We quantify this by introducing the total charge dispersion

$$\epsilon_m = \left|E_m\left(n_g = 0\right) - E_m\left(n_g = 1\right)\right| \tag{3.70}$$

which tracks the difference in energy between the qubit biased at $n_g = 0$ and $n_g = 1$ for energy level m. In the charge regime

$$\epsilon_0 = |0 - E_c| = E_c = \frac{E_c}{E_J} E_J \tag{3.71}$$

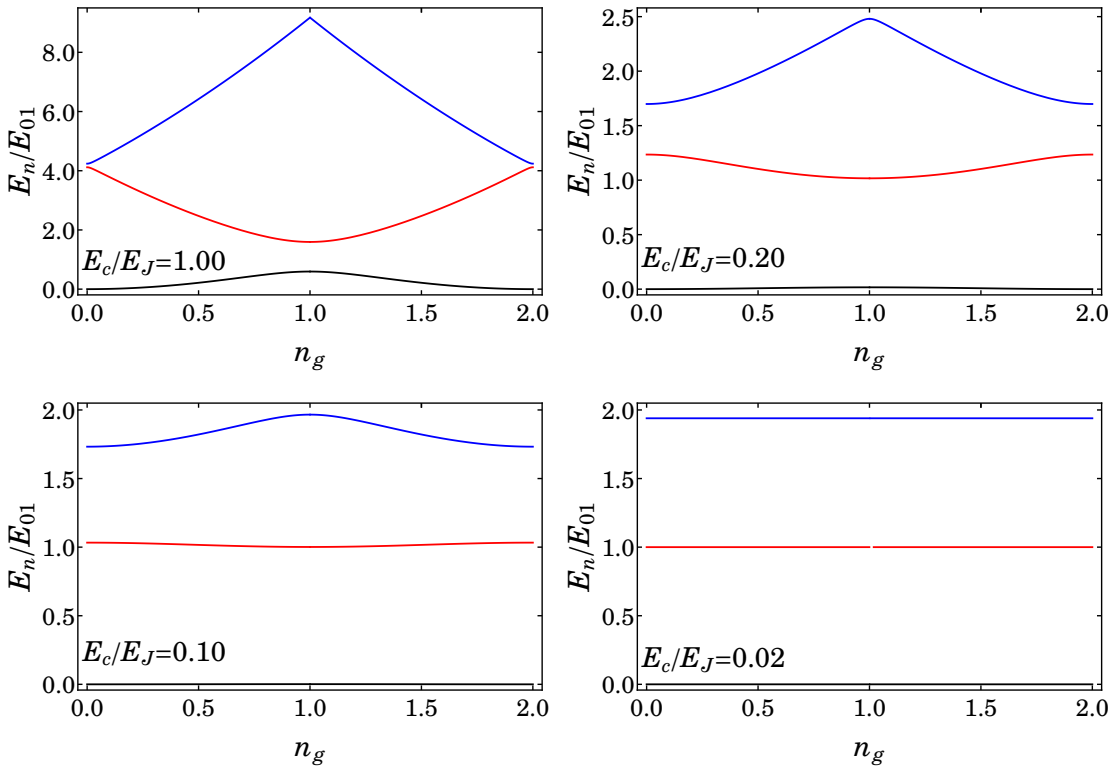

Figure 3.8: Charge dispersion in the transmon. As E_c/E_J is reduced from $E_c/E_J = 1.00$ to $E_c/E_J = 0.02$, the $n = 0$ (black), $n = 1$ (red), and $n = 2$ (blue) energy bands flatten and lose their dependence on the gate bias n_g. For clarity of illustration, the energy levels are scaled by $E_{01}\left(n_g = 1\right)$.

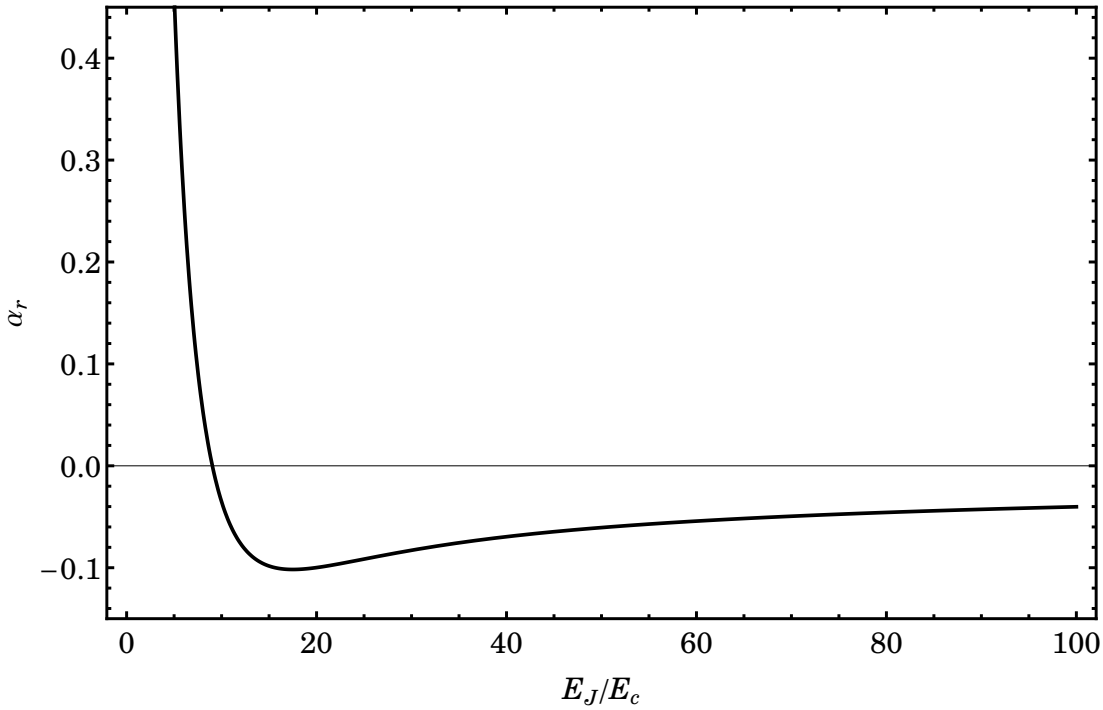

Figure 3.9: Relative anharmonicity α_r of the transmon plotted as a function of E_J/E_c. For small E_J/E_c the qubit is highly anharmonic. As E_J/E_c is increased the anharmonicity drops and crosses 0, rendering the CPB inoperable as a qubit near $E_J/E_c = 9$. However after further increase in E_J/E_c the anharmonicity becomes negative and remains small.

but as E_c/E_J is reduced the charge dispersion approaches [39]

$$\epsilon_m \approx E_c \frac{2^{4m+5}}{m!}\sqrt{\frac{2}{\pi}}\left(\frac{E_J}{2E_c}\right)^{m/2+3/4} e^{-\sqrt{8E_J/E_c}}. \tag{3.72}$$

Thus we see that the dependence of the energy levels on gate bias, and hence the sensitivity to charge noise, is exponentially suppressed. It's interesting to note that this drastic reduction of the effect of charge noise occurs for values of E_c/E_J as small as ≈ 0.1, which is still far from the typical regime of phase or flux qubits. An additional benefit of this new design is that there is no need for a gate bias line, although it comes at the expense of n_g tunability.

Along with decreased charge dispersion, lowering E_c/E_J reduces the anharmonicity of the energy levels [see Fig. 3.8]. Defining the relative anharmonicity as

$$\alpha_r = (E_{12} - E_{01})/E_{01} \tag{3.73}$$

in the small E_c/E_J limit one finds [39]

$$\alpha_r \approx -\sqrt{E_c/8E_J}. \tag{3.74}$$

While the charge dispersion decreases exponentially, the anharmonicity decreases only algebraically and maintains enough anharmonicity for the two level approximation to remain valid and operate the device as a qubit. Note that this region of sufficient anharmonicity is reached after first passing a forbidden region of $E_J/E_c = 8-10$ in which the anharmonicity passes 0 and switches sign [see Fig. 3.9].

The anharmonicity is important because the Fourier composition of qubit control pulses depends on their shape. Faster pulse rise times require larger bandwidth and increase the possibility of exciting higher lying transitions. The qubit anharmonicity limits the pulse rise time and hence the shortest pulse that may be used for qubit control. Long pulses increase operational time, countering some of the benefit of increased phase coherence or may be limited by relaxation. Finally, with reduced anharmonicity, higher levels are not as detuned and their presence may need to be accounted for to accurately model the qubit-resonator coupling and dispersive shift.

Alternatively, the transmon may be viewed as an unbiased phase qubit with a reduced critical current I_0. Since all of my measurements were in the CPB limit, I don't discuss the transmon further in this dissertation, but that avenue of research is pursued by other members of the group [117].

4 Experimental Details

4.1 Sample Fabrication

Our CPB qubit chip has two major components: the CPB itself and the readout resonator. The resonator is a simple, single layer, microscale lumped element structure whereas the CPB is a more complex, multilayer, nanoscale structure. We fabricated a multitude of dies containing the resonator structure by patterning them in parallel on a single wafer using optical lithography. After dicing the wafer, we followed this up with electron beam (e-beam) lithography based nanofabrication to produce the CPBs on individual chips.

4.1.1 Optical Lithography

Microfabrication [118, 119, 120] is the process of creating microscale and smaller structures on a flat substrate such as a silicon or sapphire wafer. Integral to this process is the technique used to transfer a desired pattern onto the target wafer. When light is used to transfer the pattern from a photomask onto a light sensitive resist, the process is called optical lithography or photolithography. In addition to transferring the pattern to the resist, it's also necessary to deposit or remove material in the desired areas.

Microfabrication typically follows one of two standard process flows. In the first method, commonly called a lift-off process, material is added to the desired areas by first coating the entire wafer with photoresist [see Fig. 4.1(a)]. The resist is then exposed to UV light through a mask containing the desired pattern and chemically developed, removing the resist in areas where it's desired to deposit material. A thin film of material is subsequently deposited on the entire wafer. In areas where the resist has been removed, the thin film will be deposited on the underlying substrate whereas elsewhere it's deposited on the photoresist. Finally the resist is chemically dissolved and this results in the removal of deposited material in all areas except where there were apertures in the resist.

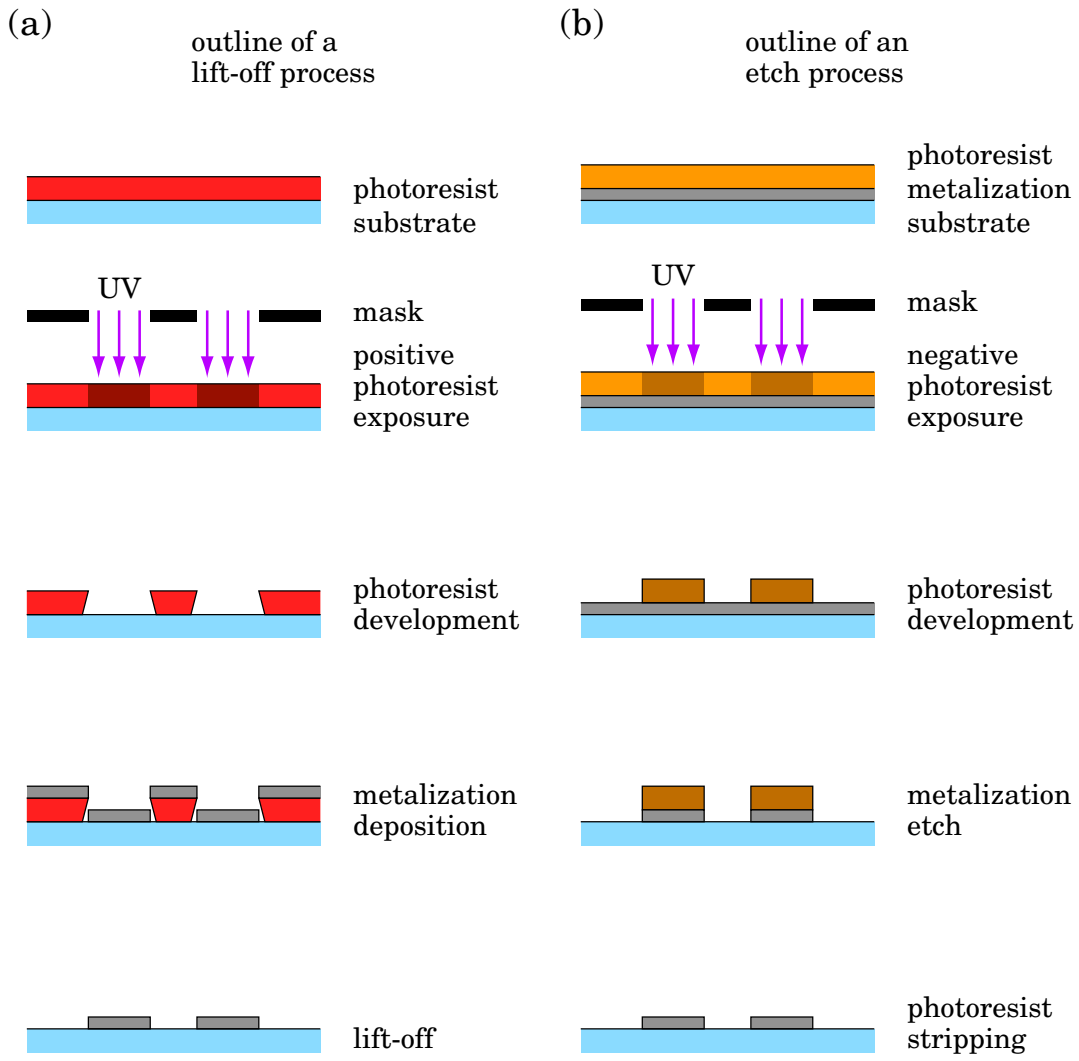

Figure 4.1: Diagrams of the two standard microfabrication process flows. (a) Lift-off is an additive technique that utilizes a resist mask to selectively add material in the desired areas. (b) Etch is a complimentary process that selectively removes material, leaving behind the desired pattern.

The second method, commonly called an etch process, may be considered the dual of the first and begins by depositing material on the entire surface of the wafer [see Fig. 4.1(b)]. The wafer is then coated with photoresist, exposed to UV light through a mask, and developed, reproducing the features on the mask. The initial layer of material is then etched using either a wet or dry process. In areas where the photoresist remains, it protects the material from removal. The resist is then removed using a wet resist stripper or a blanket dry etch process.

Although we have used both processes to produce samples, both of the devices that I studied in detail in this thesis were created using the lift-off process. The choice of one method over the other depends on details including the need to integrate the layer under consideration with previous and subsequent layers. For instance, the lack of a selective etch between the deposited material and an underlying layer will prohibit the use of the etch process. On the other hand if the material deposition process produces a conformal coating, it will not be possible to perform lift-off since the deposited material both blocks the dissolution of the underlying resist and yields rough edges in locations where lift-off does succeed.

Two different exposure techniques are commonly employed in optical lithography. Contact lithography, and the closely related proximity lithography, places a soda-lime glass mask either in contact with or offset a few microns from the wafer. A thin chromium film on the mask blocks UV transmission from a mercury-vapor lamp in the designated areas while the rest are transparent. Projection lithography uses projection masks, known as reticles, to project a reduced image from a distance in a manner similar to a slide projector. The exposed area is typically a small fraction of the wafer surface, such as a single die, and this process is repeated to cover the entire wafer. For this reason projection lithography machines are known as steppers. Steppers offer several advantages over contact aligners, such as higher resolution and reduced sensitivity to resist non-uniformity and edge bead, but are also much more complex to fine tune and operate. For both types of systems, feature size is limited by the wavelength of the light. While state of the art optical lithography is capable of producing features as small as $\approx 30\,\mathrm{nm}$ [121], for our resonator designs we only needed a resolution of $\approx 1\,\mu\mathrm{m}$. For this reason we used a simple contact aligner for resonator fabrication.

We designed the resonator wafer pattern for 3 inch wafers using L-Edit layout editor

[122] and had the corresponding $4 \times 4\,\text{inch}^2$ masks manufactured at Microtronics [123], a local business.

The choice of resist again offers two options: positive or negative. Positive photoresist becomes soluble in developer after exposure to UV light. The most common class of positive photoresists is based on diazonaphthoquinone (DNQ) mixed in novolac resin. Normally the novolac polymer is very weakly soluble in an aqueous base but additives may be used to increase the dissolution rate. DNQ is a photochemical acid generator and after exposure to UV light converts into an acid, increasing the rate of dissolution of the resist by several orders of magnitude. It's then easily and selectively washed away by the developer in the exposed regions. Conversely, unexposed negative photoresist is highly soluble in developer but after exposure to UV light becomes very weakly soluble. The physical mechanism responsible for this is UV light induced cross-linking of the polymer mediated by a photoactive additive. This renders it more inert and significantly less soluble in developer.

Resist processing begins with spin coating a thin layer of photoresist on a wafer. An excess amount of resist dissolved in a solvent is dispensed as a puddle on the wafer which is then spun at $1000 - 5000\,\text{rpm}$ for $30 - 60\,\text{sec}$ on a spinner. A combination of centrifugal force, fluid viscosity and solvent evaporation results in a uniform film. Factors such as the revolution rate, resist concentration, solvent evaporation rate and ambient environmental conditions determine the final film thickness. Following spin coating, the resist is prebaked (softbaked) at temperatures around $100 - 150\,^\circ\text{C}$. This drives off the majority of the remaining solvent which could otherwise create problems such as bubble formation or an uneven development rate. The resist is then exposed and post exposure baked (PEB) at around $\approx 100\,^\circ\text{C}$. This second bake thermally activates the diffusion of photoacid formed during exposure, helping to smooth out any non-uniformities caused by standing waves in the resist. Subsequently the resist is developed and an optional hardbake is performed. Hardbake temperatures are typically higher than for the previous two bakes, usually around $\approx 150\,^\circ\text{C}$, and serve to increase the chemical resistance of the resist. This helps the resist withstand further processing but may deform features as resist begins to flow when heated above its glass transition temperature. When the resist is no longer needed, it's removed, either by dissolving in a resist stripper or etching using an oxygen plasma in an asher.

The two resist types have different strengths and weaknesses. For example, negative resists tend to have better chemical resistance while positive resists have better step coverage. Nevertheless, the choice of which resist to use often comes down to preference. The early CPB-resonator chips fabricated by Z. Kim [71] were made on quartz or silicon using a process employing the negative resist NR9-1000PY from Futurrex [124]. By carefully controlling the exposure dose, we were able to control the sidewall profile of the resist to obtain an undercut and greatly facilitate lift-off. However when we switched to single crystal sapphire because of its lower dielectric loss tangent, we began having problems with exposure dose and lift-off. I believe this was due to the fact that sapphire is optically transparent and our wafers had only single-sided polish, resulting in excess diffuse reflection of the UV light from the backside and hence reducing our spatial and dose exposure control. To overcome this issue I switched to a bi-layer resist stack. For the top layer I used the positive resist OiR 906-10 by Fujifilm [125] while the bottom layer was LOR-5A by MicroChem [126]. LOR-5A is a non-photosensitive resist based on polymethylglutarimide (PMGI). It has a very well controlled development rate in all the standard resist developers. This allowed us to control the undercut independently of the top layer exposure parameters by overdeveloping the resist stack and eliminated our lift-off problems. The precise layer thicknesses, development procedure, and other process details I used are given in Appendix A.1.

4.1.2 Material Deposition and Etching

Many techniques are available to deposit thin films of single elements or compounds. One of the simplest methods is a type of physical vapor deposition (PVD) called evaporation which involves heating the source material in a boat or crucible at high vacuum. Typically the material melts in the boat and evaporates with some of the vapor traveling to and condensing on the substrate. The high vacuum ($10^{-6} - 10^{-8}$ Torr) is needed to allow the particles to travel the long distance (≈ 1 m) to the target without colliding with residual gas molecules. The source material may be heated by a resistive element, in which case it's called a thermal evaporator, or by bombarding it with high energy electrons from an electron gun, in which case it's called an electron beam (e-beam) evaporator. Thermal evaporators are simple but generally limited to relatively low melting point materials. E-beam evaporators may be used with almost any material but are more complex and have

other issues such as incidental low dose UV and x-ray exposure of the target. Typical deposition rates for evaporation systems are $5-10\,\text{Å/s}$.

Another commonly employed PVD method is sputtering. Sputtering is the process of ejecting atoms from the surface of a target by bombarding it with ions that typically have energies of a few hundred eV. Similar to evaporation, atoms that are ejected from the target travel to and redeposit on the surface of the substrate wafer which is typically $5-50\,\text{cm}$ away. The sputtering ions are often from a plasma formed from an inert gas, such as argon, that is generated using a strong dc or rf electric field. Depending on the configuration, the electric field responsible for generating the plasma also either directly or indirectly accelerates the ions toward the target. Unlike evaporation, sputtering takes place in a low vacuum, around $10^{-2}-10^{-3}\,\text{Torr}$, as sufficient background gas pressure is needed to generate the plasma. Consequently the target atoms diffuse due to collisions with the gas rather than travel in straight paths to the substrate. This results in a more conformal film with better step coverage in contrast to the directional deposition of evaporation. Conformality is beneficial in some situations but does make it difficult to use sputtering with a lift-off process. Other potential advantages of sputtering over evaporation include the ability to deposit materials with very high melting points, such as refractory metals, and better adhesion to the substrate due to the target atoms impacting the substrate with more energy. On the other hand, the higher background pressures needed for sputtering may result in more impurities, such as the sputtering gas, being incorporated into the film.

Chemical vapor deposition (CVD) [120] is a chemical, rather than physical, process used to deposit thin films. The substrate is exposed to a controlled combination of volatile precursors which react together or decompose on the surface to produce a film. This process produces very conformal coatings which in some cases are even able to penetrate and cover the surface area of high aspect ratio features. There are many implementations of CVD operating at pressures as high as $1\,\text{atm}$ or as low as $10^{-6}\,\text{Torr}$ with the more common tools working in the $10^{-3}\,\text{Torr}$ range. The various implementations also differ in the means by which the chemical reactions are initiated. Some use high temperatures to break down the reactants or provide a necessary activation energy. Plasma-enhanced CVD (PECVD) utilizes plasma to increase the chemical reaction rate of the precursors. The setup for PECVD is similar to sputter deposition except that the substrate is placed

at the location of the source target and the plasma is configured such that the precursors don't strike the substrate with sufficient kinetic energy to cause significant physical sputtering. Standard CVD processes are not compatible with lift-off due to the conformality of the coating and damage to the resist under the high operating temperatures used in CVD. The strength of CVD lies in the ability to deposit compounds with good stoichiometry control. It's most often used to deposit dielectric materials such as silicon or metal oxides.

Etching is the chemical removal of material from films on the substrate or the substrate itself and is classified as either a wet or dry process. During wet etching the entire substrate wafer is immersed in a bath of liquid etchant, typically a mixture of acids, bases or a buffered solution. At the conclusion of the etch, the wafer is rinsed in pure water or a similar inert solvent and then dried with nitrogen gas. All exposed surfaces of the target film are removed by a wet etchant at a nearly uniform rate, leading to an isotropic etch. This may be either problematic as the wet etch will undercut the resist mask and won't faithfully transfer the pattern to the underlying layer or beneficial if the undercut is desired to create free floating structures. Dry etching is conceptually similar to CVD in that the etchant is delivered as a gas or plasma to the surface to be removed. The etchants are chosen such that the products are highly volatile and can be pumped away after reacting with the material on the surface, exposing fresh material for further removal. The most common implementation of dry etching is reactive-ion etching (RIE) which bombards a surface with reactive ions generated from a plasma. The setup for RIE is very similar to PECVD and differs only in the choice of reactants. In fact PECVD equipment may be used as an RIE, and vice versa, merely by changing the gas chemistry. Since the reactive ions are accelerated towards the substrate, vertical surfaces receive a much smaller flux of etchant than horizontal ones, resulting in a directional or anisotropic etch. An interplay between the ambient gas pressure and the accelerating voltage or plasma power determines the relative amounts of drift and diffusion and is used to tune the anisotropy of the process. However it should be noted that if the accelerating voltage is too high, the ions may indiscriminately sputter material from the surface rather than reacting only with the target material. In addition to anisotropy, two other figures of merit are used to quantify etch processes. The etch rate describes how fast material is removal from the surface, commonly measured as the depth etched per unit time, while the selectivity is

the ratio of the etch rate of the target material to a different substance, usually the mask or the substrate material. Due to the myriad of available chemistries, wet etches usually have superior selectivities and etch rates as compared to dry processes but suffer from issues such as process complexity and possible contamination.

We used a dedicated aluminum thermal evaporator to deposit the 100 nm Al films which were then lifted-off to create the resonator structures. This was followed by a second step of lift-off processing to create Ti/Au alignment marks on the resonator wafer. These were deposited using an e-beam evaporator due to the high melting point of titanium. The purpose of the ≈ 10 nm Ti layer is to increase the adhesion of the 100 nm Au layer, which is not very reactive and might otherwise peel off from the wafer. The alignment marks are needed for the subsequent e-beam lithography used to pattern the CPB [see Sec. 4.1.3]. We also used the thermal evaporator to deposit a ≈ 12 nm aluminum anti-charging layer after spinning-on the e-beam resist stack [see Sec. 4.1.3]. This concluded our wafer wide processing as the e-beam lithography and junction fabrication steps were done on a die by die basis. The complete recipe we used to fabricate the resonators is given in Appendix A.1.

We separated the wafer into individual dies using a wafer dicing machine. The back of the wafer is attached to sticky tape which is in turn held in place by a vacuum chuck. Cuts are made along open areas between dies, called streets, using the mechanical sawing action of a rapidly-spinning water-cooled resinoid blade embedded with diamond grains. Dicing is a dirty process due to the large amount of debris and the need for cooling water. To protect the die surface during dicing we coated the entire wafer with FSC-M by Shipley (acquired by Rohm and Haas and subsequently by Dow Chemical Company [127]), a non-photosensitive and easily stripped resist.

In addition to qubits, we also made test resonators by sputtering and then etching a 150 nm Nb film. Using Nb allowed us to quickly test initial resonator designs by cooling them to 350 mK in a He-3 refrigerator rather than the more labor intensive cooldown to 25 mK in a dilution refrigerator. The superconducting transition temperature of aluminum is 1.2 K while that of niobium is 9.2 K. This means that at 350 mK thermally generated quasiparticles are not a significant source of loss in Nb resonators but can significantly limit the performance of Al resonators. We also performed similar preliminary 350 mK characterization of Al resonators. This allowed us to extract a more limited set of

information such as ω_{res}, Q_L and Q_e but not the ultimate Q_i or the qubit parameters.

4.1.3 Electron Beam Lithography

Electron beam (e-beam) lithography is a high resolution, maskless pattern generation technique that beats the diffraction limit of optical lithography by employing a beam of high energy ($10-100\,\text{keV}$) electrons to expose resist [128, 120]. The electron beam is focused to a spot as small as $\approx 1\,\text{nm}$ in diameter and raster scanned across the write area, pausing long enough at each point to expose the resist. The beam is blocked by using an electrostatic beam blanker while it's passing over areas that should remain unexposed. No physical mask is needed as only a software pattern is used to control the beam. Although this makes it a very useful research tool, the serial nature of the writing process significantly increases the exposure time.

The incident high energy electrons, called primary electrons, inelastically scatter off of the atoms or electrons in the resist, generating lower energy secondary electrons in the process. For electrons that undergo electron-electron forward scattering, the scattering angle is small and the primary electrons continue traveling through the resist and into the substrate, to depths greater than $10\,\mu\text{m}$, generating secondary electrons along the path. The primary electrons may also backscatter off of atoms with a scattering angle greater than 90°. The secondary electrons are capable of breaking chemical bonds and are responsible for most of the resist exposure. Although the beam itself is focused to a very small spot, the secondary electrons have a range of $\approx 10\,\text{nm}$ leading to typical linewidths of $\approx 50\,\text{nm}$ on our system and better on dedicated e-beam writers [129, 130].

Both positive and negative e-beam resists are available. Positive e-beam resists are commonly based on poly(methyl methacrylate) (PMMA), a high molecular weight polymer. The e-beam exposure causes chain scission, significantly increasing the dissolution rate in a solvent developer. The resist is available with a range of molecular weight formulations with a corresponding trade-off in contrast and sensitivity. Higher molecular weight PMMA requires a larger dose to expose, and hence is less sensitive, but also has a larger contrast in solubility between exposed and unexposed resist, allowing finer features to be written. Note that excessive e-beam exposure will cause the polymer to cross-link and increase its chemical resistance, in effect turning it into a negative resist. Negative e-beam resist based on hydrogen silsesquioxane (HSQ) cross-links on exposure

to e-beam, leaving behind a hydrogenated SiO_2-like compound after development.

Generating sub-100 nm features in our e-beam system requires successfully dealing with the various nuances of e-beam lithography. First, since e-beam lithography employs charged particles to expose the resist, it's necessary for the sample to be conductive in order to prevent charge build up. When the substrate wafer is composed of a conducting material such as doped silicon, this problem is naturally averted. However, in the case of an insulating substrate, such as quartz or sapphire, an anti-charging layer is needed. We deposited a ≈ 12 nm aluminum film on top of the e-beam resist to fulfill this role. This film is thin enough so as not to disrupt the exposure process but sufficiently conductive to prevent charge build up. Additionally, since e-beam resist is exposed by deep UV light or x-rays, it's important to not use e-beam or sputter deposition to deposit the anti-charging layer. Second, as has been already discussed, the primary electrons are forward scattered as they travel through the resist. This has the effect of broadening the beam and partially exposing nearby resist and is termed the proximity effect. Backscattering is less frequent but contributes significantly to the proximity effect. A workaround is to use a bi-layer resist stack. A thin, high resolution, upper resist minimizes forward scattering effects while the lower resist shields the upper resist from some of the electrons backscattered from the substrate [131, 128, 132]. The bi-layer resist stack also offers additional development parameters to tune the undercut and aid lift-off. Finally there is the need to detect an existing resonator pattern so as to align the e-beam write to it and place the CPB in the desired location. Contrast in a scanning electron microscope (SEM) image is a function of surface topography and the atomic number Z of the specimen. In our case the resist stack was 1 μm high and covered all the features, obscuring surface topography details. Additionally aluminum and sapphire have similar atomic number compositions, making it very difficult to distinguish the two. We solved this problem by depositing gold alignment marks near the write area which created small regions of very large Z contrast, and hence visibility.

Our e-beam writer was a converted JEOL 6500 SEM [133]. It operates as a standard SEM but during writing an external computer running Nanometer Pattern Generation System (NPGS) software [134] controls some aspects of the SEM. The system rasters the beam across the field of view, pausing as specified by the pattern file to expose the resist but blocking the beam when passing over areas that should remain unexposed. The e-

beam pattern is designed using a customized version of DesignCAD that comes packaged with NPGS. Our e-beam resist stack was 850 nm of MMA(8.5)MAA from MicroChem [126] followed by 120 nm of ZEP 520A from Zeon Chemicals [135]. MMA(8.5)MAA is methyl methacrylate copolymer with a significantly higher e-beam sensitivity (lower dose requirements) than PMMA while ZEP 520A is a PMMA based e-beam resist with somewhat higher sensitivity and higher chemical resistance. The two resists we chose have separate developers that are compatible with each other, allowing us to control the undercut independently of the feature size.

4.1.4 Junction Fabrication

An Al/AlO_x/Al Josephson junction is a nanoscale, multilayer structure. Complicated lithography and alignment would be required to fabricate such a structure one layer at a time. Instead we used a clever self-aligning process known as double-angle evaporation or alternatively the Fulton-Dolan bridge technique [136, 128, 137]. Double-angle evaporation is a lift-off based technique where two apertures, for forming the two leads of a Josephson junction, are separated by a suspended resist bridge. After the e-beam resist is developed, the junction is made in three consecutive steps without removing the sample die from the evaporator chamber [see Fig. 4.2]. For the first step, the sample stage is rotated and the first aluminum evaporation is done at an angle of $15° - 25°$ away from the surface normal and deposits one set of leads. For the second step, high purity oxygen is introduced into the chamber at a controlled pressure for a set amount of time. The aluminum reacts with the oxygen and aluminum oxide grows on all exposed metal surfaces. For the third step, the oxygen is pumped out and the second aluminum evaporation is performed. It's done at an angle differing from the first, typically mirrored about the surface normal. With proper choice of deposition angles one lead from the second deposition will lie on top of the other lead from the first deposition, capping the oxide to prevent further growth and forming a junction. Other leads formed by the two evaporations either completely overlap with existing leads or are isolated and hence don't contribute to the circuit. Due to the non-vertical angle of the evaporation, material will be deposited in areas near the base of the resist that are typically shadowed by the resist mask. To ensure this area is clear of resist, the undercut required for double-angle evaporation is significantly larger than that needed for standard lift-off and is commonly $0.5 - 1.0\,\mu$m.

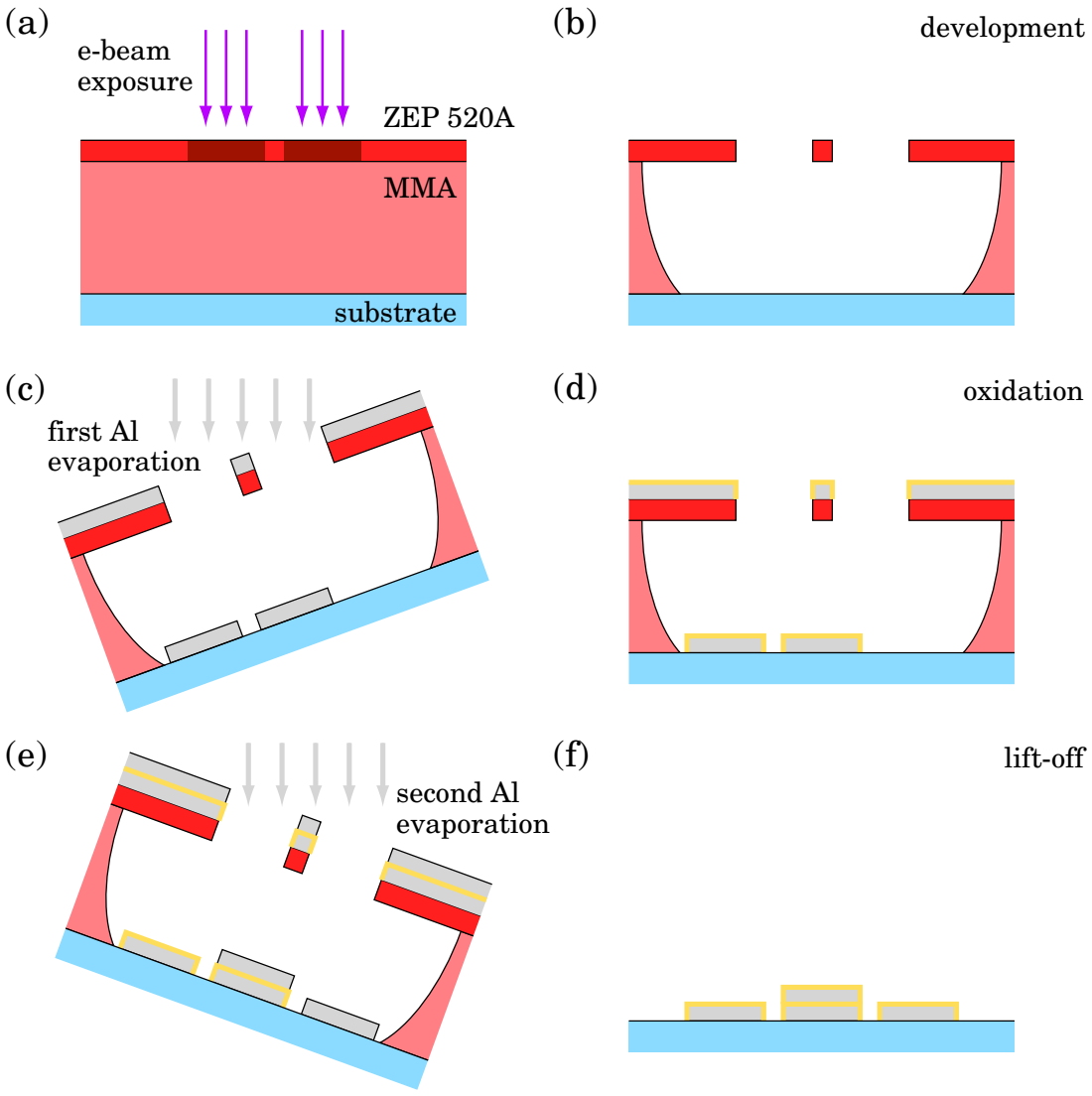

Figure 4.2: Diagram of the double-angle evaporation process. (a) The bi-layer resist stack is exposed by an e-beam and then (b) developed to produce a large undercut. The cross section view shows the two apertures separated by a suspended resist bridge. (c) The first angled Al evaporation deposits one set of features which are then (d) oxidized through a controlled exposure to pure oxygen. (e) The second angled evaporation produces another set of features with a small lateral offset from the first. The two evaporation angles are chosen such that the left lead from the second evaporation deposits directly on the right lead from the first evaporation, creating the metal-insulator-metal structure needed for a tunnel junction. (f) Resist lift-off completes the fabrication process.

We were able to achieve such large undercuts by choosing a resist stack with two compatible developers and a very sensitive bottom resist. The resist bridge may also collapse if it's too long. Ultimately this limits the maximum area of Josephson junctions that can be made with this process.

Oxidation is the most critical step of Josephson junction fabrication as it's responsible for creating the tunnel barrier. The aluminum oxide dielectric thickness sets the tunnel barrier height and the corresponding junction critical current I_0, while defects in the barrier contribute to decoherence. The critical current density, or current per area, is given by [138, 139]

$$J_0 \propto (P_{ox} t_{ox})^{-\alpha} \tag{4.1}$$

where P_{ox} is the partial pressure of oxygen in the evaporation chamber, t_{ox} is the oxidation time and α is an empirical constant. The product $P_{ox} t_{ox}$ is termed the oxygen exposure. For the high J_0 regime $\alpha \approx 1.5$ while in the low J_0 regime $\alpha \approx 0.5$—all of our samples are in the low J_0 regime. We have found that the proportionality constant of Eq. 4.1 slowly drifts with time, equipment and the operator. For this reason the standard procedure to obtain the desired critical current is to first fabricate a set of junctions using a best guess exposure and then scale the process parameters using Eq. 4.1 to correct for deviations.

Contamination during deposition and oxidation is responsible for the formation of defects in the tunnel barrier. The primary constituent of the ambient environment at $10^{-6} - 10^{-7}$ Torr is water vapor which reacts with fresh aluminum during oxidation and leads to the incorporation of impurity H ions. The approximate pressure-time product to form one monolayer is known as the Langmuir unit $L = 10^{-6}$ Torr$\cdot$s [140]. We minimize this by using a turbomolecular (turbo) pump to obtain a base pressure in our evaporator of $\approx 10^{-7}$ Torr, using heat strips to heat the chamber walls during pump down to drive off water and choosing a short, but not impractically so, oxidation time.

We also optimized the aluminum evaporation steps to reduce the impact of quasiparticles on CPB performance. Quasiparticles in a superconductor form a continuum of energies with a minimum at the superconducting gap Δ [33]. When the gap of the CPB island is larger than that of the leads, it's energetically unfavorable for quasiparticles to reside on the island. The superconducting gap Δ of aluminum films increases with

decreasing film thickness and also increasing concentration of non-magnetic impurities, including oxygen [141, 142, 143, 144]. During the evaporation process, a thin aluminum film coats not only the sample but also the walls of the evaporation chamber. This film is very reactive and acts as a getter, effectively allowing the system to achieve a lower background pressure than with the turbo pump alone. For this reason, the second evaporation is likely to give a cleaner film with a slightly lower energy gap Δ than the first film. Accordingly, we chose the order of double-angle evaporation such that the island was deposited first. Furthermore the island was made thinner than the leads, 300 Å versus 500 Å. Both of those factors increased the energy gap Δ of the island and helped protect the CPB from non-equilibrium quasiparticles. As an additional benefit, the thicker leads ensured that they would contact the island without risking a break in the region covering the step edge.

Junction fabrication is a low yield process and it's very advantageous to screen devices before committing to a long cooldown in a dilution refrigerator. The critical current I_0 of a Josephson junction scales with the geometry of the junction exactly as the inverse of its normal state tunneling resistance R_n. The Ambegaokar-Baratoff relation [33] quantifies the invariant product of the two as

$$I_0 R_n = \pi\Delta/2e. \tag{4.2}$$

Using this we may estimate the critical current of a junction by measuring its normal state resistance R_n. Although the room temperature tunneling resistance of a junction is larger than its normal state cryogenic value, the deviation is systematic. This allows us to perform rapid room temperature diagnostic characterization of potential devices. Since the disparity in the room temperature and cryogenic resistance values is systematic, we were able to use the known critical current I_0 and normal state resistance R_n of previously cryogenically characterized samples to improve our preliminary room temperature screening. With this technique we were able to estimate the critical current of well behaved devices with better than 50% accuracy.

The complete recipe we used to fabricate the CPBs is given in Appendix A.2.

4.2 Cryogenics and Filtering

Qubit operation requires cooling to sufficiently low temperatures such that higher lying states are not thermally populated and thermal fluctuations are suppressed [see Sec. 3.1], succinctly expressed as $k_B T \ll \hbar\omega_{01}$. For our CPB devices $\omega_{01}/2\pi \approx 6\,\mathrm{GHz} \approx 300 \times k_B/h\,\mathrm{mK}$ which implies that we need temperatures below $\approx 30\,\mathrm{mK}$ for optimal qubit performance. Evaporative cooling of He-4 can't produce temperatures below about 1.2 K while He-3 refrigerators only reach below about 300 mK. The most popular approach for quantum computing applications is to use a dilution refrigerator because it can reach temperatures below 20 mK with continuous operation [145, 146].

A dilution refrigerator uses the mixing of two phases of a He-3/He-4 mixture to provide cooling. Below the critical point at 860 mK the He-3/He-4 mixture spontaneously separates into two phases, the concentrated phase (nearly 100% He-3) and the dilute phase (6.6% He-3 and the balance He-4). The transfer of He-3 from the concentrated to the dilute phase is an endothermic process—it may be considered a type of "evaporation"—and provides effective cooling. Continuous operation of a dilution refrigerator is provided by extracting He-3 from the dilute phase and resupplying it to the concentrated phase.

We used an Oxford Instruments model 100 dilution refrigerator with a cooling power of 100 μW at 100 mK and a base temperature of about 25 mK. The He-3 follows a closed cycle that begins when it enters the refrigerator and is cooled to 4.2 K by the He-4 bath. It then passes through the He cold traps which freeze out any contaminants. The 1-K pot—a small volume of He-4 that is pumped on and evaporatively cooled to 1.5 K—cools the He-3 gas and condenses it to a liquid. The concentrated He-3 fluid then flows down to the mixing chamber, along the way passing and exchanging heat with the still at 0.6 K and with the returning dilute phase mixture. The mixing chamber is at the base temperature of the refrigerator and is the volume where the two phases coexist [see Fig. 4.3]. At the boundary between the two phases He-3 from the concentrated phase "evaporates" into the dilute phase, in the process cooling the mixing chamber and anything in thermal contact with it. He-3 in the dilute phase flows up to the still. A sealed He-3 pump pumps on the still, where He-3 evaporates preferentially and then exits the refrigerator, passing through the He-3 pump and liquid nitrogen cold traps before again beginning the cycle. The He-3 pump does the work of extracting He-3 from the dilute phase, keeping it from

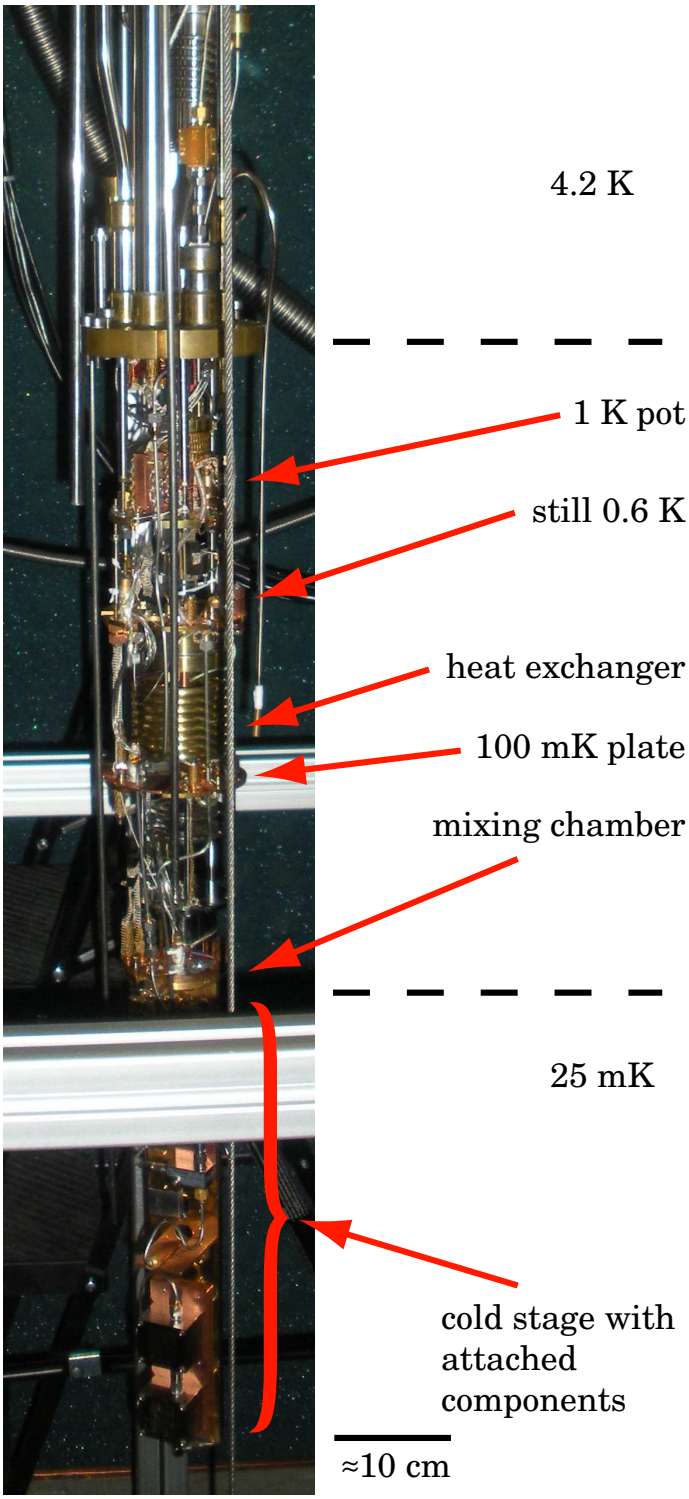

Figure 4.3: Photograph of the Oxford Instruments model 100 dilution refrigerator with all shielding cans removed. Identified are the approximate temperatures of the various components as well as the mixing chamber and the cold stage.

saturating and maintaining the refrigeration cycle.

The dilution refrigerator used for this work is a traditional design, sometimes called a wet refrigerator, and requires that the He-4 bath be refilled every three days. Newer designs, called dry refrigerators, use a pulse-tube cooler to replace the liquid helium bath, simplifying maintenance and reducing dependence on increasingly scarce He-4 supplies. The various temperature stages of a dilution refrigerator are necessary for its proper operation but also serve a very useful role in the optimal filtering and thermalization of the dc and rf lines going down to the sample at the mixing chamber.

4.2.1 Filtering and Thermalization

The primary experimental challenges in setting up the cryogenic experiment were to ensure that the system cooled to the desired base temperature and that noise from higher temperature stages or external instrumentation didn't compromise the qubit performance. The primary channels for heat and noise to propagate through are the input and output lines that connect the device to the rest of the setup. In our case this consisted of three distinct pathways—dc bias lines, rf input lines and rf output lines—each with their own filtering requirements. Infrared light leaking into the sample enclosure was another possible source of non-equilibrium noise [see Sec. 4.2.2].

The rf input line is used to drive the resonator and send microwave pump pulses to the qubit. It requires large bandwidth both due to the nature of the pulses themselves [see Sec. 4.3.2] and due to the tunability of the qubit transition frequency in the $4-8\,\mathrm{GHz}$ range. The line has a characteristic impedance of $50\,\Omega$ and is terminated by the $50\,\Omega$ output impedance of the microwave sources or mixers. This means that, if no filtering is used, the impedance seen by the qubit would be $50\,\Omega$ at a temperature of $300\,\mathrm{K}$ and the qubit performance would be impaired by the corresponding voltage noise. We can address this problem by filtering the rf input line with attenuators that uniformly reduce all incoming power—including Johnson-Nyquist noise, instrumentation noise, and qubit and resonator drive pulses—across the entire spectrum. The double sided voltage spectral density of Johnson-Nyquist noise of an impedance $Z(f)$ at a temperature T is given by [see Sec. 3.3.1]

$$S_V(f) = \frac{2hf\,\mathrm{Re}[Z(f)]}{e^{hf/k_BT}-1} \tag{3.28}$$

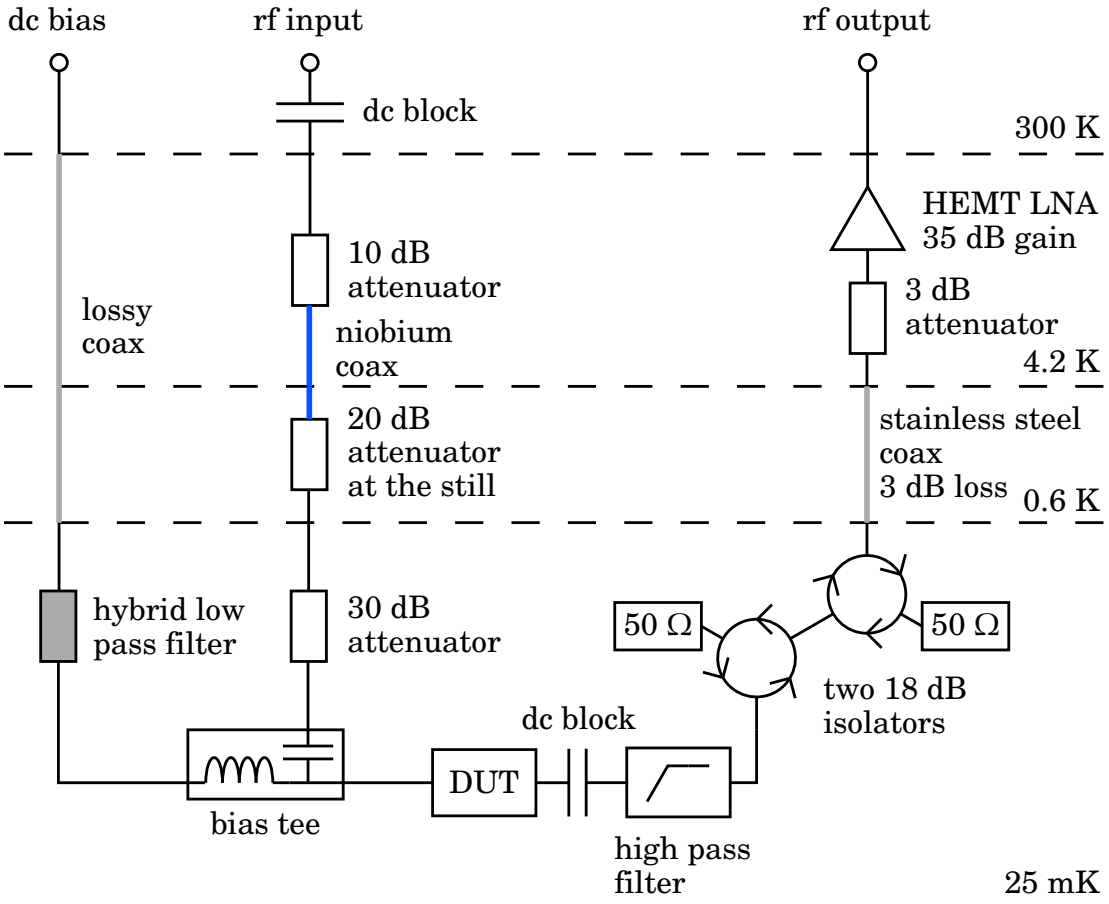

Figure 4.4: Diagram of the dilution refrigerator wiring. Two input lines, a dc bias line and an rf input line, are joined at the cold stage by a bias tee. A single rf output line allows information to be transmitted for room temperature processing. The device under test (DUT) is a CPB qubit coupled to a superconducting LC resonator. The ports label rf input and rf output connect to the corresponding ports in Fig. 4.8.

which simplifies to

$$S_V(f) = 2k_B TR \tag{4.3}$$

when $\hbar\omega < k_B T$ and $R = \mathrm{Re}[Z(f)]$. In an impedance matched system ($Z_{\mathrm{hot}} = Z_{\mathrm{cold}}$) with sample temperature T_{cold} such that $\hbar\omega < k_B T_{\mathrm{cold}}$, the power attenuation α at the cold stage required to adequately filter thermal noise is given by the particularly simple relation

$$\alpha = T_{\mathrm{hot}}/T_{\mathrm{cold}} \tag{4.4}$$

where T_{hot} is the temperature of the hot noise source. For instance, to attenuate room temperature noise in an experiment at 4.2 K it's sufficient to place a 20 dB attenuator in front of the sample. However when $\hbar\omega > k_B T_{\mathrm{cold}}$ it's necessary to use the full quantum form of the Johnson-Nyquist noise and one finds that much more attenuation is required [147]. Filtering room temperature noise below that of 25 mK requires over 60 dB of attenuation. Limited available space and cooling power of the mixing chamber make it impractical to mount all of the required attenuators at the sample. Distributing some of the components among the higher temperature stages such as the helium bath at 4.2 K and 1-K pot at 1.5 K avoids this issue. Since an attenuator is a resistive network with an impedance of 50 Ω [65], they are also thermal noise sources and can't reduce incoming noise below that given by Eq. 3.28 at their temperature.

We filtered our rf input line by placing a series of broadband dc – 40 GHz attenuators [148] consisting of a 10 dB attenuator at 4.2 K, a 20 dB attenuator at 0.6 K at the still, and a 30 dB attenuator at 25 mK [see Fig. 4.4]. Although this is a very large amount of attenuation (input power is reduced by a factor of 1,000,000), this is in fact beneficial as the powers needed to probe the resonator are in the single photon regime (≈ -110 dBm) and qubit manipulation pulses are only 20 – 30 dB larger. In addition to broadband attenuation, we used dc blocks with passband 10 MHz – 18 GHz [149] to filter out $1/f$ noise from room temperature sources such as instrumentation and for some cooldowns we included additional low or high pass filters to further remove noise outside the operational 4 – 8 GHz band.

It's important to note that as a practical matter, microwave components are rarely designed for and tested at cryogenic temperatures by the manufacturer. This may lead to significant deviations from the expected behavior in devices that rely on resistive ele-

ments and consequently all components should be tested cryogenically before their installation. In particular we have found that attenuators from some manufacturers become superconducting at the base temperature of the dilution refrigerator and for this reason we exclusively used attenuators from Midwest Microwave [148], which had only minor changes in their properties.

The rf output line has similar bandwidth requirements as the rf input line but with one additional complication. Since the signal passing through the sample is already highly attenuated, further broadband attenuation would render it too weak to detect. To get around this issue we used a $2.9-8.7\,\mathrm{GHz}$ high pass filter, Mini-Circuits model VHF-2700A [150], followed by a pair of $4-8\,\mathrm{GHz}$, $18\,\mathrm{dB}$ isolators from PAMTECH [151] at $25\,\mathrm{mK}$ [see Fig. 4.4]. An isolator is a two port, non-reciprocal, ferrite device. Signals entering port 1 propagate to port 2 while signals entering port 2 are routed to an internal $50\,\Omega$ termination. Thermal noise generated by the $50\,\Omega$ resistor is transmitted to port 1. The rating of an isolator describes how well port 1 is isolated from port 2, $18\,\mathrm{dB}$ in our isolators. This setup allowed us to pass signals to a cryogenic amplifier with minimal loss while attenuating noise from higher temperature stages. While isolators are marvelous devices, they have some drawbacks. They are bulky, generally narrow band, and don't behave well outside their designed passband. To ameliorate the latter issue we used low pass filters in series with the isolators on some cooldowns. The isolator chain was followed by a $3\,\mathrm{dB}$ attenuator and a $35\,\mathrm{dB}$ gain, low-noise, cryogenic HEMT amplifier from Caltech [152] at $4.2\,\mathrm{K}$ [see Fig. 4.4]. The $3\,\mathrm{dB}$ attenuator was needed because without it we observed strong self-oscillations in the amplifier. Amplifiers typically have high reverse isolation and directivity, meaning the HEMT amplifier also acted as a large attenuator to noise coming from readout instrumentation at room temperature.

The dc bias line has very different requirements than the rf lines. The bandwidth needed is very narrow, extending from dc to at most $1\,\mathrm{MHz}$ for very fast sweeps. On the other hand, the voltages required are much larger—a voltage of $\approx 10\,\mathrm{mV}$ gives an induced charge of $1e$ in a typical CPB. It's not practical to use wideband attenuators to filter this line as it would require source voltages of the order of $1\,\mathrm{kV}$. Reflective discrete-component low-pass filters are a good solution but have one flaw—at frequencies in the tens of GHz their behavior breaks down and they can display spurious transmission resonances. An alternative approach is to use dissipative filters. Skin effect loss in conductors scales

with frequency f as $\alpha \propto \sqrt{f}$ while dielectric loss is proportional to the loss tangent of the material and scales with frequency f as $\alpha \propto f$ [153]. Consequently a long coaxial cable of small diameter and low conductivity acts as an absorptive low pass filter [154, 155]. Alternatively the skin effect loss may be enhanced by using a copper powder filter [156, 157]. This type of filter consists of a long length of thin wire wound in a cylinder and imbedded in epoxy impregnated with very fine copper powder, significantly increasing the surface area and hence the skin effect damping. Our dc line filtering setup included both types of filters [see Fig. 4.4]. The cable running down to the sample stage was a thin, CuNi coax from COAX CO. [158]. CuNi is a poor conductor, increasing skin effect loss, and furthermore has poor thermal conductivity, reducing the heat load on the mixing chamber. In addition, I placed a hybrid capacitor-input (pi) and copper powder filter before the sample. The copper powder filter has a gentle cutoff beginning at about $\approx$ 1 GHz. Combining it with a pi filter, model 1293-001 from Spectrum Control [159], allows us to fine tune the cutoff slope and frequency, giving the combined filters a relatively sharp cutoff at $\approx$ 1 MHz. The rf input and dc bias lines were joined at the cold stage by using a $0.1-60$ GHz, model V250 bias tee from Anritsu [160]. The output coaxial cable from the bias tee was connected directly to the sample.

In addition to filtering, it's necessary to ensure that each input and output line is properly thermalized and heat sunk. Incomplete thermalization leads to components that are at a higher temperature than the refrigerator stage they are mounted to and produce excessive thermal noise. Incorrect heat sinking can also lead to a large heat load on the refrigerator and results in the cold stage heating above its base temperature. Thermal anchoring of rf lines is relatively straightforward since the attenuators used to filter noise are a resistive network and contain resistors which connect the center conductor to ground and ultimately the refrigerator.

We used coaxial cables made from materials with poor thermal conductivity and narrow cross section to limit the amount of heat conducted from higher temperature stages [see Fig. 4.4]. In situations that required poor thermal conductivity but good electrical performance we installed coax with superconducting niobium inner core and outer jacket. Thermal isolation of dc lines was accomplished the same way, by using wires constructed of poor thermal conductors. Thermal anchoring of dc lines is a more complicated because we can't simply break the outer insulation to ensure good thermal contact without also

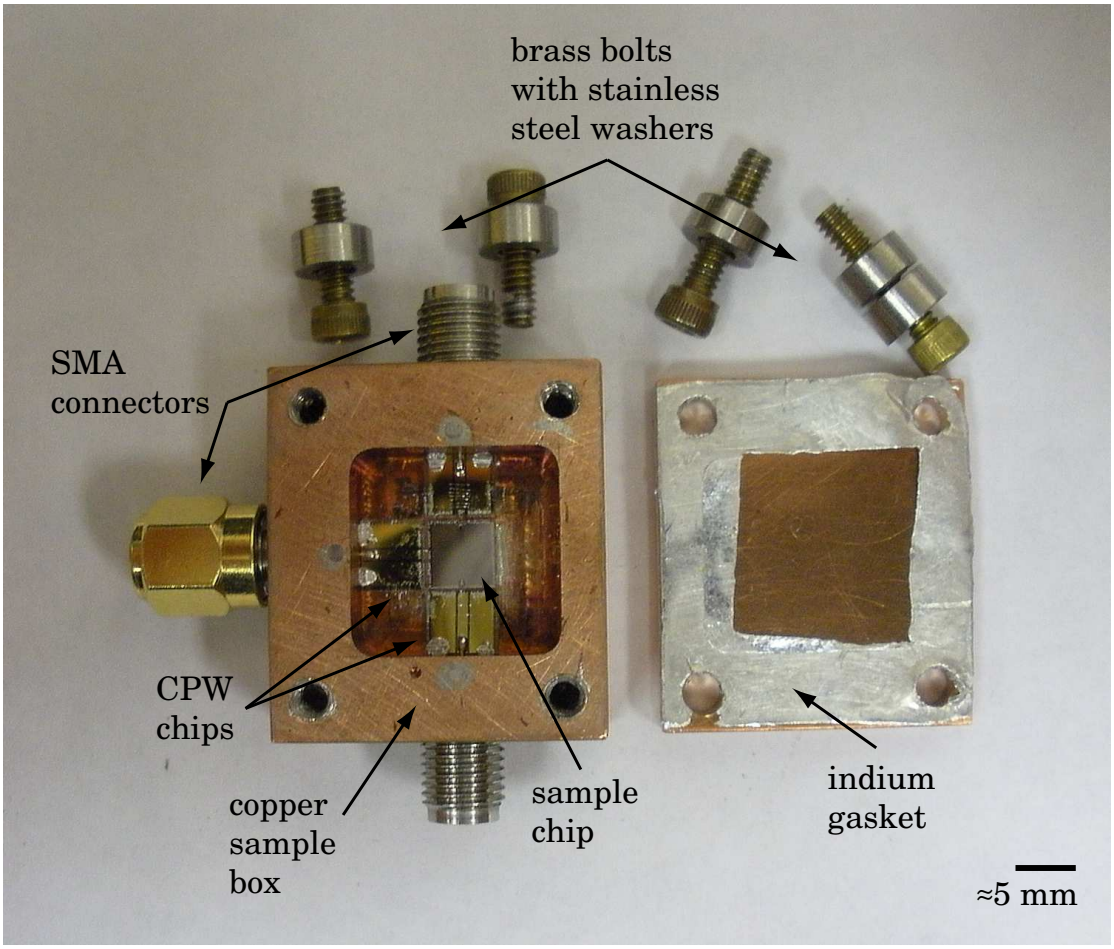

Figure 4.5: Photograph of the sample box. The sample chip is attached to the bottom of the sample box with silver paste for improved thermal contact. Connections between the sample and CPW chips are made with Al wire bonds.

creating a short. There are several approaches to overcoming this obstacle. For lines made of thin ductile copper wires, such as thermometry leads, we tightly wrap the lines around a copper post and secure them with epoxy. This compensates for the poor thermal conductivity of the insulation by greatly increasing the contact surface area. For rigid lines, we run the line through a wire surrounded by a glass bead that is soldered into hole in a copper plate. An alternative method is to replace a short length of the standard wire insulation with a thermally conducting dielectric. This is done by inserting short lengths of microstrip on a Si substrate at several points along the dc line.

4.2.2 Sample Box

The sample packaging needs to house the device die and shield it from external noise sources while allowing it to thermalize to the base temperature, provide access for input

and output lines and avoid creating spurious resonances. Our sample boxes have a $\approx 1 \times 1\,\text{inch}^2$ square base and are $\approx 0.5\,\text{inch}$ high with a separate screwed-on lid [see Fig. 4.5]. All parts are machined out of oxygen free high conductivity (OFHC) copper for good thermal conductivity and electrical shielding. The inside is hollowed out and has space for the $5 \times 5\,\text{mm}^2$ sample chip along with three to four $\approx 5 \times 5\,\text{mm}^2$ chips with lengths of coplanar waveguide (CPW) to transition from the external SMA connectors to the CPWs on the sample chip. We used silver paste to secure the device directly to the bottom of the sample box for improved thermal contact.

When the lid is tightly secured to the sample packaging, the enclosure forms a Faraday cage, shielding the sample from most environmental electromagnetic interference. However, infrared light can reach the cold stage of a dilution refrigerator and enter into a sample box through minute openings between the lid and the box [41, 42]. Such radiation has sufficient energy to break Cooper-pairs. If the intensity is sufficiently high, enough non-equilibrium quasiparticles may be generated to reduce the qubit excited state lifetime T_1 and the resonator internal quality factor Q_i. To eliminate infrared leakage, we used a ring of very soft indium wire to form a gasket between the lid and the box [see Fig. 4.5].

The most challenging aspect of designing and assembling the sample box is ensuring proper microwave performance. Impedance mismatches or transitions with large parasitic reactance need to be avoided. Both lead to spurious resonances that can decrease qubit lifetime via the Purcell effect [see Sec. 2.7], distort drive pulses, or lead to a frequency dependent transmission coefficient S_{21} requiring recalibration after each tuning of the qubit transition frequency. While we didn't have an overall formula to follow in microwave packaging and waveguide transition design, the overarching principles are to match the modes on the two sides of the transition and to minimize any parasitic elements [161, 162].

At the sample box, we used K launchers, Anritsu model K102F-R [160], to transition from coaxial cables to the CPW chip inside [see Fig. 4.5]. The Anritsu launchers are K connectors which are backward compatible with SMA connectors but offer superior performance up to 40 GHz. We chose the dimensions of the CPW center strip and gap width [66] to provide a good match to the dimensions of the launcher center pin and dielectric diameter, improving the transition from the coaxial to the CPW mode. Finally

we used a glob of indium wire and multiple wire bonds to connect the CPW ground strips to the box ground. This ensures that the ground strips have good electrical contact to the ground along their entire length and suppresses propagation through undesired modes such as the parallel plate waveguide or slotline modes [66].

Similar steps were taken to optimize the CPW chip-to-sample transition. In our package there was a $\approx 0.5\,\mathrm{mm}$ gap between the CPW chip and the sample die, unlike the SMA launcher and CPW chip which fit snugly against each other [see Fig. 4.5]. This gap was bridged by wire bonds, which as a good rule of thumb have $1\,\mathrm{nH/mm}$ of inductance per length. We minimized this series inductance by making the wire bonds as short as possible and putting many in parallel, further reducing the total inductance. We took steps to improve the mode matching by tapering the dimensions of the CPW on the sample to coincide with the dimensions of the CPW on the CPW chip. Furthermore, the CPW chip and sample were made on substrates of similar height and dielectric constant and aligned with respect to the center conductors of their respective CPWs.

4.3 Qubit Control

Qubit control electronics are used to set the values of the Hamiltonian parameters, specifically the reduced gate voltage $n_g = C_g V_g/e$ and the applied flux Φ [see Sec. 2.3], and generate the microwave pulses used to perform qubit operations [see Sec. 4.3]. The Hamiltonian parameters are either kept at a constant value or varied on time scales not much faster than $1\,\mathrm{ms}$. The hardware required to generate such signals is simple. Qubit manipulation pulses on the other hand have carrier frequencies in the $4-8\,\mathrm{GHz}$ range with stringent requirements on pulse shape, carrier phase and other criteria. The instrumentation needed to generate such pulses is complex and requires careful calibration.

4.3.1 External Parameters

The applied flux Φ was generated by the magnetic field of a superconducting solenoid magnet located inside the Dewar housing the dilution refrigerator. According to manufacturer's specifications, a current of $1\,\mathrm{mA}$ in the magnet produces a magnetic field of $1\,\mathrm{G}$ in the center of the solenoid where the sample is located. We constructed a current source by placing a computer controlled digital-to-analog converter (DAC) voltage source

in series with a 1 kΩ resistor. The desired magnetic field was set by turning on the heat switch, which heats a section of the solenoid and breaks the superconducting loop, changing the current in the loop using the current source, turning off the heat switch, and then turning off the current. This leaves the magnet in persistent current mode at the current we set, and with the magnetic field generated by it. No filtering is needed for the magnet current bias line as it's weakly coupled to the qubit and relatively isolated from external noise sources while in persistent current mode.

The gate voltage bias V_g was supplied by a Tektronix AFG3102 function generator [163] followed by a room temperature 100 : 1 voltage divider. The divider output was then connected to the dc bias line [see Sec. 4.2.1]. We used a sawtooth waveform with a typical period of 200 μs and a peak-to-peak voltage of several volts during experiments that required a V_g sweep and a fixed voltage output while performing experiments at a fixed value $n_g = C_g V_g/e$. The AFG3102 function generator was controlled by a computer via GPIB, allowing us to quickly switch output waveforms and speed up data acquisition. During experiments where we swept the gate voltage, the function generator sync output triggered the oscilloscope used for data acquisition [see Sec. 4.4].

4.3.2 Microwave Pulse Shaping

We used resonant or near resonant microwave pulses to control the state of the CPB qubit [see Sec. 4.3]. Pulse duration, amplitude, and phase must all be carefully controlled as errors in any of those quantities can lead to improper algorithm execution and increased effective dephasing. Microwave pulses can be generated either by direct synthesis using a high speed DAC or by using mixers to modulate a continuous carrier wave. Direct synthesis of pulses above 1 GHz is prohibitively expensive, so we employed the modulation technique for our pulse shaping setup. The modulation method combines a DAC to generate the pulse envelope with mixers to modulate a pure tone generated by a microwave source [see Fig. 4.6]. In the frequency domain, modulation adds a spread of Fourier components centered around the carrier frequency to the pulse spectrum. The bandwidth of these components is determined by the envelope rise time and shape and must be narrow enough so as not to excite higher qubit states.

A frequency mixer is a three port, nonlinear component that takes voltage inputs $A(t)$ at the intermediate frequency (IF) port and $B(t)$ at the local oscillator (LO) port and

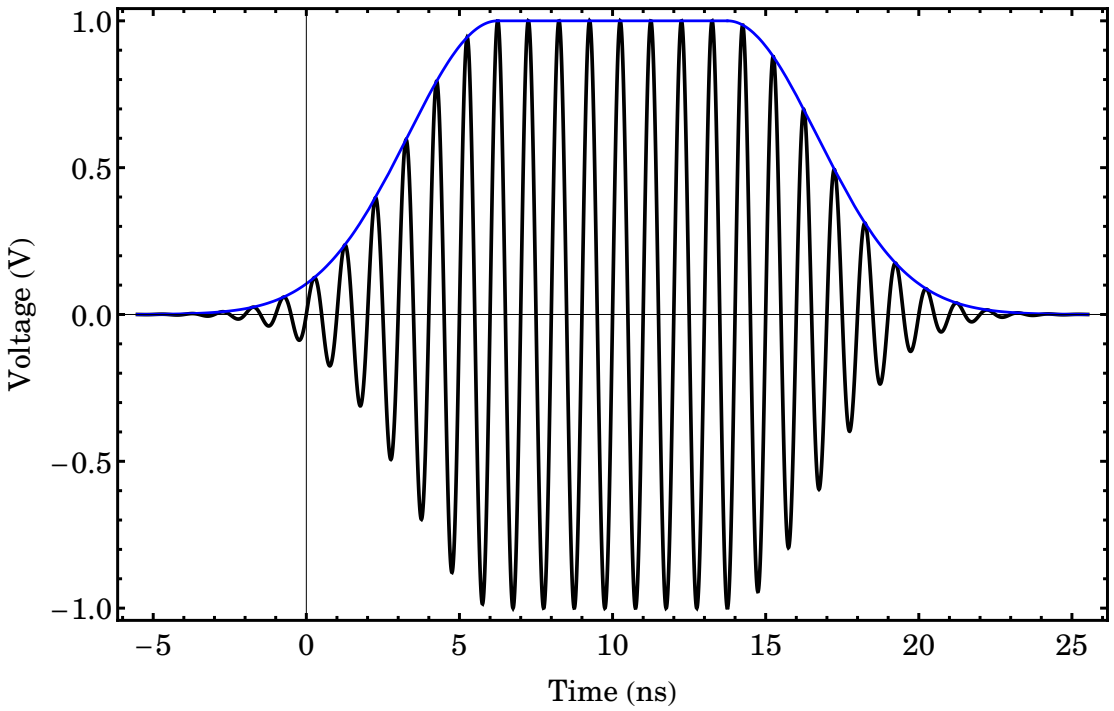

Figure 4.6: Time trace of a representative qubit control pulse. In this example, the pulse (black) consists of a 1 GHz, 2 Vpp microwave carrier tone modulated by a 5 ns rise time, 20 ns long envelope (blue). The rise time is defined as the time taken by the envelope to increase from 10% to 90% of its final value.

outputs the product $A(t)B(t)$ at the radio-frequency (RF) port [65]. If the LO input is a pure tone, then a slow varying IF input $A(t)$ amplitude modulates the LO input with the IF signal. If both the IF and LO inputs are sine waves at the corresponding angular frequencies ω_{IF} and ω_{LO} with phases ϕ_{IF} and ϕ_{LO} then we can use a trigonometric product identity to write the RF output as

$$\begin{aligned}\sin\left(\omega_{\mathrm{IF}}t+\phi_{\mathrm{IF}}\right)\sin\left(\omega_{\mathrm{LO}}t+\phi_{\mathrm{LO}}\right) &= \frac{1}{2}\cos\left(\omega_{\mathrm{RF}}t+\phi_{\mathrm{IF}}-\phi_{\mathrm{LO}}\right)\\ &\quad -\frac{1}{2}\cos\left((\omega_{\mathrm{IF}}+\omega_{\mathrm{LO}})t+\phi_{\mathrm{IF}}+\phi_{\mathrm{LO}}\right)\end{aligned} \tag{4.5}$$

where we have defined $\omega_{\mathrm{RF}} = |\omega_{\mathrm{IF}} - \omega_{\mathrm{LO}}|$ as the difference frequency. The sum frequency $\omega_{\mathrm{IF}} + \omega_{\mathrm{LO}}$ can be removed by a low pass filter, leading to the simplified RF output

$$V_{\mathrm{mix}} = \frac{1}{2}\cos\left(\omega_{\mathrm{RF}}t+\phi_{\mathrm{IF}}\right) \tag{4.6}$$

where we have for convenience set $\phi_{\mathrm{LO}} = 0$. In this mode of operation the mixer down-converts a signal at ω_{IF} to one at ω_{RF}. Note that the LO signal typically must fall in a

specified range for proper mixer operation.

An IQ mixer, also known as a quadrature IF mixer, is a composite device consisting of several mixers, hybrid couplers and other microwave components. It extends the amplitude modulation capabilities of a mixer by also allowing for phase modulation. The single IF port is replaced by two inputs, the in-phase I and the quadrature Q ports. Internally, the supplied LO signal $\sin(\omega_{\mathrm{LO}}t)$ is divided by a hybrid coupler into an in-phase $\sin(\omega_{\mathrm{LO}}t)$ tone and an out-of-phase $\cos(\omega_{\mathrm{LO}}t)$ tone. These two tones are then individually amplitude modulated by the $I(t)$ and $Q(t)$ voltage inputs and finally recombined by another hybrid coupler to produce the RF output. Using trigonometric identities, we can rewrite the output as

$$\begin{aligned} I(t)\sin(\omega_{\mathrm{LO}}t)+Q(t)\cos(\omega_{\mathrm{LO}}t) &= A(t)\cos\big(\phi(t)\big)\sin(\omega_{\mathrm{LO}}t)+A(t)\sin\big(\phi(t)\big)\cos(\omega_{\mathrm{LO}}t) \\ &= A(t)\sin\big(\omega_{\mathrm{LO}}t+\phi(t)\big) \end{aligned} \tag{4.7}$$

where $A^2(t)=I^2(t)+Q^2(t)$ and $\phi(t)=\arctan(Q(t)/I(t))$. These definitions explicitly give the amplitude and phase modulation as functions of the $I(t)$ and $Q(t)$ inputs.

We implemented a pulse shaping setup capable of arbitrary envelope and phase control [165] [see Fig. 4.7(a)]. The pulse envelope $I(t)$ and $Q(t)$ voltage values are entered into a computer and sent to a 1 GSa/s DAC board via an Ethernet cable. The DAC board was designed by J. Martinis at UCSB [164] and assembled by S. Waltman of High Speed Circuit Consultants [166] [see Fig. 4.7(b)]. It has two pairs of differential voltage output channels for I and Q control and four auxiliary outputs for timing and triggering of other instruments. The I and Q voltage outputs are followed by absorptive low pass Gaussian filters model 5915 from Picosecond Pulse Labs [167] with a -3 dB point of 100 MHz and a pulse rise time of 3.5 ns. These filters remove any high frequency DAC instrumentation noise and give the pulse envelope a Gaussian profile, eliminating ringing and overshoot. Unlike standard reflective filters, they absorb the filtered signal and hence remove reflections which could degrade performance. However, a Gaussian filter's roll-off is smoother and gentler than many filters [168], resulting in a larger pulse bandwidth that must be considered if there are other nearby qubit levels. The differential outputs from the DAC are amplified by two differential amplifiers to remove voltage offsets and boost the voltage to better drive the IQ mixer. The outputs of the two differential amplifiers are

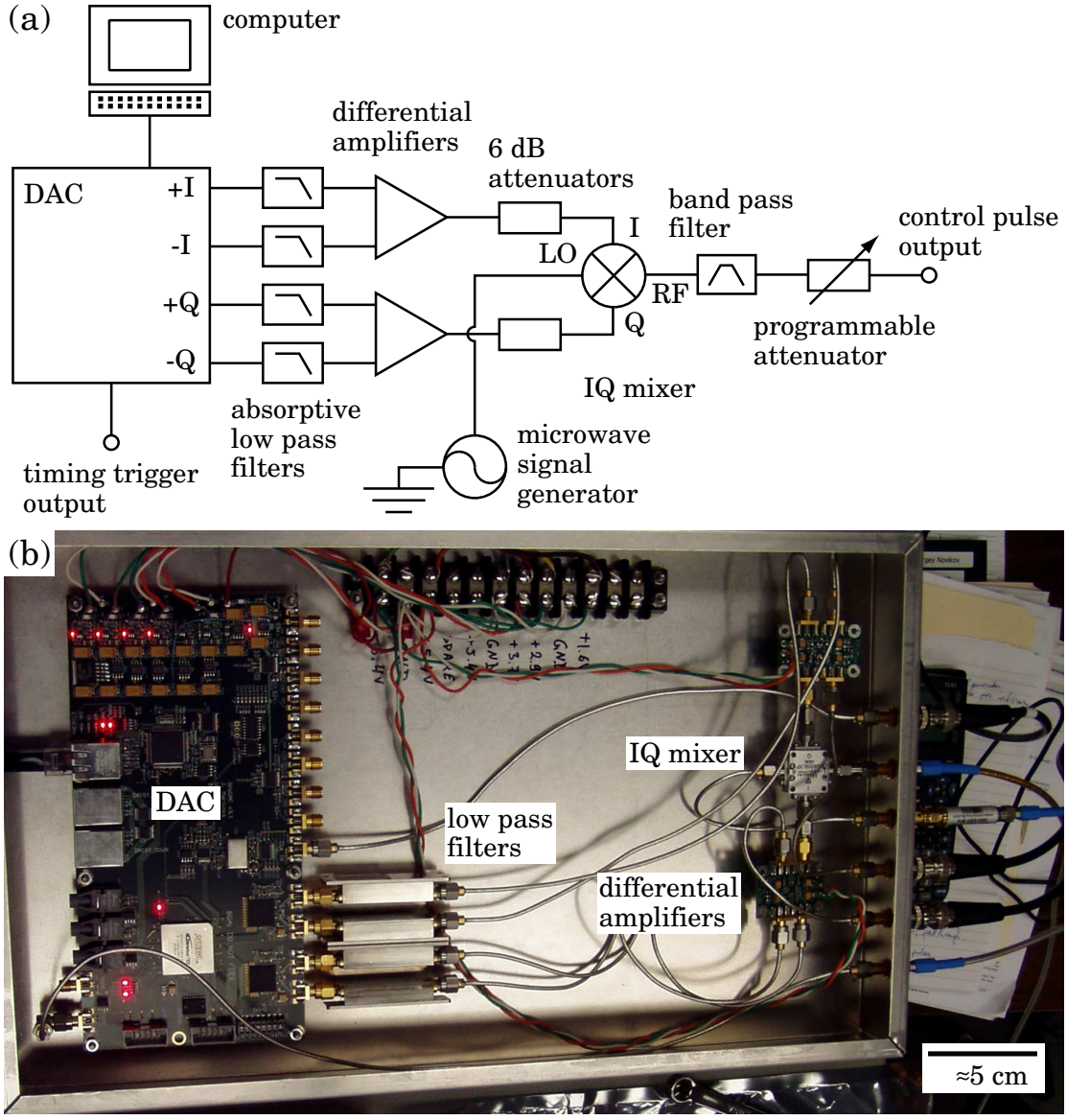

Figure 4.7: (a) Schematic of the pulse shaping setup. The shape for the pulse envelope is generated on a computer and sent to the DAC board which stores it and in turn outputs the control voltages necessary to modulate the carrier tone using an IQ mixer. The control pulse output is connected to the corresponding port in Fig. 4.8. (b) Photograph of a portion of the Martinis-style [164] pulse shaping setup containing the DAC board and IQ mixer. Photograph courtesy of S. Novikov.

each passed through 6 dB attenuators and then connected to the I and Q ports of an IQ mixer. Although the IQ mixer is designed to have 50 Ω input impedance at all ports, in practice it has relatively high return loss and the 6 dB attenuators improve overall system performance by suppressing standing waves. We used a Marki Microwave IQ mixer model IQ-4509 [169] with an LO and RF working bands of 4.5 – 9.0 GHz. The high power LO tone was generated by an Agilent 83650B signal generator [170] that was wired directly to the LO port of the IQ mixer. A bandpass filter on the RF output, with passband selected to match the qubit transition frequency E_J/h, removed unwanted higher order mixer products from the signal. The RF signal was attenuated by an Aeroflex model 8311 programmable attenuator [149] to allow for increased range of pulse amplitudes, and finally connected to the rf input line. All components were locked to a 10 MHz rubidium frequency standard model FS725 from Stanford Research Systems (SRS) [171].

Although we took precautions to filter noise outside the signal band and minimize impedance mismatches, mixer imperfections still impeded our ability to shape the control pulses. Fortunately, the impact of these imperfections can be minimized with proper calibration techniques. While an ideal pulse has zero amplitude in the off state, in practice some LO power leaks through the mixer to the RF port even when the I and Q voltages are zero. This off-state power may cause slow Rabi oscillations or produce a mixed state with an above equilibrium excited state population. As the leaked LO signal is a weaker and possibly phase shifted form of the LO input, it's possible to use a dc bias to null the leakage [172]. We used a gradient descent search algorithm to find the values of the I and Q bias voltages that minimized the LO leakage and applied those values in the pulse off state. Using this approach we were able to achieve an on-off ratio of 60 dB or better [165].

The phase and amplitude modulation described by Eq. 4.7 breaks down in a real mixer due to arm imbalance and crosstalk. Arm imbalance may be due to imperfections in the hybrid couplers dividing the input LO power or variation in mixer conversion gain between the two arms. Such imbalance manifests as a difference between the output RF amplitudes when identical voltage levels are applied to the I or Q ports. Crosstalk may also be caused by imperfections in the hybrid couplers and appears as an in-phase component in the output RF signal when voltage is applied to the quadrature Q port of the IQ mixer and vice versa. Both of these flaws contribute to amplitude and phase deviations in the output qubit control pulses that lead to errors during execution of complex qubit

algorithms such as spin echo or state tomography.

We quantified mixer errors by sending voltage signals to either the I or Q ports and measuring the amplitude of the in-phase and quadrature components of the output RF signal. We may conveniently represent the IQ mixer transformation with phasor-like notation. If I_{in} and Q_{in} are the in-phase and quadrature IQ mixer port inputs, we may write the output RF signal I_{out} and Q_{out} components as

$$\begin{aligned}\begin{pmatrix} I_{\text{out}} \\ Q_{\text{out}} \end{pmatrix} &= \begin{pmatrix} 1+i_{\text{imb}} & iq_{\text{cross}} \\ qi_{\text{cross}} & 1+q_{\text{imb}} \end{pmatrix} \begin{pmatrix} I_{\text{in}} \\ Q_{\text{in}} \end{pmatrix} \\ &= \hat{M}_{\text{IQ}} \begin{pmatrix} I_{\text{in}} \\ Q_{\text{in}} \end{pmatrix} \end{aligned} \tag{4.8}$$

where i_{imb} and q_{imb} quantify the arm imbalance, and iq_{cross} and qi_{cross} quantify the crosstalk. An ideal IQ mixer would have $i_{\text{imb}} = q_{\text{imb}} = iq_{\text{cross}} = qi_{\text{cross}} = 0$, i.e. an identity transformation. By measuring the components of the IQ mixer transformation matrix and then inverting it, we generate a correction matrix $\hat{M}_{\text{corr}} = \hat{M}_{\text{IQ}}^{-1}$. We can then apply the correction matrix to the I_{in} and Q_{in} values before sending them to the mixer. This corrects for the mixer errors and results in the desired behavior as demonstrated by

$$\begin{aligned}\begin{pmatrix} I_{\text{out}} \\ Q_{\text{out}} \end{pmatrix} &= \hat{M}_{\text{IQ}}\hat{M}_{\text{corr}} \begin{pmatrix} I_{\text{in}} \\ Q_{\text{in}} \end{pmatrix} \\ &= \hat{I} \begin{pmatrix} I_{\text{in}} \\ Q_{\text{in}} \end{pmatrix}. \end{aligned} \tag{4.9}$$

With this approach we have been able to obtain pulse phase and amplitude deviations of less than 1% [165].

4.4 Qubit State Readout

The qubit state is encoded in the phase and amplitude of the transmitted resonator probe signal [see Sec. 2.6]. This encoding can be represented as a transformation of the input probe signal $A_{\text{in}}\cos(\omega_{res}t)$ according to

$$A_{\text{in}}\cos(\omega_{res}t) \rightarrow A_{\text{out}}(t)\cos\left(\omega_{res}t + \phi_{\text{out}}(t)\right). \tag{4.10}$$

The purpose of the qubit readout apparatus is to extract the time varying transmitted amplitude $A_{\text{out}}(t)$ and phase $\phi_{\text{out}}(t)$. There are two demodulation techniques applicable in this scenario: homodyne and heterodyne detection [173].

Homodyne detection is conceptually the simplest of the two detection schemes and may be viewed as operating an IQ mixer in reverse. When the LO input is a strong drive signal at ω_{res} and the RF input is $A_{\text{out}}(t)\cos\left(\omega_{res}t+\phi_{\text{out}}(t)\right)$, the I and Q port outputs $I(t)$ and $Q(t)$ are related to $A_{\text{out}}(t)$ and $\phi_{\text{out}}(t)$ via $A_{\text{out}}^2(t) = I^2(t)+Q^2(t)$ and $\phi_{\text{out}}(t) = \arctan(Q(t)/I(t))$. In effect the mixer down-coverts the input signal from ω_{res} to dc by mixing it with an LO tone at the same frequency and producing I and Q port outputs that correspond to the in-phase and quadrature components. The homodyne outputs $I(t)$ and $Q(t)$ can then be filtered, digitized by an analog-to-digital converter (ADC), and further processed on a computer to extract the amplitude $A_{\text{out}}(t)$ and phase $\phi_{\text{out}}(t)$. The simplicity of the homodyne detector setup is its biggest asset and the dc signals output by the IQ mixer are easy to work with. However, dc outputs are also highly susceptible to instrumentation offsets and drifts and $1/f$ and other low frequency noise.

In heterodyne detection, the signal is down-converted to an intermediate frequency (IF) rather than dc. This avoids low frequency noise and offsets but requires an additional demodulation step to extract the signal phase $\phi_{\text{out}}(t)$ and amplitude $A_{\text{out}}(t)$. Another practical benefit to heterodyne detection is that any LO signal that leaks through the mixer is mixed to a different frequency and won't drown out the weak incoming RF signal. In our implementation, after mixing down from ω_{res} to ω_{IF}, the IF signal $A_{\text{out}}(t)\cos\left(\omega_{\text{IF}}t+\phi_{\text{out}}(t)\right)$ was acquired with an ADC and sent to a computer. It was then copied and multiplied by a digitally synthesized $\cos(\omega_{\text{IF}}t)$ or $\sin(\omega_{\text{IF}}t)$ waveform. The low pass filtering to remove the $\cos(2\omega_{\text{IF}}t)$ or $\sin(2\omega_{\text{IF}}t)$ components was implemented in the form of an average over one period of the IF signal. The average values of $I(t)$ and $Q(t)$ in a window of duration $T_{\text{IF}} = 2\pi/\omega_{\text{IF}}$ are given by

$$\langle I(t)\rangle = \frac{1}{T_{\text{IF}}}\int_t^{t+T_{\text{IF}}} A_{\text{out}}(t)\cos\left(\omega_{\text{IF}}t+\phi_{\text{out}}(t)\right)\cos(\omega_{\text{IF}}t)\,d\tau \tag{4.11}$$

$$\langle Q(t)\rangle = \frac{1}{T_{\text{IF}}}\int_t^{t+T_{\text{IF}}} A_{\text{out}}(t)\cos\left(\omega_{\text{IF}}t+\phi_{\text{out}}(t)\right)\sin(\omega_{\text{IF}}t)\,d\tau. \tag{4.12}$$

If needed, the average amplitude $\langle A_{\text{out}}(t)\rangle$ and phase $\langle\phi_{\text{out}}(t)\rangle$ can then be calculated from the $\langle I(t)\rangle$ and $\langle Q(t)\rangle$ values. In practice the signal is recorded as a sequence of dis-

crete data points with spacing determined by the ADC acquisition rate and the integrals are approximated by sums. The bandwidth of this detection technique is limited by the averaging over one IF period and is consequently proportional to the IF frequency. This bandwidth doesn't limit our measurements as we can select an IF frequency faster than the resonator bandwidth $\kappa \approx 1\,\mathrm{MHz}$ but still slow enough to be easily digitized; i.e. we are typically limited by the resonator bandwidth.

For qubit measurements, the physical implementation of heterodyne detection requires a very large degree of phase and frequency stability in the ω_{res} and ω_{LO} tones. Any relative phase or frequency change in the two signals manifests itself as a spurious change in the extracted phase, indistinguishable from a genuine change in the phase of the transmitted resonator probe signal. While a drift of 1 Hz or 2π rad during a period of a few minutes is an error of only $\approx 10^{-12}$, it would be disastrous for a phase sensitive measurement with an averaging time of the same duration.

To circumvent the stringent requirement on phase and frequency stability, we adopted a setup similar to the internal workings of a vector network analyzer or rf lock-in [174]. This involves splitting the ω_{res} and ω_{LO} signals at the source using directional couplers [see Fig. 4.8]. One branch was sent to the resonator and then demodulated while the other was sent directly to a second mixer for identical heterodyne detection. We used the second branch as a phase and amplitude reference. The recorded data was calibrated on the computer during post-processing according to $\langle A_{\mathrm{cal}}(t)\rangle = \langle A_{\mathrm{out}}(t)\rangle / \langle A_{\mathrm{ref}}(t)\rangle$ and $\langle \phi_{\mathrm{cal}}(t)\rangle = \langle \phi_{\mathrm{out}}(t)\rangle - \langle \phi_{\mathrm{ref}}(t)\rangle$. This method also compensates for small fluctuations in the source power of the ω_{res} and ω_{LO} tones.

The ω_{res} and ω_{LO} tones were generated by two Agilent 83732B signal generators [170] and divided into the resonator probe and reference arms of the circuit by a pair of MAC Technology model C3205-6, 4 – 8 GHz 6 dB directional couplers [175] [see Fig. 4.8]. The coupled output of the directional coupler splitting the ω_{LO} tone was connected to the LO input of the reference arm mixer while the through output was passed through a Mini-Circuits SHP-1000 1000 MHz high pass filter [150] and then connected to the LO input of the probe arm mixer. The through output of the directional coupler splitting the ω_{res} tone was connected to the RF input of the reference arm mixer. The mixers chosen for both arms were Marki Microwave double-balanced, 4 – 8 GHz LO/RF, dc to 4 GHz IF mixers model M1-0408 [169]. The coupled output of the ω_{res} directional coupler was

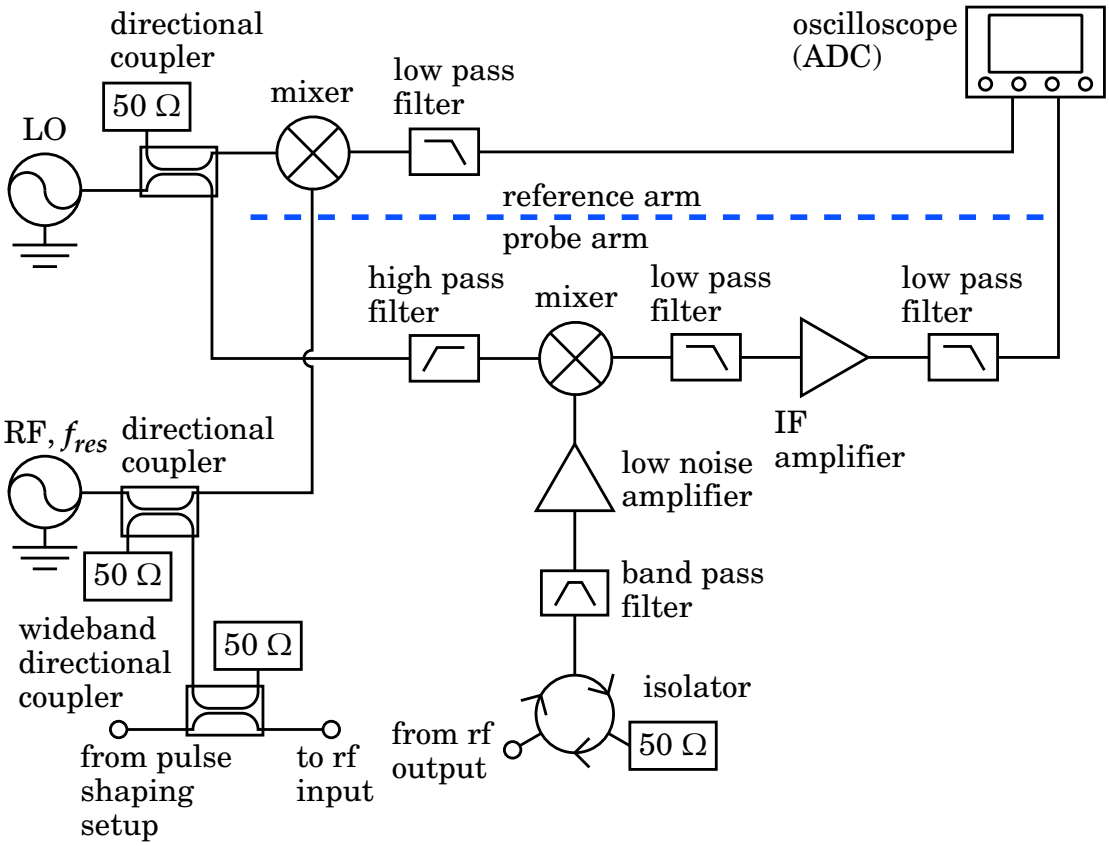

Figure 4.8: Schematic of the coherent heterodyne detection setup. Signals from the LO and RF microwave sources are split and sent down two branches. The probe arm measures the response of the device under test (DUT) while the reference arm provides a phase and amplitude signal to calibrate the probe output. The rf input and rf output ports are connected to the matching ports in Fig. 4.4 while the qubit control pulses come from the output port in 4.7(a).

combined with the qubit control pulses by an Agilent model 87301D, 1 – 40 GHz 13 dB broadband directional coupler [170] and then connected to the rf input line descending into the refrigerator.

The transmitted signal from the sample box was amplified by a cryogenic HEMT amplifier [see Sec. 4.2.1] and exited the dilution refrigerator through the rf output line. The rf output line was first filtered by a Pasternack Enterprises model PE8714 4.9 – 5.9 GHz bandpass filter [176], followed by a Pasternack Enterprises model PE8302 4 – 8 GHz, 18 dB isolation isolator and then amplified by a Miteq model AMF-4F-04000800-12-10P 4 – 8 GHz, 38 dB gain low noise amplifier (LNA) [177]. The isolator prevented any reflected signal from returning through the rf output line while the bandpass filter reduced the overall power entering the room temperature low noise amplifier. The resonator probe signal power at the output of the sample box was in some cases as few as 10 dB above the thermal noise floor at 25 mK, which meant it required a large amount of amplification to bring it up to easily measurable levels. However, the cryogenic and room temperature low noise amplifiers don't selectively amplify only the desired signal but all signal and noise in their operational bandwidth. A gain of 35 dB followed by 38 dB would result in a very large integrated output power at the room temperature low noise amplifier, exceeding its compression point, reducing gain, and overloading the mixer and other components. The model PE8714 4.9 – 5.9 GHz bandpass filter served to filter out this amplified noise floor and keep the total power level down.

The output of the low noise amplifier was connected to the RF input of the probe arm mixer. The IF output of the probe arm mixer was filtered with Picosecond Pulse Labs model 5915 35 MHz absorptive low pass Gaussian filter [167], amplified with a Mini-Circuits model ZFL-500LN 0.1 – 500 MHz, 28 dB gain IF amplifier [150], further filtered by a Mini-Circuits SLP-30 30 MHz low pass filter, and finally digitized. The IF output of the reference arm mixer was filtered by a Mini-Circuits SLP-30 30 MHz low pass filter and then digitized. All components were locked to the same 10 MHz rubidium frequency standard as used in the pulse shaping setup [see Sec. 4.3.2].

At the time of my experiments, we didn't have a dedicated analog-to-digital converter but instead used an Agilent 54855A Infiniium digital oscilloscope as an ADC. A standalone ADC would have offered improved throughput and data processing capabilities but this wasn't essential for these experiments as gate bias n_g jumps and drift limited

the speed with which I could acquire data. I used an IF of 2 MHz for most of the time resolved experiments and an IF of 0.5 MHz for slow parameter sweeps. The IF acquisition sample rate was either 10 or 20 times the IF, corresponding to a setting of 10 MSa/s or 20 MSa/s on the oscilloscope, and I typically averaged the signal 500 to 5000 times. Finally, I note that although the IF acquisition sample rate could have been any value sufficient to properly record the waveform as given by the Nyquist-Shannon sampling theorem [173], but the digital windowed average is significantly easier to compute when the ADC sampling rate is an integer multiple of the IF.

5 Preliminary Qubit Characterization

5.1 Locating the Qubit

Due to the nanoscale size of the junctions, CPB fabrication tends to be low yield and prone to defects. Additionally, the CPB junctions form a closed loop and only the test junctions placed on the same die may be characterized at room temperature [see Sec. 4.1.4]. Although I have found good agreement between the Josephson energy E_J of the test and qubit junctions, I have no simple way to determine the charging energy E_c of the CPB or the presence of any serious defects in the tunnel barrier. It typically took me several attempts before I found a device with acceptable parameters. The first action I took after cooling down a new sample to base temperature was to spectroscopically locate the resonator frequency and then sweep n_g to find the perturbation due to the CPB. If the CPB was operational I would then determine its parameters. Of the two devices I studied in detail, I inherited Device 1 from Z. Kim, who performed the initial characterization and lifetime studies on it [71]. Rather than discussing my work in chronological order, I first discuss my preliminary characterization of Device 2. The main experimental work I performed on both samples is covered in Chapter 6.

5.1.1 Extracting Resonator Parameters

I began my characterization of Device 2 by measuring the transmitted voltage ratio S_{21}. Using the coherent heterodyne readout I synchronously stepped the frequencies of the ω_{res} and ω_{LO} microwave sources and recorded the transmitted and referenced amplitude $\langle A_{\mathrm{cal}}(t)\rangle$ and phase $\langle \phi_{\mathrm{cal}}(t)\rangle$ [see Fig. 5.1]. I used a ω_{res} source power of $-12\,\mathrm{dBm}$ which based on previous characterization corresponds to approximately 50 photons in the resonator. The gate voltage bias was set to $V_g = 0\,\mathrm{V}$ and no external flux Φ was applied. I extracted the resonator parameters $\omega_{res}/2\pi = 5.472\,\mathrm{GHz}$, $Q_L = 35{,}000$, $Q_i = 147{,}000$,

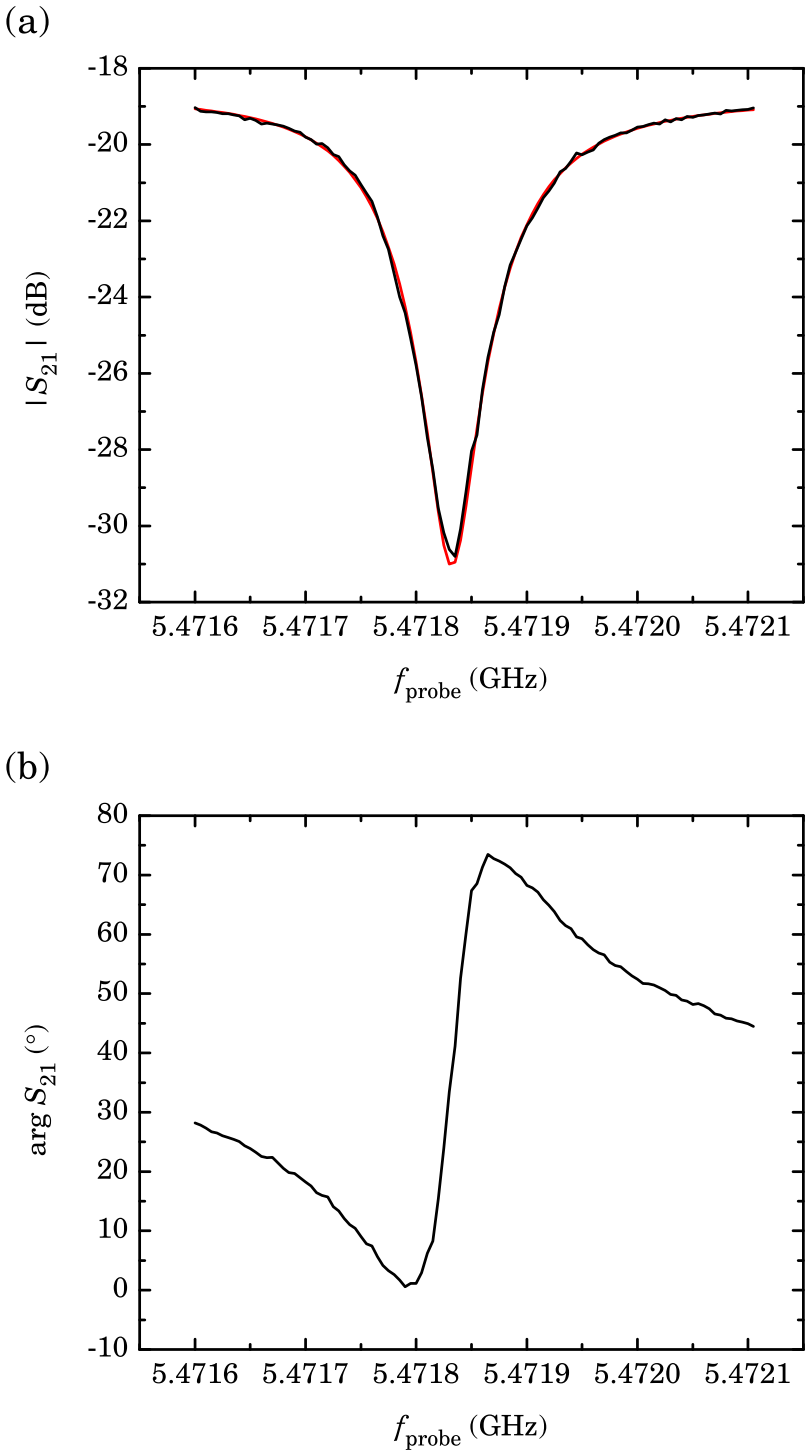

Figure 5.1: Transmission parameter (a) amplitude ($|S_{21}|$, black) and (b) phase ($\arg S_{21}$, black) of the resonator of Device 2. The amplitude curve was fit (red) to extract $\omega_{res}/2\pi = 5.472\,\text{GHz}$, $Q_L = 35{,}000$, $Q_i = 147{,}000$, and $Q_e = 47{,}000$.

and $Q_e = 47{,}000$ by fitting the measured resonance curve to a modified form of Eq. 2.41 [see Table 1.1]. The fitting algorithm was developed by M. Khalil and included an additional term to account for possible impedance mismatches present in the input and output transmission lines [178].

Although the resonators rarely have performance issues since flawed ones are easily screened out during visual inspection on a microscope, the extracted resonator parameters provide quantitative confirmation that they are behaving as expected. Additionally the resonance angular frequency ω_{res} and loaded quality factor Q_L give the decay rate $\kappa = \omega_{res}/Q_L = 0.98\,\mathrm{MHz}$ which is needed during optimization of qubit readout [see Sec. 5.3] and the calculation of the Purcell effect [see Sec. 2.7].

The stability of the resonance frequency also provides some hints about the condition of the CPB qubit. In the dispersive limit, when the CPB qubit is in the ground state the resonance frequency is given by

$$\omega_{res}\left(n_g\right) = \omega_{res} - \chi\left(n_g\right) = \omega_{res} - g^2\left(n_g\right)/\left(\omega_{CPB}\left(n_g\right) - \omega_{res}\right) \tag{5.1}$$

where ω_{res} without the explicit n_g dependence is the bare resonance frequency [see Sec. 2.5.1]. Consequently any charge noise that significantly changes the gate bias n_g, such as e or sub-e charge jumps, would cause corresponding changes in the observed resonance frequency. I occasionally saw such fluctuations during preliminary device testing. They are not necessarily a problem if they are present during the first few days to a week after the initial cooldown as I found that this noise tends to die down on this time scale. In fact in the short-term such fluctuations are a useful indicator that there is a functional CPB coupled to the resonator. However, a sudden increase in fluctuations of the resonance frequency after the device has been cold for a while is not a good sign. It may simply mean I have accidentally heated the device, such as by applying too much power, or that a TLS has become active. This was the case with Device 1, which after many months of excellent performance developed a very strong charge fluctuator that persisted even after thermal cycling and rendered the qubit inoperable.

5.1.2 Gate Bias Sweep

Having determined the properties of the resonator, I next performed a pair of experiments to confirm the status of the CPB. The first involves sweeping the gate bias n_g while probing the resonator at a fixed frequency, typically ω_{res}. To sweep n_g I used a sawtooth voltage waveform with a repetition time of $200\,\mu$s and a typical peak to peak voltage of several volts sufficient to cover $-2 < n_g < 2$. The slow repetition rate ensures that the gate bias n_g is effectively constant during the acquisition time for a single data point, determined by the IF period, of $2\,\mu$s. For gate sweeps that zoomed in on a small n_g range $-0.2 < n_g < 0.2$ I used an even slower repetition time of 1 ms.

The CPB ground to first excited state transition frequency $\omega_{CPB}(n_g)$ varies as a function of n_g from a minimum of $E_J/\hbar$ to a maximum of $4E_c/\hbar$ [see Sec. 2.3.1]. Additionally the effective qubit-resonator coupling strength $g(n_g)$ has a weak dependence on n_g through the dipole term $|\langle g|\hat{N}|e\rangle|$, which decreases by about 1/2 as n_g changes from 1 to 0 or 2. Consequently the dispersive shift $\chi(n_g)$ is maximum near $n_g = 1$ when $\omega_{CPB} < \omega_{res}$, maximum exactly at $n_g = 1$ when $\omega_{CPB} > \omega_{res}$, and falls to a negligible value at $n_g = 0$ and $n_g = 2$ [see Sec. 2.5.1]. Sweeping n_g tunes the ground state resonance frequency $\omega_{CPB}(n_g)$ between the maximally shifted value $\omega_{res} - \chi$ and the bare resonance frequency ω_{res}. When I probe the resonator at a fixed frequency while sweeping the gate bias n_g, the resonator transmission curve S_{21} acts as a transfer function, converting changes in the resonance frequency to changes in transmitted amplitude and phase.

Figure 5.2(a) shows a plot of one such sweep with a source gate voltage range of 12 Vpp. Periodic modulation of the resonance frequency is clearly visible. This is a positive confirmation of a functional CPB coupled to the resonator. From the CPB Hamiltonian the modulation is known to have a period of $2e$, which is $\Delta n_g = 2$ in reduced gate voltage [see Sec. 2.2]. I measured a source gate voltage period of $V_{g,2e} = 1.678$ V which, accounting for the 100 : 1 voltage divider and using $n_g = C_g V_g/e$, gives a gate capacitance of $C_g = 19.1$ aF.

It's not possible to conclude from the gate bias sweep data alone that the period is $2e$, as in the ideal case, or $1e$ due to quasiparticles. The typical approach we have used in the past is to introduce quasiparticles, for example by heating the sample to several hundred mK, and looking for a halving of the period. If the period halves, the original period must have been $2e$ but if no halving is observed it was $1e$. I didn't need to take such measures for Device 2 as there was a small amount of non-equilibrium quasiparticles present even

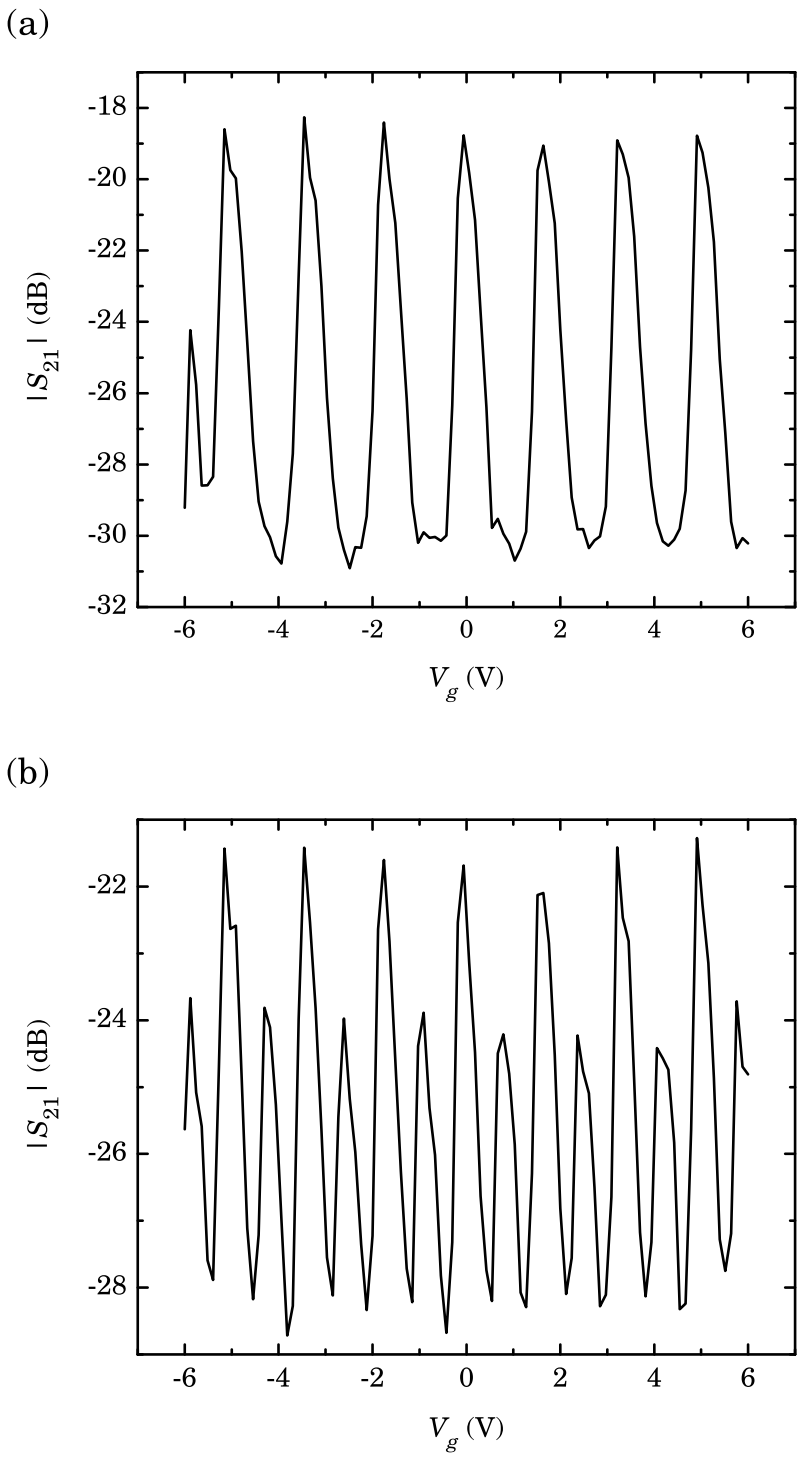

Figure 5.2: (a) Gate voltage sweep of Device 2 with f_{probe} set at 5.47183 GHz. The period $V_{g,2e} = 1.678\,\text{V}$ corresponds to a gate capacitance of $C_g = 19.1\,\text{aF}$. (b) Example of a gate voltage sweep with an e jump approximately midway through the acquisition process. The $|S_{21}|$ curve was obtained by averaging repeated scans of $S_{21}(V_g)$ over an interval of about a minute.

at the base temperature of 25 mK. These quasiparticles manifested themselves as $1e$ offset charge jumps occurring with a random delay between about one and several minutes. A $1e$ jump occurred during the averaging of the gate bias sweep plotted in Fig. 5.2(b). The original features seen in Fig. 5.2(a) are doubled, have reduced amplitude, and are offset by exactly half of the original period, providing evidence both for the presence of non-equilibrium quasiparticles and $2e$ periodicity.

5.1.3 Single Tone Spectroscopy

I followed up the gate bias sweep with an experiment that directly measures the ground state resonance frequency $\omega_{res}(n_g)$. Termed single tone spectroscopy [71], it involves sweeping the gate bias n_g while probing the resonator at a fixed frequency, stepping the probe frequency, and then repeating the process. Figure 5.3 shows the data plotted as a 2D color intensity plot with the gate bias n_g on the x-axis and probe frequency f_{probe} on the y-axis. A line cut at constant probe frequency f_{probe} corresponds to a gate bias sweep while a line cut at constant n_g corresponds to the transmitted voltage ratio $S_{21}(n_g)$.

Single tone spectroscopy provides much information about the qubit and the resonator. As discussed earlier, the CPB is sufficiently detuned at $n_g = 0$ to consider the dispersive shift $\chi(n_g = 0)$ negligible. By taking a line cut at $n_g = 0$ and fitting to extract the resonance frequency I confirmed that the ω_{res} extracted earlier was indeed at $n_g = 0$ and not a different value due to a charge offset. The n_g dependence of the ground state resonance frequency $\omega_{res}(n_g)$ contains information about the qubit transition frequency ω_{CPB}. If the qubit is above the resonator, $E_J/\hbar = \omega_{CPB}(n_g = 1) > \omega_{res}$, then the dispersive shift $\chi(n_g)$ decreases when moving away from $n_g = 1$ and the resonance frequency $\omega_{res}(n_g)$ increases [see Fig. 5.3(a)]. On the other hand if I change E_J to move the qubit below the resonator, $E_J/\hbar = \omega_{CPB}(n_g = 1) < \omega_{res}$, then the dispersive shift $\chi(n_g)$ has opposite sign and increases when moving away from $n_g = 1$ because the qubit transition frequency moves closer to the resonator. After the two resonantly cross the dispersive shift switches sign and begins to decrease [see Fig. 5.3(b)]. Hence by examining the single tone spectroscopy data I can immediately conclude where the CPB transition frequency is relative to the resonator. Additionally from this data I find $\chi(n_g = 1) = \omega_{CPB}(n_g = 0) - \omega_{CPB}(n_g = 1)$ or $\chi(n_g = 1)/2\pi = 290\,\text{kHz}$ [see Fig. 5.3(a)]. Once ω_{CPB} is known, the value of the dispersive shift can be used to calculate the qubit-resonator coupling strength g. The value

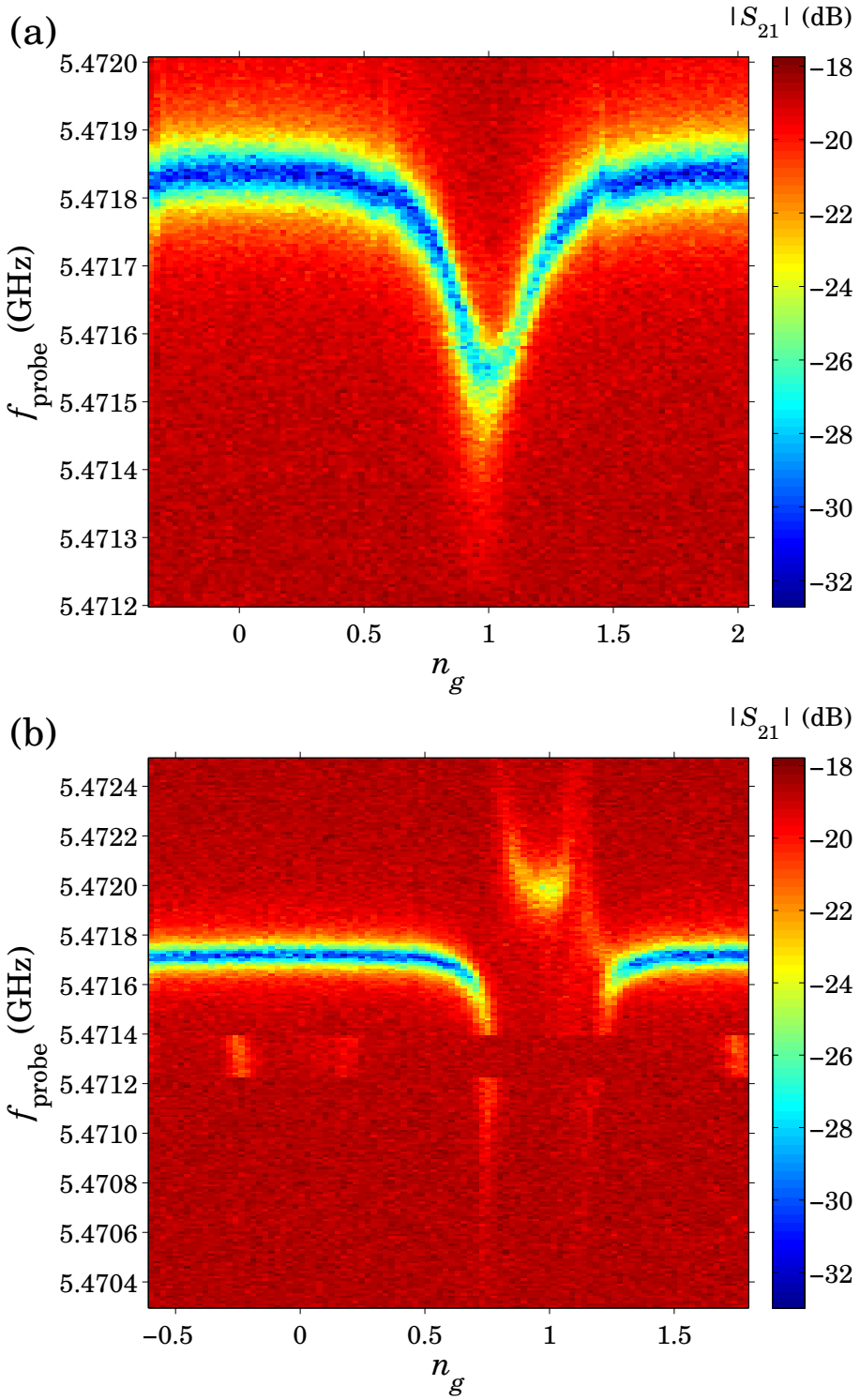

Figure 5.3: Single tone spectroscopy of Device 2. (a) The qubit is above the resonator $\omega_{CPB}\left(n_g = 1\right) > \omega_{res}$ and the dispersive shift of the resonator decreases away from $n_g = 1$. The small features at $n_g \approx 1 \pm 0.4$ are of unknown origin. (b) After changing E_J, the qubit is below the resonator $\omega_{CPB}\left(n_g = 1\right) < \omega_{res}$. The dispersive shift grows until the resonant crossing at $n_g \approx 1 \pm 0.2$ and then rapidly decreases. Note that while recording this data, an e jump occurred between 5.4712 GHz and 5.4714 GHz.

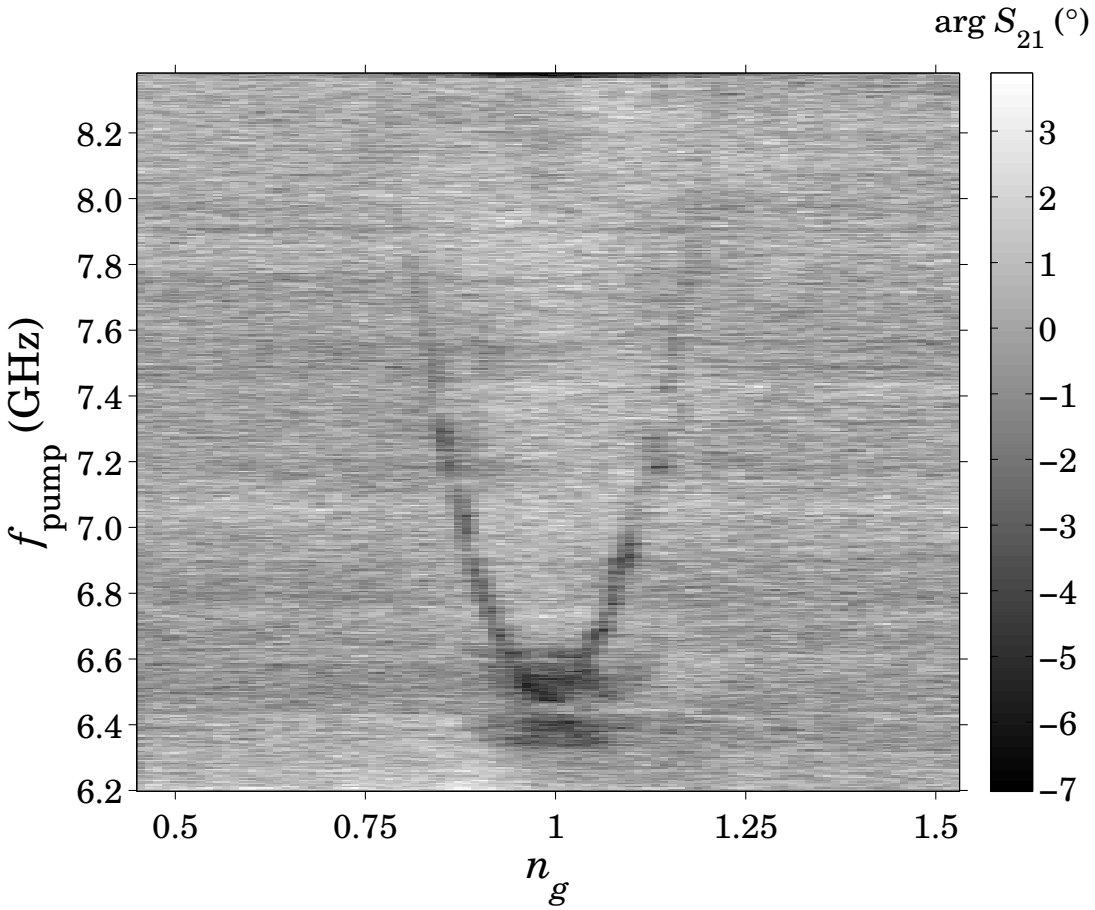

Figure 5.4: Two tone spectroscopy of Device 1, representative of a typical CPB spectrum. The blurring of the bottom of the parabola is due to charge noise.

of $\chi\left(n_g = 1\right)/2\pi = 0.29\,\text{MHz}$ also indicates that the sample is not in the small dispersive shift limit since $\chi/2\pi > \kappa/2\pi = 0.156\,\text{MHz}$ [see Sec. 2.6.1] and consequently that the optimal readout probe frequency is either $\omega_{CPB}\left(n_g = 1\right)$ or $\omega_{CPB}\left(n_g = 1\right) + 2\chi$.

5.2 Extracting Qubit Parameters

After completing resonator and indirect qubit characterization, I proceeded to a direct study of the qubit and the extraction of its parameters. Although the gate bias sweep and single tone spectroscopy were discussed as indirect experiments, they continued to be valuable tools. For example, I made regular use of the gate bias sweep to correct for charge offsets and drift [see Sec. 5.3].

5.2.1 Two-Tone Spectroscopy

Two tone spectroscopy is a method for measuring the CPB transition frequency $\omega_{CPB}(n_g)$. To perform two tone spectroscopy, I set the probe at a fixed frequency, typically $f_{\text{probe}} = (\omega_{res} - \chi)/2\pi$, the ground state resonance frequency at $n_g = 1$ as determined by single tone spectroscopy. I then swept the gate bias n_g through a small range around $n_g = 1 \pm 0.2$ while applying a second continuous pump tone f_{pump}. This second pump tone was at a power sufficient to saturate the CPB ground to excited state transition, typically between $-10\,\text{dBm}$ and $-20\,\text{dBm}$ source power when bypassing the pulse shaping setup. When the pump tone f_{pump} matches the CPB transition frequency $\omega_{CPB}(n_g)/2\pi$, the qubit is excited to a $50\% - 50\%$ mixed state. We may view this as causing the resonance frequency of the resonator to vary between $\omega_{res} - \chi$ and $\omega_{res} + \chi$, on average spending an equal amount of time in each state. As the probe tone f_{probe} is on resonance half the time and off resonance the other half, the net result is that the transmitted amplitude is the average of the on and off resonance values [see Sec. 2.6]. A similar situation holds for the transmitted phase. If the data is plotted as a 2D color intensity plot with the gate bias n_g on the x-axis and pump frequency f_{pump} on the y-axis, the qubit spectrum, if present, shows up as a parabola [see Fig. 5.4].

While first looking for the qubit, such as after the initial cooldown or a thermal cycle, I used a wide f_{pump} frequency range with coarse steps. After locating the CPB parabola minimum E_J/h, I narrowed the sweep to a smaller $\approx 1\,\text{GHz}$ range with finer steps. Rather than the expected single parabola, I observed multiple parabolas in Device 2 [see Fig. 5.5(a)]. This is an indication that something out of the ordinary is happening. Most likely this behavior is caused by coupling to TLS defects and typically this can severely degrade the qubit performance or even render it inoperable. However in the case of Device 2 everything else appeared to be working so I continued using the sample. I also performed additional characterization of the anomalous spectrum of Device 2 [see Ch. 8] in parallel with the planned experimental studies of decoherence in CPB qubits [see Ch. 6].

Fitting the theoretical CPB transition frequency versus n_g curve [see Eq. 2.21] to the experimental data allowed me to extract estimates for the major CPB parameters. An example fit to the preliminary two tone data for Device 2 is shown in Fig. 5.5(b). There are two parabolas present and the model I developed to explain the data is discussed in Ch. 7. Here, I fit both parabolas individually and extracted a set of CPB parameters

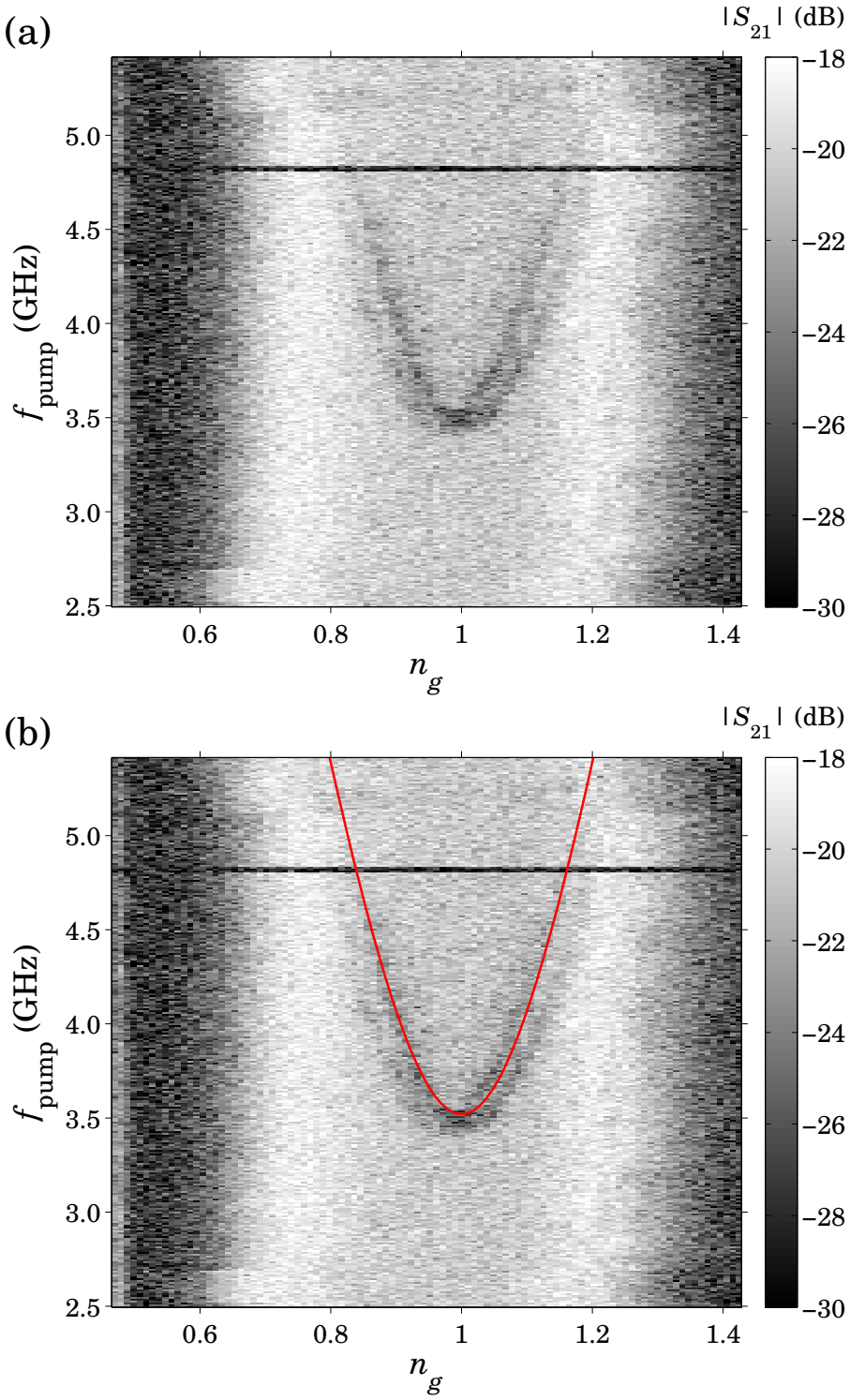

Figure 5.5: (a) Preliminary two tone spectroscopy of Device 2 showing an anomalous spectrum consisting of two offset parabolas. (b) Same plot as (a) but with a manually fit curve to the top parabola to extract qubit parameters $E_{c,\text{bot}}/h = 5.1\,\text{GHz}$ and $E_{J,\text{bot}}/h = 3.52\,\text{GHz}$.

from each. I found $E_{c,\mathrm{bot}}/h = 3.85\,\mathrm{GHz}$ and $E_{J,\mathrm{bot}}/h = 3.45\,\mathrm{GHz}$ for the lower parabola and $E_{c,\mathrm{top}}/h = 5.1\,\mathrm{GHz}$ and $E_{J,\mathrm{top}}/h = 3.52\,\mathrm{GHz}$ for the higher parabola [see Table 1.1]. Although it doesn't make sense to have two sets of parameters for the same physical device, I continued independently characterizing the multiple parabolas until I developed a theory to account for this spectral multiplicity.

In addition to the CPB parameters, I also estimated the qubit-resonator coupling strength $g/2\pi \approx 15\,\mathrm{MHz}$ using the now known value of the detuning $\Delta = \omega_{CPB} - \omega_{res}$ and the dispersive shift $\chi = g^2/\Delta$ determined from single tone spectroscopy [see Table 1.1]. The uncertainty in g is due to the presence of multiple parabolas, which indicate there are several levels close to the resonator, each of which cause their own dispersive shifts and sum to the total dispersive shift.

5.2.2 External Flux Dependence

Having established the CPB parameters without an applied external magnetic flux, I proceeded to tune the E_J [see Sec. 2.3]. The goals were to first determine E_J^{sum} and then set E_J to the desired operating point. Note that although there is no applied magnetic field during cooldown, the Earth's magnetic field along with local magnetic materials can result in some flux through the CPB loop and hence I can't assume that the initial flux bias is at $\Phi/\Phi_0 = 0$. Additionally, the applied magnetic field doesn't have a simple relationship to the flux through the CPB loop. A combination of effects—including local flux screening, focusing, flux jumps due to the Meissner effect, and flux quantization [33] in the superconductors surrounding the CPB, especially in the closed loop around the entire circuit formed by the resonator ground plane—contribute to the effective qubit flux bias. Altogether these effects lead to a complicated nonlinear and hysteretic relationship between the current applied to the superconducting solenoid magnet and the flux through the CPB.

I found that the best approach to tuning E_J is to slowly change the current in the superconducting magnet while tracking E_J using two tone spectroscopy. However, this only works for small field adjustments—in my experience applying a field greater than a few Gauss leads to a flux jump. In order to change E_J by a large amount I employed a trial and error approach. I first applied a relatively large field of $\approx 5\,\mathrm{G}$ to cause a flux jump, then reset the field to $0\,\mathrm{G}$ and determined E_J using two tone spectroscopy. If the

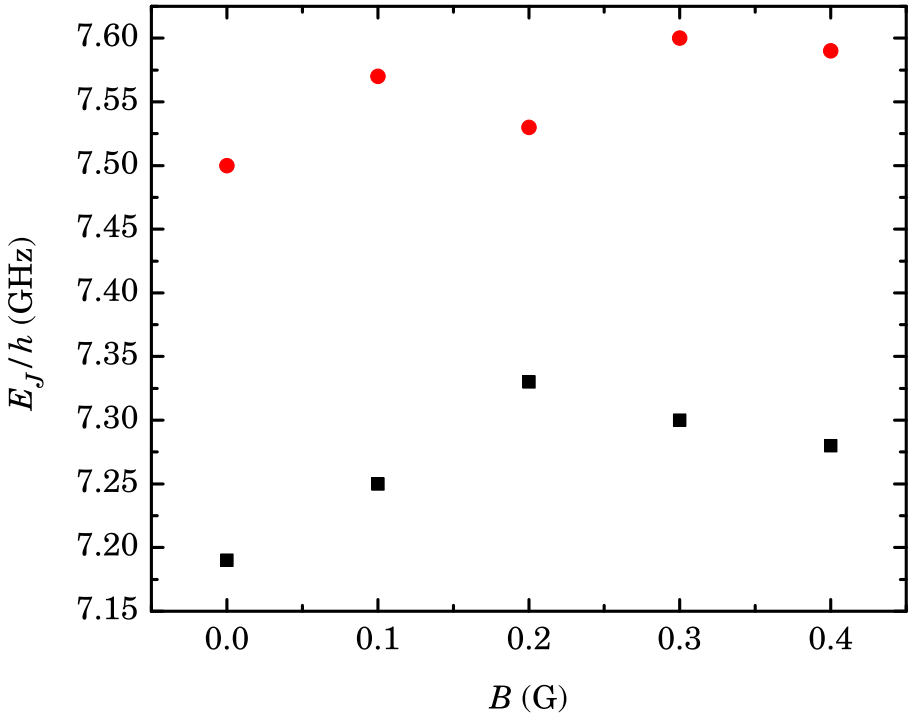

Figure 5.6: E_J/h versus external magnetic field B for Device 2. Black squares are data for the bottom parabola and show $E^{\text{sum}}_{J,\text{bot}}/h = 7.33\,\text{GHz}$ while red circles are data for the top parabola and show $E^{\text{sum}}_{J,\text{top}}/h = 7.60\,\text{GHz}$.

E_J was near the target value, I fine tuned it and proceeded with further experiments, otherwise I repeated the process.

Using this method for Device 2 I determined the maximum E^{sum}_J and then set E_J near E^{sum}_J. I stepped the magnet current through a range of values and at each point I took two-tone spectroscopy. I fit the data to extract $E_{J,\text{top}}(\Phi)$ and $E_{J,\text{bot}}(\Phi)$, the E_J values for each parabola. The results are plotted in Fig. 5.6. I separately tracked the two parabolas and found $E^{\text{sum}}_{J,\text{bot}}/h = 7.33\,\text{GHz}$ and $E^{\text{sum}}_{J,\text{top}}/h = 7.60\,\text{GHz}$. These value were close to the design value and allowed operation of the qubit near the double sweet spot at $n_g = 1$ and $\Phi/\Phi_0 = 0$. I did one experiment at $E_J/h = 7.2\,\text{GHz}$ [see Sec. 5.2.3] to extract the value of g but for the rest of the measurements ran with $E_J/h \approx 7\,\text{GHz}$ as I found the qubit to be more stable there.

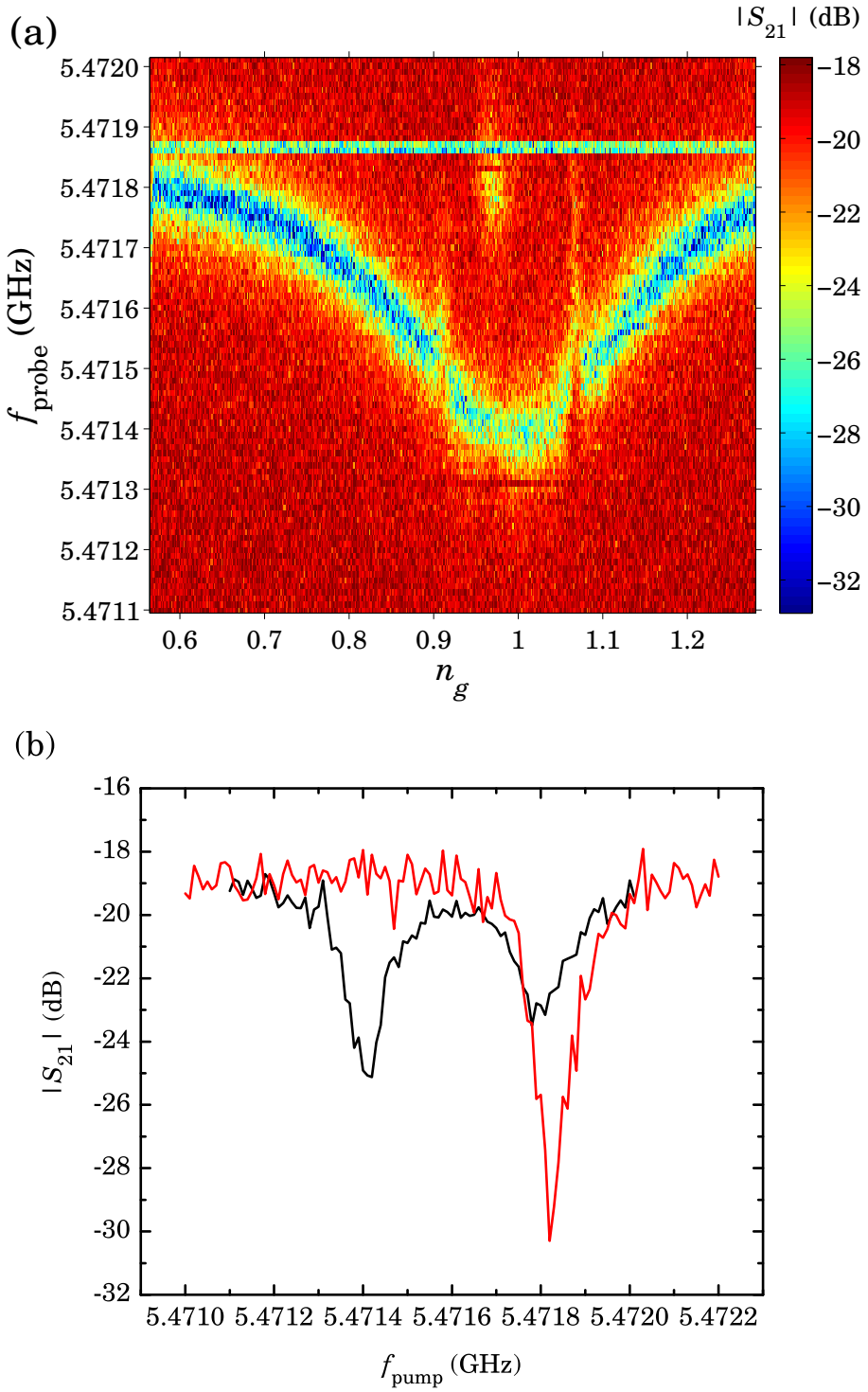

Figure 5.7: (a) Single tone spectroscopy with a pump tone at $f_{\text{pump}} = E_{J,\text{bot}}/h$ for Device 2. The feature at $n_g \approx 0.95$ and $f_{\text{probe}} \approx 5.4718\,\text{GHz}$ is the resonance when the qubit is in the excited state. (b) Line cut at $n_g = 1$ (black) displaying the two dispersively shifted resonator states $\omega_{res} \pm \chi_{\text{bot}}$ and line cut at $n_g = 0$ (red) showing the bare resonator resonance ω_{res}. Note that the bare resonance (red) is at almost the same frequency as the excited state resonance rather than symmetrically between the two dispersively shifted frequencies.

5.2.3 Single-Tone Spectroscopy With a Pump Tone

I used single tone spectroscopy with a pump tone present to observe the two dispersively shifted resonance frequencies $\omega_{res} - \chi$ and $\omega_{res} + \chi$ due to the two qubit states. This technique is similar to two-tone spectroscopy except that the pump tone $f_{\text{pump}} = E_J/h$ is held constant while the probe tone f_{probe} is stepped through a range encompassing both $\omega_{res} - \chi$ and $\omega_{res} + \chi$. The gate bias n_g is swept through a small range around $n_g = 1 \pm 0.2$. Near $n_g = 1$ the pump tone f_{pump} is resonant with the CPB transition frequency $\omega_{CPB}\left(n_g = 1\right)/2\pi = E_J/h$ and the qubit is excited to a $50\% - 50\%$ mixed state. Just as in two tone spectroscopy, we may view the mixed qubit state as causing the resonance frequency of the resonator to vary between $\omega_{res} - \chi$ and $\omega_{res} + \chi$, on average spending an equal amount of time in each state. Stepping the probe frequency f_{probe} through its range and recording the transmitted signal samples both of the resonance dips, albeit at reduced amplitude. The data is presented in the same way as standard single tone spectroscopy, as a 2D color intensity plot with the gate bias n_g on the x-axis and probe frequency f_{probe} on the y-axis. Features that are present in single tone spectroscopy are still present, but there is one additional new feature, the dip corresponding to the $\omega_{res} + \chi$ resonance [see Fig. 5.7(a)]. By taking a line cut at $n_g = 1$ and fitting the two dips to Lorentzian lineshapes, I was able to extract the two dispersively shifted resonance frequencies [see Fig. 5.7(b)].

In the previous paragraph, I simplified the discussion by neglecting effects from having multiple CPB spectral parabolas seen in Device 2. These parabolas imply the existence of two hybrid qubit-TLS levels with similar detunings from the resonator. If the qubit-resonator couplings of the two levels, g_{bot} and g_{top}, are both non-negligible, each level will produce a corresponding dispersive shift χ_{bot} and χ_{top} [39, 74]. In this case the resonance frequency when the qubit is in the ground state is $\omega_{res} - \chi_{\text{bot}} - \chi_{\text{top}}$ and, for example, it's $\omega_{res} + \chi_{\text{bot}} - \chi_{\text{top}}$ when the qubit is excited to the state corresponding to the transition of the bottom parabola. The difference of the two resonance frequencies is $2\chi_{\text{bot}}$ and allows me to accurately extract g_{bot} without making assumptions about ω_{res} based on $n_g = 0$ data.

I obtained the data in Fig. 5.7(a) on Device 2 with a pump tone $f_{\text{pump}} = E_{J,\text{bot}}/h$ set to the lower parabola minimum. The excited state dip lies at the same frequency as $\omega_{res}\left(n_g = 0\right)$, rather than symmetrically reflected about it, the expected position if the

dispersive shift was only due to one level [see Fig. 2.9(a)]. From fits to the line cuts at $n_g = 1$ [see Fig. 5.7(b)] I extracted $\chi_{\text{bot}}/2\pi = 180\,\text{kHz}$, which is is about half the total dispersive shift. Combining this with the detuning $\Delta_{\text{bot}}/2\pi = 1.73\,\text{GHz}$ determined using two tone spectroscopy I extracted the qubit-resonator coupling strength $g_{\text{bot}}/2\pi = 17.6\,\text{MHz}$. Since χ_{bot} happened to be half the total dispersive shift, I extracted the same numbers for the top parabola. I don't have an explanation why the two dispersive shifts were so close in value but I suspect it was a coincidence as this relation didn't hold at other E_J values. Finally this observation of a total dispersive shift that is the sum of two contributions is strong evidence that the qubit and TLS were coherently coupled [see Ch. 8].

5.3 Qubit Readout Optimization

Characterization of the qubit excited state lifetime T_1 or coherence time T_2 requires keeping the gate bias fixed at the sweet spot $n_g = 1$. Although this sounds easy in theory, in practice it may be the most difficult part of operating a charge qubit. While the external voltage bias V_g is stable and simple to control, local charge motion near the CPB results in the effective gate bias n_g undergoing randomly occurring drifts and offsets of unpredictable magnitude. Consequently, the operating point may, during the course of a single sweep, move far enough from the sweet spot at $n_g = 1$ to detune the pump tone $f_{\text{pump}} = E_J/h$ from the transition frequency $\omega_{CPB}(n_g \neq 1)$. Alternatively, the drift or offset may not be large enough to detune the qubit and the pump tone but still significant enough to move the qubit off of the sweet spot and increase its sensitivity to charge noise, introducing a large uncertainty and variance in T_1 or T_2. Proper operation of a charge qubit requires constant monitoring and readjustment of the voltage bias V_g as described in the next section. On a bad day, even a single spectral curve or Rabi oscillation could take many hours to acquire.

5.3.1 Dealing With Charge Noise

I can categorize the charge noise I observed into three types: e jumps, sub-e jumps, and slow drifts. Of the three, e jumps were the easiest to deal with. They were relatively rare, easy to detect and easy to correct. Two examples of e jumps in Device 2 are visible in two tone spectroscopy taken on the day of the cooldown [see Fig. 5.8(a)] near 4.35 GHz and

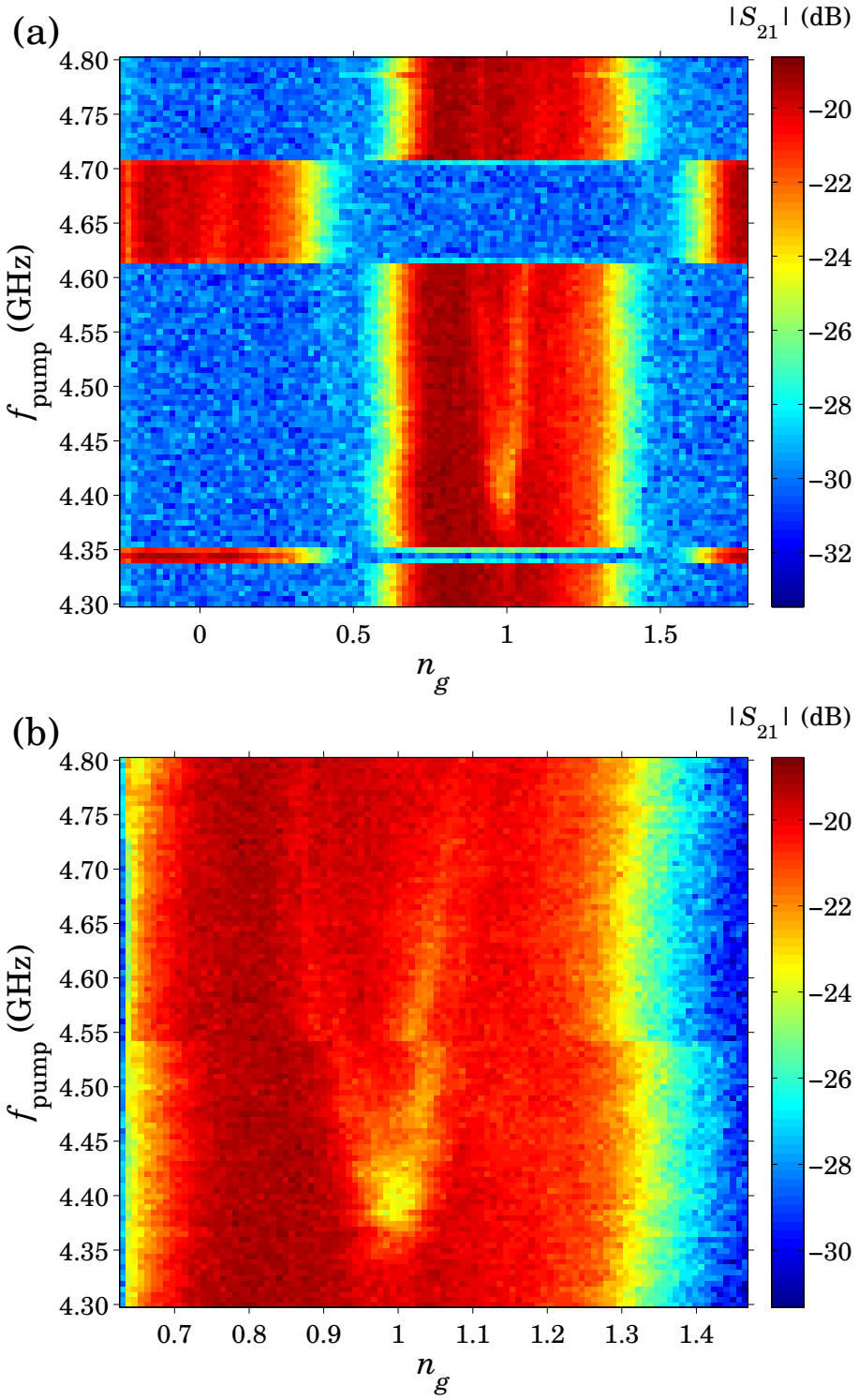

Figure 5.8: Examples of charge noise in two tone spectroscopy of Device 2. (a) Wide n_g sweep shows charge drift along with e jumps near 4.35 GHz and 4.65 GHz. (b) Zoomed in n_g sweep shows charge drift and a sub-e jump near 4.55 GHz. Each scan took $\approx 1-2$ min to acquire.

4.65 GHz. At those points in the scan the dispersive shift "hump" suddenly jumps from $n_g = 1$ to $n_g = 0$ and then returns after a short duration (the entire scan took $\approx 1-2$ min to acquire). When an e jump occurred, I waited a short amount of time until it returned and then resumed the experiment in progress. If it didn't return, I assumed the new position was the current equilibrium value and adjusted the voltage bias V_g, using the fact that $e/C_g = 0.839$ V to speed up the process.

Charge drift and sub-e jumps were more frequent and harder to deal with. Drift is present throughout the zoomed in two tone spectroscopy in Fig. 5.8(b), along with a sub-e jump near 4.55 GHz. These were harder to detect during the course of an experiment and I needed to develop intuition for deciding when the gate bias deviated too far from $n_g = 1$. The clues I looked for were reduced contrast in the qubit excited state response or small changes in the ground state resonance frequency. I compensated for both sub-e jumps and charge drift by performing a gate bias sweep, determining the voltage bias V_g corresponding to $n_g = 1$, setting the bias to that value, and proceeding with the experiment. This procedure required manual intervention and took me about a minute to execute. On a good day, the average time between sub-e jumps and significant charge drift would be long enough for me to take data after performing the compensation routine. On a bad day, these events were too frequent and I spent the majority of my time adjusting the gate bias rather than taking data. This process was effectively a low-frequency charge locked loop.

In addition to compensating for charge offsets during an experiment, I also adjusted the readout process and post-processed the data to minimize or remove the effect of charge offsets. I found that the optimal number of averages of the IF signal was between 500 and 2000, taking $\approx 1-10$ s to record a single n_g scan or fixed n_g data point. This represents a trade-off between a short averaging time, which reduces the probability of a charge offset occurring during the acquisition, and a long averaging time, which improves the signal-to-noise ratio of the recorded signal. If I needed high quality data consisting of n_g sweeps, such as two tone spectroscopy, I took the data in short spans of the y-axis variable and later stitched it together to create the final plot. In between recording the slices, I adjusted the gate voltage bias V_g as needed and also discarded and re-recorded slices corrupted by significant charge offsets. In some cases I further post-processed the data to remove small charge offsets present in each n_g scan. I used the background ground state

transmitted signal present in two tone spectroscopy as a fiducial feature to automatically align each individual n_g scan within a slice before stitching all the slices together. This technique also allowed me to acquire multiple slices at the same parameters and then average them together.

Experiments at a fixed n_g, such as Rabi oscillations [see Sec. 5.4.3], required a different approach. While recording Rabi oscillations, I interspersed monitoring the ground state response during each run for indications of significant charge offsets. If the run was significantly corrupted I would discard it, if a few points were affected, I would save it. The gate voltage V_g was adjusted between runs as needed. The data points of a Rabi oscillation are independent, meaning that as I stepped the pulse length duration, points with a different duration could be acquired in any order and sorted later. I used this fact to post-select the data, discarding any data points in a single run which the recorded ground state response indicated were corrupted by a charge offset. Finally all such runs were averaged together to produce the final Rabi oscillation curve.

The charge offsets discussed so far took place on a timescale of seconds or longer. Higher frequency charge noise was also present in my devices, altering the gate bias n_g on a timescale of milliseconds. Since this occurred during the averaging of a single IF ensemble, I wasn't able to compensate for it. This noise manifested itself as a reduction in the readout contrast: by detuning the qubit from the pump tone f_{pump} for a fraction of the ensemble members, the qubit remained in the ground state when it should have been excited and reduced the average response. This phenomena didn't impact my ability to study the devices but does explain why the maximum excited state probability reached during measurements such as T_1 or Rabi oscillations varied on a daily basis [see Ch. 6].

Although charge offsets are the biggest hindrance to performing experiments with a CPB, I also observed slow E_J drift. The E_J of a particular parabola would gradually change by $\approx 1-2\,\text{MHz}$ during the course of a day. This wasn't a major problem during a single experiment but did force me to recalibrate E_J and π pulse length when performing day-long qubit characterization. It also meant that I had to recalibrate the system every morning. I don't know the exact physical origin of this effect but I suspect it was due to vortex motion or small changes in the local magnetic field.

5.3.2 Pulsed Probe Readout

The ac Stark shift complicates accurate determination of the qubit transition frequency and can shorten the qubit dephasing time [see Sec. 2.8]. To minimize complications from the ac Stark shift, I used a pulsed probe readout during experiments, such as Rabi oscillations and Ramsey fringes, where it would interfere with the result. The pulsed probe scheme involves sending a microwave pulse at frequency f_{probe} to determine the qubit state only after the qubit manipulation has been performed. Pulsing the probe also allows driving the resonator with a higher power signal than during weak continuous readout, improving the signal-to-noise ratio.

In my implementation of pulsed readout I used two $10\,\mu$s long pulses, the first before any qubit manipulation to record the ground state transmission and the second $30-40\,\mu$s after the end of the first pulse to record the qubit state immediately after the qubit control sequence. I used the first probe pulse as a reference to identify gate bias n_g charge offsets. The experimental setup for pulsed probe measurements was nearly identical to the setup for weak continuous monitoring. The main differences were that I changed the f_{probe} microwave source from continuous to triggered pulsed output and used the auxiliary outputs on the DAC board to trigger $10\,\mu$s long pulses at the proper times.

In the pulsed probe technique the transmitted amplitude time response is a convolution of the resonator rise time and the average qubit state dynamics [25, 80, 79]. When probe power is first turned on, the resonator transmission response rings up in a time $1/\kappa$ to the steady state value corresponding to the qubit state. If the qubit lifetime T_1 is much longer than the resonator response time $1/\kappa$, the resonator transmission characteristics faithfully follow the average qubit state as it decays. That was the case for Device 1 and this made interpreting and optimizing the pulsed probe readout simple. Device 1 was also in the small dispersive shift limit [see Sec. 2.6.1]. For this device I recorded the phase response $2/\kappa \approx 2\,\mu$s after the start of the second probe pulse and converted it to the qubit excited state probability using the known ground state phase response at $n_g = 1$ and the bare resonator phase response at $n_g = 0$.

If the qubit lifetime T_1 is longer but not drastically so than the resonator response time $1/\kappa$, then the qubit excited state probability decays by a non-negligible amount during the resonator ring up and soon after. That was the case for Device 2. In this case I compensated for the qubit decay by averaging the resonator in-phase voltage response in

a window starting $2/\kappa \approx 2\,\mu$s after the start of the second probe pulse and extending for several μs. The boxcar filter also improved the signal-to-noise ratio of the readout. I optimized the averaging window length by recording the full decay curve and then adjusting it to the maximum length consistent with the T_1 of the qubit. This procedure was similar to the lifetime T_1 characterization of the qubit [see Sec. 5.4.1]. Unfortunately, due to the complicated multiple parabola spectrum and dispersive shifts of Device 2 I wasn't able to calibrate the in-phase voltage into an absolute qubit excited state probability.

I encountered another unexpected complication with the pulsed probe readout of Device 2: the readout worked with some of the spectral parabolas but not all of them. For example, I found that the pulsed probe functioned as expected for the bottom parabola at $E_{J,\mathrm{bot}}/h = 7.06\,$GHz in Fig. 8.1(a). In contrast, the top parabola at $E_{J,\mathrm{top}}/h = 7.25\,$GHz in Fig. 8.1(a) didn't respond to the pump tone if the resonator probe tone was absent.

In order to better understand why the pulsed probe only worked on some of the parabolas, I carried out an experiment that smoothly transitioned from a weak continuous readout to pulsed probe. In addition to the probe f_{probe} and pump f_{pump} tones, I added a third continuous tone f_{third} detuned by $140\,\mathrm{kHz} \approx \kappa/2\pi$, the approximate linewidth of the resonator, from the probe signal. This tone was output by an additional Agilent 83732B signal generator [170], attenuated by a 10 dB attenuator, and added to the rf input line with a MAC Technology model C3205-6, $4-8\,$GHz 6 dB directional coupler [175] [see Fig. 5.9(a)]. I chose the attenuator and coupler values such that the powers of the probe and third tones would have similar magnitudes at the rf input. After confirming that everything continued working normally with the addition of the third tone, I stepped its power while performing pulsed probe spectroscopy [see Sec. 5.4.2].

I fit the recorded spectral peaks to a Lorentzian curve and plotted the peak depth versus third tone power [see Fig. 5.9(b)]. The peak depth is proportional to the third tone power in the range of values I tested, explaining why I didn't see anything when I attempted standard pulsed probe readout. I don't have an underlying explanation for this behavior. It may be that the resonator is involved in these spectral features or, alternatively, it may have been a coincidence and the third tone is indirectly providing the energy needed to put the qubit-TLS system in a state which then responds to the pump tone.

When I took this data the behavior with the pulsed probe was not a priority and I soon moved on to do qubit performance characterization. Since then, I have considered a possi-

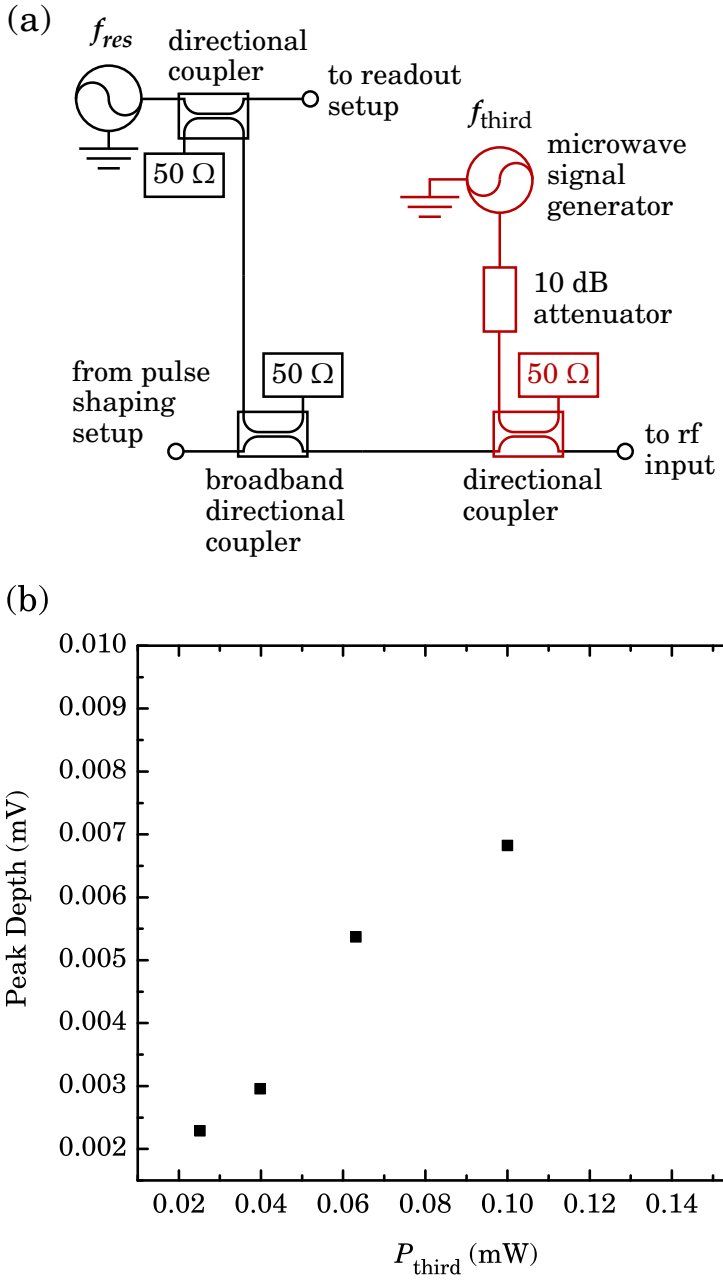

Figure 5.9: (a) Simplified diagram of the modified setup to perform pulsed probe readout with an additional third continuous tone f_{third}. (b) Voltage amplitude of the qubit spectral peak measured with a pulsed probe readout versus continuous third tone source power P_{third}.

ble experiment that might have cleared up the situation. The idea is to step the third tone f_{third} frequency over a wide range at a constant output power while performing pulsed probe spectroscopy and noting the frequency dependence of the spectral peak depth. From this data it should be possible to determine whether the resonator is directly involved or not in the anomalous spectral features. If the spectral peak is visible only when the third tone is within a few linewidths κ of the resonance frequency ω_{res}, it indicates that the resonator is involved in this behavior. On the other hand, if the spectral peak is visible for a wide range of third tone frequencies, it suggests that this behavior is due to a TLS activated in that frequency range.

5.4 Qubit Performance Measurements

The extracted CPB parameters of Device 2 were close to the designed values—$E_{J,\max}/h \approx 7\,\text{GHz}$ and $E_c/E_J \approx 1$. Although it had an anomalous spectrum, I decided to keep it and proceed to study the performance. A first round of measurements was carried out at $n_g = 1$, $E_{J,\text{bot}}/h = 7.06\,\text{GHz}$, and $E_{J,\text{top}}/h = 7.25\,\text{GHz}$ and included measurements of the lifetime T_1, the spectroscopic coherence time T_2^*, and the length of a π pulse along with a calibration of the number of photons in the resonator as a function of probe power. Although in the discussion that follows I present the experiments separately, in practice they were tied together and fed back on each other. For example, the T_1 measurement was needed to optimize the pulsed probe readout [see Sec. 5.3]. The pulsed probe was then used to measure the bare transition frequency $\omega_{CPB}/2\pi$ and the spectral width. This in turn allowed me to perform a pulsed probe T_1 measurement. Finally, measurements such as the lifetime and spectral width had to be repeated along with two tone spectroscopy every time E_J changed, either due to manual adjustment or drift. In the following chapters I won't describe these steps in detail but simply quote any relevant extracted parameters.

5.4.1 Excited State Lifetime T_1

I used several closely related approaches to measure the qubit excited state lifetime T_1. The methods differed in readout style—weak continuous versus pulsed probe—and method of qubit excitation—long saturation pulse or π pulse. The π pulse was calibrated by using Rabi oscillations [see Sec. 5.4.3] while the saturation pulse just needed to be

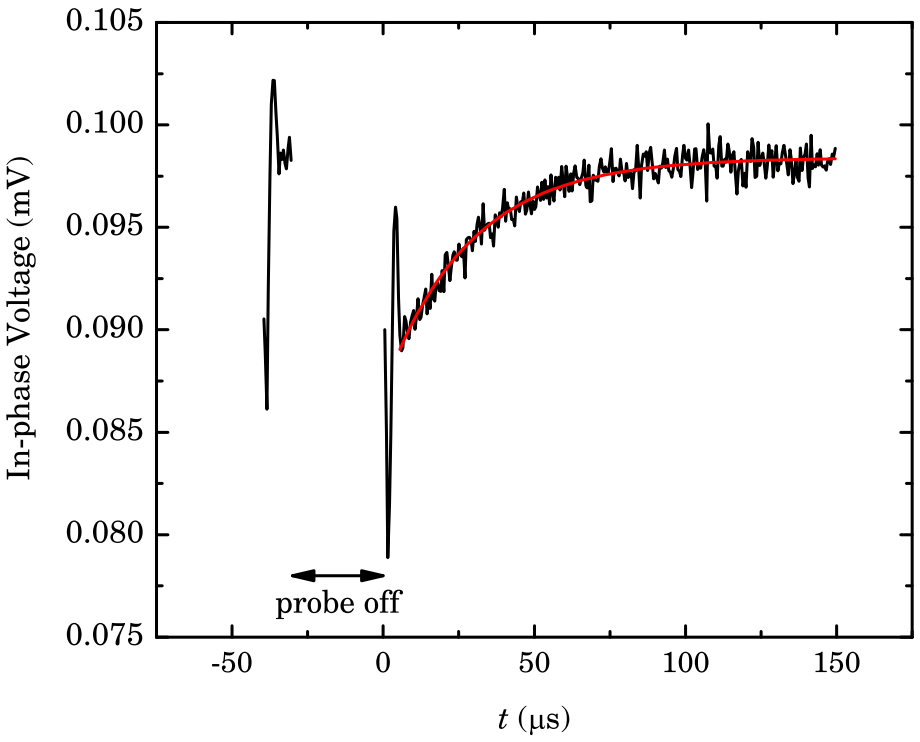

Figure 5.10: Pulsed probe measurement of relaxation of Device 2 (black) following a long saturation pulse. The red curve shows a fit to an exponential decay. The extracted lifetime is $T_1 = 28.1\,\mu$s. The gap in the signal is the period when the probe was turned off and the large swings in the in-phase voltage at the beginnings of the two sections of data is a signature of resonator ring-up. The saturation pulse was applied between $t = -5\,\mu$s and $t = 0\,\mu$s.

sufficiently longer than the Rabi oscillation decay time T' to ensure that the qubit was excited to a $50\%-50\%$ mixed state. The lifetime should be the same for all these methods so this allowed me to check for consistency. In general, after verifying that they agreed, I used whichever one was more convenient. Most commonly that was the pulsed probe readout with a saturation pulse because it had a good signal-to-noise ratio and didn't require a calibrated π pulse.

I began by pumping the qubit at $\omega_{CPB}/2\pi$, as determined from two tone spectroscopy. For this technique I used a long saturation pulse and recorded the decay of the excited state probability while continuously monitoring with a weak probe tone. An exponential fit to the decay region of the data gave me a preliminary T_1 estimate. I then used this T_1 estimate to optimize the pulsed probe readout. I next used this readout to measure the spectral peak [see Sec. 5.4.2]. By fitting to this peak, I extracted the bare transition

frequency $\omega_{CPB}/2\pi$ with the resonator in the ground state. Finally, I repeated the lifetime measurement using a pulsed probe readout. The benefit of using a pulsed probe readout is that it has a higher signal-to-noise ratio, and this allows me to obtain better fits and hence extract a better estimate of T_1.

Fig. 5.10 shows a plot of the transmitted in-phase voltage versus time t for a pulsed probe T_1 measurement at $E_{J,\mathrm{bot}}/h = 7.06\,\mathrm{GHz}$. The saturation pulse had a duration of $5\,\mu\mathrm{s}$ and ended at time $t = 0\,\mu\mathrm{s}$. The $30\,\mu\mathrm{s}$ gap in the data between $t = -30\,\mu\mathrm{s}$ and $t = 0\,\mu\mathrm{s}$ corresponds to the period when the probe power was turned off. Ringing is visible during the first $\approx 1\,\mu\mathrm{s}$ after the probe power is turned on. From a least squares exponential fit to the decaying region of the curve, I extracted a qubit lifetime of $T_1 = 28.1\,\mu\mathrm{s}$. Although this is a good fit and implies a high degree of confidence in the extracted value, repeat measurements of the lifetime T_1 show day to day and intraday variation as large as $20-40\%$.

5.4.2 AC Stark Shift and Spectral Width

Up to this point, I employed circuit QED concepts only for qubit readout and ignored much of the interesting physics of the qubit-resonator interaction. The AC Stark shift [see Sec. 2.8] in my devices was large enough that I could see the effect of a few photons on the qubit and it allowed me to calibrate the average number of photons $\bar{n}$ in the resonator as a function of probe power. I need this information to determine what is the appropriate probe power to use for weak continuous readout and to find the critical photon number $n_{\mathrm{crit}} = \Delta^2/4g^2$—it was important during experiments with a high probe power for $\bar{n}$ not to exceed n_{crit}. In Device 2, at a detuning of $\Delta/2\pi \approx 1\,\mathrm{GHz}$ and qubit-resonator coupling strength $g/2\pi \approx 15\,\mathrm{MHz}$, the critical photon number was $n_{\mathrm{crit}} \approx 1100$. Z. Kim found a similar $n_{\mathrm{crit}} \approx 2500$ for Device 1 [71]. I sometimes used large probe powers corresponding to a few hundred photons; I didn't approach the limit $\bar{n} > n_{\mathrm{crit}}$ where the dispersive approximation breaks down.

The AC Stark effect both shifts and broadens the qubit transition frequency. It's most readily observed by recording the spectral peak while probing the resonator with a weak continuous tone. I kept the gate bias fixed at $n_g = 1$ and continuously probed the resonator at a set power while stepping the frequency of the continuous pump through a range of values around $E_{J,\mathrm{top}}/h = 7.25\,\mathrm{GHz}$ and recording the transmitted voltage. I re-

peated this for a range of probe powers, starting at what I typically consider a high source power and decreasing it until the signal-to-noise ratio became too low. Each spectral peak was fit to a Gaussian lineshape to extract the center frequency and width. While both Gaussian and Lorentzian lineshapes gave good fits to the data, I chose to use the results of the Gaussian fits because that is the theoretically predicted lineshape when dephasing due to the AC Stark shift dominates [see Sec. 2.8].

Figure 5.11(a) shows a plot of the extracted qubit transition frequency versus probe source power along with a linear least squares fit to the data. The line is a good fit to the data, indicating agreement with theory. The error bars represent the fit error and are difficult to make out on this scale. I believe the spread in the data is due to changes in $\omega_{CPB}/2\pi$ caused by gate bias n_g charge offsets or E_J drift. The AC Stark shift per photon is $2\chi_{\text{top}}/2\pi = 360\,\text{kHz}$, which allows me to calculate the number of photons in the resonator $\bar{n}$ at a given source power. Finally, the y intercept is a useful estimate of the bare qubit transition frequency and provides a good starting point when first performing pulsed probe spectroscopy.

The width of the qubit spectral peak versus photon number is plotted in Fig. 5.11(b). I fit the data to a square root function to see how well the dependence of the width $2\nu_{\text{HWHM}}$ on photon number agreed with theory. Although the functional fit is good, the prefactor is 2.87 MHz, about a factor of ≈ 8 larger than the expected $2\chi_{\text{top}}/2\pi = 360\,\text{kHz}$. This suggests that the photon number fluctuations were larger than for a Poisson distribution and may have been caused by the qubit being in a $50\% - 50\%$ mixed state. In this situation the resonator resonance frequency stochastically switches between the two dispersively shifted states and the probe tone f_{probe} is on resonance only half the time. Rather than maintaining a single steady state coherent state, the system fluctuates between two states, with a corresponding increase in the photon number variance.

I estimate this increase in variance by assuming that the photon state switched between two Poisson distributions, one with a high average photon number n_{high} and the other with a low average photon number n_{low}. I define two new variables $\bar{n} = \left(n_{\text{high}} + n_{\text{low}}\right)/2$ and $s = \left(n_{\text{high}} - n_{\text{low}}\right)/2$, where $\bar{n}$ is the average number of photons in the resonator and s is half the difference between n_{high} and n_{low}. Using the Poisson distribution probability density function $P\left(k;\mu\right) = e^{-\mu}\mu^k/k!$ where μ is the mean and $k \in \mathbb{N}$ [106], I find the photon

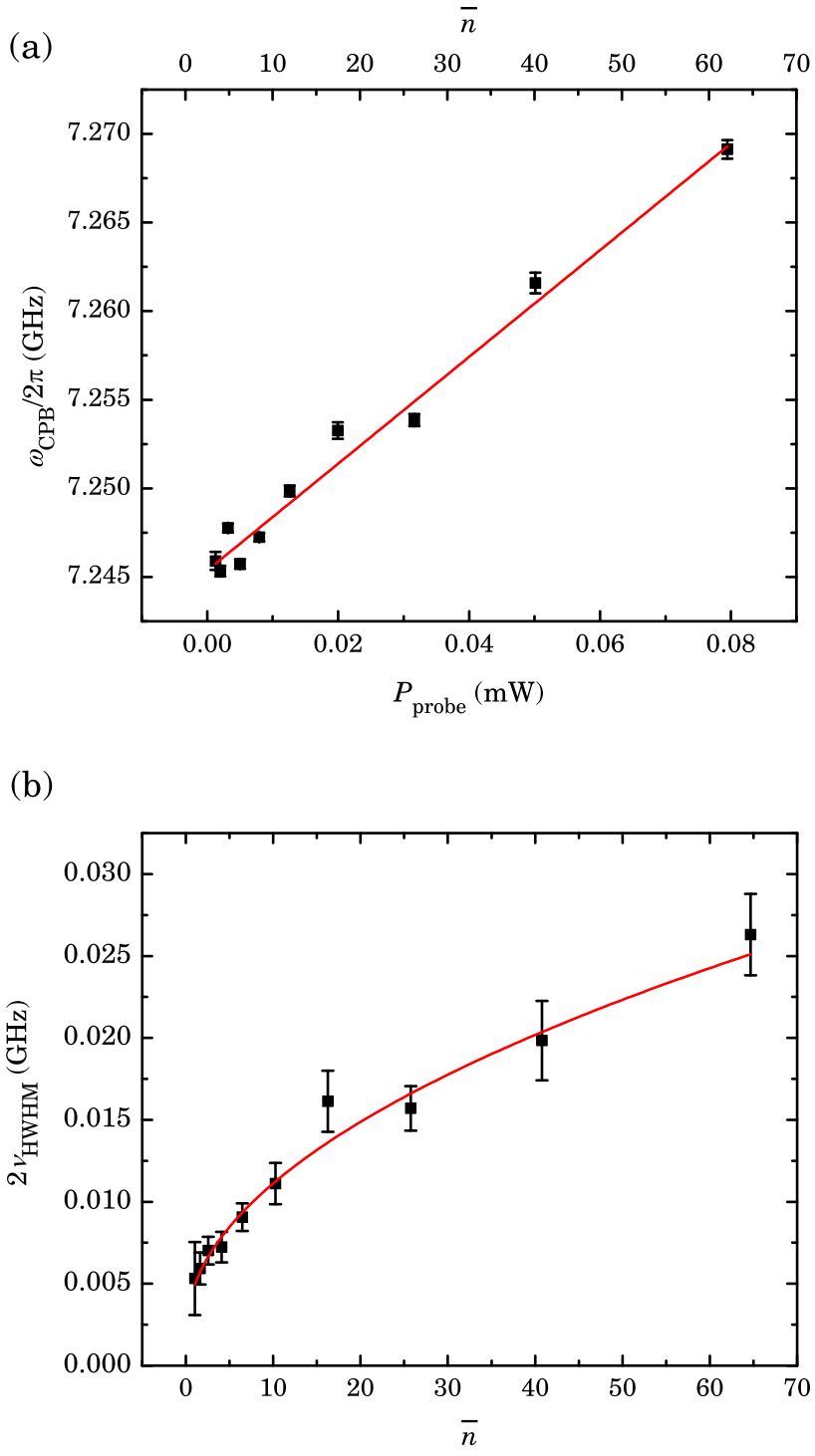

Figure 5.11: (a) Change in the transition frequency $\omega_{CPB}/2\pi$ versus probe power P_{probe} in Device 2, demonstrating the AC Stark shift. The data (black squares) is well fit by a line (red curve) and, along with the AC Stark shift per photon $2\chi_{\text{top}}/2\pi = 360\,\text{kHz}$, allows me to calibrate the average number of photons $\bar{n}$ at a given probe power. (b) Spectral broadening in Device 2 due to fluctuations in the photon number about the mean $\bar{n}$. There is good agreement of the data (black squares) with the expected constant plus $\sqrt{\bar{n}}$ scaling (red curve).

number variance

$$\begin{aligned}\sigma^2 &= \frac{1}{2}\sum_{k\in\mathbb{N}}(k-\bar{n})^2\left(P(k;\bar{n}-s)+P(k;\bar{n}+s)\right)\\ &= \bar{n}+s^2. \end{aligned} \tag{5.2}$$

The variance of the Poisson distribution is $\bar{n}$ [106] and I find that when the photon state switches between two distributions, the variance is increased by s^2. If I assume $\bar{n}=25$ and that the switching happens on average every $2\,\mu\text{s}\approx 2/\kappa$, then $n_{\text{high}}=4n_{\text{low}}$. This is a reasonable time scale for the switching because $2\,\mu\text{s}\approx\sqrt{T_1T_2}$ and it's also close to the period of typical Rabi oscillations for Device 2. With these numbers I find that the standard deviation of photon number, and hence the qubit spectral width, is approximately ≈ 3 times larger than for a steady state coherent state. This is less than the factor of ≈ 8 increase I observed but may nevertheless explain some of the discrepancy in photon number fluctuations.

The AC Stark shift experiment naturally leads into pulsed probe measurements of the spectral width. Both experiments reduce dephasing caused, respectively, by the probe and pump tones and employ similar setups. By this point I had the information needed to fully optimize pulsed probe readout and I was able to record the qubit spectral peak without any photons in the resonator in Device 2. I kept the gate bias fixed at $n_g=1$, stepped the continuous pump frequency through a range of values around $E_{J,\text{bot}}/h=7.06\,\text{GHz}$ and recorded the transmitted voltage with a pulsed probe readout. I repeated the sweeps at various pump powers, starting close to the maximum output power of the pulse shaping setup and decreasing it until the qubit no longer responded. The low power AC Stark shift data provided a good initial estimate of the bare transition frequency $\omega_{CPB}/2\pi$, which I then confirmed by fitting the spectral peak to a Lorentzian lineshape.

Figure 5.12(a) shows a typical spectral peak in Device 2. Here the pump frequency is on the x-axis and the in-phase transmitted voltage is on the y-axis. Also shown are data both before the pump pulse and a Lorentzian least squares fit. In addition to the bare transition frequency $\omega_{CPB}/2\pi$, which is needed for all other pulsed probe experiments, I extracted additional peak parameters which provide two more useful pieces of information. By tracking the peak amplitude as a function of pump power, I was able to determine the minimum power sufficient to saturate the qubit to a $50\%-50\%$ mixed state. This way

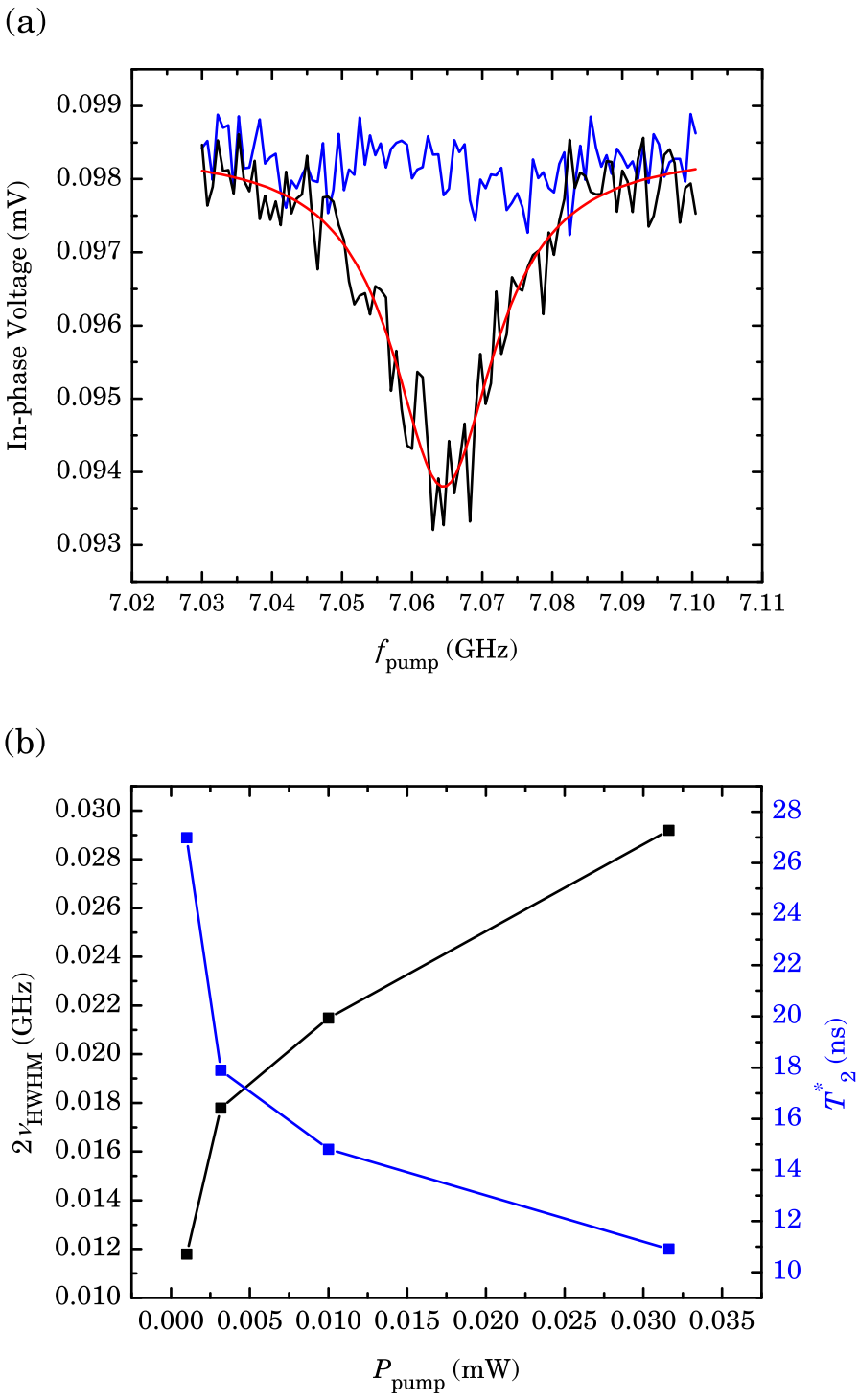

Figure 5.12: (a) Spectral peak (black) and the corresponding signal before the qubit pump pulse (blue) recorded with a pulsed probe readout. The data is fit to a Lorentzian lineshape (red) to extract the bare transition frequency $E_{J,\mathrm{bot}}/h = 7.064\,\mathrm{GHz}$ and the spectral width $2\nu_{\mathrm{HWHM}} = 0.018\,\mathrm{GHz}$. (b) Spectral width (black) and spectroscopic coherence time T_2^* (blue) versus source power P_{pump}.

I was able to fully pump the qubit without producing excessive power broadening [see Sec. 3.2]. Finally, the spectral width at low pump power gives me the unbroadened spectroscopic coherence time T_2^* [see Fig. 5.12(b)]. Using $T_2^* = 1/2\pi\nu_{\mathrm{HWHM}}$ [see Sec. 3.4.1] I estimated $T_2^* \approx 30\,\mathrm{ns}$ for the bottom spectral parabola. I wasn't able to directly measure the coherence time of the top spectral parabola since pulsed probe readout didn't work there. However, using AC Stark shift data at low probe power I extracted a spectroscopic coherence time $T_2^* \gtrapprox 60\,\mathrm{ns}$ which indicates that the coherence time $T_2 \gtrapprox 60\,\mathrm{ns}$ [see Sec. 3.2].

5.4.3 Rabi Oscillations

The last experiment I did as part of the preliminary qubit characterization was to observe Rabi oscillations. Rabi oscillations are the simplest example of coherent qubit control and explore qubit dynamics and coherence in the time domain, rather than the frequency domain. For Device 2, I biased the qubit at $n_g = 1$ and pumped at $E_{J,\mathrm{bot}}/h = 7.06\,\mathrm{GHz}$, as determined by pulsed probe spectroscopy, with a fixed duration pulse. The qubit ground state before the pump pulse and excited state probability after were recorded with pulsed probe spectroscopy. This ensemble average was then repeated for a range of pump pulse durations. I selected the pump pulse step size and maximum duration so as to be able to both sufficiently sample the Rabi oscillations and observe their decay while keeping the total number of data points, and hence total acquisition time, reasonably short. The acquisition time per sweep was typically a few minutes and it took about an hour to record the $10-15$ sweeps I averaged to obtain Rabi oscillations with a good signal-to-noise ratio [see Fig. 5.13(a)]. I began with a pump power sufficient to saturate the qubit, again as determined by pulsed probe spectroscopy, and increased or decreased it as needed to record faster or slower Rabi oscillations.

Figure 5.13(a) shows the excited state probability versus pump pulse duration and a fit to an exponentially damped sinusoid. The fit allowed me to extract the Rabi oscillation decay time $T' \approx 200\,\mathrm{ns}$ and Rabi frequency $\Omega_{R,0} = 20\,\mathrm{MHz}$. While the Rabi frequency was very repeatable, I observed a large variation in T' values, similar to the T_1 case, with variation greater that 50%.

The extracted Rabi frequency allows me to calibrate the π and $\pi/2$ pulse durations at a particular pump power for use in Ramsey fringes and spin echo experiments. The π

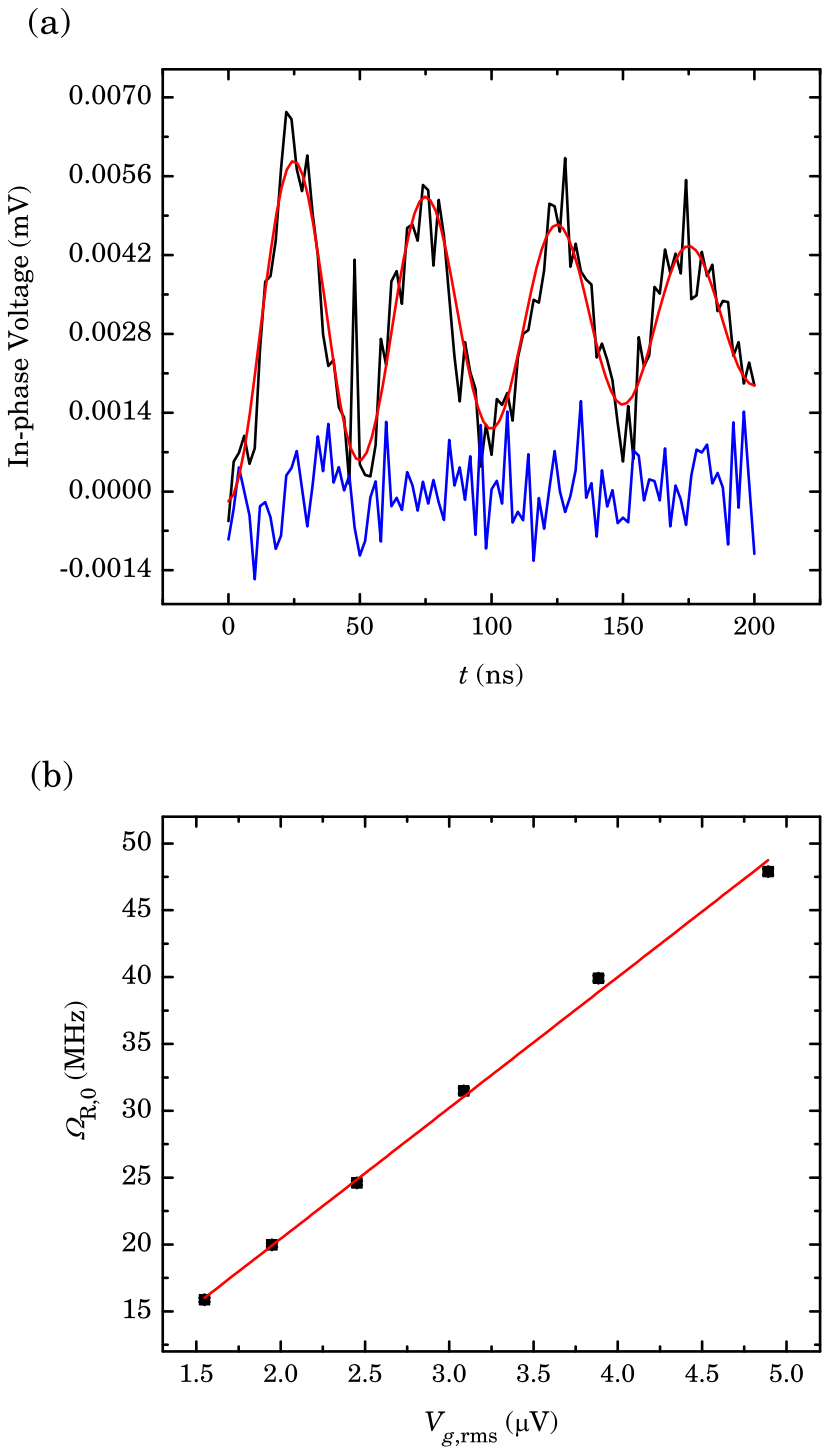

Figure 5.13: (a) Rabi oscillations (black) and the corresponding qubit ground state signal (blue) recorded with a pulsed probe readout. The data is fit to an exponentially damped sinusoid (red) to extract the Rabi oscillation decay time $T' \approx 200\,\mathrm{ns}$ and Rabi frequency $\Omega_{R,0} = 20\,\mathrm{MHz}$. (b) Rabi frequency versus rms ac gate voltage (at frequency f_{pump}) along with a linear fit (red).

pulse is given by half the Rabi period and the $\pi/2$ pulse by a quarter of the Rabi period. I repeated and fit Rabi oscillations at different pump powers and plotted the extracted Rabi frequency versus pump amplitude [see Fig. 5.13(b)]. A line gives an excellent fit to the data, confirming the linear scaling of the Rabi frequency with pump amplitude. Additionally, the slope (9.79 MHz/μV for Fig. 5.13(b)) may be used as a measure of the coupling of the qubit to the drive signal or, in general, to any perturbation that couples via the charge degree of freedom. I also attempted to record Rabi oscillations at the top spectral parabola using a weak continuous readout but obtained poor results due to degraded coherence and readout contrast and other anomalous effects.

6 Decoherence and Reproducibility Experiments

6.1 Overview of Results for Device 1

A significant fraction of my thesis work consisted of the dephasing studies of Device 1. That device was fabricated and its parameters were characterized by Z. Kim [59, 71]. A large part of the motivation for the design was the desire to construct a CPB coupled to a lumped-element resonator that would have an improved qubit lifetime by avoiding the multimode Purcell effect [67]. Unlike $\lambda/2$ and $\lambda/4$ resonators, which have many relatively close lying harmonics, the lumped element resonator design of Device 1 has a fundamental frequency of 5.45 GHz but no higher modes up to 28 GHz. The design proved successful, both due to the intended reason and fortuitous features.

The layout and fabrication process of Device 1 was nearly identical to that of Device 2 [see Ch. 4 and Sec. 6.1.1]. The lumped element resonator consisted of a parallel combination of an inductor with inductance $L \approx 2\,\mathrm{nH}$ and a capacitor with capacitance $C \approx 400\,\mathrm{fF}$ [see Fig. 6.1(a)]. Z. Kim extracted, and I later confirmed, a resonance frequency of $\omega_{res}/2\pi = 5.446\,\mathrm{GHz}$ with loaded quality factor $Q_L = 22{,}000$, internal quality factor $Q_i = 32{,}000$, and external quality factor $Q_e = 70{,}000$. The CPB consisted of a $150\,\mathrm{nm} \times 2.5\,\mu\mathrm{m}$ superconducting island connected through two parallel $150\,\mathrm{nm} \times 150\,\mathrm{nm}$ Josephson tunnel junctions to superconducting leads and the reservoir [see Fig. 6.2(a)]. The qubit had a charging energy of $E_c/h = 6.24\,\mathrm{GHz}$, a maximum Josephson energy of $E_J^{\mathrm{sum}}/h = 19\,\mathrm{GHz}$, a gate capacitance between the transmission line and island of $C_g = 4.5\,\mathrm{aF}$, and a qubit-resonator coupling strength of $g/2\pi = 5\,\mathrm{MHz}$.

When the qubit was tuned to $E_J/h \approx 4\,\mathrm{GHz}$ and biased at the sweet spot $n_g = 1$, the qubit lifetime was an astounding $T_1 \approx 200\,\mu\mathrm{s}$ [59], more than an order of magnitude longer than the best previously reported results [38]. We tuned the E_J over one octave in fre-

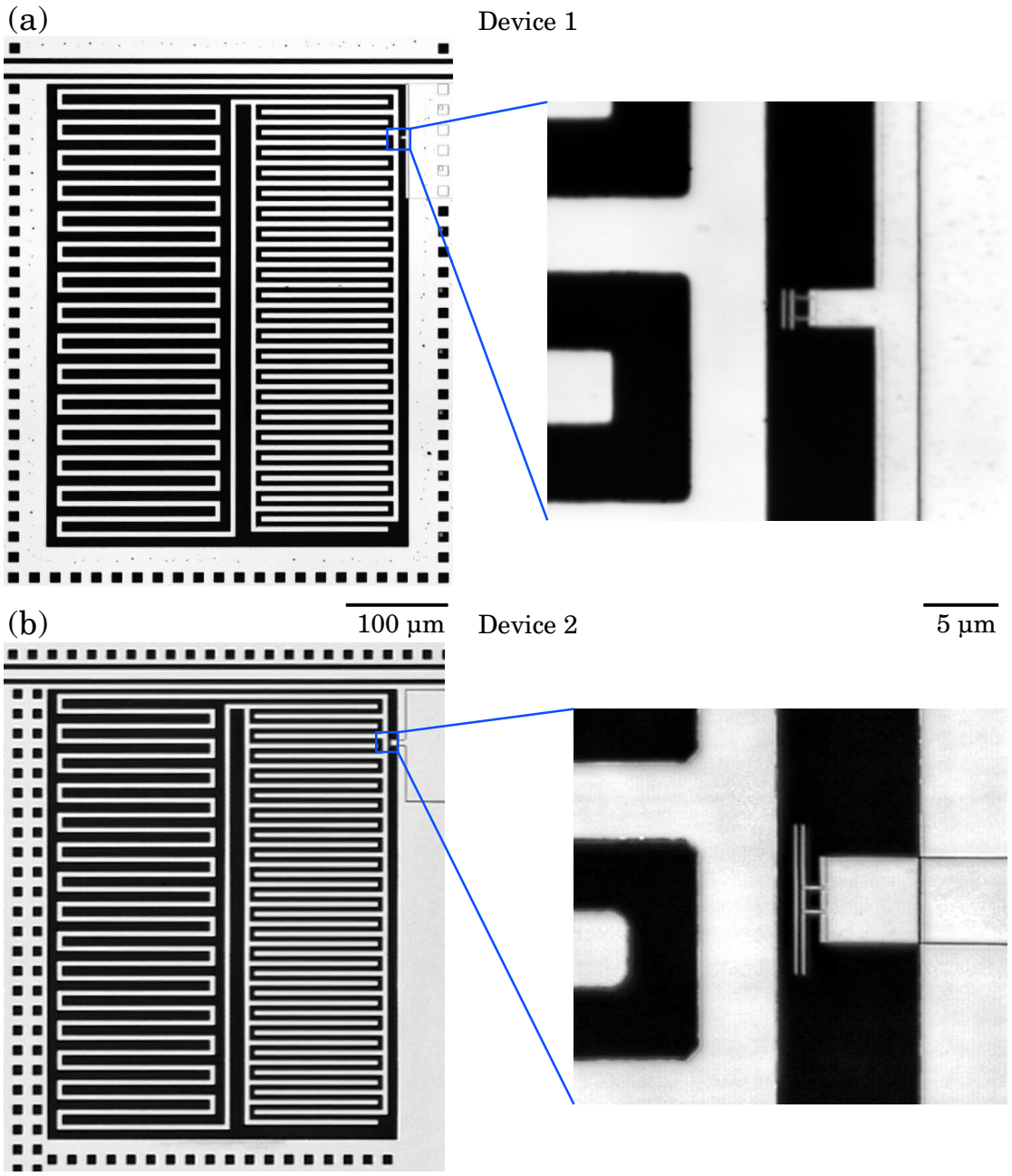

Figure 6.1: (a) Microscope image of the lumped element resonator and a zoom in of the area containing the CPB for Device 1. (b) Similar pair of images for Device 2. The resonator components are identified in Fig. 2.4 while Fig. 6.2 shows SEM images of the two CPBs.

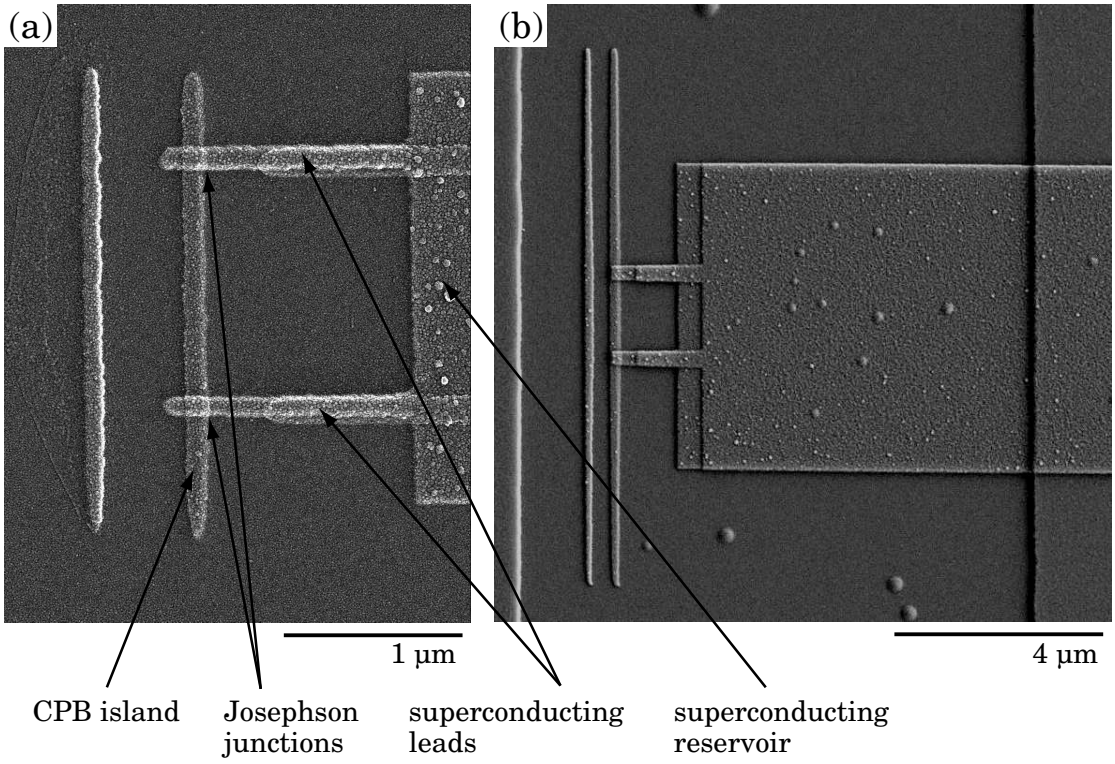

Figure 6.2: SEM images of the CPBs of (a) Device 1 and of (b) Device 2. The CPB island, Josephson junctions, superconducting leads, and ground are identified for Device 1 and are similarly located in Device 2. The longer CPB island and larger junction area of Device 2 are the two main design differences from Device 1. The stray parallel island is a signature of double-angle evaporation [see Sec. 4.1.4].

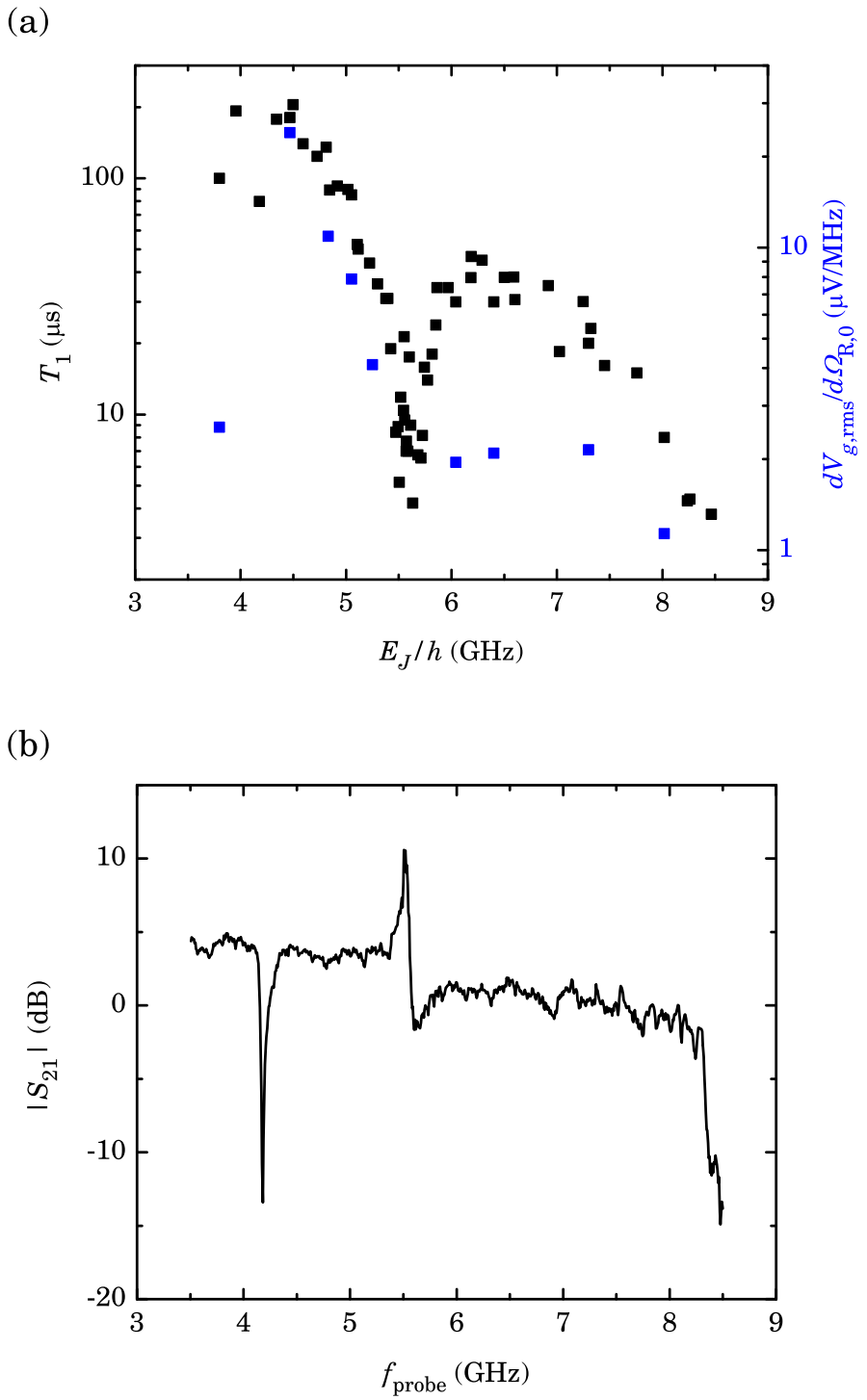

Figure 6.3: (a) Lifetime T_1 (black squares) and decoupling $dV_{g,\mathrm{rms}}/d\Omega_{R,0}$ (blue squares) data as a function of Josephson energy E_J/h of Device 1. The lifetime and decoupling are well correlated and follow a similar trend. Dips in the T_1 near $E_J/h = 4.18\,\mathrm{GHz}$ and $E_J/h = 5.44\,\mathrm{GHz}$ correspond to resonances in (b) the transmission amplitude $|S_{21}|$ of the lines. The resonator resonance dip at $\omega_{res}/2\pi = 5.446\,\mathrm{GHz}$ is too narrow to be resolved in this plot.

quency, between 3.8 – 8.5 GHz, and observed a largely monotonic decrease of the lifetime from the maximum near $E_J/h \approx 4\,\text{GHz}$ to a low of $T_1 \approx 10\,\mu\text{s}$ at $E_J/h \approx 8\,\text{GHz}$ [see Fig. 6.3(a)]. Several localized depressions of the qubit lifetime were present in this overall trend. Two of the dips were correlated to spurious resonances in the rf input and output lines as determined by the transmission amplitude $|S_{21}|$ [see Fig. 6.3(b)]. Specifically, the depression of T_1 near $E_J/h = 4.18\,\text{GHz}$ is likely due to the sample package while the depression around $E_J/h = 5.67\,\text{GHz}$ corresponds to a self-resonance of the cryogenic amplifier. Finally, the dip at $E_J/h = 5.44\,\text{GHz}$ is consistent with the Purcell effect [see Sec. 2.7].

A key result on Device 1 concerned the coupling between the qubit and the microwave drive. We found the coupling by determining the scaling of the Rabi frequency $\Omega_{R,0}$ with the microwave drive voltage $V_{g,\text{rms}}$ [see Sec. 4.3]. We observed a strong correlation between the qubit lifetime and the inverse of the coupling between the qubit and the transmission line. This suggested that the decoupling of the CPB from the transmission line was a key reason for obtaining the long relaxation time [see Fig. 6.3(a)] [59].

In addition to the lifetime measurements, preliminary Ramsey fringes data at $E_J/h \approx 6\,\text{GHz}$ yielded a decoherence time $T_2 = 70\,\text{ns}$. These coherence measurements allowed us to place bounds on the charge noise affecting the CPB. Assuming charge is the dominant noise source, the relaxation time suggests an upper bound on the spectral density of charge noise at $f = 4.5\,\text{GHz}$ of $S_q(f = 4.5\,\text{GHz}) \leq 10^{-18}\,e^2/\text{Hz}$. This value is approximately an order of magnitude smaller than that reported by Vion *et al.* [38]. Similarly, if we assume low frequency charge noise of the form $S_{q,1/f}(f) = A_q^2/f$, the dephasing time implies a bound of $S_q(f = 1\,\text{Hz}) \leq \left(9 \times 10^{-3}\right)^2 e^2/\text{Hz}$ which is roughly consistent with other measurements of $1/f$ charge noise [101, 43, 38, 81].

6.1.1 Follow-up Decoupling Experiment

Although it wasn't possible to alter the qubit-transmission line coupling of Device 1, it was possible to test the observed correlation between decreases in the lifetime T_1 and spurious resonances. The opportunity to perform such an experiment presented itself when we modified the grounds of the CPW launchers in the sample box. This change shifted the box resonance from 4.2 GHz to 3.5 GHz [see Fig. 6.4]. I remeasured the qubit-transmission line coupling $d\Omega_{R,0}/dV_{g,\text{rms}}$ at $E_J/h = 4.5\,\text{GHz}$ and found that it increased

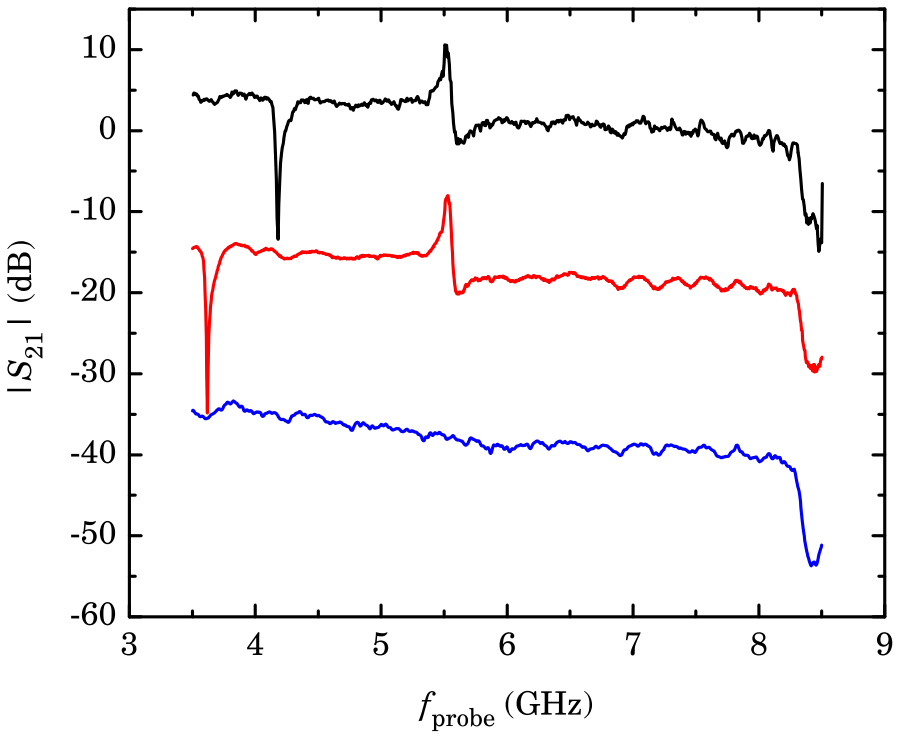

Figure 6.4: History of the system transmission amplitude $|S_{21}|$. The top curve (black) is the system transmission amplitude $|S_{21}|$ during the lifetime and coupling characterization of Device 1 carried out by Z. Kim [59, 71] [see Fig. 6.3(b)]. I recorded the middle curve (red) after modifying the grounds of the CPW launchers. This shifted the box resonance from 4.2 GHz to 3.5 GHz and was the situation during my dephasing measurements of Device 1. Afterward, we installed a different cryogenic amplifier and placed Device 2 in a different sample box. As seen in the bottom curve (blue), this removed both the box resonance and the self-resonance of the amplifier at 5.67 GHz. The curves have been offset by 20 dB for clarity.

from 0.13 MHz/μV before the change to 0.53 MHz/μV after. There was a corresponding decrease in the qubit relaxation time T_1 from 205 μs to 61 μs. While this is consistent with the previously observed correlation and indicates some degree of repeatability, at this point it's not clear if this is a general trend that may be utilized to improve qubit performance or a coincidence unique to this sample. Furthermore, it may be that the correlation between the qubit-transmission line coupling and excited state lifetime is not a general trend but valid only near transmission line resonances.

6.2 Dephasing of Device 1

Two questions naturally arose following Z. Kim's results on Device 1. While the relaxation time provides a measure of the high frequency noise affecting the qubit [see Sec. 3.3], the character of the noise at low frequencies was unclear. Low frequency noise is responsible for dephasing and it can be quantified by performing Ramsey fringes and spin echo experiments [see Sec. 3.4]. Additionally, it wasn't clear if we could reconcile the exceptionally low bound on the spectral density of high frequency charge noise with the more typical low frequency bound suggested by the preliminary Ramsey fringes. Second how reproducible was the long qubit lifetime? Specifically, would other devices following the same design display enhanced qubit lifetime and would the close relationship between the lifetime T_1 and the decoupling $dV_{g,\mathrm{rms}}/d\Omega_{R,0}$ persist?

My dephasing studies of Device 1 are discussed in this section while the reproducibility of the lifetime and decoupling results in Device 2 is addressed in Sec. 6.3.

6.2.1 Pulsed Probe Rabi Oscillations

Qubit decay and Rabi oscillation frequency aren't affected by dephasing from AC Stack effect. This allowed Z. Kim to employ the simpler and more convenient weak continuous readout in his work [59]. After I inherited the sample, I set up a pulsed probe readout in order to perform the dephasing characterization. Subsequently, with assistance from S. Novikov, I implemented and calibrated the pulse shaping setup necessary for more complex experiments such as state tomography.

The first experiment I performed with the new setup was to record pulsed probe Rabi oscillations at $E_J/h = 5.949$ GHz [see Fig. 6.5]. The plot shows clean oscillations of fre-

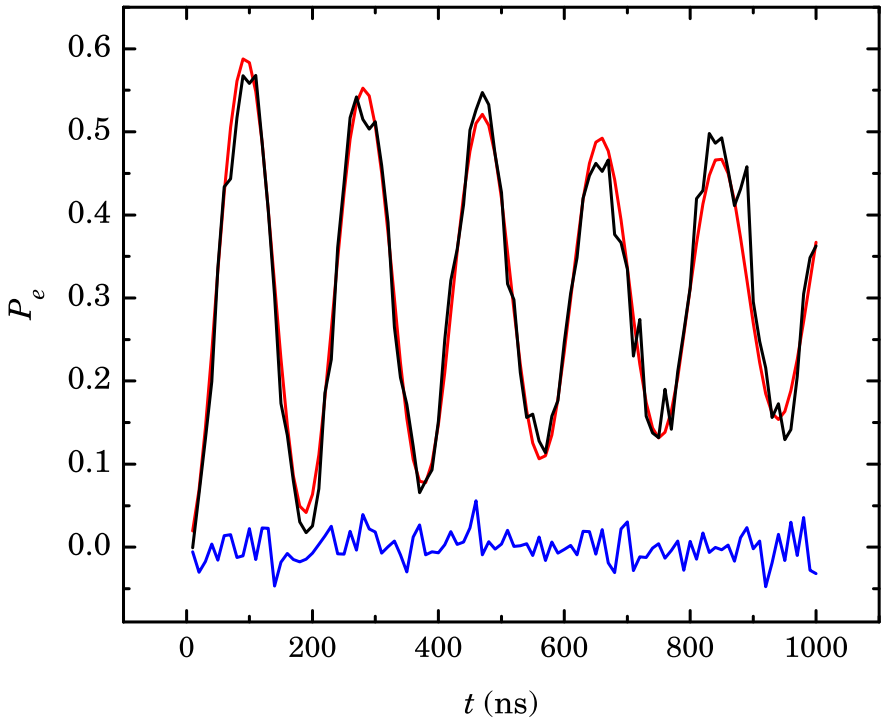

Figure 6.5: Rabi oscillations (black) and the corresponding qubit ground state signal (blue) at $E_J/h = 5.949\,\text{GHz}$ recorded with a pulsed probe readout for Device 1. The data is fit to an exponentially damped sinusoid (red) to extract the Rabi oscillation decay time $T' = 1.4\,\mu\text{s}$ and Rabi frequency $\Omega_{R,0} = 5.32\,\text{MHz}$. The signal was averaged $5000 - 10,000$ times and the ground state has a standard deviation of $\sigma_{P_e} = 0.0184$.

quency $\Omega_{R,0} = 5.32\,\text{MHz}$ with an exponentially decaying envelope of $T' = 1.4\,\mu\text{s}$, consistent with data acquired by Z. Kim [59], confirming that everything was functioning as expected. My data for Device 1, along with that collected by Z. Kim, had Rabi oscillation decay times T' in the range $1-2\,\mu\text{s}$. Although it's possible to perform detailed noise spectroscopy using Rabi oscillations [179], I didn't observe any consistent pattern in the Rabi oscillation decay times as a function of Rabi frequency.

6.2.2 State Tomography

Quantum state tomography is a process of reconstructing the quantum state of a qubit by making a complete set of measurements on the Hilbert space of the qubit. In addition to verifying the ability to prepare and manipulate pure states—a requirement of operating the CPB as a qubit [see Sec. 3.1]—it's also a rigorous test of the pulse shaping setup.

I performed a variant of state tomography by first preparing the qubit in a given state and then systematically rotating the state to cover the Bloch sphere. I examined the four states $|g\rangle$, $|e\rangle$, $(|g\rangle + |e\rangle)/\sqrt{2}$, and $(|g\rangle + i\,|e\rangle)/\sqrt{2}$. The ground state $|g\rangle$ was prepared by waiting sufficiently long for the qubit to relax. The excited state $|e\rangle$ was prepared by starting in $|g\rangle$ and then making a π rotation around the x-axis. The duration of the necessary pulse was extracted from previous measurements of Rabi oscillations. The two superposition states $(|g\rangle + |e\rangle)/\sqrt{2}$ and $(|g\rangle + i\,|e\rangle)/\sqrt{2}$ were prepared by starting from $|g\rangle$ and making $\pi/2$ rotations around the y-axis and x-axis, respectively. Immediately after the preparation pulse I applied resonant control pulses of varied phase and duration to drive Rabi oscillations. In the co-rotating frame, this is equivalent to rotating the prepared state around vectors on the equator. The resulting data was plotted as polar 2D color intensity plots [see Fig. 6.6]. Each pixel in each plot represents the average of $5000-10{,}000$ measurements of the excited state probability P_e.

I found it was easiest to develop an intuitive understanding of the data by considering the effects of rotations on a point on the Block sphere in the co-rotating sphere. When the qubit is prepared in one of the states that lie at the poles, namely $|g\rangle$ or $|e\rangle$, continuous rotation about any equatorial vector produces sinusoidal oscillation of the excited state probability P_e, i.e. Rabi oscillations. The ground and excited states differ by 180° in the phase of these oscillations. For states that lie on the equator, such as $(|g\rangle + |e\rangle)/\sqrt{2}$ or $(|g\rangle + i\,|e\rangle)/\sqrt{2}$, rotations about an orthogonal vector again result in sinusoidal oscillations

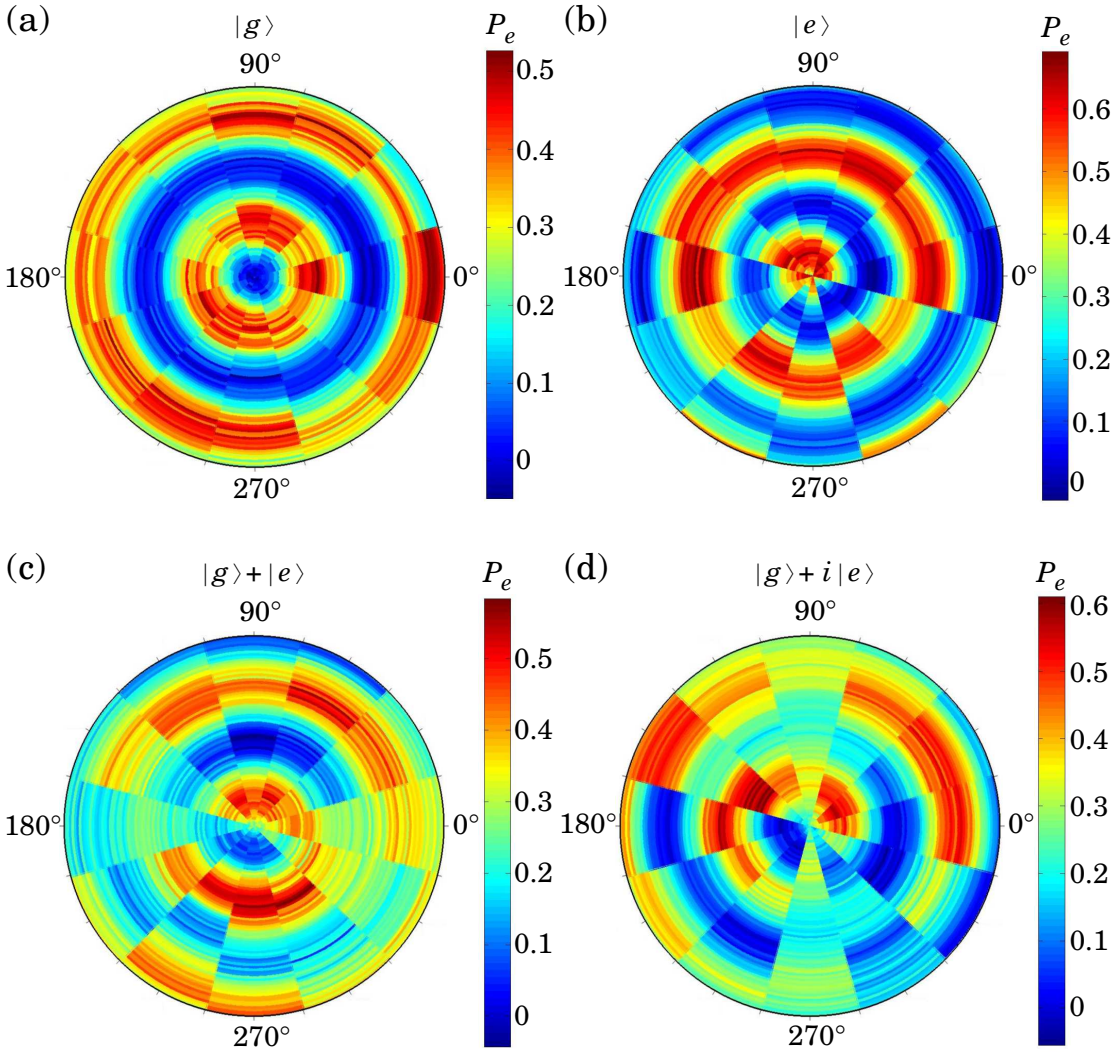

Figure 6.6: State tomography of Device 1. I prepared the qubit in one of the four states (a) $|g\rangle$, (b) $|e\rangle$, (c) $(|g\rangle + |e\rangle)/\sqrt{2}$, or (d) $(|g\rangle + i\,|e\rangle)/\sqrt{2}$ and then recorded Rabi oscillations with various pump tone phases. Each such oscillation is displayed along the corresponding radius on the polar 2D color intensity plot. The total pulse duration (the radius of the polar plot) is 150 ns with a step size of 2 ns.

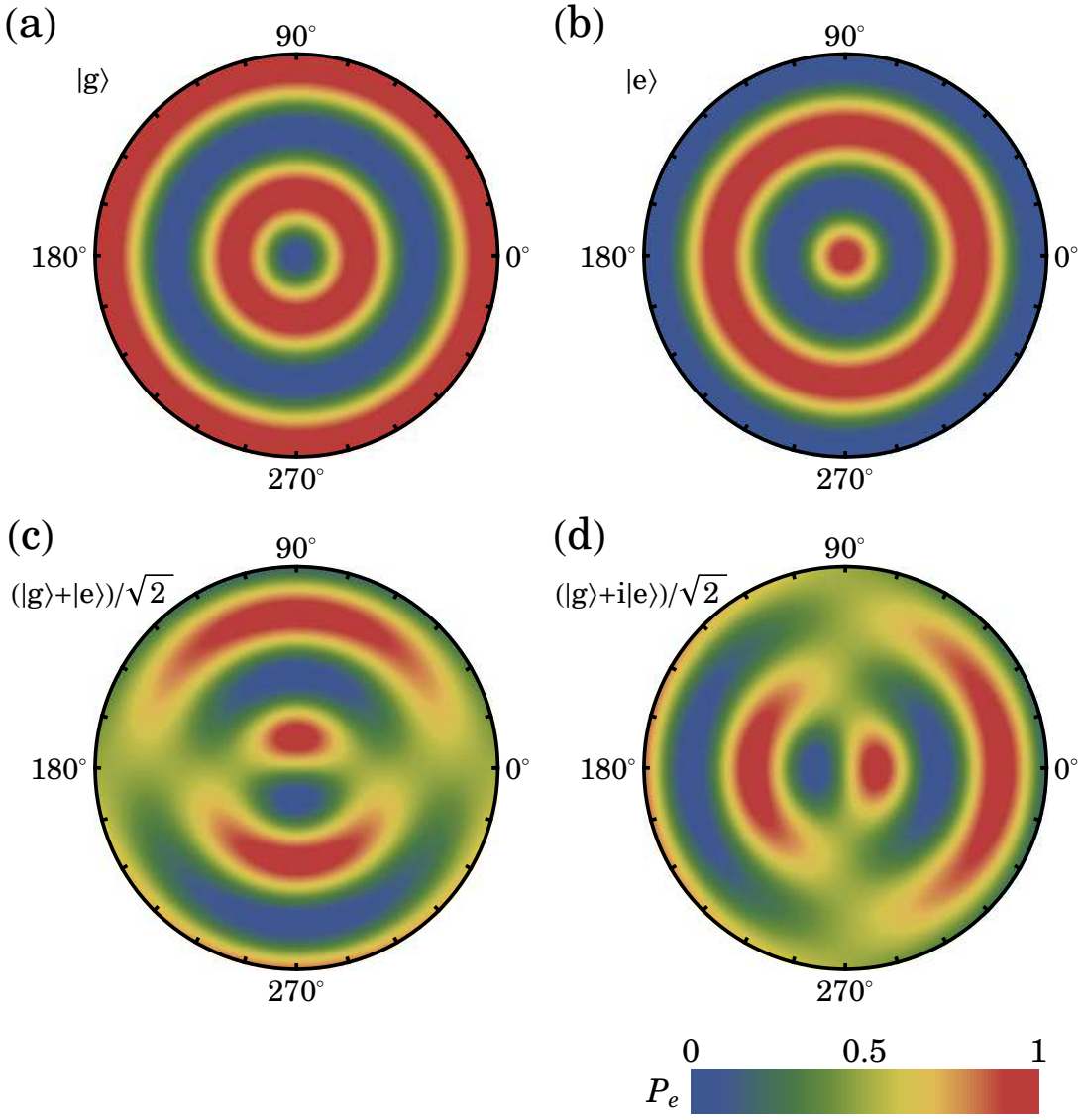

Figure 6.7: Theoretical state tomography plots. The qubit starts in one of the four states (a) $|g\rangle$, (b) $|e\rangle$, (c) $(|g\rangle + |e\rangle)/\sqrt{2}$, or (d) $(|g\rangle + i\,|e\rangle)/\sqrt{2}$ and then undergoes Rabi oscillations around various axes in the x-y plane in the co-rotating frame. Each such oscillation is displayed along the corresponding radius on the polar 2D color intensity plot. The Rabi frequency is the same as in Fig. 6.6 and the total Rabi oscillation duration (the radius of the polar plot) is 150 ns.

of the excited state probability P_e, while rotations about a parallel vector don't change the state. Rotations about any other vector result in oscillations with the same period but with the amplitude reduced by $\sin\varphi$ where φ is the angle between the state and rotation vectors. Consequently the states that lie on the x-axis and the y-axis produce the same color intensity plot, rotated by 90° relative to each other.

The state tomography data shown in Fig. 6.6 is in good qualitative agreement with theory [see Fig. 6.7], indicating that I can control the quantum state of the qubit and that the pulse shaping system is working as designed. The main deviations from ideal behavior—variations in readout contrast and Rabi frequency—are likely due to low frequency charge noise and slow E_J drift [see Sec. 5.3.1]. The constituent Rabi oscillations for each initial state took a day to acquire and, when combined in a single plot, the effects of charge noise and E_J drift are clear. I didn't attempt a quantitative analysis of the state tomography data as it was clear that small errors in state preparation or pulse shaping would be obscured by the drift. In principle, such analysis could be utilized to quantify state preparation or qubit gate fidelity and is currently being pursued on more stable qubit designs, such as the transmon, by other group members [165].

6.2.3 Ramsey Fringes

I expanded on the preliminary Ramsey fringes data for Device 1 [see Sec. 3.4.1] by recording Ramsey fringes at a series of detunings. At $n_g = 1$, the bare qubit transition frequency $E_J/h = 6.2586\,\text{GHz}$ was determined from pulsed probe spectroscopy. The duration of a $\pi/2$ pulse, 28.4 ns with 39 dB pump attenuation bypassing the pulse shaping mixers, was extracted from fits to pulsed probe Rabi oscillations. I used the standard Ramsey pump pulse sequence [see Sec. 3.4.1]. I first pulsed the probe to record the ground state phase, then I applied a detuned $\pi/2$ pulse, waited a delay time t, applied a second, in-phase $\pi/2$ pulse, and finally I pulsed the probe again and recorded the phase of the transmitted signal. I repeated the sequence with the delay time t stepped through a range of values, typically up to several hundred nanoseconds with a step size of a few nanoseconds. This process resulted in a single Ramsey fringes curve at a given detuning. I carried out these measurements for detunings of ±15 MHz, ±10 MHz, and ±5 MHz.

From a least squares fit of an exponentially damped sinusoid to the excited state probability P_e versus delay time t, I extracted the Ramsey frequency $\Delta\nu_\text{R}$ and Ramsey decay

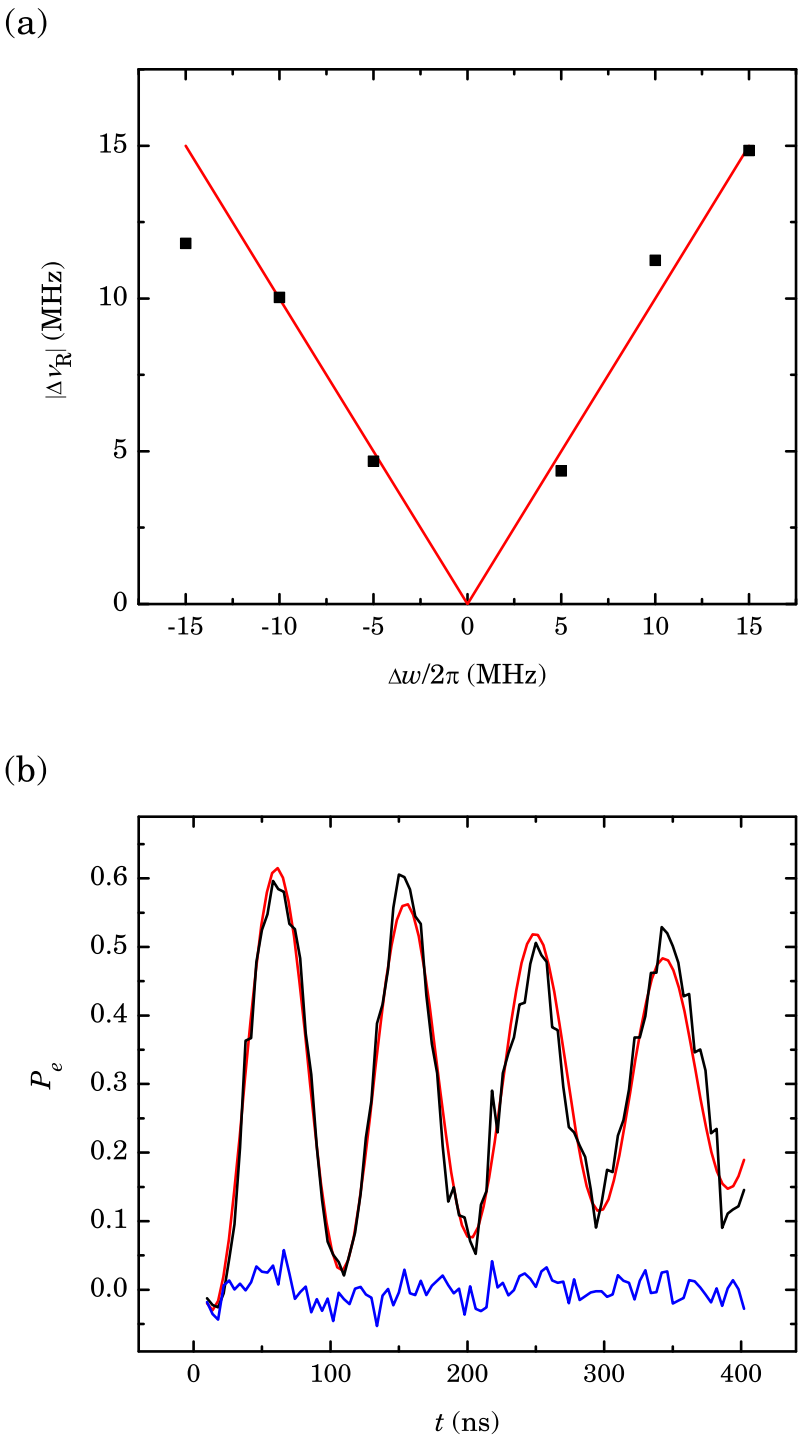

Figure 6.8: (a) Ramsey frequency $\Delta\nu_R$ data (black squares) and theory (red) versus the pump tone detuning $\Delta\omega = \omega_{CPB} - \omega_{\mu w}$ in Device 1. (b) Ramsey fringes (black) and the corresponding qubit ground state signal (blue) recorded with a pulsed probe readout. The data is fit to an exponentially damped sinusoid (red) to extract the decoherence time $T_2 = 508\,\text{ns}$ and Ramsey frequency $\Delta\nu_R = 10.61\,\text{MHz}$.

time T_2 of each curve. The decoherence times T_2 were all in the $40-75\,\mathrm{ns}$ range, consistent with the preliminary data. I also plotted the extracted Ramsey frequency $\Delta\nu_\mathrm{R}$ versus the pump tone detuning $\Delta\omega = \omega_{CPB} - \omega_{\mu w}$ [see Fig. 6.8(a)]. Although theoretically $\Delta\nu_\mathrm{R} = \Delta\omega/2\pi$, there is both an x-offset and deviations from linearity present in the data. The offset is probably due to an error in the initial E_J estimate while the nonlinearity is probably due to a small E_J drift during the several hours it took took acquire the Ramsey fringes.

Soon after I began my dephasing characterization of Device 1, it developed a problem. Due to strong, incoherent interaction with a TLS, the two tone spectrum appeared twinned and other measurements were difficult or impossible to perform. Thermal cycling to $4.2\,\mathrm{K}$ under various conditions didn't eliminate the problem. I annealed the sample by warming up to room temperature and also took that opportunity to add additional low pass filters to the dc bias line and bandpass filters to the rf output line. This resolved the issue and I resumed taking Ramsey fringes. While this addition didn't reduce charge drift or offset jumps, it did seem to improve performance when the qubit was stable. The subsequent data set had a decoherence time $T_2 = 171\,\mathrm{ns}$ at $E_J/h = 5.956\,\mathrm{GHz}$ and a detuning of $-10\,\mathrm{MHz}$. After I modified the experimental setup to facilitate and improve gate voltage tuning, I recorded another Ramsey fringes data set at the same parameters with a decoherence time $T_2 = 508\,\mathrm{ns}$ [see Fig. 6.8(b)]. Unfortunately, these clean data sets were interspersed with periods of heavy charge noise and I wasn't able to record Ramsey fringes that were better than those shown in Fig. 6.8(b).

The coherence time T_2 is given by the relaxation time T_1 and the pure dephasing time T_φ as

$$1/T_2 = 1/2T_1 + 1/T_\varphi. \tag{3.14}$$

At $E_J/h = 5.956\,\mathrm{GHz}$, the lifetime of Device 1 was $T_1 = 34.5\,\mu\mathrm{s}$. Since $T_2 \ll 2T_1$, the coherence time T_2 was limited by the pure dephasing time T_φ [see Sec. 3.2]. This allowed me to discard the T_1 contribution to the coherence time and approximate the pure dephasing time as $T_\varphi \approx T_2 = 508\,\mathrm{ns}$.

Knowing the coherence time T_2 allows me to place a bound on the low frequency charge noise $S_q(f = 1\,\mathrm{Hz})$ affecting the qubit if I make an assumption about the shape of the noise spectrum. It's typically found that $1/f$ charge noise of the form $S_{q,1/f}(f) \approx A_q^2/f$ affects

these types of devices [101, 112, 43, 38, 81]. This reduces the problem from one with an arbitrary function $S_q(f)$ to one with a single parameter A_q I can place bounds on. Furthermore, I need to assume that charge noise is the dominant noise source, i.e. the contributions of flux or critical current noise to dephasing are negligible. I used the sweet spot charge sensitivity $D_{n_g 2,z} = 8E_c/E_J$, whose value is determined by two tone spectroscopy and ensemble measurement time $\omega_{\text{avg}}/2\pi \approx 25\,\text{Hz}$ in Eq. 3.54, which describes dephasing due to quadratically coupled wideband $1/f$ noise, and obtained

$$\left|f_{z,\text{Ram}}(T_2)\right| = 1/e = \left|\exp\left[-\left(\frac{4E_c}{E_J}\frac{A_q^2}{\pi}T_2 \ln\left(\omega_{\text{avg}}T_2\right)\right)^2\right]\right|. \tag{6.1}$$

I solved for A_q and extracted a bound on the noise amplitude of $S_q(f = 1\,\text{Hz}) \leq \left(3 \times 10^{-3}\right)^2 e^2/\text{Hz}$. This value is similar to that reported for similar charge qubits [81, 43, 38, 101] and would be only weakly affected if the $1/f$ charge noise has a high frequency cutoff ω_c.

My reasons for characterizing the dephasing of Device 1 at $E_J/h \approx 6\,\text{GHz}$ were purely pragmatic. The relaxation time T_1 at that flux bias is a respectable $\approx 30\,\mu\text{s}$, as opposed to at Josephson energies $E_J/h > 7\,\text{GHz}$ where it falls close to $10\,\mu\text{s}$. I found that the qubit was simpler to operate and had less gate charge offsets and drift for $E_J/\hbar > \omega_{res}$ as compared to operating with $E_J/\hbar < \omega_{res}$. Although it would have been interesting to characterize the dephasing at more operating points, I wasn't able to do so. Additionally, I didn't observe any large variations of the spectral width in the range $E_J/h = 3.8 - 8.5\,\text{GHz}$ which would have implied corresponding changes in the low frequency charge noise. Finally, the most interesting operating point, the double sweet spot at $n_g = 1$ and $E_J/h = E_J^{\text{sum}}/h = 19\,\text{GHz}$ wasn't accessible with my setup.

6.2.4 Spin Echo

A spin echo experiment is a natural follow up to the Ramsey fringes experiment as it offers additional information about the spectral density of the noise [see Sec. 3.4.2]. I recorded spin echoes at $n_g = 1$, a bare qubit transition frequency of $E_J/h = 6.059\,\text{GHz}$, a $\pi/2$ pulse duration of 24 ns, and a π pulse duration of 48 ns with 4 dB pump attenuation through the pulse shaping mixers. As with the Ramsey fringes, the parameters were calibrated with pulsed probe spectroscopy and Rabi oscillations. After recording the ground state phase with a probe pulse, I applied a $\pi/2$ pulse, waited a delay time $t/2$, applied a π

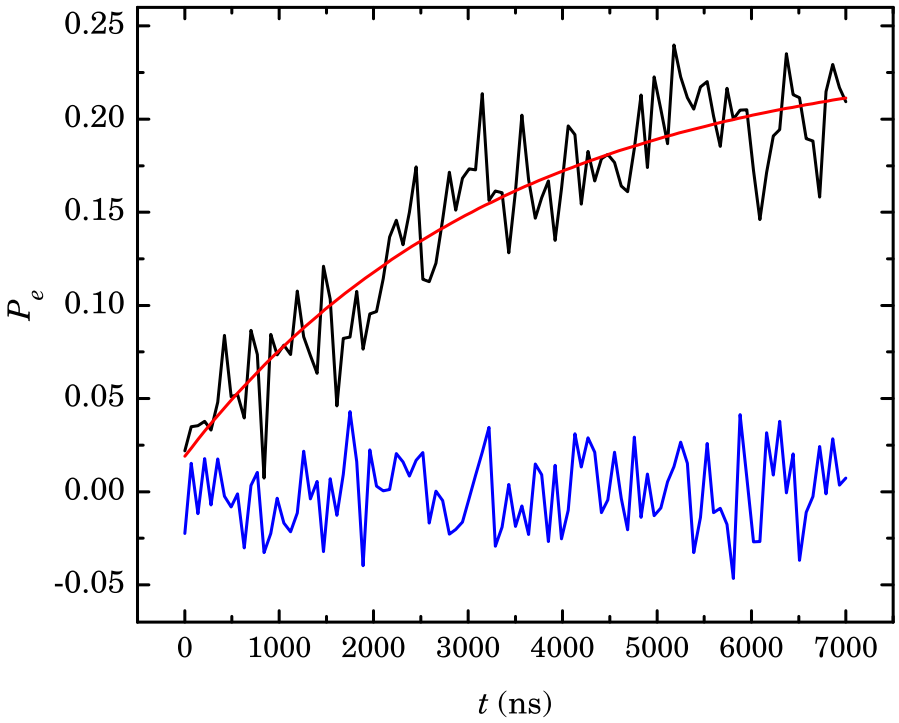

Figure 6.9: Spin echo (black) and the corresponding qubit ground state signal (blue) recorded with a pulsed probe readout. The data is fit to an exponential decay (red) to extract the spin echo decay time $T_{\text{echo}} = 3340\,\text{ns}$.

Table 6.1: Summary of the decoherence times and charge noise bounds for Devices 1 and 2.

device	Device 1	Device 2
decoherence		
T_1	$30-200\,\mu$s	$4-30\,\mu$s
T_2	$200-500$ ns	$\gtrapprox 60$ ns
T_2^*	—	≈ 60 ns
T_φ	$200-500$ ns	$\gtrapprox 60$ ns
T_{echo}	$2.4-3.3\,\mu$s	—
T'	$1-2\,\mu$s	$0.2-1.8\,\mu$s
noise bounds		
$S_q(f=4.5\,\text{GHz})$	$\leq 10^{-18}\,e^2/\text{Hz}$	$\leq 10^{-17}\,e^2/\text{Hz}$
$S_q(f=1\,\text{Hz})$	$\leq \left(3\times10^{-3}\right)^2\,e^2/\text{Hz}$	$\leq \left(1\times10^{-2}\right)^2\,e^2/\text{Hz}$

pulse 90° out of phase with the first, waited a second delay time $t/2$, applied the last qubit $\pi/2$ pulse 180° out of phase with the first, and then recorded the excited state probability with a probe pulse. I repeated this for a range of delay times t up to several microseconds to obtain the spin echo decay curve [see Fig. 6.9]. This is a slightly modified spin echo sequence with the last $\pi/2$ pulse out of phase, rather than in phase, with the first as I found it easier to collect data if the qubit ended in the ground, rather than the excited state, at the end of the pulse sequence.

I extracted spin echo decay times T_{echo} in the $2.4-3.3\,\mu$s range by fitting the excited state probability P_e versus delay time t to an exponential decay [see Fig. 6.9]. Similar to the Ramsey fringes decay time T_2, the spin echo decay time in Device 1 satisfied $T_{\text{echo}} \ll 2T_1$ and hence wasn't significantly limited by relaxation. The fact that $T_{\text{echo}} \gg T_2$ is consistent with a noise spectral density that falls with frequency, i.e. the presence of excess low frequency charge noise. The exact magnitude of the improvement contains additional information about the noise spectrum. The coherence enhancement ratio expected for wideband $1/f$ noise is $T_{\text{echo}}/T_2 \approx 4.5$ [see Sec. 3.4.2]. Based on the best spin echo and Ramsey fringe decay times, I observed an enhancement of $T_{\text{echo}}/T_2 \approx 6$. Assuming that the noise spectrum affecting the qubit is $1/f$ with a soft cutoff and employing the corresponding spin echo decay function [see Eq. 3.62], I find a high frequency noise cutoff of $\omega_c/2\pi \approx 0.2\,$MHz. For comparison, Ithier *et al.* [22] observed a cutoff at $\omega_c/2\pi \approx 0.4\,$MHz in a quantronium, a qubit design derived from the CPB. If I extrapolate the $1/f$ charge noise as determined by Ramsey fringes alone to 4.5 GHz, the result

is $S_q(f = 4.5\,\text{GHz}) \leq 2 \times 10^{-15}\, e^2/\text{Hz}$. This bound is three orders of magnitude larger than that extracted from the T_1 data [see Sec. 6.1]. Although this doesn't contain any information about the location of a high frequency noise cutoff, it's consistent with one. A possible follow up experiment to expand on the noise spectrum analysis I have performed with spin echo is to use multi-pulse dynamical decoupling schemes to extract the full noise spectrum [179, 180].

Table 6.1 contains a summary of the coherence times and charge noise bounds for Device 1.

6.2.5 Noise Bounds Considerations

There are several topics about the noise bounds that are worth discussing. First, I also considered an alternative analysis that assumed flux, not charge, was the dominant noise source responsible for dephasing in the qubit. If I assume $1/f$ flux noise of the form $S_\Phi(f) = A_\Phi^2/f$ is linearly coupled to the CPB and use Eq. 3.50, I obtain a bound on the noise amplitude of $S_\Phi(f = 1\,\text{Hz}) \leq \left(5 \times 10^{-6}\right)^2 \Phi_0^2/\text{Hz}$. This value is larger, but not unreasonably so, than the typical value of $S_\Phi(f = 1\,\text{Hz}) \lessapprox \left(1 \times 10^{-6}\right)^2 \Phi_0^2/\text{Hz}$ reported for similar Josephson devices [179, 104, 103, 105]. However, since this analysis required the incorrect assumption that charge noise was negligible, it's just a bound and can't provide a good estimate of the flux noise amplitude. On the other hand, it does imply that if future qubit designs are able to reduce either the charge noise amplitude or their sensitivity to it by about an order of magnitude, then flux noise could become a significant constraint on coherence times if the device isn't biased at the double sweet spot.

A more general question is the soundness of using the best recorded coherence times to place bounds on the noise. I believe it's the correct approach provided it's understood that the noise itself varied. Unless I have reason to believe a particular trace or decay curve is a spurious outlier, each data set corresponds to a valid observation of the physical system. Consequently each data set may be used to extract a bound on the noise and by using the best coherence time, I'm simply selecting the smallest upper bound for the noise.

I can also speculate as to why I observed such a large range of decoherence times. During my dephasing characterization experiments, I set the gate bias $n_g = 1$. However, since the gate control isn't perfect, the actual operating point may have slightly deviated from the sweet spot, either due to my inability to exactly locate it or from small drifts

and offsets during the data acquisition. To quantify the effect of such a control error, I calculated the Ramsey fringes decay time T_2 at $n_g = 1+\varepsilon$, including both the linear and quadratic coupling terms and assuming a typical spectral density of charge noise. I found that the Ramsey fringes decay time T_2 is reduced by half in a range $\varepsilon \approx \pm 0.007$ around $n_g = 1$ and another half in a range $\varepsilon \approx \pm 0.016$ around $n_g = 1$. For comparison, a reasonable estimate of my resolution when locating and setting the gate bias voltage is $5-10\,\mathrm{mV}$ which corresponds to gate bias resolution of $\Delta n_g = 0.006-0.012$. Consequently I could set the operating point within the sweet spot but not necessarily at the exact optimal point. This, combined with charge offsets and drift, could explain a factor of 2 to 4 variation in the decoherence times.

6.3 Reproducibility of the Lifetime and Decoupling Results

Soon after the completion of the spin echo experiment for Device 1, a strongly coupled TLS resurfaced. This time, thermal cycling to 4.2 K or annealing at room temperature were to no avail and I decided to move on to a new sample. B. Suri and I fabricated, cooled down, and tested several qubits. The first few of these were either non-functional or behaved very anomalously and were discarded. Eventually I found a working sample and this became Device 2. We mounted Device 2 in a different sample box and also replaced the cryogenic amplifier. These changes removed all the major spurious resonances in our setup [see Fig. 6.4(c)]. The main experimental goal for this device was to test the reproducibility of the lifetime and decoupling results observed in Device 1.

6.3.1 Design Changes for Device 2

While Device 2 was intended to examine the reproducibility of the results of Device 1, it wasn't an identical copy as a few small changes were made to the design. The resonator used for Device 2 had slightly stronger coupling to the transmission line, as evident in the reduced external quality factor of $Q_{e,\mathrm{Dev2}} = 47{,}000$ versus $Q_{e,\mathrm{Dev1}} = 70{,}000$ [see Fig. 6.1(b)]. This design change was made to decrease the ring-up time of the resonator and consequently reduce the impact of charge noise by reducing the data acquisition time [see Sec. 5.3.1]. Device 2 also had a much higher internal quality factor, $Q_{i,\mathrm{Dev2}} = 147{,}000$ versus $Q_{i,\mathrm{Dev1}} = 32{,}000$, but this discrepancy was due to uncontrolled variation during

fabrication.

The CPB in Device 2 also had several small design changes. The Josephson junction dimensions were increased from 150 nm × 150 nm in Device 1 to 350 nm × 150 nm in Device 2 [see Fig. 6.2(b)]. This increased the area by a factor of approximately ≈ 2, resulting in a larger junction capacitance C_j and hence a smaller charging energy $E_c = e^2/2\left(C_j + C_g\right)$. The aim was to further reduce sensitivity to charge noise [see Sec. 3.4]. In my experience fabrication of larger area junctions is more reliable but this most likely was a marginal benefit because it also leads to more TLS's. Changing the charging energy E_c also necessitated making some other changes. The qubit-resonator coupling strength scales as $g \propto C_g/C_\Sigma \propto C_g E_c$ [see Sec. 2.5]. To compensate for the reduced E_c and increase the coupling g to facilitate readout, the superconducting island was made longer, 150 nm × 10 μm in Device 2 versus 150 nm × 2.5 μm in Device 1. The CPB loop area remained the same. Finally, Device 2 had a lower maximum Josephson energy $E^{\text{sum}}_{J,\text{Dev2}}/h = 7.33\,\text{GHz}$. This allowed operation at the double sweep spot at reduced gate voltage $n_g = 1$ and external flux bias $\Phi = 0$. This was partly fortuitous as there were large variations in the fabricated Josephson energy—even after all the precautions and room temperature screenings [see Sec. 4.1.4]. It's also worth noting that the maximum Josephson energy $E^{\text{sum}}_{J,\text{Dev1}}/h = 19\,\text{GHz}$ of Device 1 was not intended to be that high.

6.3.2 T_1 and Rabi Coupling in Device 2

After carrying out preliminary characterization of Device 2 [see Ch. 5], I proceeded to measure the lifetime T_1 and the decoupling $dV_{g,\text{rms}}/d\Omega_{R,0}$ at various transition frequencies $\omega_{CPB}/2\pi$ in the range 4.0 – 7.3 GHz. The specifics of how I tuned the Josephson energy E_J are discussed in Sec. 5.2.2, the relaxation time T_1 measurement procedure is discussed in Sec. 5.4.1, and the extraction of Rabi coupling $d\Omega_{R,0}/dV_{g,\text{rms}}$ is discussed in Sec. 5.4.3. Due to the multiple spectral parabolas in Device 2, it was ambiguous at first as to which parabola should be used to measure the lifetime and the decoupling. I soon found that I was able to record excited state decay and Rabi oscillations with a weak continuous readout for all the parabolas and that there was no apparent discrepancy between the relaxation time T_1 measurements at the different parabolas. This is puzzling as the lifetime T_1 should vary with state composition in a composite system. A possible explanation is that the TLS lifetime is the same order of magnitude as the CPB lifetime

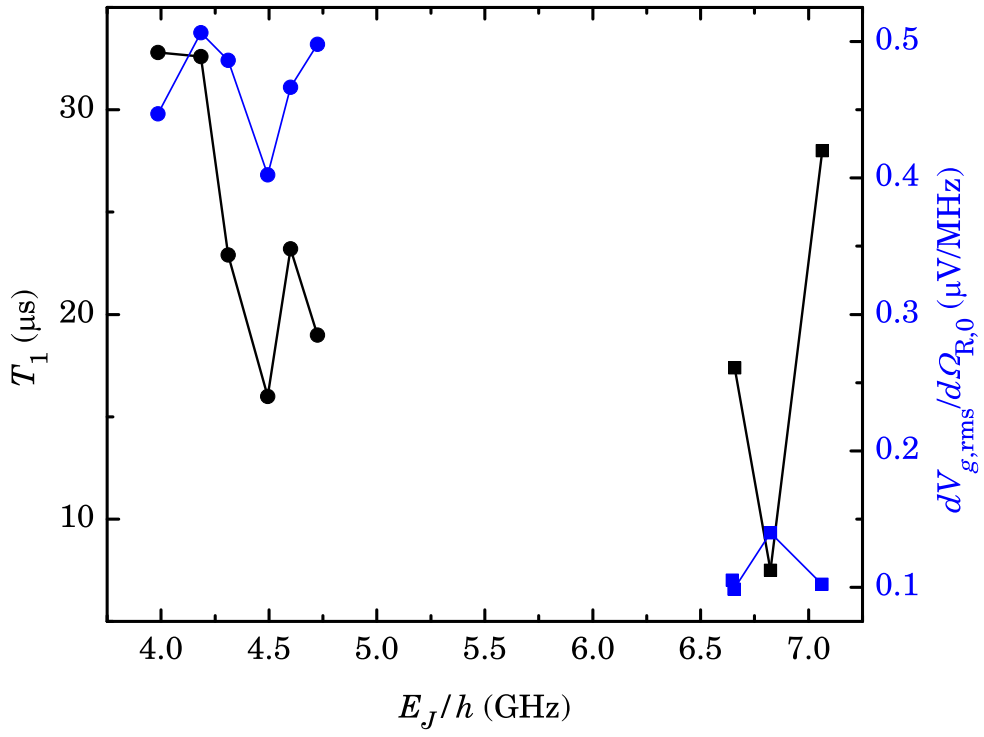

Figure 6.10: Summary of the measured lifetime T_1 (black circles and squares) and decoupling $dV_{g,\mathrm{rms}}/d\Omega_{R,0}$ (blue circles and squares) as a function of Josephson energy E_J/h for Device 2. For $E_J/h < \omega_{res}/2\pi = 5.472\,\mathrm{GHz}$ the measurements were made on the lowest lying parabola (circles) while for $E_J/\hbar > \omega_{res}$ the third highest parabola (squares) was measured. The lifetime and decoupling are only roughly correlated.

and the difference in T_1 between the parabolas was hidden by the large variation in my T_1 measurements [see Sec 5.4.1]. For consistency I decided to use parabolas for which the pulsed probe readout was functional. For qubit transition frequencies below the resonator $E_J/\hbar < \omega_{res}$ this was the lowest lying parabola [see Fig. 8.6] while above the resonator $E_J/\hbar > \omega_{res}$ it was the third highest [see Fig. 8.1].

The aggregate excited state lifetime T_1 and decoupling $dV_{g,\mathrm{rms}}/d\Omega_{R,0}$ data is plotted versus transition frequency in Fig. 6.10. The gap in the data between $5.0-6.5\,\mathrm{GHz}$ corresponds to a region where none of the parabolas were visible [see Figs. 8.3 and 8.4]. I believe this loss of visibility was due to a charged fluctuator that was activated in this frequency range [see Sec. 8.2.1]. Although the data is sparse, based on the overall trend I conclude that the decoupling $dV_{g,\mathrm{rms}}/d\Omega_{R,0}$ is generally correlated with the lifetime T_1. Also, the qualitative behavior of Device 2 resembles that of Device 1. In both samples the excited state lifetime T_1 [see Fig. 6.11(a)] and the decoupling $dV_{g,\mathrm{rms}}/d\Omega_{R,0}$ [see Fig.

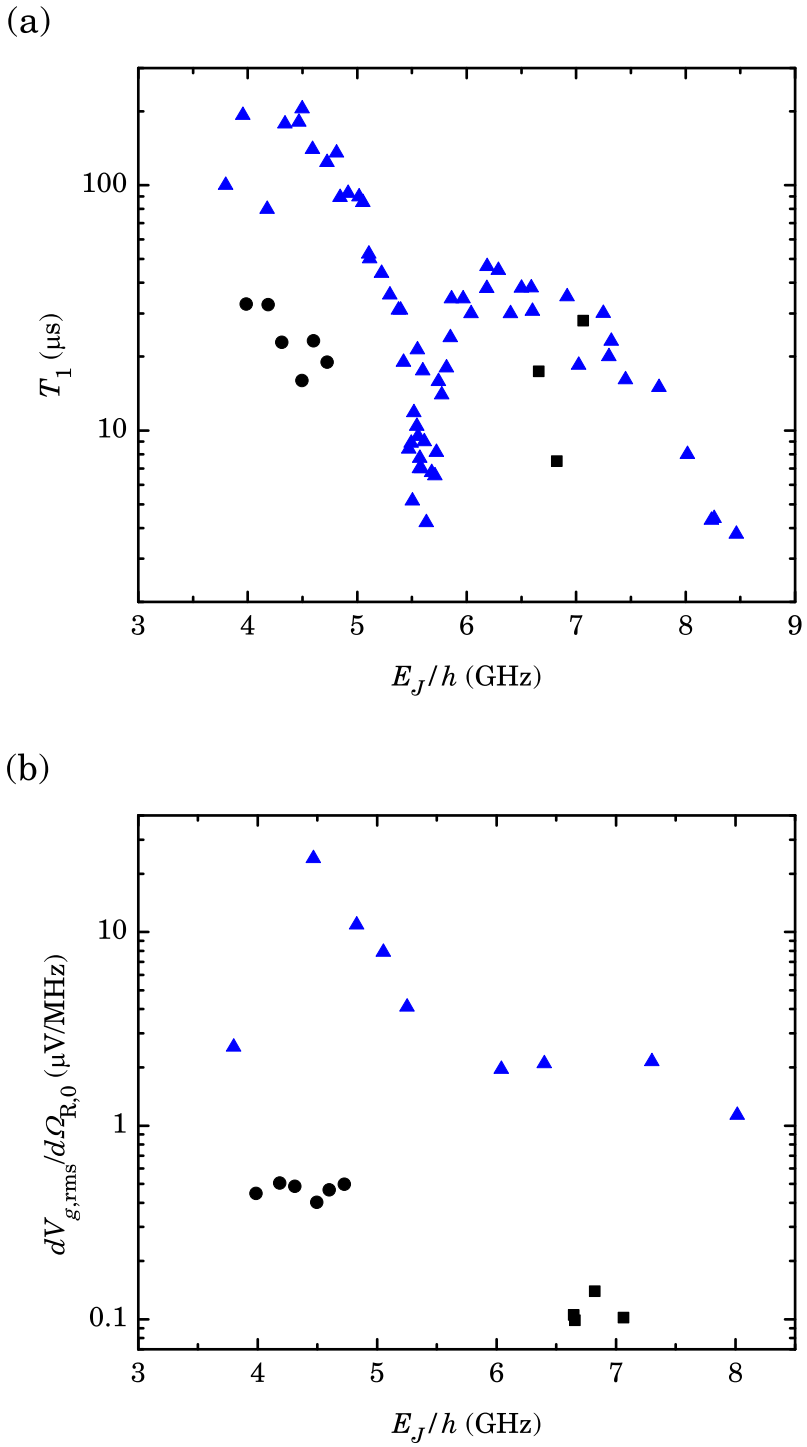

Figure 6.11: Comparison of the (a) lifetime and (b) decoupling between Devices 1 and 2. Black circles are data for Device 2 measured on the lowest parabola when tuned below the resonator. Black squares were measured on the third highest parabola when tuned above the resonator in Device 2. Blue triangles are data from Device 1. In both plots the data follows similar trends as a function of the Josephson energy E_J/h, but Device 1 typically has an order of magnitude longer T_1 and $dV_{g,\mathrm{rms}}/d\Omega_{R,0}$ that Device 2 has.

6.11(b)] drop when the qubit is tuned above the resonator $E_J/\hbar > \omega_{res}$. Although below the resonator $E_J/\hbar < \omega_{res}$ the relaxation times of Device 2 are about a factor of 5 shorter than those of Device 1, above the resonator $E_J/\hbar > \omega_{res}$ they are nearly identical [see Fig. 6.11(a)]. The best performance for Device 2, $T_1 \approx 30\,\mu$s, is not as impressive as that of Device 1 but is nevertheless quite long, suggesting some level of reproducibility of the lifetime results. Note also that Device 2 was about $\approx 10-20$ times more strongly coupled than Device 1 and this is consistent with the shorter T_1 in Device 2 being due to coupling to the transmission line.

Differences in the design and fabrication may explain some of the measured differences between the two qubits. The larger coupling of the CPB to the transmission line in Device 2 may be partly due to the stronger coupling—reflected in the smaller Q_e—between its resonator and the transmission line. The sensitivity to voltage noise of a CPB is proportional to $E_c C_g$ [see Eq. 3.26]. While Device 2 had a smaller E_c ($E_{c,\mathrm{Dev1}} = 6.24\,$GHz versus $E_{c,\mathrm{Dev2}} = 4.3\,$GHz), the CPB island was longer leading to a larger C_g ($C_{g,\mathrm{Dev1}} = 4.5\,$aF versus $C_{g,\mathrm{Dev2}} = 19.1\,$aF) and a net increase in the sensitivity. Relaxation due to strong interactions with charged defects [61] may be another reason for the lower excited state lifetime T_1 in Device 2 since the larger area of the Josephson junctions would lead on average to a larger number of defects. Finally, Device 1 had no conspicuous splittings in the transition spectrum while Device 2 had visible splittings and an anomalous multi-parabola spectrum [see Sec. 8.1.1].

Finally, from the lifetime T_1 I can place a bound on the high frequency spectral density of charge noise affecting Device 2. Assuming relaxation due to charge noise is the dominant decay mechanism, combining Eqs. 3.24 and 3.27, I find that the spectral density of charge noise S_q can be written as [181, 82]

$$S_q(\omega_{CPB}/2\pi) = \left(\frac{e\hbar}{2E_c}\right)^2 \frac{1}{T_1}. \tag{6.2}$$

The qubit lifetime at $E_J/h = 4.5\,$GHz is $T_1 \approx 16\,\mu$s and this places a bound on the charge noise of $S_q(f = 4.5\,\mathrm{GHz}) \leq 10^{-17}\,e^2/\mathrm{Hz}$. This value is an order of magnitude greater than the bound $S_q(f = 4.5\,\mathrm{GHz}) \leq 10^{-18}\,e^2/\mathrm{Hz}$ obtained for Device 1 but is close to that reported for other charge qubits [38]. Alternatively, if I assume that qubit relaxation is due to dielectric loss in the amorphous AlO_x junction tunnel barrier, the loss tangent is [see Sec.

3.3.1]

$$\tan\delta = \frac{1}{\omega_{CPB} T_1}\left(\frac{E_J}{4E_c}\right). \tag{6.3}$$

I find $\tan\delta = 6\times10^{-7}$ at $E_J/h = 4.5\,\mathrm{GHz}$ in Device 2. This is an order of magnitude larger than $\tan\delta = 4\times10^{-8}$ in Device 1 [59] but is about three orders of magnitude smaller than typical results for amorphous dielectrics at low temperatures and low microwave powers [98].

6.3.3 Dephasing in Device 2

I wasn't able to carry out detailed dephasing experiments such as Ramsey fringes to measure T_2 in Device 2. Based on spectral linewidth measurements at $E_{J,\mathrm{bot}}/h = 7.06\,\mathrm{GHz}$ and $E_{J,\mathrm{top}}/h = 7.25\,\mathrm{GHz}$ at low pump power I extracted a spectroscopic coherence time $T_2^* \approx 60\,\mathrm{ns}$ [see Sec. 5.4.2]. This implies that the decoherence time $T_2 \gtrapprox 60\,\mathrm{ns}$. The lifetime at that E_J was $T_1 = 28.1\,\mu\mathrm{s}$ [see Sec. 5.4.1]. Similar to the case of Device 1, $T_2 \ll 2T_1$ in Device 2, indicating that the coherence time T_2 was limited by the pure dephasing time T_φ and I can estimate $T_\varphi \approx T_2 \gtrapprox 60\,\mathrm{ns}$. Using this coherence time in Eq. 6.1 leads to a low frequency charge noise bound of $S_q(f = 1\,\mathrm{Hz}) \leq \left(1\times10^{-2}\right)^2 e^2/\mathrm{Hz}$. This is almost an order of magnitude decrease in the dephasing time or increase in the noise as compared to Device 1. There was a similar, although not as drastic, decrease in the Rabi oscillation decay times, from $T' = 1-2\,\mu\mathrm{s}$ for Device 1 to $T' = 0.2-1.8\,\mu\mathrm{s}$ for Device 2. I don't have an explanation for this increase in charge noise but it's consistent with sample-to-sample variation I've observed and may be due to uncontrolled variations in the fabrication such as the quality of the junction oxide or the number of strongly coupled TLS's.

Table 6.1 contains a summary of the coherence times and charge noise bounds for Device 2.

7 CPB-TLS Interaction Theory

7.1 The Physical Origin of Defects and Dissipation

In the discussion so far I have focused little attention on the physical origin and microscopic details of defects and dissipation. I addressed thermal Johnson-Nyquist noise [see Sec. 3.3.1] and instrumentation noise [see Sec. 4.2.1], but I treated lossy materials and $1/f$ noise empirically. Dielectric loss and $1/f$ charge noise, the two intrinsic loss mechanisms most relevant to charge qubits, are believed to originate from charged two-level systems (TLS) in the material [182, 183, 184, 185, 98, 186, 187, 188, 189]. A TLS is any physical system where the two lowest energy levels are sufficiently separated from the higher levels such that they may be safely neglected in determining the system properties and dynamics. Although TLS's dominate the low temperature behavior of most amorphous materials [190, 191, 192], their microscopic details are poorly understood and insight into their nature would be beneficial, both to quantum computing and the study of material properties in general.

7.1.1 Two-Level Systems

There are many models and theories of the microscopic physical origin of TLS's. I will briefly discuss those responsible for flux, charge, and critical current noise, which are the three types most applicable to superconducting qubits. For example, flux noise may be due to pinned flux vortices or unpaired electron spins on the surface of the qubit, with the dominant mechanism determined by such factors as the wire width, the junction area, and the ambient field [193, 194, 195, 102]. Charge noise is understood to be caused by moving ions located in the amorphous dielectric or on the surfaces and at interfaces between materials constituting the qubit. These could be impurity ions such as H^+ or OH^- or various kinds of vacancies that tunnel between two positions. Another potential

source is electrons hopping between charge trapping centers or low coordination bonds [60, 196, 197, 61].

Some critical current noise can have the same underlying physical origins as charge noise. If an ion is located in the tunnel barrier, then its motion may modulate the height of the tunnel barrier and consequently the critical current of the junction [198, 196, 199, 200, 201]. The closely spaced topology of a Josephson junction may also lead to physics not present in isolated charged TLS's. Specifically the interaction between the trapping centers and the bulk superconductor may lead to the formation of Andreev subgap states or weak Kondo states at subgap energies [202, 203]. Of course critical current noise can also be caused by flux motion or magnetic field changes.

Despite many years of research, experimental evidence regarding the precise microscopic identity of TLS's is hard to come by. Furthermore, while aggregate effects of many TLS's, such as $1/f$ noise or dissipation, are easy to measure, individual TLS interactions or effects are much harder to observe. The strong coupling of qubits to their local environment is both a blessing and a curse, hindering their performance but also allowing unique opportunities to study individual TLS's in detail.

7.1.2 Qubit-TLS Interactions

Qubit-TLS interactions may be broadly categorized based on three criteria: the qubit-TLS coupling strength g_{TLS}, whether the energies of the two systems are resonant or not, and the nature of the interaction of the TLS with the qubit. There is not a unique definition of the boundary between strong and weak coupling but it's usually determined by comparing the coupling strength g_{TLS} to the relevant decoherence rates in the system. If the coupling strength is smaller than the decoherence rates of the qubit $g_{TLS} \ll \Gamma_1, \Gamma_2$ the coupling is said to be weak, while if $g_{TLS} \gg \Gamma_1, \Gamma_2$ it's strong. TLS's in superconducting qubits are classified into three types—charge, flux, or critical current—depending on which parameter the TLS couples to.

The aggregate effects of many weakly coupled, non-resonant TLS's include various flavors of $1/f$ noise, broadband dielectric loss, inhomogeneous broadening, and decreased measurement fidelity in qubits [204, 22, 98, 205, 206, 207]. A single resonant and quantum-coherently coupled TLS typically produces an avoided crossing, also called a splitting, in the qubit spectrum. In this context a quantum-coherent coupling can be defined as

a coupling that gives a coherent rate of energy exchange $2g_{TLS}$ that exceeds the decoherence rates $\Gamma_1, \Gamma_2, \Gamma_{1,TLS}, \Gamma_{2,TLS}$ of both of the sub-systems. This is synonymous with strong coupling. Unintended avoided level crossings have been reported in virtually all superconducting qubit designs including phase, flux, charge, quantronium, and transmon [208, 209, 206, 210, 204, 205, 61, 22, 116]. Qubit performance is usually severely degraded near a splitting [61, 211, 212, 56, 206]. Analytic expressions for the reduction in coherence of a qubit due to coupling to a TLS exist [213, 185] but are difficult to employ in practice because they depend on the qubit-TLS coupling strength g_{TLS} and the coherence times of both the qubit T_1, T_2 and the TLS $T_{1,TLS}, T_{2,TLS}$, TLS parameters which are difficult to measure or determine from fundamental theory. The theoretical results also predict complex behavior such as non-exponential excited state probability decay, which if observed would provide strong evidence of coherent qubit-TLS coupling. Experimentally, Z. Kim observed an order of magnitude increase in a CPB decay rate Γ_1 near a spectroscopic avoided level crossing [61].

Quantum-coherent coupling between a qubit and a TLS opens the possibility of manipulating an individual TLS and studying its microscopic properties. For instance, coherent oscillations between a qubit and a TLS have been observed [208] and the TLS has been proposed and demonstrated as a quantum memory [214, 215]. More pertinent to the study of the nature of TLS's, strong qubit-TLS interactions allow the microscopic details of the TLS to be determined [61, 216, 217]. It's theoretically possible but experimentally challenging to identify the exact nature of the qubit-TLS interaction in phase and flux qubits [218]. On the other hand, in charge qubits the island and gate voltages will modulate the energy of a charged TLS. Z. Kim found that by taking detailed spectroscopy of resolvable splittings, it was possible to confirm models of TLS physical origin and extract microscopic parameters included in the model [61, 60].

While a weak, resonant, qubit-TLS interaction would produce the same qualitative effects as a strong interaction, the splitting would be too small to resolve. The decrease in qubit coherence due to such an interaction is also expected to be less than if the coupling were strong. Z. Kim reported using localized increases in the qubit decay rate Γ_1 as markers to help locate avoided crossings in the qubit spectrum [61]. In a similar fashion, one expects that small localized increases in the qubit decay rate may correspond to weak, resonant qubit-TLS interactions that don't produce detectable splittings. Of course such

features may also be due to coupling to some other, non-TLS mode.

To the best of my knowledge strong, non-resonant qubit-TLS interactions have not been previously reported. In such a scenario the qubit and TLS interaction would be strong enough such that they would form an effective four-level system. Transitions from the combined system ground state to states that involve a significant qubit component would be expected to be detectable with the same readout as that used for pure qubit transitions. Depending on the shape of the TLS spectrum, this may produce an apparent twinning of the qubit spectrum or other highly anomalous spectral features. The TLS spectrum may also be visible if the readout used responds to changes of the pure TLS states, such as the case with a charged fluctuator and a charge sensitive rf-SET readout [61]. The effect on qubit coherence is difficult to predict and would depend on a variety of factors such as the nature of the qubit-TLS coupling and the intrinsic TLS coherence times. It's reasonable to assume that the composite system relaxation rate would be influenced by the relaxation rates of the individual qubit and TLS sub-systems but it may not necessarily scale as the system component fractions. For instance, theoretical examination of a model system consisting of a TLS coupled to a qubit found that the lifetime T_1 depends on the relaxation and dephasing rates of the qubit and TLS, the coupling strength, and the form of the qubit-TLS coupling Hamiltonian [213, 185].

Although I have classified TLS's into three types, a particular TLS may belong to more than one class. A charge hopping in the tunnel barrier or a flux vortex hopping near the junction would, respectively, couple to the charge and flux degrees of freedom of a superconducting qubit but both would also modulate the critical current. If defects in the tunnel barrier are prevalent, it's reasonable to believe that there would be similar numbers of charge and critical current TLS's. While there are many reports of critical current fluctuations in Josephson junction devices [199, 200, 201], there don't appear to be reports of critical current TLS's in Josephson junction based qubits. This may be due to the lower temperature used with qubits or to the difficulty of distinguishing a critical current fluctuator from a charge or flux fluctuator. Alternatively, the smaller area of qubit junctions as compared to those of conventional junction devices leads to fewer TLS's and reduced odds that one of those TLS's would be in the right parameter space to produce observable critical current fluctuations.

In this chapter, I derive a model Hamiltonian for a CPB coupled to a charged TLS lo-

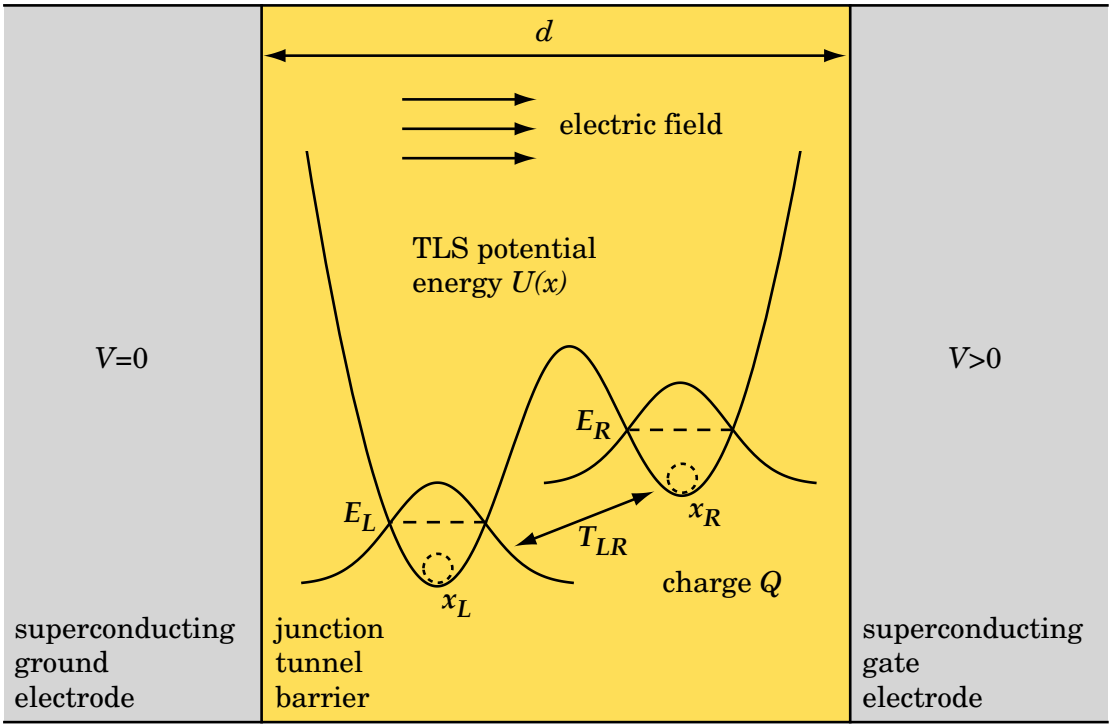

Figure 7.1: Potential energy of a charged TLS in a junction tunnel barrier of thickness d. The fluctuator has charge Q, can be localized at positions x_R or x_L with corresponding energies E_R or E_L, and can tunnel between the two wells with energy T_{LR}.

cated in the junction tunnel barrier. I will assume the qubit and TLS couple via both their charge interaction and the TLS modulating the Josephson energy of the CPB. I discuss two different interaction regimes and the corresponding spectra, the effect of the various model parameters on the system spectrum, and finally extend the model to include the effect of multiple TLS's. In Chapter 8, I present my data on the spectroscopy of Device 2 and discuss my fits of the model developed here, draw conclusions about physical properties of the CPB and TLS, and detail other anomalous spectral features in Device 2.

7.2 CPB Coupled to a TLS

My discussion here builds on a model developed by F. C. Wellstood [60] and employed by Z. Kim to fit avoided level crossings in the spectrum of a CPB [61]. The model assumes a charged point particle physically located in the junction tunnel barrier [see Fig. 7.1]. This fluctuator acts as a two-level system that can tunnel between two minima of the local potential energy landscape [see Fig. 7.1].

I first consider the electrostatic interaction between the TLS and the CPB. To help keep track of potential emergent effects, I begin with just two non-interacting TLS's. As in the

derivation of the CPB Hamiltonian [see Sec. 2.2], I calculate the charging energy minus the work done by the gate voltage source. Taking the total electrostatic energy of the system U_{el}, given by Eq. 2.10, and subtracting the work $W_{el} = 2eV_gC_g/C_\Sigma$ done by the gate voltage source when the number of Cooper-pairs on the island changes [see Eq. 2.12] and the work W_k done when the k-th fluctuator changes position results in

$$E_{el} = \frac{1}{2}C_g\left(V_g - V_i\right)^2 + \frac{1}{2}C_jV_i^2 - W_{el} - \sum_{k=1}^{2} W_k. \tag{7.1}$$

Here V_g is the voltage bias applied to the gate capacitance C_g, V_i is the potential of the island, and C_j is the junction capacitance, the same definitions I used in the simple CPB case [see Sec. 2.2].

I determine W_k by considering the changes in the induced polarization charges when the TLS's move. Green's reciprocation theorem [83] gives the polarization charge $Q_{p,k}$ induced on the island of the CPB by the k-th fluctuator as

$$Q_{p,k} = -\frac{x_k}{d}Q_k \tag{7.2}$$

where Q_k is the charge of the k-th fluctuator, x_k is its distance from the ground plate of the junction, and d is the thickness of the junction tunnel barrier [see Fig. 7.1]. The total charge on the island is constant for fixed n and consequently a complementary charge of $-\left(Q_{p,1} + Q_{p,2}\right)$ is distributed over the rest of the island. This induces charges on both the gate and junction electrodes in proportion to the capacitance ratio, with the induced gate charge Q_g given by

$$Q_g = -\left(\frac{x_1}{d}Q_1 + \frac{x_2}{d}Q_2\right)\frac{C_g}{C_\Sigma} \tag{7.3}$$

where $C_\Sigma = C_j + C_g$. The gate voltage source does work equal to

$$\begin{aligned}\sum_{k=1}^{2} W_k &= Q_gV_g \\ &= \frac{e}{C_\Sigma}\left(\frac{x_1}{d}Q_1 + \frac{x_2}{d}Q_2\right)n_g\end{aligned} \tag{7.4}$$

when this charge moves to the gate electrode. Finally, the island potential is

$$V_i = \frac{1}{C_\Sigma}\left(C_gV_g + 2ne\right) + \frac{1}{C_\Sigma}\left(\frac{x_1}{d}Q_1 + \frac{x_2}{d}Q_2\right). \tag{7.5}$$

Substituting Eqs. 7.4 and 7.5 into 7.1 and simplifying results in

$$E_{el} = E_c\left(2n - n_g + \sum_{k=1}^{2}\frac{Q_k}{e}\frac{x_k}{d}\right)^2 + E_c\left(\frac{C_j}{C_g} - 1\right)n_g^2. \tag{7.6}$$

The second term doesn't depend on n and hence has no effect on CPB dynamics and may be discarded. The first term contains the TLS contributions, which behave similar to gate voltage offsets.

Dropping the last term in Eq. 7.6 and expanding the first product gives

$$\begin{aligned} E_{el} &= E_c\left(2n - n_g\right)^2 + 2E_c\left(2n - n_g\right)\left(\frac{Q_1}{e}\frac{x_1}{d}\right) + 2E_c\left(2n - n_g\right)\left(\frac{Q_2}{e}\frac{x_2}{d}\right) \\ &\quad + \frac{Q_1^2}{2C_\Sigma}\left(\frac{x_1}{d}\right)^2 + \frac{Q_2^2}{2C_\Sigma}\left(\frac{x_2}{d}\right)^2 + \frac{Q_1 Q_2}{C_\Sigma}\left(\frac{x_1}{d}\frac{x_2}{d}\right), \end{aligned} \tag{7.7}$$

making explicit each electrostatic energy contribution. The first term is the charging energy of a CPB without any TLS's [see Eq. 2.13] and the next two are the CPB-TLS electrostatic interactions. The following two terms are capacitive corrections to the individual TLS electrostatic potential energies while the last term is an indirect TLS-TLS electrostatic interaction mediated by the CPB capacitance. All these terms may be viewed as originating from the boundary conditions placed on the electric field by the capacitor plates.

To construct the Hamiltonian of the combined CPB+TLS_1+TLS_2 system, I add to the electrostatic free energy [see Eq. 7.6] the junction Josephson energy [see Sec. 2.2] and the kinetic and potential energies of both fluctuators, resulting in

$$\hat{H}_{sys} = \hat{H}_{CPB} + \sum_{k=1}^{2}\hat{H}_{TLS,k} + \sum_{k=1}^{2}\hat{H}_{CPB-k} + \hat{H}_{12}. \tag{7.8}$$

$\hat{H}_{CPB}$ is the CPB Hamiltonian in the absence of any TLS's, given by

$$\hat{H}_{CPB} = E_c\left(2\hat{N} - n_g\right)^2 - E_J\cos\hat{\gamma}, \tag{2.14}$$

followed by a sum of the TLS Hamiltonians $\hat{H}_{TLS,k}$. The Hamiltonian of the k-th fluctuator is

$$\hat{H}_{TLS,k} = \frac{\hat{p}_k^2}{2m_k} + \frac{Q_k^2}{2C_\Sigma}\left(\frac{\hat{x}_k}{d}\right)^2 + U_k(\hat{r}_k) \tag{7.9}$$

where $\hat{p}_k$ is the momentum operator, $\hat{r}_k = \hat{x}_k\hat{x} + \hat{y}_k\hat{y} + \hat{z}_k\hat{z}$ is the position operator, m_k is the mass, U_k is the local potential, and $\hat{x}$, $\hat{y}$, and $\hat{z}$ are the Cartesian coordinates unit vectors. The CPB interaction with the k-th TLS term $\hat{H}_{CBP-k}$ is

$$\hat{H}_{CPB-k} = 2E_c\left(2\hat{N} - n_g\right)\left(\frac{Q_k}{e}\frac{\hat{x}_k}{d}\right) \tag{7.10}$$

while $\hat{H}_{12}$ accounts for TLS-TLS coupling and is given by

$$\hat{H}_{12} = \frac{Q_1Q_2}{C_\Sigma}\left(\frac{\hat{x}_1}{d}\frac{\hat{x}_2}{d}\right) + U_{12}(\hat{r}_1, \hat{r}_2). \tag{7.11}$$

The first term of Eq. 7.11 is the indirect TLS-TLS coupling term I identified in Eq. 7.7 while U_{12} represents any direct interaction between the two systems. U_{12} is likely to be very small due to shielding by the junction electrodes unless the charges are in close physical proximity, i.e. $|\hat{r}_1 - \hat{r}_2| \lessapprox d$.

To simplify analysis of the model, I will now limit the rest of the discussion in this section to the case of a single charged fluctuator coupled to the CPB. Furthermore, I will make explicit use of the two-level approximation to simplify the TLS Hamiltonian $\hat{H}_{TLS,1}$. In this case, if the defect is localized in one of the two wells of its local potential, which in the absence of tunneling have energies $E_{R,1}$ and $E_{L,1}$ [see Fig. 7.1], then the Hamiltonian may be written as the 2×2 matrix

$$\mathbb{H}_{TLS,1} = \begin{pmatrix} E_{L,1} & T_{LR,1} \\ T_{LR,1} & E_{R,1} \end{pmatrix} \tag{7.12}$$

where $T_{LR,1}/\hbar$ is the tunneling rate between the two wells and the position basis states used are defined by $\hat{x}_1\left|x_{R,1}\right\rangle = x_{R,1}\left|x_{R,1}\right\rangle$ and $\hat{x}_1\left|x_{L,1}\right\rangle = x_{L,1}\left|x_{L,1}\right\rangle$. Without loss of generality I can set $E_{L,1} = 0$ and $x_{L,1} = 0$. This Hamiltonian yields an isolated fluctuator with an excited state transition energy of $\hbar\omega_{TLS,1} = \sqrt{E_{R,1}^2 + 4T_{LR,1}^2}$.

The total CPB+TLS system Hamiltonian can be placed in block matrix form using CPB charge n and TLS position x basis states $|n, x\rangle$ as

$$\mathbb{H} = \begin{pmatrix} \mathbb{H}_L & \mathbb{T}_1 \\ \mathbb{T}_1 & \mathbb{H}_R \end{pmatrix} \tag{7.13}$$

where $\mathbb{T}_1 = T_{LR,1}\mathbb{I}$, $\mathbb{I}$ is the $N \times N$ identity matrix, and $\mathbb{H}_L$ and $\mathbb{H}_R$ are the CPB Hamiltonians with the TLS localized in either the left or right well. N is the number of charge states needed to accurately represent the CPB Hamiltonian and, for instance, if $E_c \gg E_J$ then $N = 2$ is sufficient. In this case $\mathbb{H}_L = \mathbb{H}_{CPB}$, given by Eq. 2.20, while

$$\mathbb{H}_R = \begin{pmatrix} E_c\left(0-n_g\right)^2 + E_{int,1}\left(0-n_g\right) + E_{R,1} & -E_J/2 \\ -E_J/2 & E_c\left(2-n_g\right)^2 + E_{int,1}\left(2-n_g\right) + E_{R,1} \end{pmatrix} \tag{7.14}$$

where $E_{int,1} = 2E_c Q_{TLS,1} x_{R,1}/ed$ is the CPB-TLS charge interaction energy.

I can now generalize the model by including a Josephson interaction term. The physical origin for this interaction is that the charged TLS can modulate the tunnel barrier linking the superconducting wavefunctions in the two electrodes of the tunnel junction, and consequently modulate the Josephson energy E_J of the CPB. Such an effect has already been theoretically explored as a possible source of critical current noise and analytical results are available for the exact change in the Josephson energy E_J as a function of TLS position and dipole moment [196]. Here I construct a simpler model by assuming an effective change of the Josephson energy $\Delta E_{J,1}$ as the TLS tunnels between its two wells. This can be implemented by making the substitution $E_J \to E_J + \Delta E_{J,1}\hat{\sigma}_{z,1}/2$ in the CPB Hamiltonian $\hat{H}_{CPB}$ [see Eq. 2.14] where $\hat{\sigma}_{z,1}$ is a Pauli matrix in the TLS position basis. In block matrix representation this corresponds to the substitution $E_J \to E_J + \Delta E_{J,1}/2$ in $\mathbb{H}_L$ and $E_J \to E_J - \Delta E_{J,1}/2$ in $\mathbb{H}_R$. Explicitly the new matrices are

$$\mathbb{H}_L = \begin{pmatrix} E_c\left(0-n_g\right)^2 & -\left(E_J + \Delta E_{J,1}/2\right)/2 \\ -\left(E_J + \Delta E_{J,1}/2\right)/2 & E_c\left(2-n_g\right)^2 \end{pmatrix} \tag{7.15}$$

and

$$\mathbb{H}_R = \begin{pmatrix} E_c\left(0-n_g\right)^2 + E_{int,1}\left(0-n_g\right) + E_{R,1} & -\left(E_J - \Delta E_{J,1}/2\right)/2 \\ -\left(E_J - \Delta E_{J,1}/2\right)/2 & E_c\left(2-n_g\right)^2 + E_{int,1}\left(2-n_g\right) + E_{R,1} \end{pmatrix}. \tag{7.16}$$

7.2.1 Resonant Qubit-TLS Interaction

The single TLS model derived in the previous section has two distinct regimes corresponding to resonant and non-resonant qubit-TLS interaction. If the excited state of the TLS is resonant with the first excited state of the CPB at some value of the gate voltage

n_g, an avoided crossing is produced at that point in the parameter space of energy and gate voltage. On the other hand, if the TLS excited state energy lies below the CPB transition minimum the CPB spectrum is twinned. The first regime was observed by Z. Kim, who found resonant splittings in the spectrum of a CPB and fit the spectrum to a single TLS model [61]. In Chapter 8, I describe similar work I carried out studying the twinned and quadrupled spectrum of Device 2, which I fit to both the single and double TLS non-resonant interaction models. In this section and the next I present a typical calculated spectrum from each regime and then discuss the effect of each model parameter on the system's spectrum.

I obtained the transition spectrum by first plugging in representative values of the model parameters into the system Hamiltonian $\mathbb{H}$ [see Eq. 7.13] and then numerically diagonalizing it in Mathematica. This produces a set of eigenvectors $\{\vec{x}_n\}$ and corresponding eigenvalues $\{\lambda_n\}$. The eigenvalues are the energies of the various levels and the transition frequency from the ground state to the nth excited state of the system is given by $f_n = (\lambda_{n+1} - \lambda_1)/h$. The eigenvectors may be used to form the unitary matrix needed to transform other operators to the eigenbasis or to calculate projections of the eigenvectors onto other states such as basis states of the uncoupled system.

Figure 7.2 shows a resonant system spectrum calculated using parameter values $E_c/h = 5.0\,\text{GHz}$, $E_J/h = 5.0\,\text{GHz}$, $E_{R,1}/h = 10.0\,\text{GHz}$, $E_{int,1}/h = 2.0\,\text{GHz}$, $\Delta E_{J,1}/h = 2.0\,\text{GHz}$, and $T_{LR,1}/h = 5.0\,\text{GHz}$. The excitation spectrum that corresponds to mainly the CPB is colored red while the excitation spectrum mainly due to the TLS is colored green. I'm able to identify the pure transitions in this manner because the subsystems are weakly coupled away from the avoided crossings, with complete decoupling corresponding to $\Delta E_{J,1}/h = 0\,\text{GHz}$. The CPB only transition is very similar to the CPB spectrum in the absence of TLS's [see Fig. 2.3(b)] while the TLS only transition resembles a rounded saw-tooth. This saw-tooth is more evident in the spectrum of Fig. 7.4(b) which has the TLS tunneling rate $T_{LR,1}/h = 0\,\text{GHz}$. The reset of the TLS spectral line at $n_g = 1$ is due to a Cooper-pair tunnel on or off the CPB island and it's width depends on the sharpness of the charge staircase [see Fig. 2.2]. The entire spectrum is $2e$ periodic if the TLS is located inside the junction dielectric or on the CPB island surface. Finally it's noteworthy that the two splittings near $f \approx 15\,\text{GHz}$ are not identical but are of differing sizes and located asymmetrically in frequency f and gate voltage n_g.

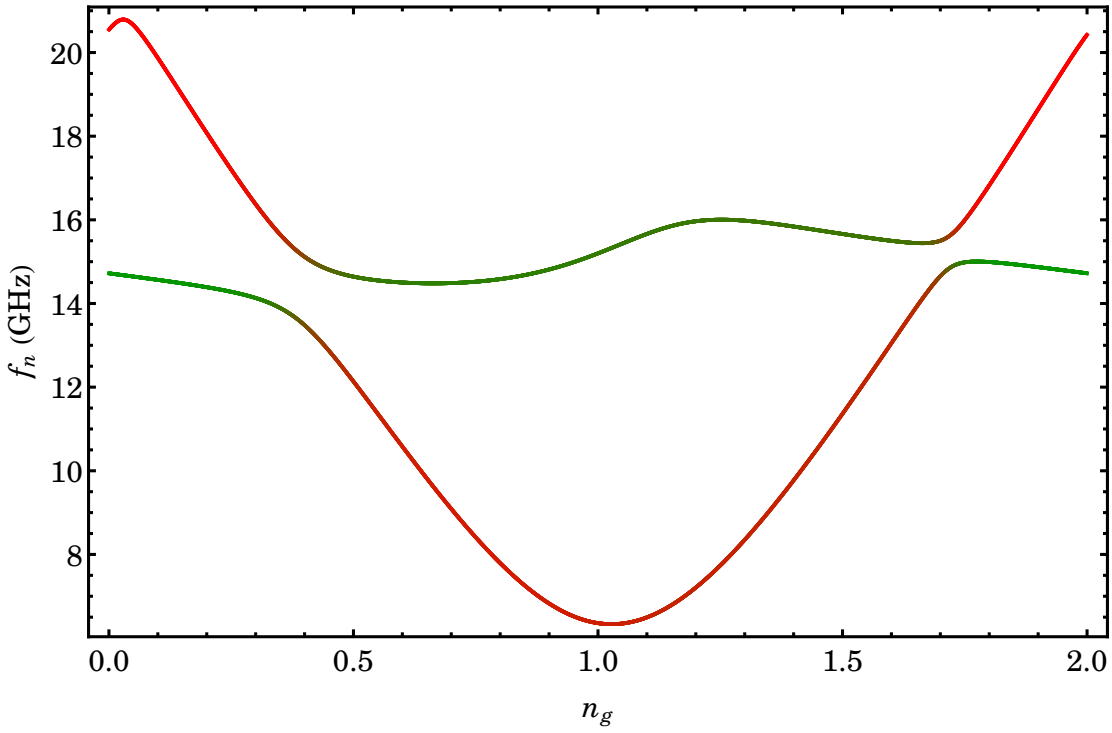

Figure 7.2: Example of a resonant CPB-TLS system spectrum. The curve color identifies the transition, with red corresponding to a CPB excitation and green to a TLS excitation. The spectrum was calculated using parameter values $E_c/h = 5.0\,\text{GHz}$, $E_J/h = 5.0\,\text{GHz}$, $E_{R,1}/h = 10.0\,\text{GHz}$, $E_{int,1}/h = 2.0\,\text{GHz}$, $\Delta E_{J,1}/h = 2.0\,\text{GHz}$, and $T_{LR,1}/h = 5.0\,\text{GHz}$.

To illustrate the qualitative effects of each model parameter in the resonant regime, I recalculated the system spectrum while setting one of the TLS parameters to 0. The spectrum in Fig. 7.3(a) has $E_{R,1}/h = 0\,\text{GHz}$ and all other parameters the same values as in Fig. 7.2. In this figure and others in this section, the red curve is the nearly pure CPB transition, the green curve the nearly pure TLS transition, and the dashed curve is the spectrum of Fig. 7.2 reproduced for easy comparison. From Fig. 7.3(a), it's evident that the main effect of $E_{R,1}$ is to shift the TLS transition along the frequency axis. There is also some distortion of the CPB parabola due to, in this example, the TLS line traversing close to the CPB parabola minimum. $E_{int,1}$ sets the slope of the TLS transition saw-tooth curve, as can be seen in Fig. 7.3(b), where $E_{int,1}/h = 0\,\text{GHz}$ while the rest of the parameters have their original values.

The primary effect of $\Delta E_{J,1}$ is a change in the effective curvature of the CPB spectrum with secondary changes including a frequency shift of the TLS transition saw-tooth curve and an increase of the avoided crossing splitting size. An example of this is shown in Fig. 7.4(a) where $\Delta E_{J,1}/h = 0\,\text{GHz}$ but the rest of the parameters retain their previous values.

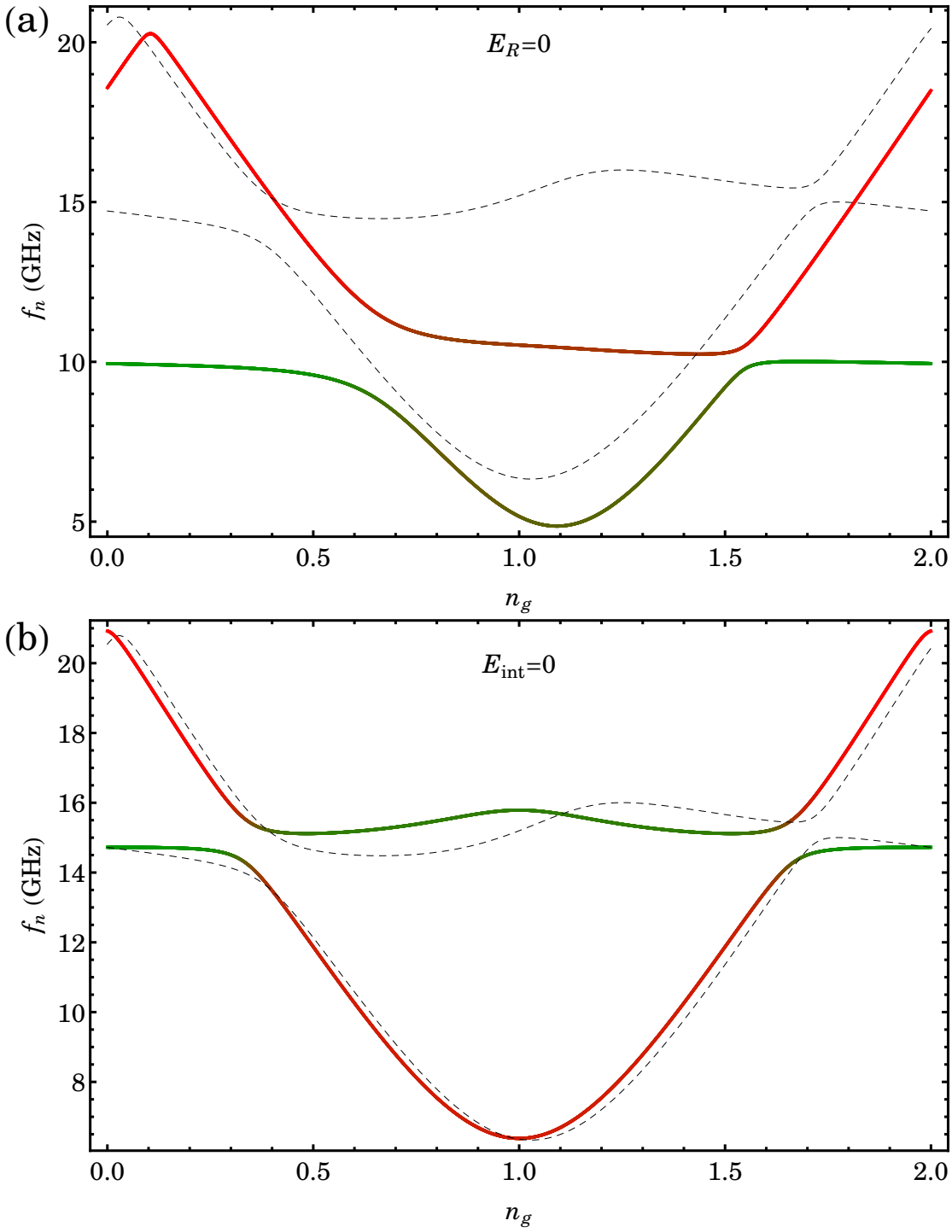

Figure 7.3: (a) Resonant system spectrum with $E_{R,1}/h = 0\,\text{GHz}$. The main effect of $E_{R,1}$ is to shift the TLS transition along the frequency axis. (b) Resonant system spectrum with $E_{int,1}/h = 0\,\text{GHz}$. The main effect of $E_{int,1}$ is to set the slope of the TLS transition saw-tooth curve. In both plots the dashed curve is the original spectrum from Fig. 7.2.

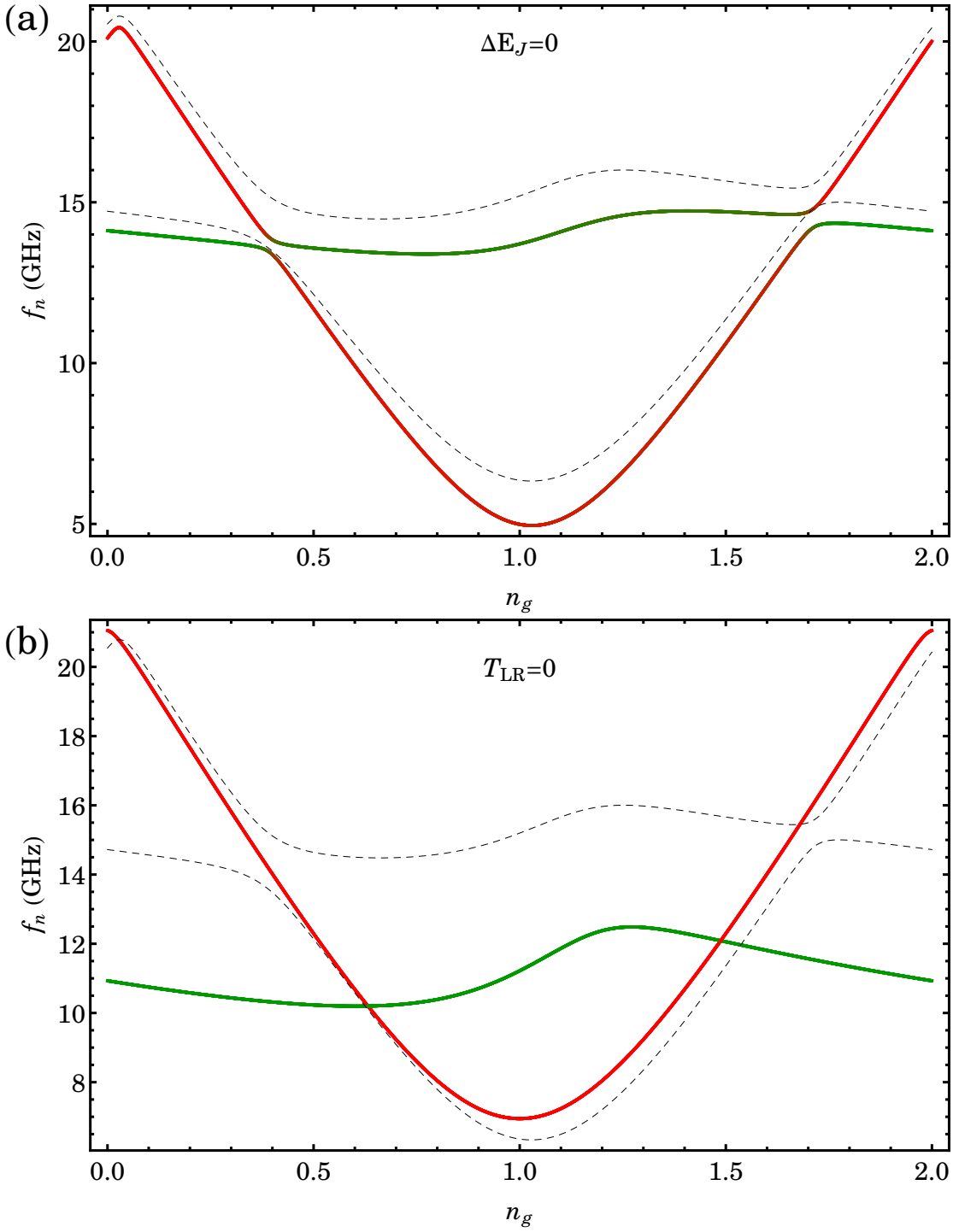

Figure 7.4: (a) Resonant system spectrum with $\Delta E_{J,1}/h = 0\,\mathrm{GHz}$. The main effects of $\Delta E_{J,1}$ are to change the effective curvature of the CPB spectrum and shift the frequency of the TLS transition saw-tooth curve. (b) Resonant system spectrum with $T_{LR,1}/h = 0\,\mathrm{GHz}$. The main effects of $T_{LR,1}$ are to determine the avoided crossing splitting size and alter the slope of the TLS spectral curve. In both plots the dashed curve is the original spectrum from Fig. 7.2.

Note that it's possible to produce a system spectrum very similar to the one of Fig. 7.4(a) by instead adjusting the values of E_J, $E_{R,1}$, and $T_{LR,1}$. To conclusively distinguish the effect of $\Delta E_{J,1}$ from E_J, it's necessary to also examine higher excited states of the system. If $\Delta E_{J,1}/h = 0\,\mathrm{GHz}$, then the curvature of higher excited states will be consistent with a single E_J value. On the other hand, if $\Delta E_{J,1}/h \neq 0\,\mathrm{GHz}$, then the curvature of higher excited states will be determined either by $E_J - \Delta E_{J,1}$ or $E_J + \Delta E_{J,1}$, depending on the TLS component of the particular state. Finally, the avoided crossing splitting size scales with $T_{LR,1}$, which also alters the slope of the TLS saw-tooth spectral curve, making it more shallow the larger $T_{LR,1}$ is relative to $E_{int,1}$ as can be seen in Fig. 7.4(b).

In the discussion so far I have included the effect of the various model parameters on the TLS spectral curve. This information can be used only if the nearly pure TLS spectrum can be detected, as was the case for the characterization performed by Z. Kim [61]. He was able to observe the faint TLS only transition using the charge sensitive RF-SET readout [61]. However, depending on the nature of the qubit-state readout, the readout may or may not respond to changes of the TLS state. Fortunately, it's still possible to extract all the TLS parameters entirely from the nearly pure CPB spectrum if the TLS is coupled to the CPB via charge and critical current. The sizes of the two splittings, their position in gate voltage n_g and frequency f, and the curvature of the CPB excited states provide enough constraints to determine the values of $E_{R,1}$, $E_{int,1}$, $\Delta E_{J,1}$, and $T_{LR,1}$.

7.2.2 Non-resonant Qubit-TLS Interaction

The strong non-resonant qubit-TLS interaction regime occurs when the TLS transition lies below the CPB transition for all values of the gate voltage n_g and the coupling is sufficiently strong so that the joint CPB plus TLS transition is distinguishable and visible with the qubit readout. In this case the qubit spectrum is twinned and, considered individually, each parabola is similar to the spectrum of a TLS-free CPB.

Figure 7.5 shows an example of such a twinned spectrum, generated using parameter values $E_c/h = 5.0\,\mathrm{GHz}$, $E_J/h = 4.0\,\mathrm{GHz}$, $E_{R,1}/h = 3.0\,\mathrm{GHz}$, $E_{int,1}/h = -1.5\,\mathrm{GHz}$, $\Delta E_{J,1}/h = 1.5\,\mathrm{GHz}$, and $T_{LR,1}/h = 0.5\,\mathrm{GHz}$. Unlike in the resonant case, there is no distinct region with an avoided crossing and the eigenstates contain both TLS and CPB components that are significant at all values of the gate voltage n_g. For instance, at $n_g = 1$ the lowest green curve may be decomposed into a 79% TLS excitation, a 4% CPB excitation, and

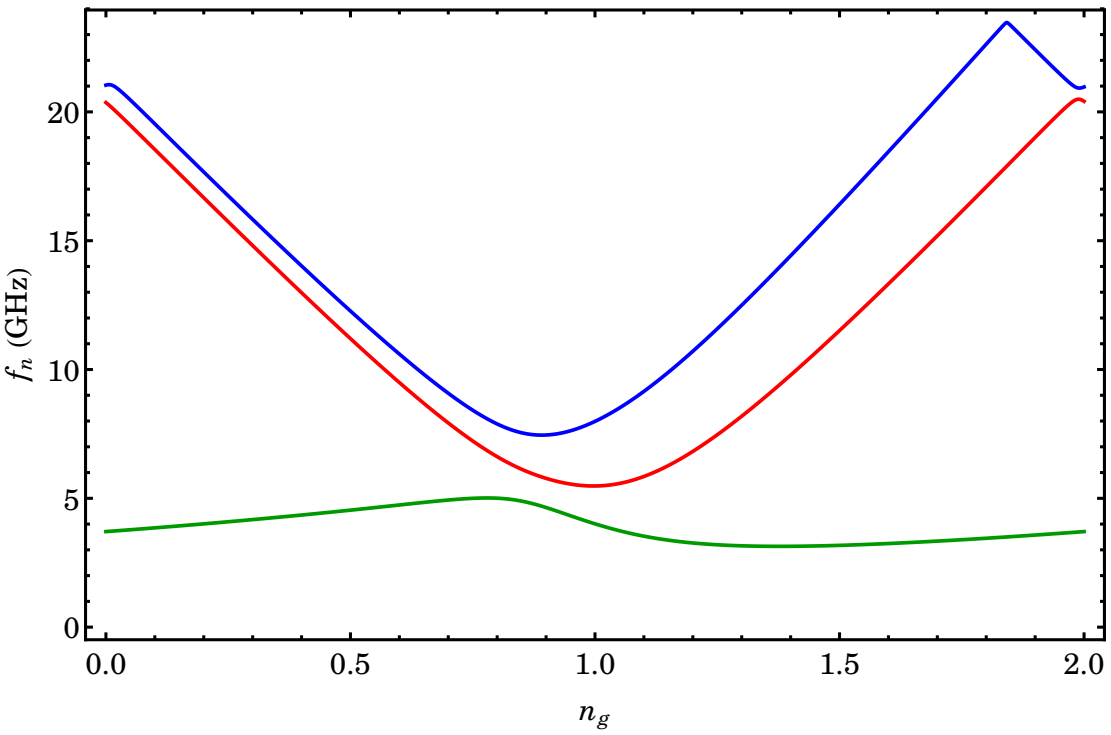

Figure 7.5: Example of the three lowest lying transitions for a non-resonant CPB-TLS system spectrum. The curves are colored green, red, and blue in order of increasing transition energy. The spectrum was calculated using parameter values $E_c/h = 5.0\,\text{GHz}$, $E_J/h = 4.0\,\text{GHz}$, $E_{R,1}/h = 3.0\,\text{GHz}$, $E_{int,1}/h = -1.5\,\text{GHz}$, $\Delta E_{J,1}/h = 1.5\,\text{GHz}$, and $T_{LR,1}/h = 0.5\,\text{GHz}$.

a 17% joint CPB plus TLS excitation. The lower red parabola is composed of a 95% CPB excitation and a 5% TLS excitation while the upper blue parabola is a 17% TLS excitation and a 83% joint CPB plus TLS excitation. Hence while I may state that the red parabola corresponds predominantly to a pure CPB excitation, the other two curves have significant excited CPB contributions as well.

The effect of the model parameters on the system spectrum in the non-resonant regime is more complex than in the resonant case. In the resonant case the parameters tended to largely influence the TLS spectral line, in the non-resonant case they also have significant impact on the shape and position of the twinned CPB-like spectrum. In addition to shifting the TLS transition along the frequency axis, $E_{R,1}$ also offsets one of the parabolas relative to the other along the frequency axis. An example of this is shown in Fig. 7.6(a) which was generated with $E_{R,1}/h = 0\,\text{GHz}$ and all other parameters with the same values as Fig. 7.5. In this case what was the higher energy (blue) parabola in Fig. 7.5 moves below what was the lower energy (red) parabola. This produces an avoided crossing near $n_g \approx 1.1$ and two distorted, parabola-like curves. $E_{int,1}$ creates an offset along the n_g axis that is different for each parabola. $E_{int,1}$ also tilts one of the parabolas and affects the slope of the TLS transition saw-tooth curve. This may be seen in Fig. 7.6(b) where $E_{int,1}/h = 0\,\text{GHz}$ while the rest of the parameters have their original values. As a consequence of setting $E_{int,1}/h = 0\,\text{GHz}$, the higher energy (blue) parabola is shifted $\Delta n_g \approx 0.1$ to the right and the slope of the TLS saw-tooth becomes flat.

The Josephson coupling $\Delta E_{J,1}$ produces offsets along the frequency axis and changes the effective curvature of one of the parabolas, in addition to shifting the frequency of the TLS transition saw-tooth curve. This is illustrated in Fig. 7.7(a), which has $\Delta E_{J,1}/h = 0\,\text{GHz}$ and all the other parameters unchanged. Here the lower energy (red) parabola is shifted down and has higher curvature. Note that the frequency offsets due to $E_{R,1}$ and $\Delta E_{J,1}$ may add or subtract from each other, determining the resultant offset between the two CPB-like parabolas. The relatively small $1-2\,\text{GHz}$ offset between the red and blue curves is due to a cancellation of the frequency offsets produced by $E_{R,1}$ and $\Delta E_{J,1}$. Alternatively, if the sign of one of the terms were switched, it would produce a larger offset.

The last model parameter, $T_{LR,1}$, determines the size of any avoided crossings that are present in the spectrum. An example of this is the avoided crossing in Fig. 7.6(a).

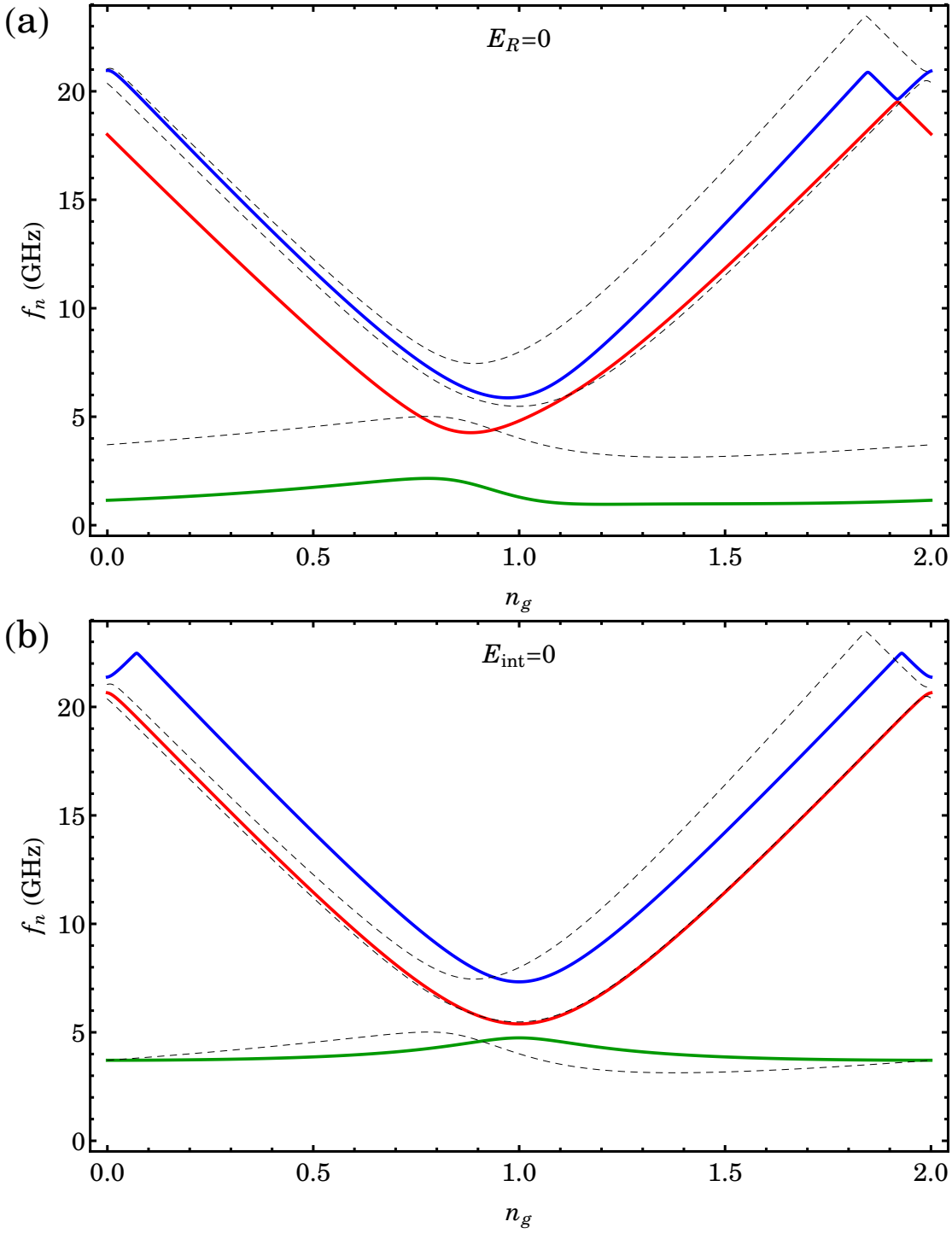

Figure 7.6: (a) Non-resonant system spectrum with $E_{R,1}/h = 0\,\text{GHz}$. The main effects of $E_{R,1}$ are to shift the TLS transition along the frequency axis and to offset in frequency one of the parabolas relative to the other. (b) Non-resonant system spectrum with $E_{int,1}/h = 0\,\text{GHz}$. The main effects of $E_{int,1}$ are to set the slope of the TLS transition saw-tooth curve and offset along the gate voltage n_g axis and tilt one of the parabolas. In both plots the dashed curve is the original spectrum from Fig. 7.5.

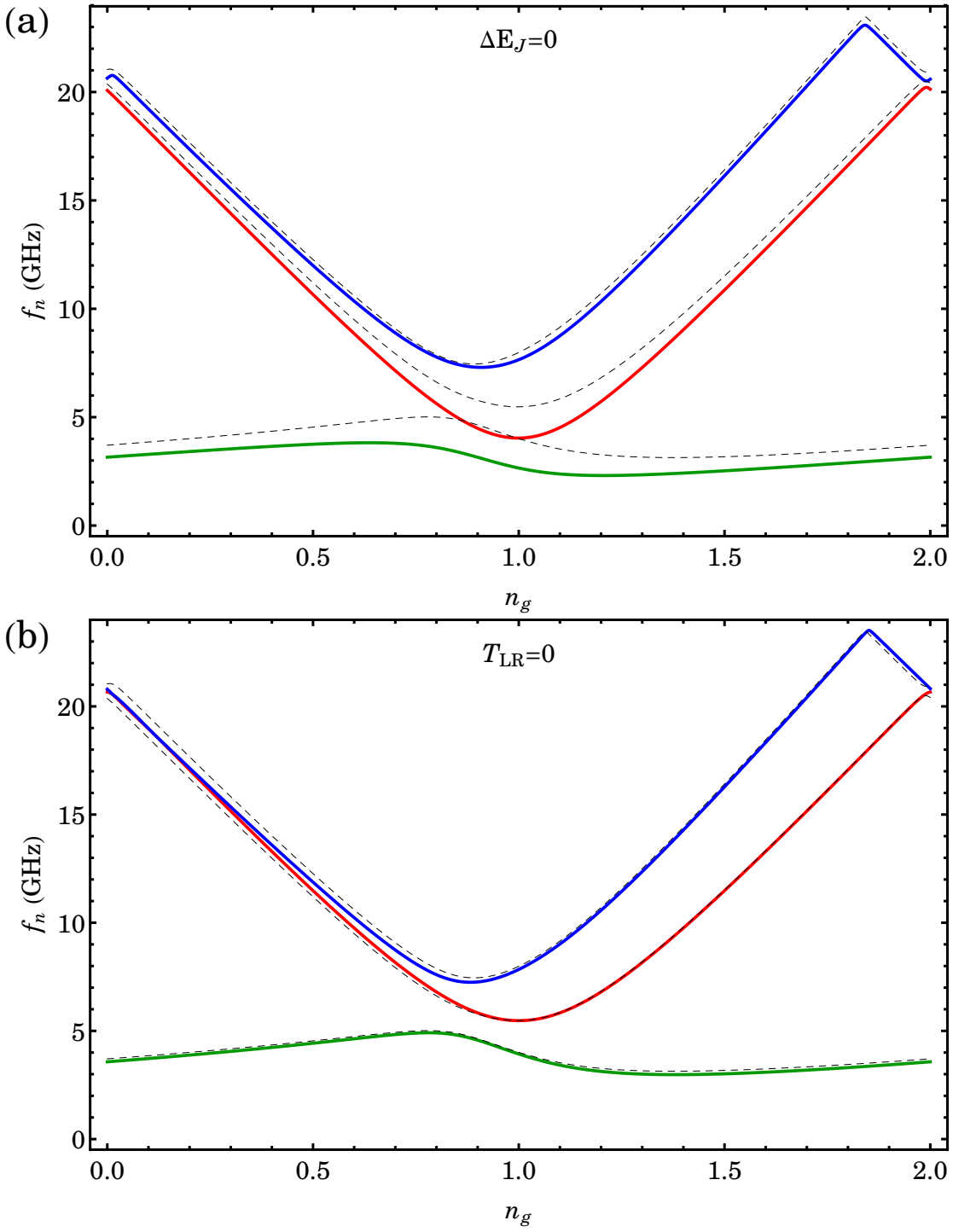

Figure 7.7: (a) Non-resonant system spectrum with $\Delta E_{J,1}/h = 0\,\text{GHz}$. The main effects of $\Delta E_{J,1}$ are to produce an offset in frequency between the parabolas, change the effective curvature of one of the parabolas, and shift the frequency of the TLS transition saw-tooth curve. (b) Non-resonant system spectrum with $T_{LR,1}/h = 0\,\text{GHz}$. The main effects of $T_{LR,1}$ are to determine the size of any avoided crossings or to repel close-lying transition curves. In both plots the dashed curve is the original spectrum from Fig. 7.5.

A similar effect is seen in Fig. 7.7(b), where $T_{LR,1}/h = 0\,\text{GHz}$. Comparing the solid and dashed curves reveals that, in the gate voltage range $n_g \approx 0 - 0.7$, $T_{LR,1}$ acts to repel the two transitions (red and blue curves) even though there is no actual degenerate crossing of the two levels. $T_{LR,1}$ also determines the transition rate induced by a gate perturbation between the ground state and excited states involving the TLS. Specifically the matrix element $\langle g | \partial\hat{H}/\partial n_g | f \rangle$ between initial state $|g\rangle$ and final state $|f\rangle$ scales with $T_{LR,1}$ when $|f\rangle$ has a significant TLS component. Although this doesn't impact the shape of the system spectrum, it does determine the extent to which a transition responds to a pump pulse and hence its visibility.

7.2.3 Extension to Multiple TLS's

The single TLS model is in good agreement with my spectral twinning data when the CPB transition frequency ω_{CPB} is above the resonator ω_{res} [see 8.1.2]. However, when I tuned the CPB transition frequency ω_{CPB} below the resonator ω_{res}, the spectral lines became quadrupled rather than twinned [see Sec. 8.1.1]. This behavior is consistent with a CPB coupled to two TLS's. The idea is that the four CPB-like curves may roughly be associated with a transition involving the CPB and either none, one, or both of the TLS's.

To proceed I reintroduce the model of two TLS's coupled to a CPB. Block matrix form allows me to conveniently write the system Hamiltonian as

$$\mathbb{H} = \begin{pmatrix} \mathbb{H}_{LL} & \mathbb{T}_1 & \mathbb{T}_2 & \mathbb{T}_{12} \\ \mathbb{T}_1 & \mathbb{H}_{RL} & \mathbb{T}_{12} & \mathbb{T}_2 \\ \mathbb{T}_2 & \mathbb{T}_{12} & \mathbb{H}_{LR} & \mathbb{T}_1 \\ \mathbb{T}_{12} & \mathbb{T}_2 & \mathbb{T}_1 & \mathbb{H}_{RR} \end{pmatrix}. \tag{7.17}$$

Here $\mathbb{T}_1 = T_{LR,1}\mathbb{I}$, $\mathbb{T}_2 = T_{LR,2}\mathbb{I}$, and $\mathbb{T}_{12} = T_{12}\mathbb{I}$ where T_{12} accounts for any direct TLS-TLS coupling and the indices refer to the first or second TLS. $\mathbb{I}$ is the $N \times N$ identity matrix where N is the number of charge states chosen to represent the CPB Hamiltonian. $\mathbb{H}_{ij}$ with $i, j \in \{L, R\}$ is the CPB Hamiltonian with the respective TLS localized in either the left or right well. This form of the system Hamiltonian makes it apparent how the model can be generalized to include more TLS's. The block matrix grows to $2^m \times 2^m$ where m is the number of TLS's in the model. The diagonal blocks are CPB Hamiltonians with the TLS's localized in all the possible permutations of left and right wells, while the off-

diagonal terms are the various TLS tunneling and coupling terms.

If I use $N = 2$ charge basis states to represent the CPB Hamiltonians on the diagonal of Eq. 7.17, then $\mathbb{H}_{LL}$ is very similar to $\mathbb{H}_L$ and is given by

$$\mathbb{H}_{LL} = \begin{pmatrix} E_c\left(0-n_g\right)^2 & -\left(E_J+\Delta E_{J,1}/2+\Delta E_{J,2}/2\right)/2 \\ -\left(E_J+\Delta E_{J,1}/2+\Delta E_{J,2}/2\right)/2 & E_c\left(2-n_g\right)^2 \end{pmatrix}. \tag{7.18}$$

The forms of $\mathbb{H}_{RL}$ and $\mathbb{H}_{LR}$ are similar to that of $\mathbb{H}_R$ and include the electrostatic energy contribution of one of the TLS's. Specifically $\mathbb{H}_{RL}$ accounts for the first TLS

$$\mathbb{H}_{RL} = \begin{pmatrix} E_c\left(0-n_g\right)^2+E_{int,1}\left(0-n_g\right) & -\left(E_J-\Delta E_{J,1}/2+\Delta E_{J,2}/2\right)/2 \\ +E_{R,1} & \\ -\left(E_J-\Delta E_{J,1}/2+\Delta E_{J,2}/2\right)/2 & E_c\left(2-n_g\right)^2+E_{int,1}\left(2-n_g\right) \\ & +E_{R,1} \end{pmatrix} \tag{7.19}$$

while $\mathbb{H}_{LR}$ accounts for the second TLS

$$\mathbb{H}_{LR} = \begin{pmatrix} E_c\left(0-n_g\right)^2+E_{int,2}\left(0-n_g\right) & -\left(E_J+\Delta E_{J,1}/2-\Delta E_{J,2}/2\right)/2 \\ +E_{R,2} & \\ -\left(E_J+\Delta E_{J,1}/2-\Delta E_{J,2}/2\right)/2 & E_c\left(2-n_g\right)^2+E_{int,2}\left(2-n_g\right) \\ & +E_{R,2} \end{pmatrix}. \tag{7.20}$$

Finally $\mathbb{H}_{RR}$ includes the contributions of both TLS's and the CPB mediated TLS-TLS interaction term of the form $E_{int,1}E_{int,2}/2E_c$. Explicitly I find

$$\mathbb{H}_{RR} = \begin{pmatrix} E_c\left(0-n_g\right)^2+E_{int,1}\left(0-n_g\right) & \\ +E_{int,2}\left(0-n_g\right)+E_{R,1} & -\left(E_J-\Delta E_{J,1}/2-\Delta E_{J,2}/2\right)/2 \\ +E_{R,2}+E_{int,1}E_{int,2}/2E_c & \\ & E_c\left(2-n_g\right)^2+E_{int,1}\left(2-n_g\right) \\ -\left(E_J-\Delta E_{J,1}/2-\Delta E_{J,2}/2\right)/2 & +E_{int,2}\left(2-n_g\right)+E_{R,1} \\ & +E_{R,2}+E_{int,1}E_{int,2}/2E_c \end{pmatrix}. \tag{7.21}$$

I determined the transition frequencies using the same approach as for the single TLS Hamiltonian [see Sec. 7.2.1]. I numerically diagonalized Eq. 7.17 using Mathematica and

then calculated the transition frequency from the ground state to the nth excited state of the system using $f_n = (\lambda_{n+1} - \lambda_1)/h$ where λ_n is the corresponding eigenvalue.

8 CPB-TLS Interaction Experiments

8.1 Non-resonant CPB-TLS Interaction

During my initial characterization of Device 2 [see Ch. 5], its anomalous twinned spectrum stood out and concerned me, especially as a possible reason to reject it as a viable CPB qubit. However, after I observed that the qubit performance was largely unaffected, I proceeded with the lifetime and decoupling studies [see Ch. 6] while simultaneously recording detailed spectroscopy for later examination. At the time I strongly suspected this behavior was due to coupling to a TLS but I didn't yet have a model to explain it. After the conclusion of my experimental work with Device 2, I developed the necessary model [see Ch. 7] and deduced that this was an instance of a strong, non-resonant CPB-TLS interaction. In this chapter I present my results in a more logical but not chronological order. I first present my spectroscopy of Device 2 at various flux bias values and then fit those spectra to models with non-resonant single and double TLS's. I next present my reasons for eliminating other possible models and discuss what conclusions I can draw from my fits. Finally in Sec. 8.2 I discuss other spectral anomalies I observed in Device 2 but didn't model.

8.1.1 System Spectrum

Following the preliminary characterization of Device 2, I took detailed two tone spectroscopy [see Sec. 5.2.1] with the Josephson energy E_J set near E_J^{sum}. For all of these high resolution two tone measurements, I used a continuous pump tone power slightly above that needed to saturate the qubit transitions and a continuous probe tone power corresponding to approximately $\bar{n} \approx 25$ photons in the resonator. I employed my previously discussed procedures to improve the quality of the data [see Sec. 5.3.1], which included recording multiple frequency slices of spectroscopy, post-processing them by ref-

erencing to a common background feature to remove gate voltage V_g offsets, and then averaging and stitching the slices together to obtain the final spectrum.

Fig. 8.1(a) shows the high quality two tone spectrum taken with the Josephson energy E_J tuned near E_J^{sum}. Due to flux jumps and hysteresis of the local flux though the CPB loop [see Sec. 5.2.2], I'm not able to specify the actual flux bias Φ/Φ_0 of the CPB and will instead identify the plots by the transition frequency of the lowest visible parabola. Using this naming convention I will refer to Fig. 8.1(a) as the 7.06 GHz spectrum. Two parabolas with different curvatures and offset from each other by ≈ 0.25 GHz in frequency and ≈ 0.04 in reduced gate bias are clearly visible. Other notable features include a significant widening of the bottom of the highest spectral parabola and weak sections of two more parabolas in the top right of the image. The horizontal dark line at ≈ 7.39 GHz is due to a brief e jump during measurement while small sharp horizontal offsets at 30 MHz intervals are due to imperfect stitching of the spectrum slices. They are most prominent in this plot as this was my first high quality two tone spectrum and I hadn't yet optimized the stitching procedure.

I adjusted the external flux bias to lower the Josephson energy E_J of the CPB and took the 6.65 GHz spectrum [see Fig. 8.1(b)]. The spectrum appears cleaner due to improved gate offset correction and a larger number of averages. Again two parabolas with varied curvature are visible, this time offset ≈ 0.17 GHz in frequency and ≈ 0.04 in reduced gate voltage. Broadening of the bottom left of the higher parabola is also present and coincides with a decrease in the visibility of the lower parabola. A new and interesting feature is the faint TLS ghost between $6.75 - 6.85$ GHz, consisting of a curved line connecting the two sides of the lower parabola. It bears a strong resemblance to a saw-tooth TLS only transition [see Fig. 7.2], similar to that observed by Z. Kim [61]. The lack of an obvious associated splitting at the intersection of the ghost and the lower parabola suggest it may be due to a resonant interaction with TLS with a small tunneling energy T_{LR}.

As I continued tuning down the Josephson energy E_J, I discovered another anomaly in the system spectrum. Dubbed the dead zone, I found that between $\approx 5.6 - 6.5$ GHz the system spectrum had very low visibility and, where it was visible, was highly distorted. Fig. 8.2 shows two examples of spectroscopy taken with the Josephson energy E_J lying within the dead zone. For example, in the ≈ 6.50 GHz spectrum [see Fig. 8.2(a)], taken with E_J near the top of the dead zone, the bottom parabola is only partially visible.

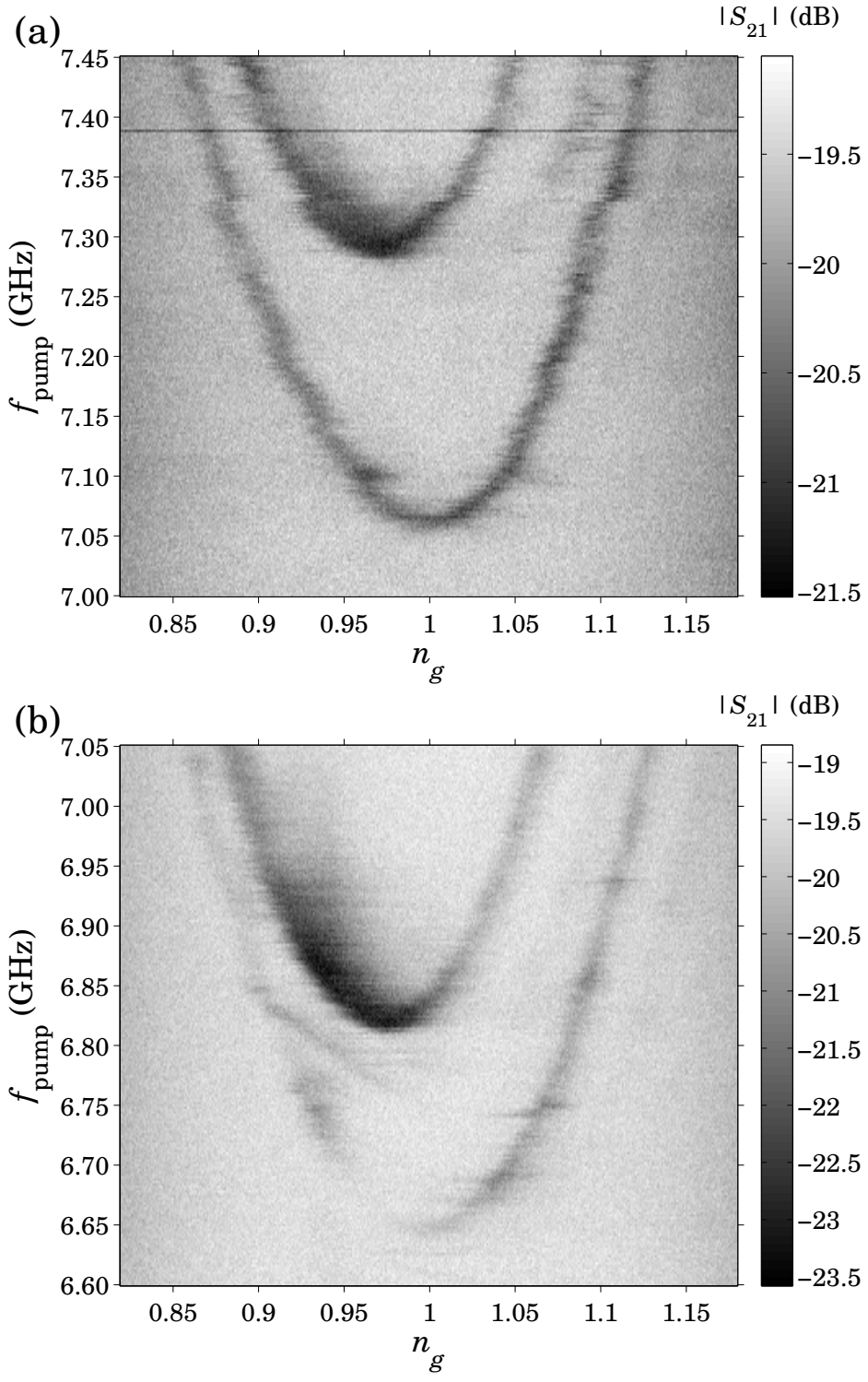

Figure 8.1: (a) Gray scale image showing transmitted amplitude plot of the 7.06 GHz two tone spectrum of Device 2. The dark horizontal line at ≈ 7.39 GHz is a noise artifact. (b) Transmitted amplitude plot of the 6.65 GHz two tone spectrum. A faint TLS ghost is visible between 6.75 – 6.85 GHz. A pair of CPB-like parabolas with differing curvatures and offset in frequency f_{pump} and reduced gate bias n_g is present in both data sets.

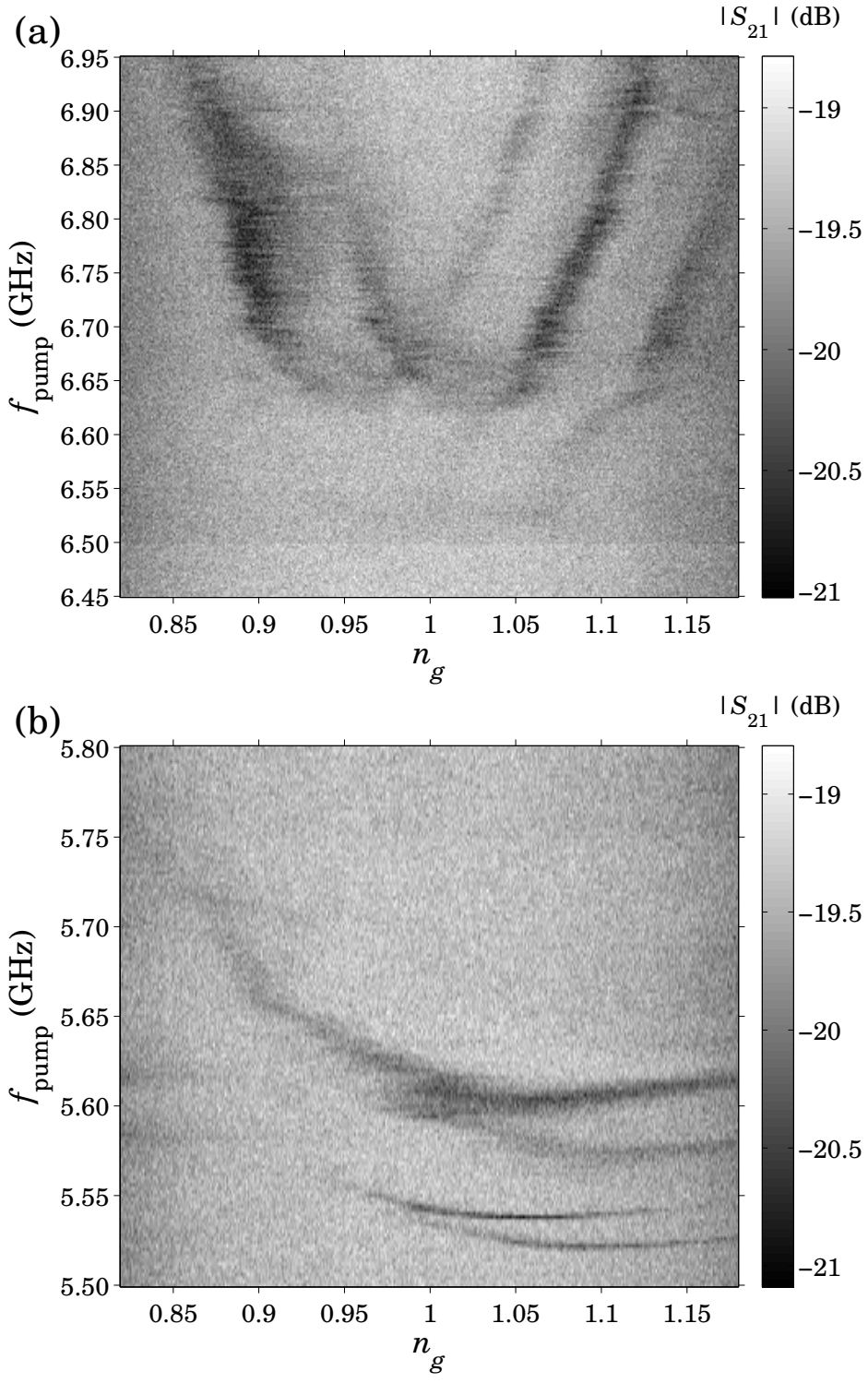

Figure 8.2: (a) Transmitted amplitude plot of the $\approx 6.50\,\mathrm{GHz}$ two tone spectrum of Device 2. The spectrum appears doubly twinned, possibly due to the effect of a discrete charge fluctuator. (b) Transmitted amplitude plot of the $5.52\,\mathrm{GHz}$ two tone spectrum. The parabolas are quadrupled and highly distorted. Both data sets illustrate the effect of the dead zone between $\approx 5.6 - 6.5\,\mathrm{GHz}$.

Furthermore, the entire spectrum appears twinned, possibly due to a discrete charge fluctuator affecting the gate voltage n_g. The 5.52 GHz spectrum [see Fig. 8.2(b)], taken with E_J adjusted near the bottom of the dead zone, is even more striking as four highly distorted parabolas are present. This quadrupling, rather than twinning of the CPB spectrum, foreshadowed the system spectrum at even lower Josephson energy E_J values.

Below the dead zone and the resonator resonance at $\omega_{res}/2\pi = 5.472$ GHz, the system spectrum returned to its CPB-like appearance with one significant difference—it was quadrupled rather than twinned. This was difficult to make out at first but became clearer as the Josephson energy E_J was set lower and lower. The start of this progression is visible in Figs. 8.3 and 8.4 which contain, respectively, the 5.20 GHz and 5.05 GHz spectra. I included both the transmitted amplitude and phase for each spectrum because I found that for these data sets, some features were more prominent in one or the other and viewing both side by side presented a more complete picture. The lowest two parabola are offset by $n_g \approx 0.02$ in gate voltage and less than 20 MHz in frequency. This is most easily seen in the phase data of the 5.05 GHz spectrum [see Fig. 8.4(b)]. However, above the resonator and near the bottom of the dead zone, the two parabolas curve sharply outward at ≈ 5.7 GHz on the left and ≈ 5.6 GHz on the right. I'm not certain of the origin of this behavior although it's reminiscent of an avoided crossing with a charged TLS with a very large tunneling energy T_{LR} [see Fig. 7.2]. The two highest parabolas are very difficult to resolve in these two data sets although it's possible to make them out in the phase data of the 5.20 GHz spectrum [see Fig. 8.3(b)]. Finally, there is another TLS ghost visible at ≈ 6.0 GHz in the transmitted phase of both of the spectra.

As I tuned the Josephson energy E_J further such that all four parabola were lying below the dead zone and the resonator, the system spectrum became more recognizable and CPB-like. Figure 8.5 contains the 4.85 GHz spectrum, taken in two sections with one below the resonator [see Fig. 8.5(b)] and one above [see Fig. 8.5(a)]. Unfortunately there was a higher than average amount of charge noise that day [see Sec. 5.3.1] and the spectrum is not very high quality. The two lowest parabola are offset by $n_g \approx 0.02$ in gate voltage and less than 20 MHz in frequency and are relatively easy to identify. On the other hand, the two highest parabola are very faint but I believe the bottom of one of them can be made out at ≈ 5.3 GHz. The spectrum above the resonator contains sections of all four spectral parabolas. The dark vertical stripes at $n_g \approx 0.9 \pm 0.01$, $n_g \approx 1.04$,

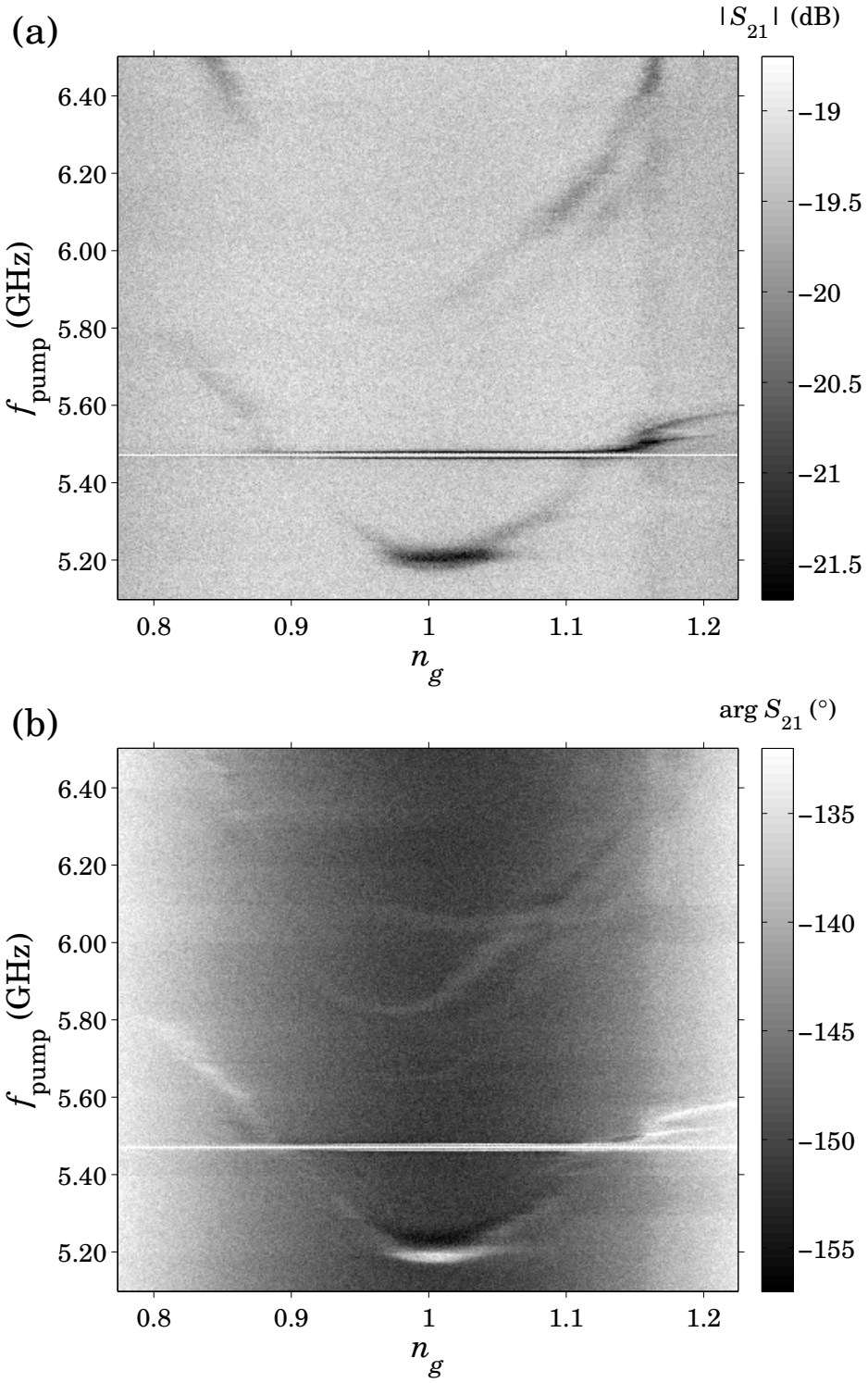

Figure 8.3: (a) Transmitted amplitude and (b) phase plots of the 5.20 GHz two tone spectrum of Device 2. The horizontal bands at 5.472 GHz are artifacts due to the resonator. A TLS ghost is visible at ≈ 6.0 GHz in the transmitted phase.

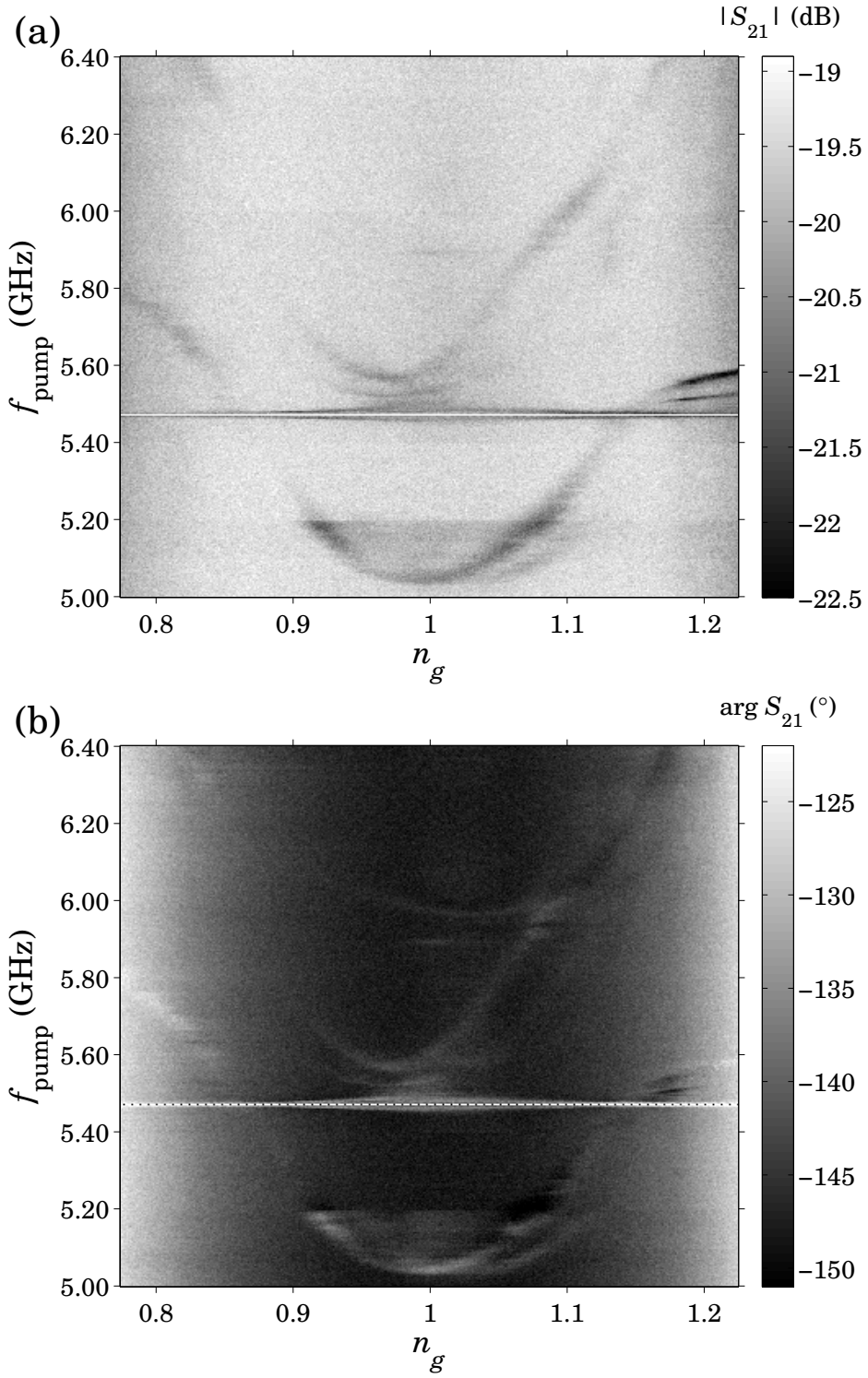

Figure 8.4: (a) Transmitted amplitude and (b) phase plots of the 5.05 GHz two tone spectrum of Device 2. The horizontal bands at 5.472 GHz are artifacts due to the resonator. A TLS ghost is visible at ≈ 6.0 GHz in the transmitted phase.

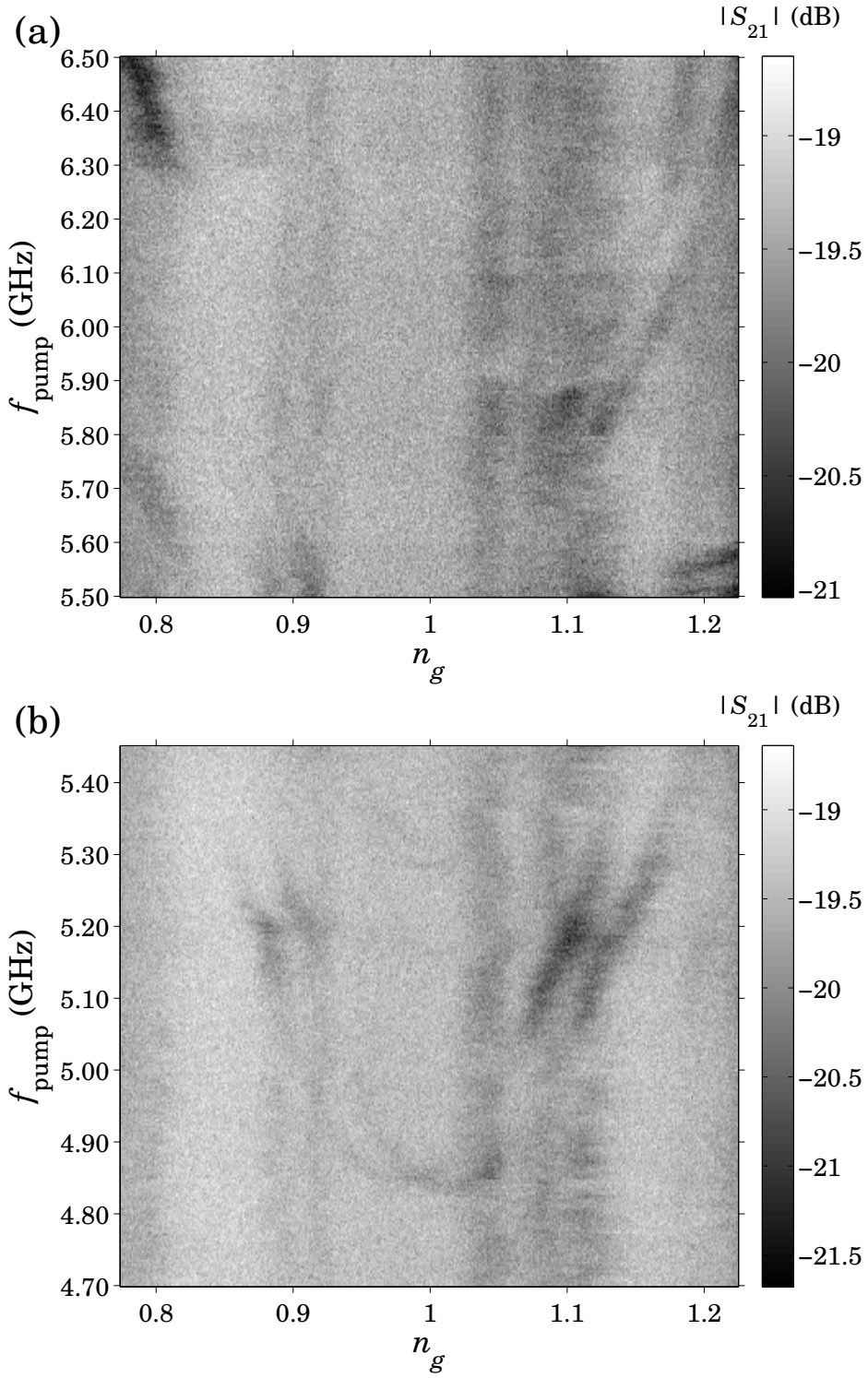

Figure 8.5: (a) Top and (b) bottom sections of the transmitted amplitude of the 4.85 GHz two tone spectrum of Device 2. Although difficult to make out due to the dead zone between $\approx 5.6 - 6.5$ GHz, four distorted CPB-like parabolas are present.

and $n_g \approx 1.1$ are due to the resonant crossings between the two highest parabolas of the CPB and the resonator. A degeneracy between the CPB and the resonator results in an avoided crossing of size $2g(n_g)$ (the vacuum Rabi splitting) [see Sec. 2.5.1] and shifts the resonance at that n_g away from ω_{res} regardless of the state of the qubit. This shift produces a similar effect to the dispersive shift $\chi(n_g)$ I used to readout the state of the qubit [see Sec. 5.2.1]. In this case the result is a decrease in the transmitted signal which is visible as a dark vertical band in the gray scale plot. I'm not certain why only the upper set of parabolas produces such features as I would expect them to be visible for all the parabolas.

When the Josephson energy E_J was near the lowest end of the range I studied, I was able to acquire some clear high quality spectroscopy that showcased the spectral quadrupling in Device 2. Four parabolas are present and easy to resolve in both the 4.45 GHz spectrum [see Fig. 8.6(a)] and the 3.95 GHz spectrum [see Fig. 8.6(b)]. In both cases the lower set of parabolas are offset by $n_g \approx 0.02$ in gate voltage and less than 20 MHz in frequency while the upper set is offset by $n_g \approx 0.03$ in gate voltage and ≈ 50 MHz in frequency. The upper set is ≈ 400 MHz higher than the lower set and there is variation in the curvature of all the parabolas. Besides the higher visibility of the lower pair, there are no other significant differences between the CPB-like parabolas. It's also noteworthy that there are no resolvable avoided crossings present wherever two parabolas happen to intersect. As in the 4.85 GHz spectrum [see Fig. 8.5(b)], the dark vertical stripes are due to resonant crossings between the CPB transitions and the resonator and again only some of the expected set of lines are visible.

The spectroscopy presented in Fig. 8.6 is qualitatively different from what I observed after initially cooling down the sample [see Fig. 5.5(a)]. Specifically the upper pair of parabolas weren't present in the preliminary data. This may be because the upper pair was too faint to be visible in that data set. Alternatively, the properties of the TLS's coupled to the CPB may have changed in the first week after cooldown as the system equilibrated. Finally, I didn't perform detailed spectroscopy below 4 GHz because this was outside the range of several microwave components in the measurement chain [see Sec. 4.3].

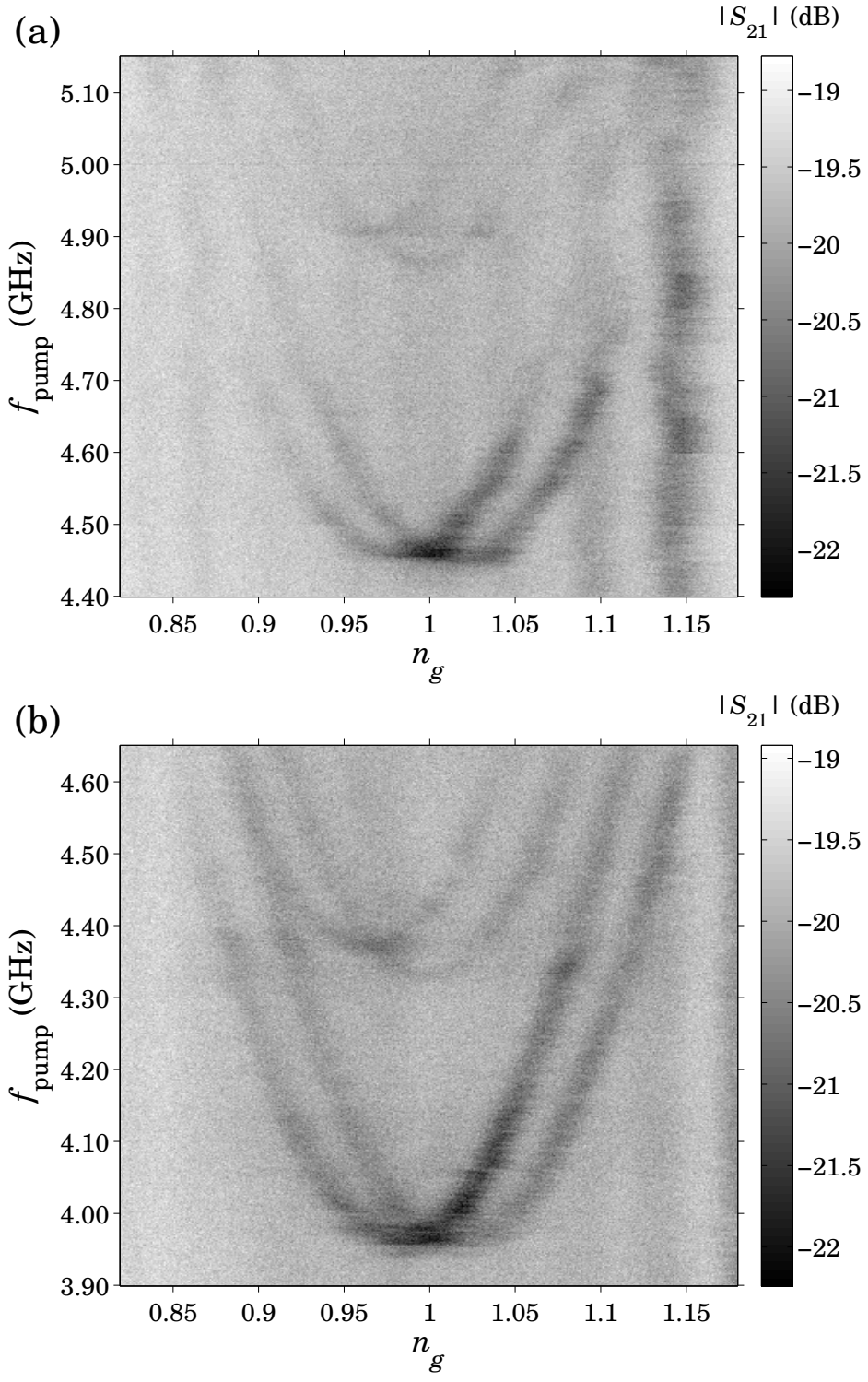

Figure 8.6: (a) Transmitted amplitude plot of the 4.45 GHz two tone spectrum of Device 2. (b) Transmitted amplitude plot of the 3.95 GHz two tone spectrum. Four CPB-like parabolas with differing curvatures and offset in frequency f_{pump} and reduced gate bias n_g are present in both data sets. The dark vertical stripes at $n_g = \{0.83, 0.87, 1.09, 1.13\}$ are due to resonant crossings between the CPB transitions and the resonator.

8.1.2 Fits to the Single and Double TLS Models

Before I could develop a model to explain my data, I needed to deduce the most likely nature of the interaction between the qubit and the TLS responsible for this behavior. The first consideration is whether the fluctuator is coherently or incoherently coupled to the qubit. An incoherently coupled fluctuator may be viewed as acting effectively like a changing external control parameter. For example, an incoherently coupled critical current fluctuator or flux fluctuator would cause fluctuations in E_J and yield two values of the resonator dispersive shift χ in addition to twinning of the qubit spectral parabolas. If the dispersive shift χ were twinned then either the ground state resonator frequency would also be twinned or the resonator linewidth would be broadened. Instead of either of those effects, I observed a total dispersive shift χ_{tot} consistent with contributions from two or more levels [see Sec. 5.2.3], implying a coherently coupled TLS. Furthermore, previous instances of an incoherently coupled fluctuator, such as the TLS that caused the demise of Device 1 [see Sec. 6.2.3] [71] or as reported by others [74], rendered the qubit inoperable. This wasn't the case in Device 2 as I was able to measure reasonable excited state lifetimes T_1 in the $4-30\,\mu$s range and record Rabi oscillations with decay times comparable to those of Device 1 [see Ch. 6].

Having established that the qubit and TLS were coherently coupled, I next had to figure out how the qubit was coupled to the TLS. One possibility was that the curvature changes and frequency offsets between the various spectral parabolas could be caused by a flux fluctuator, such as a moving vortex, that modulates the Josephson energy $E_J(\Phi)$. If it was a vortex, its effect would be minimal when the applied flux is minimal and increase as $E_J(\Phi)$ is reduced by an external flux bias [see Sec. 3.4]. Instead, as I reduced the Josephson energy $E_J(\Phi)$ by applying a magnetic field, I saw the opposite trend in the spectroscopy [see Sec. 8.1.1], indicating that a flux fluctuator couldn't produce the measured spectrum.

An important clue about the identity of the fluctuator is that the shifts in gate voltage n_g and frequency offsets between the parabolas are correlated. This suggests a defect that is coupling to more than one degree of freedom. Altogether these observations suggest a TLS that's coupled to the CPB via both charge and critical current. One possibility for such a TLS is a charged defect located in the AlO_x tunnel barrier that modulates the junction critical current. The spectrum of a qubit containing this type of TLS would be $2e$

periodic in gate voltage, which is consistent with my observations [see Sec. 5.1.2].

Based on this identification of a charge and critical current fluctuator, I developed the corresponding model described in Chapter 7. Using this model I fit the theoretical spectrum to my measured spectroscopy data. Considering that the spectrum was twinned above the dead zone but quadrupled below, I first used the single TLS model and fit only the top pair of parabolas. The solid red curves in Fig. 8.7(a) show the predicted transitions for the 7.06 GHz spectrum [see Fig. 8.1(a)]. Similarly Fig. 8.7(b) contains the fits to the 6.65 GHz spectrum [see Fig. 8.1(b)], Fig. 8.8(a) contains the fits to the 4.45 GHz spectrum [see Fig. 8.6(a)], and Fig. 8.8(b) contains the fits to the 3.95 GHz spectrum [see Fig. 8.6(b)]. The optimal fit parameters for the single TLS model are summarized in Table 8.1. All the fits look reasonable except for the obvious difference that the model only yields two parabolas in Fig. 8.8. The remaining data sets weren't fit because their spectra were either too faint or too distorted, most likely by an effect or interaction outside the scope of the model.

I obtained the model spectra by numerically diagonalizing the system Hamiltonian [see Eq. 7.13] with Mathematica and then fitting it to the data. I manually explored the range of possible parameter values and selected that which I thought gave the best fit. I wasn't able to use least squares fitting to automatically and objectively fit the data because of the complexity of calculating the spectrum from the system Hamiltonian and because the best representations I had of the spectrum were gray scale plots. Since in Device 2 the charging and Josephson energies were of the same magnitude ($E_c \approx E_J$) I included $N = 4$ charge states in the CPB Hamiltonian block matrices to accurately represent the qubit.

The primary effects of each model parameter were described in Sec. 7.2.2. This served as an excellent guide for selecting both the initial values and a direction to explore in the parameter space in order to improve subsequent fit iterations. I found that I could vary the fit parameters by about 20% and still maintain a reasonable fit. This was partly due to the complementary effects of the Josephson coupling $\Delta E_{J,1}$ and the TLS well asymmetry $E_{R,1}$ in producing the frequency offset between the CPB-like parabolas. A related consideration was the TLS transition energy $\hbar\omega_{TLS,1}$, set by $E_{R,1}$, $T_{LR,1}$, and $\Delta E_{J,1}$. Although I can't say with certainty that I observed a TLS-only transition [see Sec. 8.2.2], I knew that $\hbar\omega_{TLS,1}$ needed to be sufficiently high, in the $1-2$ GHz range, so as not to be thermally excited. If the TLS was in its excited state, there would have been additional

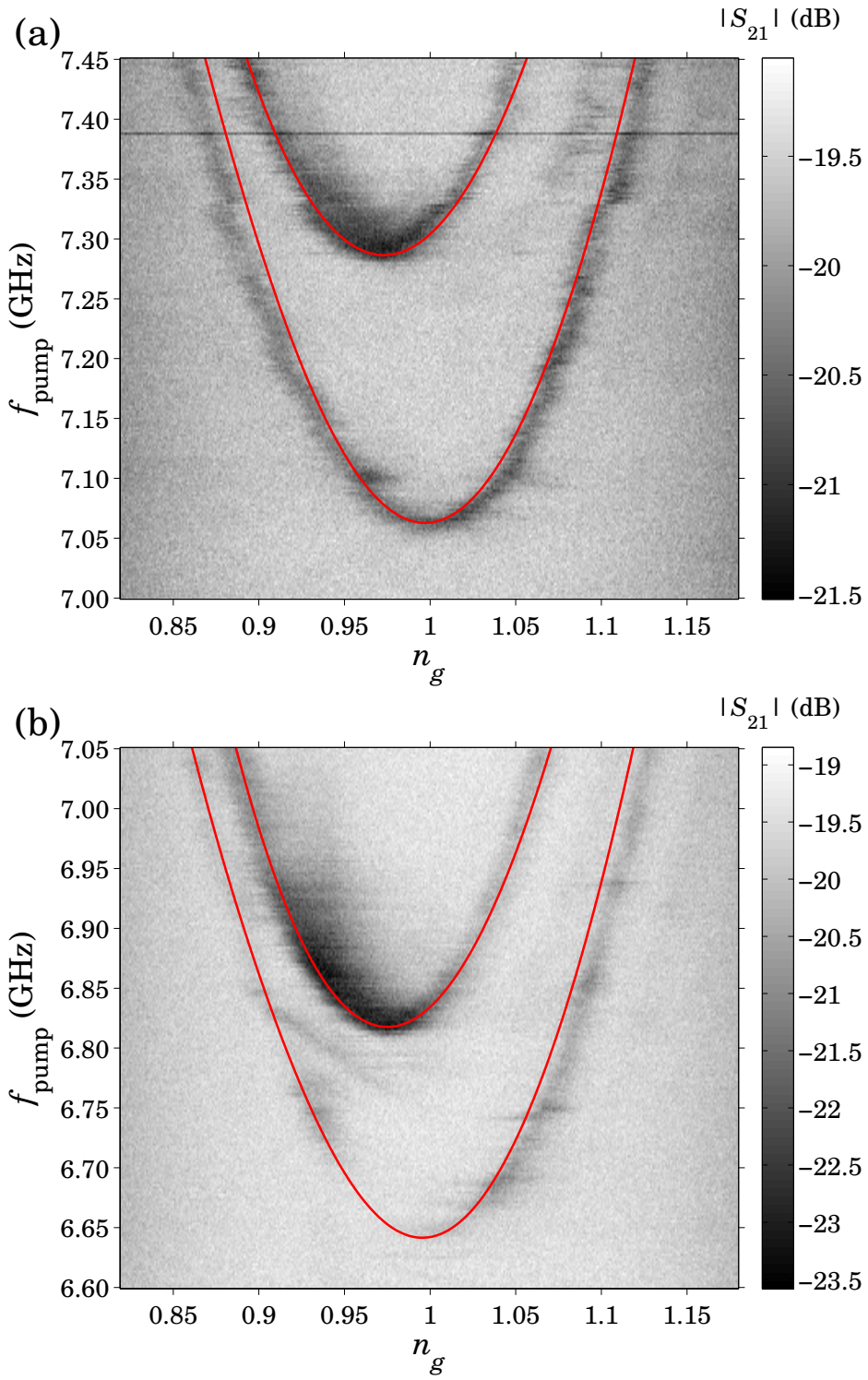

Figure 8.7: Fits (red) of the single TLS model to (a) the 7.06 GHz spectrum [see Fig. 8.1(a)] and (b) the 6.65 GHz spectrum [see Fig. 8.1(b)] of Device 2. The optimal fit parameters are summarized in Table 8.1.

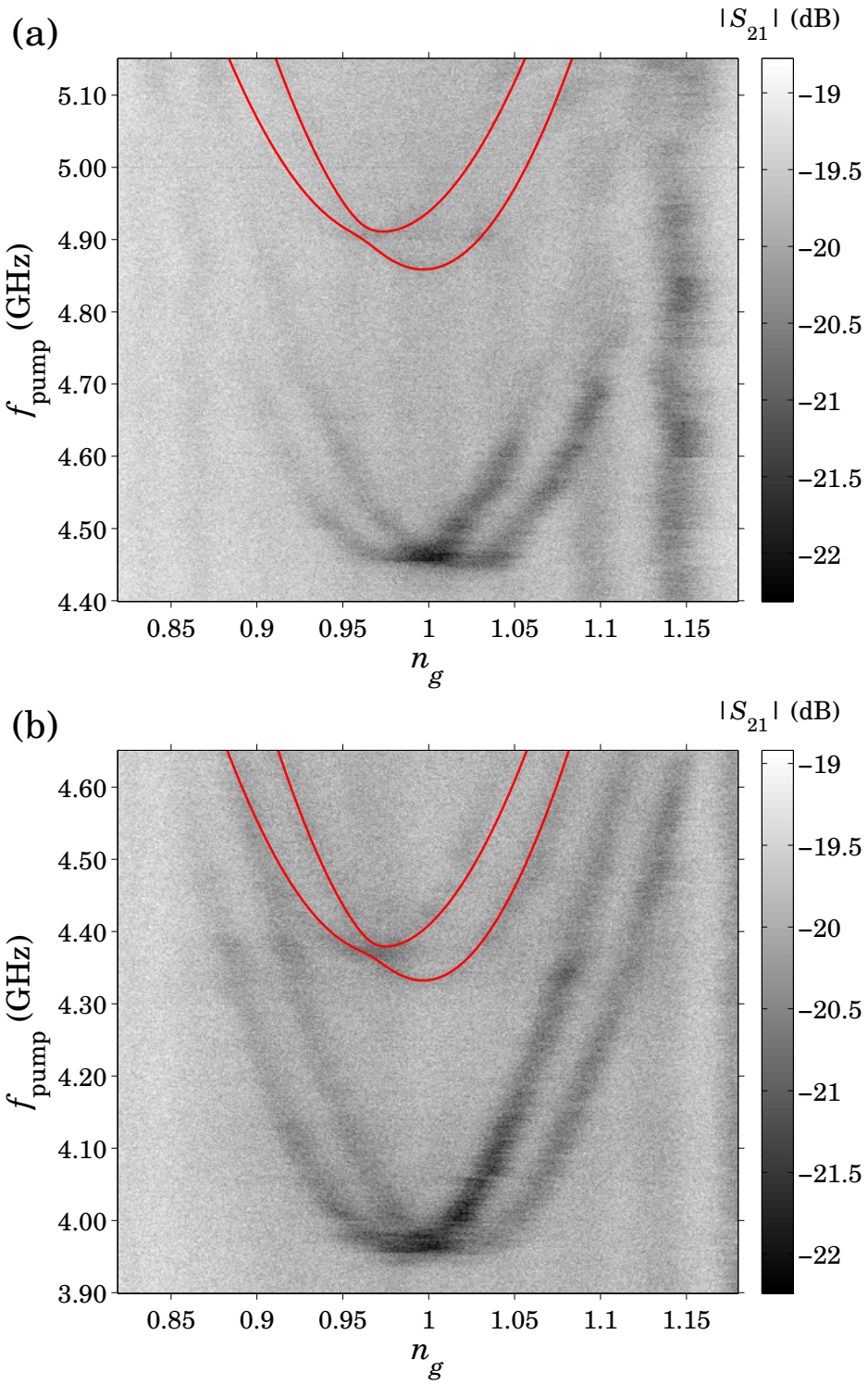

Figure 8.8: Fits (red) of the single TLS model to (a) the 4.45 GHz spectrum [see Fig. 8.6(a)] and (b) the 3.95 GHz spectrum [see Fig. 8.6(b)] of Device 2. The optimal fit parameters are summarized in Table 8.1.

Table 8.1: Optimal fit parameters of the single TLS model to the 7.06 GHz, [see Fig. 8.1(a)], the 6.65 GHz [see Fig. 8.1(b)], the 4.45 GHz [see Fig. 8.6(a)], and the 3.95 GHz [see Fig. 8.6(b)] spectra.

spectrum	3.95 GHz	4.45 GHz	6.65 GHz	7.06 GHz
model parameter (GHz)				
E_c/h	4.5	4.5	4.5	4.5
E_J/h	3.64	4.16	5.93	6.33
$\Delta E_{J,1}/h$	1.50	1.54	1.84	2.02
$E_{R,1}/h$	0.62	0.62	0.62	0.62
$E_{int,1}/h$	0.35	0.35	0.35	0.35
$T_{LR,1}/h$	0.01	0.01	0.06	0.06

Table 8.2: Optimal fit parameters of the double TLS model to the 4.45 GHz [see Fig. 8.6(a)] and the 3.95 GHz [see Fig. 8.6(b)] spectra.

spectrum	3.95 GHz	4.45 GHz
model parameter (GHz)		
E_c/h	4.3	4.3
E_J/h	2.79	3.43
$\Delta E_{J,1}/h$	1.36	1.40
$E_{R,1}/h$	0.62	0.62
$E_{int,1}/h$	−0.40	−0.40
$T_{LR,1}/h$	0.00	0.00
$\Delta E_{J,2}/h$	−1.00	−0.68
$E_{R,2}/h$	−0.82	−0.69
$E_{int,2}/h$	0.13	0.15
$T_{LR,2}/h$	0.04	0.04
T_{12}/h	0.04	0.04

transitions in the model that I didn't observe. The TLS tunneling strength $T_{LR,1}$ was also bounded by a pair of constraints. The fact that I couldn't resolve clear avoided crossings between the various parabolas placed an upper bound on the $T_{LR,1}$ value. $T_{LR,1}$ also needs to be sufficiently large because the visibility of parabolas with a significant TLS component scales with $T_{LR,1}$ [see Sec. 7.2.2].

I followed up the above analysis by fitting the double TLS model to data sets where the spectrum was quadrupled. The solid red curves in Fig. 8.9(a) are the fits to the 4.45 GHz spectrum [see Fig. 8.6(a)] while Fig. 8.9(b) shows the fits to the 3.95 GHz spectrum [see Fig. 8.6(b)]. The optimal fit parameters for the double TLS model are summarized in Table 8.2. Again, the fits look reasonable. I excluded data sets where the spectroscopy was too faint, too distorted, or didn't clearly show 4 parabolas. The fitting procedure that I followed and the parameter value considerations were the same as in the single TLS model case.

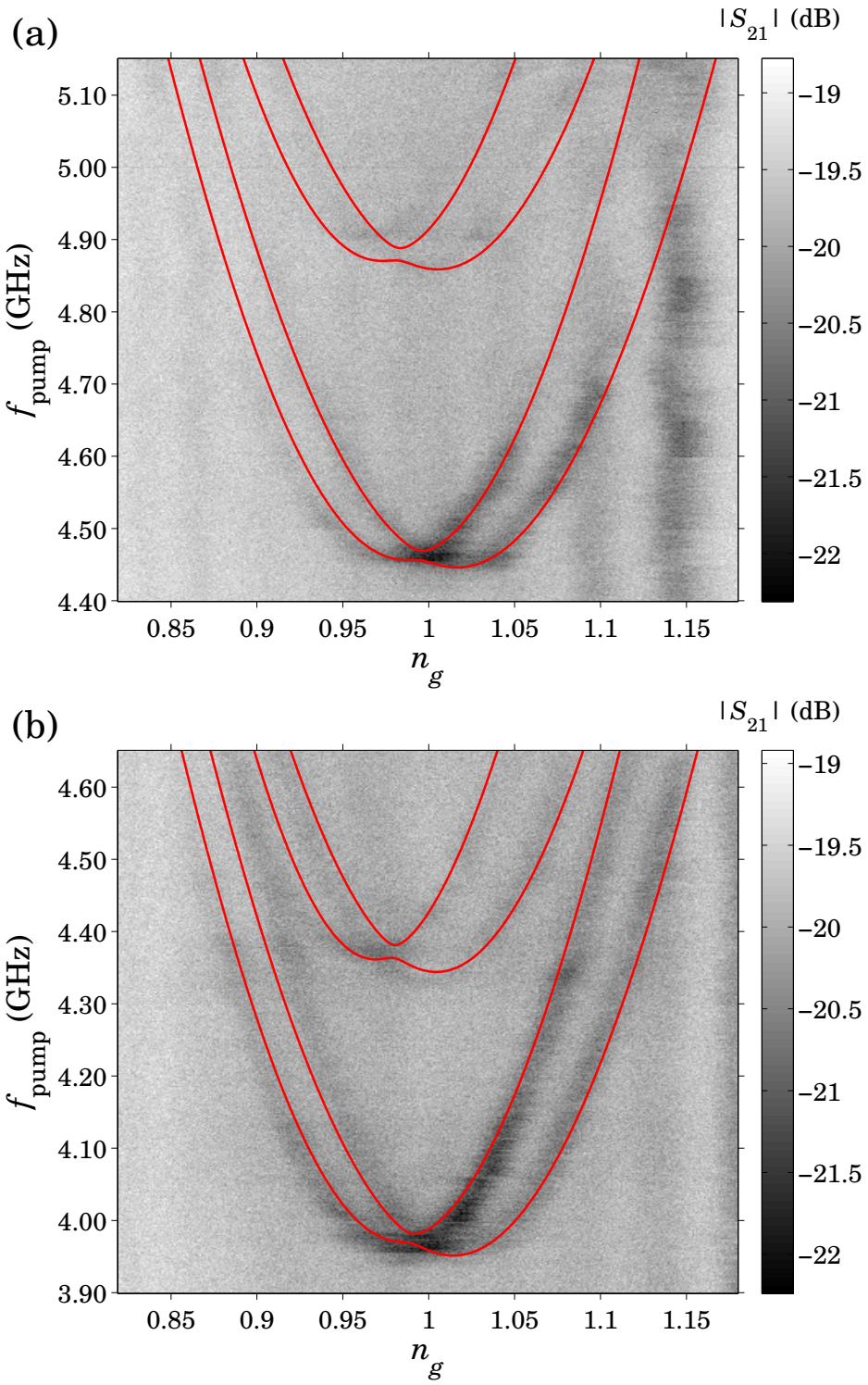

Figure 8.9: Fits (red) of the double TLS model to (a) the 4.45 GHz spectrum [see Fig. 8.6(a)] and (b) the 3.95 GHz spectrum [see Fig. 8.6(b)] of Device 2. The optimal fit parameters are summarized in Table 8.2.

The fit parameters for both the single and double TLS model cases turned out individually to be very self-consistent. As would be expected, only E_J and $\Delta E_{J,k}$ needed to be adjusted between data sets at different external flux bias values. The only exception was a change in $T_{LR,1}$ in the single TLS model fits, which varied whether the qubit was below or above the resonator ω_{res} and the dead zone. I interpret this self-consistency as an indication that the model is a reasonable description of the underlying physics and it was able to satisfactorily capture the microscopic details.

The fit E_c and E_J values changed between the single and double TLS models. The decrease in E_J is consistent with the fact that in the double TLS model the effective Josephson energy is given by $E_{J,\text{eff}} = E_J \pm \Delta E_{J,1} \pm \Delta E_{J,2}$, as compared to $E_{J,\text{eff}} = E_J \pm \Delta E_{J,1}$ for the single TLS model. There was a corresponding change in E_c because the curvature, which shouldn't change, depends on the ratio $E_c^2/E_{J,\text{eff}}$. The TLS and coupling parameters, such as the charge coupling $E_{int,1}$, also changed when switching from the single to the double TLS model. This indicates that the double TLS model is needed to explain the full quadrupled spectrum and suggests that there's significant interaction between the TLS's.

8.1.3 Discussion and Comparison to the Resonant Case

Based on the optimal fit parameters, I can draw several conclusions regarding the properties of the CPB and the TLS's. The fractional change of the Josephson energy $\Delta E_{J,k}/E_J \approx 30-40\%$ is quite large. A single TLS is expected to block or modulate tunneling in an area of about $\Delta A \approx 1-10\,\text{nm}^2$ [219, 201]. Assuming a uniform tunnel barrier and that each junction in Device 2 has area $A = 350\,\text{nm} \times 150\,\text{nm}$ [see Sec. 6.3], $\Delta A \approx 1-10\,\text{nm}^2$ would correspond to a relative change in the Josephson energy of $\Delta E_{J,k}/E_J = \Delta A/A \approx 2\times10^{-5} - 2\times10^{-4}$ in Device 2, a result which is much smaller than my extracted values. On the other hand, if the junction tunnel barrier was non-uniform with a few dominant conduction channels, a TLS located near one of the channels could produce a large relative change in the Josephson energy. Non-uniform tunnel barriers have been reported in Al/AlO_x/Al junctions [220] and is a possible explanation for the observed behavior.

The two TLS parameters contain information about the physical nature of the defects and also allow me to estimate their relaxation time T_{TLS}. The longitudinal relaxation

rate of a TLS in an amorphous solid is limited by phonon emission to

$$\frac{1}{T_{TLS}} = \Gamma_{TLS} \geq \alpha \hbar \omega_{TLS} T_{LR}^2 \coth(\hbar\omega_{TLS}/2k_B T) \tag{8.1}$$

where T is the temperature and α is a material dependent constant [221]. Using the fit parameters of Z. Kim and his estimate of the TLS lifetime $T_{TLS} \approx 100\,\text{ns}$ [61], I estimated $1/\alpha \approx 10^2\,\mu\text{s}\cdot\text{GHz}^3\cdot h^3$ for the dielectric AlO_x in the tunnel junction barrier. Using this value and my fit parameters for Device 2, I placed an upper bound of $T_{k,TLS} \lessapprox 1\,\text{ms}$ on the excited state lifetime of both TLS's. Transitions to the excited states of Device 2 involve both pure CPB and TLS components and consequently the total decay rate is a weighted average of the pure CPB and TLS decay rates [see Sec. 7.1.2]. A long lived TLS is consistent with the reasonably long qubit lifetimes $T_1 \approx 4-30\,\mu\text{s}$ I observed and differs from the qubit lifetime suppression caused by short lived TLS's reported by Z. Kim [61].

All of the TLS tunneling elements $T_{LR,k} \lesssim 0.06\,\text{GHz}$ are small compared to the other energy scales in the system. This indicates that the defects are tunneling between well isolated sites. There's also a surprising relationship between the various tunneling parameters. If I assume two independent fluctuators, the most likely scenario due to the strong shielding of electric fields in the dielectric of the junction by the electrodes, then the individual TLS's should have $T_{LR,1} \neq 0$ and $T_{LR,2} \neq 0$ but the TLS-TLS coupling strength should be $T_{12} = 0$. My fits on the other hand give $T_{LR,2} \neq 0$ and $T_{12} \neq 0$ but $T_{LR,1} = 0$. This suggests that either the TLS's are coupled to each other or that the two TLS's are in reality a more complicated structure, such as multiple levels of the same defect.

When the Josephson coupling $\Delta E_{J,k}$ is set to zero, the model becomes equivalent to that used by Z. Kim to describe avoided crossings in a CPB [61] and I may directly compare the fit parameters of the two samples. My TLS tunneling rates $T_{LR,k}$ are substantially smaller than the $3-13\,\text{GHz}$ range found by Z. Kim. Similarly, my well asymmetry energies $E_R = 0.6-0.8\,\text{GHz}$ are significantly less than the $E_R = 7-39\,\text{GHz}$ reported by Z. Kim. I can also estimate the minimum hopping distance of the defects. Starting with the definition of the CPB-TLS charge interaction energy $E_{int} = 2E_c Q_{TLS} x_R/ed$ [see Sec. 7.2] and assuming a TLS charge of $Q_{TLS} = e$ and a tunnel barrier thickness of $d = 1\,\text{nm}$, I find minimum hopping distances of $0.2\,\text{Å}$ and $0.45\,\text{Å}$ for the two TLS's in Device 2. This agrees reasonably well with the estimate of $0.32-0.83\,\text{Å}$ obtained by Z. Kim [61] and is also a

reasonable value given that $\approx 1-2$Å is a typical interatomic distance in an amorphous dielectric.

My CPB-TLS interaction conclusions are interesting for several reasons. Unlike the avoided crossings characterized by Z. Kim [61] and others [208, 204, 22, 209, 205, 116, 206, 210], my data is an example of a strong non-resonant qubit-TLS interaction. To the best of my knowledge, this is the first report of this type of interaction in a superconducting qubit. The nature of the coupling is also novel. The fluctuator is coupled to the CPB charge qubit via both the charge and critical current degrees of freedom. This type of joint coupling has been theoretically suggested [196] but apparently hasn't been experimentally reported until now. While non-uniform tunnel barriers in Al/AlO$_x$/Al junctions have been previously examined [220], my work highlights the importance of junction non-uniformity in the context of superconducting qubits. Specifically, interaction between tunneling hot spots and nearby defects could limit qubit performance and suggests that the situation could be improved by making more uniform junctions.

The reason this behavior was observed in Device 2 is undoubtedly due to a combination of random events and sample selection bias. A strong, non-resonant qubit-TLS interaction requires that the TLS parameters be in small section of the full parameter space. Specifically the coupling needs to be sufficiently large that the twinned parabolas are resolvable yet the TLS transition frequency needs to be low enough so that an avoided crossing isn't formed. Additionally, as is the case in Device 2, it helps if the frequency offsets due to ΔE_J and E_R counteract each other and the total frequency offset between the twinned parabolas isn't so large so that one of them is missed during spectroscopy. By chance all of this occurred in Device 2. Finding two such defects in the same sample is even less likely but the TLS fit parameters suggest they are related.

Selection bias is also an important factor during initial device characterization. I decide which samples to keep and which to discard based on how well they perform as a qubit. However, if a sample has especially conspicuous features, such as an anomalous spectrum, many groups would throw it out and move on to a cleaner looking device. Instead, in the case of Device 2 I decided to study it in detail even though it didn't meet all the design criteria of the qubit. Samples with conspicuously anomalous features may also have unusual parameter values. There is also an element of luck in this selection process. For example, if Device 2 was coupled only to a critical current fluctuator, I might

have assumed the resulting frequency offset between the twinned parabolas was due to an incoherent flux fluctuator. In that scenario I would have either discarded it or thermal cycled it, which could have changed the TLS properties, and ultimately I would have never thoroughly characterized an instance of strong, non-resonant qubit-TLS interaction.

The single and double TLS model was largely successful in explaining the spectral twinning and quadrupling but there is still room for expansion to account for other anomalous dynamics or spectral features. One logical generalization would be the inclusion of the resonator. This would allow a theoretical calculation of the expected dispersive shift and a comparison with my data. Furthermore, it might elucidate if the resonator was involved in the formation of the dead zone—its lower boundary lies very close to ω_{res}—or if it's responsible for the transition from a twinned to a quadrupled spectrum—a transition that took place near ω_{res}. A full solution of the system dynamics including the resonator may also explain why only half of the spectral parabolas were visible when measured with a pulsed probe.

8.2 Spectral Anomalies in Device 2

The multiplicity of parabolas was the most prominent anomalous feature of the spectrum of Device 2 but it wasn't the only one. In this section I detail some of the other anomalies I observed. These weren't studied in detail and I didn't track their behavior with changing flux bias but the discussion here is intended to paint a more complete picture of the sample behavior.

8.2.1 The Dead Zone

I have already discussed some aspects of the dead zone in the system spectrum [see Sec. 8.1.1]. In addition to two tone spectroscopy, I recorded single tone spectroscopy with a pump tone [see Sec. 5.2.3] for most values of the flux bias. In general this served a diagnostic role and didn't contain new information that I haven't already presented. However, when the qubit was tuned near the dead zone, the single tone spectroscopy also displayed some peculiar behavior.

I first noticed this effect when the Josephson energy E_J was tuned near the top of

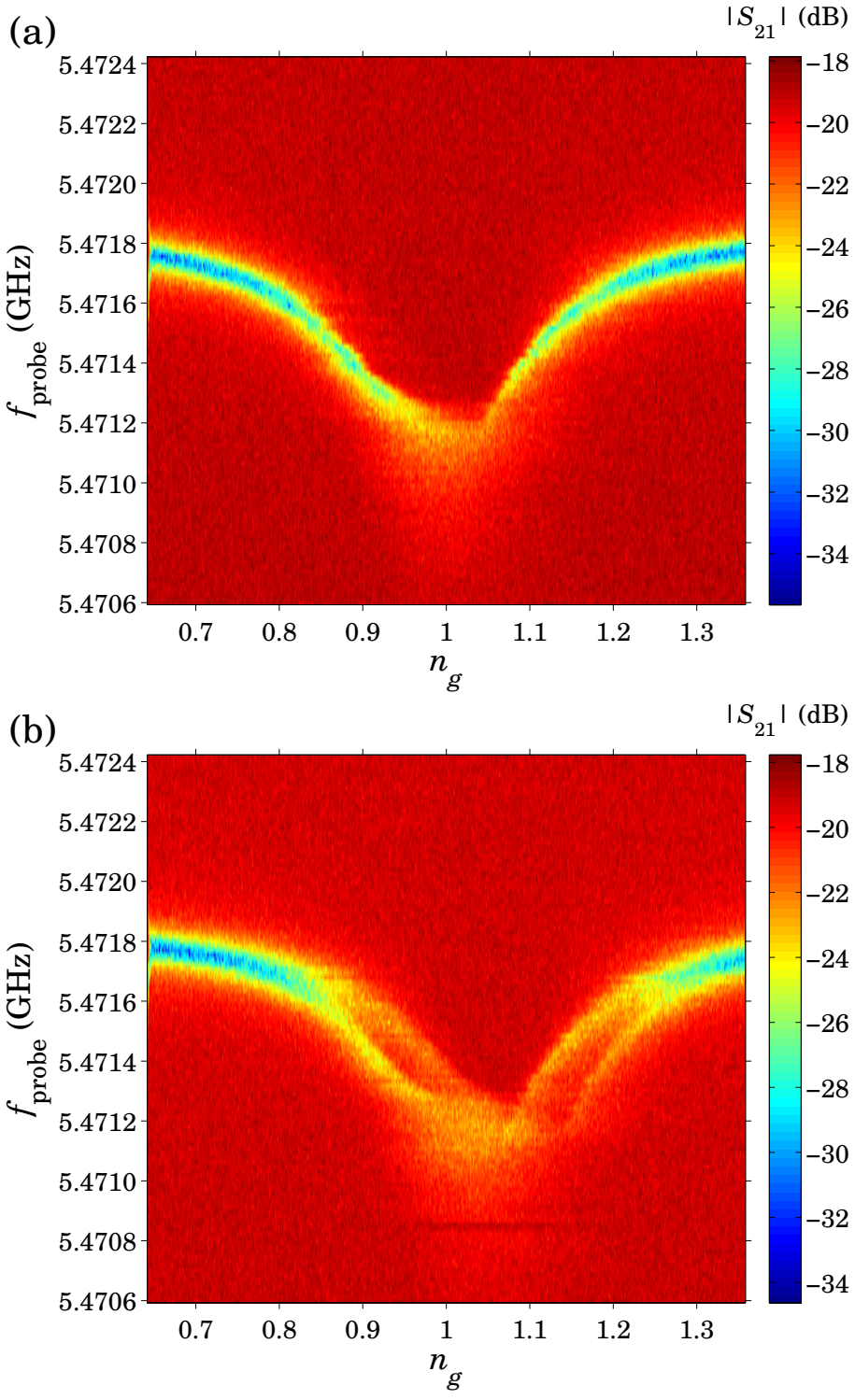

Figure 8.10: (a) Single tone spectroscopy in the dead zone with the pump tone (qubit drive) off in Device 2. (b) Single tone spectroscopy in the dead zone with a pump tone at 6.40 GHz, ≈ 0.10 GHz below the nearest CPB transition. A twinned copy of the resonator ground state response is visible, offset by ≈ 0.05 along reduced gate bias n_g.

the dead zone, at a flux bias corresponding to the ≈ 6.50 GHz spectrum [see Fig. 8.2(a)]. With the pump tone turned off, the single tone spectroscopy was slightly distorted but otherwise typical [see Fig. 8.10(a)]. When I applied a pump tone below the CPB transition frequency, for example at 6.40 GHz [see Fig. 8.10(b)], the ground state resonance frequency $\omega_{res}(n_g)$ twinned rather than remaining unchanged as would be expected. The twinning along the gate bias axis n_g appears to be caused by a strong, incoherent charge fluctuator coupled to the CPB. It persisted as I tried various pump tone frequencies below about ≈ 6.65 GHz but disappeared above that point and was replaced by the ordinary dip corresponding to the $\omega_{res} + \chi$ resonance [see Sec. 5.2.3]. I also found that as I decreased the pump tone power, the twinned ground state resonance became fainter and gradually disappeared, appearing the same as when the pump tone is off. I didn't pursue this issue further.

One possible explanation for this effect is a microwave activated charged TLS. An applied microwave tone could drive random switching of a charged TLS with a transition energy below ≈ 6.65 GHz. The effect on the CPB would be very similar to a low energy, thermally activated charged fluctuator. It would produce the twinned resonator ground state I observed and may also explain the loss of visibility of the CPB spectral parabolas in the dead zone. In contrast to this charge fluctuator, a microwave induced critical current fluctuator with a modulation of $\Delta I_0 = 0.13\,\mu$A of a maximum critical current $I_0 = 35.78\,\mu$A has been reported in a phase qubit [222].

8.2.2 Other Spectral Anomalies

Other spectral anomalies I observed in Device 2 were very similar to the TLS transition ghosts I identified in some of the system spectra [see Sec. 8.1.1]. These spectral anomalies are likely TLS transitions but unlike the aforementioned ghosts, these didn't have an accompanying CPB spectrum. The first TLS-like feature was visible in the ≈ 5.8 – 6.0 GHz range [see Fig. 8.11(a)] when the lowest CPB transition was tuned to 4.31 GHz. It's a very good match to a saw-tooth TLS only transition [see Fig. 7.2]. The light vertical stripes present in the data are due to resonant crossings between the CPB and the resonator occurring at $\omega_{res}/2\pi = 5.472$ GHz. The second TLS-like feature was even more interesting and was recorded while I was doing wide frequency sweeps during the detailed characterization of the 7.06 GHz spectrum. It's visible at ≈ 1.88 – 1.90 GHz [see Fig. 8.11(b)], far

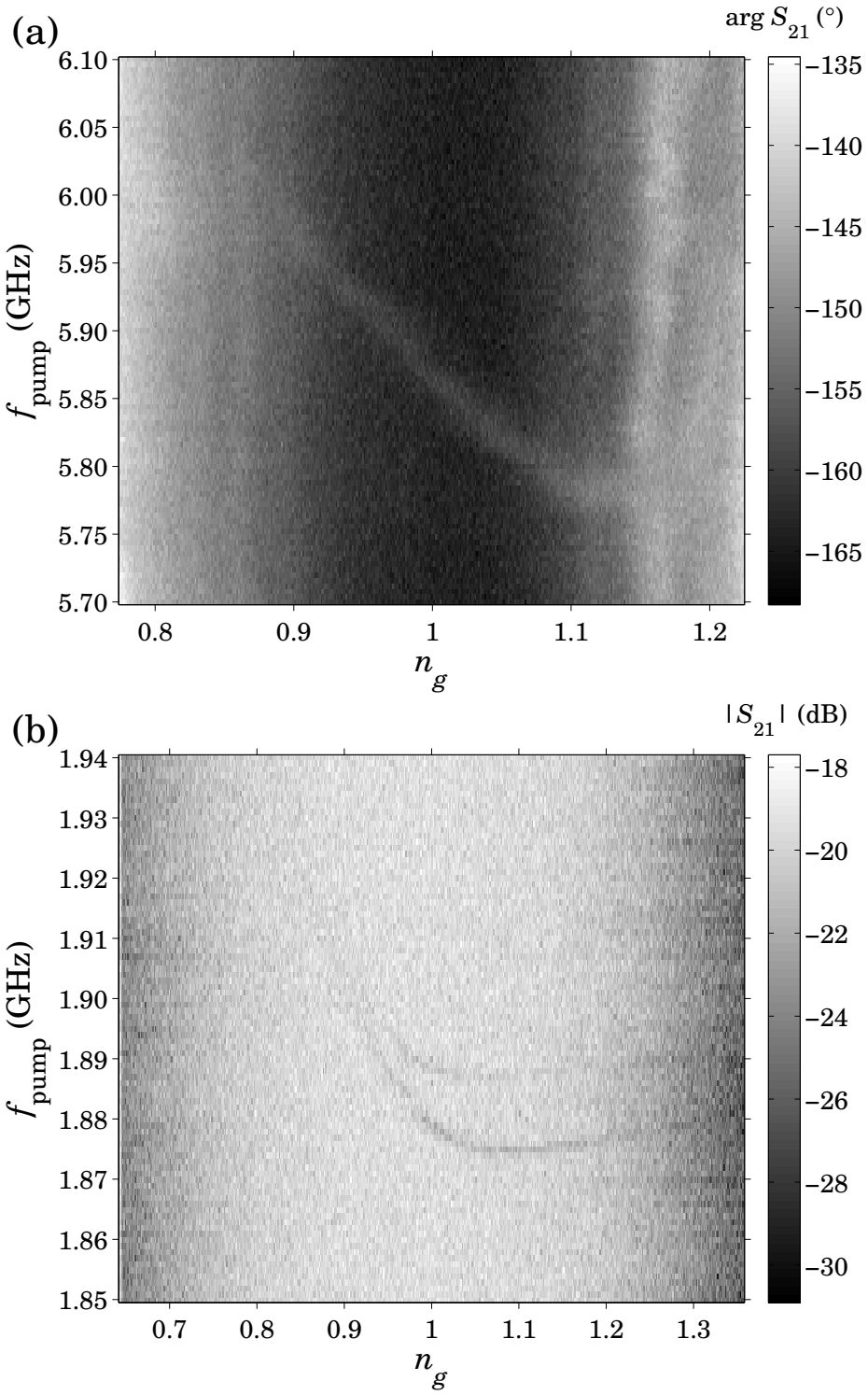

Figure 8.11: Two tone spectroscopy of TLS ghosts in Device 2. (a) A TLS transition in the $\approx 5.8-6.0\,\mathrm{GHz}$ range, present when the lowest CPB transition was tuned to 4.31 GHz. (b) A TLS transition in the $\approx 1.88-1.90\,\mathrm{GHz}$ range, far below the CPB spectrum at 7.06 GHz [see Fig. 8.1(a)].

below the CPB transitions. While its structure is unexpected—it doesn't resemble a saw-tooth and has two closely spaced curves—it does lie in the frequency range predicted by the model for the excitation energy of the non-resonantly coupled TLS's. Unfortunately I wasn't able to verify if this was indeed the same TLS or merely a coincidence. I didn't do any detailed studies or modeling of the ghost spectra but their presence and visibility, as compared to Device 1 which had at most a few small avoided crossings, may be evidence of a larger than average number of defects in Device 2. This would make it more likely that a rare event, such as a strong, non-resonant TLS coupling to the CPB, occur in the sample.

9 Conclusions

9.1 Overview of Main Results

My thesis work consisted of two related projects. The first group of experiments characterized the coherence properties of two CPB qubits coupled to thin-film lumped-element resonators and studied the relationship between one aspect of that coherence, the excited state lifetime, and the coupling of the qubit to the CPW transmission line used to transmit the pump and probe signals [see Ch. 6]. An additional goal was to determine if the exceptionally long lifetime T_1 observed in Device 1 could be reproduced in other samples. My second project explored in detail the behavior of two-level system defects in the Josephson junction of Device 2, another potential cause of decoherence [see Ch. 8]. I developed a model of a charge and critical current coupled fluctuator and used it to successfully fit the observed anomalously quadrupled system spectrum [see Ch. 7]. In the process I also extracted microscopic parameters of the TLS.

9.1.1 Dephasing and Reproducibility of Long Lifetime Qubits

The fabrication, initial characterization and lifetime studies of Device 1 were carried out by Z. Kim [59, 71]. He found that the device had an impressive excited state lifetime, reaching a maximum of just over $200\,\mu$s, and that this lifetime was correlated directly with the decoupling of the qubit from the transmission line. I continued working on that sample, focusing on dephasing due to low frequency noise to compliment the characterization of high frequency noise performed by Z. Kim [see Ch. 6]. I recorded Ramsey fringes, extracted decoherence times T_2 in the range $200-500\,$ns, and determined a corresponding bound of $S_q(f=1\,\text{Hz}) \leq \left(3\times10^{-3}\right)^2 e^2/\text{Hz}$ on the $1/f$ charge noise affecting the CPB. I also carried out spin echo experiments and found echo decay times T_{echo} in the $2.4-3.3\,\mu$s range, implying a high frequency $1/f$ charge noise cutoff of $\omega_c/2\pi \approx 0.2\,$MHz.

This low frequency noise bound is similar to that reported for other charge qubits and CPB based devices. Extrapolating the low frequency noise to higher frequencies produces a value much larger than the bound given by the relaxation measurements, a value of $S_q(f = 4.5\,\mathrm{GHz}) \leq 10^{-18}\,e^2/\mathrm{Hz}$. This discrepancy is consistent with the high frequency noise cutoff I deduced from spin echo measurements.

After completing the dephasing characterization of Device 1, I fabricated a new qubit sample to address the question of the reproducibility of the long lifetime and decoupling correlation results. The design of Device 2 was nearly identical to that of Device 1 except for two changes. Device 2 had a larger E_J/E_c ratio which gave a small reduction in the charge sensitivity of the CPB and the resonator was more coupled to the transmission line to increase the readout bandwidth. Through single and two-tone spectroscopy and external parameter sweeps, I determined device parameters including the cavity resonance frequency $\omega_{res}/2\pi = 5.472\,\mathrm{GHz}$, loaded quality factor $Q_L = 35{,}000$, the CPB charging energy $E_c/h = 4.3\,\mathrm{GHz}$, the maximum Josephson energy $E_J^{\mathrm{sum}}/h = 7.33\,\mathrm{GHz}$, and the qubit-resonator coupling strength $g/2\pi \approx 15\,\mathrm{MHz}$. It was at this time that I discovered the device displayed an anomalously twinned transition spectrum. I decided to study the spectrum in detail [see Ch. 8] in parallel with the lifetime experiments.

The qubit lifetime experiments consisted of systematic measurements of the relaxation time T_1 and Rabi decoupling $dV_{g,\mathrm{rms}}/d\Omega_{R,0}$ at Josephson energies E_J in the range $4.0 - 7.3\,\mathrm{GHz}$. The lifetime of Device 2 was a respectable $4 - 30\,\mu\mathrm{s}$, shorter than that of Device 1 but still long lived, indicating that the design and fabrication were relatively robust. The decoupling of the Device 2 qubit was reduced as compared to Device 1. The relaxation time T_1 and Rabi decoupling $dV_{g,\mathrm{rms}}/d\Omega_{R,0}$ data showed a general correlation. Furthermore, the trends of both of those quantities followed a similar pattern in both of the samples I studied, with the lifetime falling in both cases when the CPB was tuned above the resonator. While I didn't perform a thorough characterization of the low frequency noise affecting Device 2, the spectroscopic coherence time $T_2^* \approx 60\,\mathrm{ns}$ allowed me to bound the low frequency $1/f$ charge noise by $S_q(f = 1\,\mathrm{Hz}) \leq \left(1 \times 10^{-2}\right)^2 e^2/\mathrm{Hz}$.

Overall my results for Device 2 suggested some level of reproducibility of the exceptional relaxation time T_1 found for Device 1. Design and fabrication factors may explain the differences between the two samples. The increase in the readout bandwidth may have simultaneously contributed to stronger coupling of the qubit to the environment.

The larger junctions, designed to lower the charging energy E_c and hence reduce sensitivity to charge noise, would have led on average to a larger number of total defects which could contribute to qubit dephasing or relaxation.

9.1.2 Critical Current and Charge Coupled Fluctuators

In order to better understand what was happening in Device 2 and explain the anomalous behavior, I recorded detailed two tone spectroscopy for a broad range of Josephson energy E_J values. The most striking feature was the spectral multiplicity. When E_J was tuned above the resonator resonance at $\omega_{res}/2\pi = 5.472\,\mathrm{GHz}$ the system spectrum was twinned, containing two CPB-like parabolas with differing curvatures and offset from each other both in frequency and gate voltage. When E_J was tuned below the resonator resonance the system spectrum was quadrupled, consisting of four CPB-like parabolas again with differing curvatures and offset from each other in frequency and gate voltage. In addition to the spectral multiplicity I found other anomalies such as the dead zone in the $\approx 5.6 - 6.5\,\mathrm{GHz}$ range, where the system spectrum had either very low visibility or was highly distorted. Several discrete splittings and TLS transition ghosts were also visible, both signatures of interactions with defects.

Based on the available evidence, I concluded that the behavior was best explained by a TLS coupled to the CPB via both charge and critical current. I constructed a model for this scenario and explored two of its regimes. In the case of resonant interaction between the qubit and the TLS, avoided crossings are formed at the points of degeneracy and a saw-tooth TLS-only transition may be detectable by some readouts. The second scenario is a non-resonant interaction in which the TLS energy lies below the CPB excited state and manifests itself as twinning of the CPB spectrum. When the interaction energies are small relative to the CPB charge E_c and Josephson E_J energies, the twinned spectra retain the CPB-like parabola shape. It was also possible to identify which model parameters influenced factors such as the tilt, frequency offset, or gate bias offset between the twinned parabolas.

I fit the model spectrum to the data sets which had sufficiently visible CPB-like parabolas. I selected the single TLS model for the top two parabolas of the twinned and quadrupled spectra and then the double TLS model for the entire quadrupled spectra. The fitting was performed by hand, with me varying the parameters until I settled on what I found

to give the best result. All the fits were a good match to the data. Besides providing a theoretical explanation of the underlying behavior, the model fit parameters allowed me to extract microscopic TLS parameters such as the minimum hopping distance of $0.2-0.45\,\text{Å}$ assuming a TLS charge of e. I obtained surprisingly small TLS tunneling rates $T_{LR,k}$, signifying that the defects were tunneling between well isolated sites and also suggesting that the two TLS's may be interacting. On the other hand, the fractional change of the Josephson energy $\Delta E_{J,k}/E_J \approx 30-40\%$ was quite large. This suggests that the tunnel junction had a non-uniform barrier with a few tunneling hot spots and the defect was located close to one of those hot spots.

My CPB defect studies led to several novel observations. Unlike most reports of TLS effects or properties, mine were due to a coherent non-resonant interaction and produced spectral multiplicity rather than an avoided crossing. I also made the first experimental observation of joint charge and critical current CPB-TLS coupling, verifying theoretical predictions of such an effect. Non-uniform tunnel barriers in Al/AlO_x/Al junctions aren't new but my analysis of the phenomena in superconducting qubits highlights its importance and potential impact on device performance.

9.2 Future Outlook

The positive lifetime reproducibility results indicate that decoupling the qubit is a good avenue to follow in order to further improve qubit relaxation rates. Similar results have been obtained by embedding transmon qubits into three dimensional cavity resonators [32, 223], where the isolation from the environment comes from physically removing all leads contacting the qubit. The planar lumped-element LC resonators I used in my research have complex electromagnetic modes and I don't have a thorough understanding of how exactly the qubit couples to the transmission line. Improving this knowledge would allow for more systematic changes of the coupling and more predictable qubit performance. This may be obtained by carrying out finite element simulations of the full device, including both the resonator and the qubit, and examining how the qubit-transmission line coupling behaves with design changes. Alternatively, if the simulation proves infeasible or doesn't give results which agree with the data, it may be possible to develop qubit coupling rules of thumb by fabricating a variety of designs and performing rapid

characterization of the lifetime and decoupling.

The dephasing data indicates that the current device design doesn't address that issue. One approach to do so would be to adopt charge insensitive qubit designs derived from the CPB, such as the transmon [see Sec. 3.6] or the fluxonium [40, 224]. It may be advantageous to do this transition gradually and test the performance of intermediate designs as the large shunting capacitors found in the transmon may increase the coupling to the transmission line. Alternatively, there appears to be large variation in the number of TLS's and the low frequency charge noise from sample to sample. It would be beneficial to investigate what fabrication factors, especially during junction oxidation, affect this. The CPB, due to its wide tunability and strong interaction with charge defects, is particularly well suited to the task of characterizing individual Josephson junction defects.

Due to the stochastic nature of the TLS's themselves, it's difficult to propose specific follow up experiments. One particular area I could have explored, and that could be tried if a similar defect is encountered in the future, is to demonstrate both resonant and non-resonant qubit-TLS interaction. By tuning the Josephson energy E_J sufficiently low, I should be able to change from the non-resonant to the resonant case and possibly observe the transition from a twinned spectrum to one with an avoided crossing. Alternatively, I could have annealed Device 2 at room temperature to change the properties of the TLS's. If there were no strongly coupled TLS's after the anneal, this would have allowed me to determine what effect such TLS's had on the lifetime and coherence properties of the CPB.

The non-uniform nature of the tunnel barrier carries implications for qubit fabrication. If only those defects that are near a hot spot contribute significantly to critical current fluctuations, then it may not be necessary to remove all defects from an ideal qubit. Once the defect density is sufficiently low, most devices won't suffer any performance degradation as any defects present likely won't be located near a hot spot. Paradoxically, improving the uniformity of Josephson tunnel barriers may increase critical current noise since a uniform barrier would sense the contribution of all TLS's. Detailed studies of the microscopic properties of TLS's would also tie in to efforts to reduce the number of defects introduced during junction fabrication. If spectroscopy and modeling is able to identify or bound the nature of the TLS's, such as whether they are located in the junction dielectric or at the interface between the dielectric and the electrodes, this information might offer

clues as to how they are introduced during fabrication and in turn how to eliminate them.

Appendix A

Fabrication Recipes

A.1 Resonator Fabrication Recipe for Device 2

Resonator layer lithography

1. (optional) clean the 3 in sapphire wafer with acetone, methanol, isopropyl alcohol solvent rinses for 60 s in each solvent, blow dry with nitrogen
2. (optional) clean the wafer with an oxygen plasma using the RIE recipe DANDESCU for 30 s, O_2 flow 16 sccm, chamber pressure 200 mTorr, rf power 100 W
3. puddle LOR-5A on the wafer and spin at 4000 RPM for 60 s, produces a $\approx 0.5\,\mu$m thick resist film
4. prebake at 180 °C for 60 s on a hot plate
5. puddle OiR 906-10 on the wafer and spin at 3500 RPM for 60 s, produces a $\approx 1.1\,\mu$m thick resist film
6. prebake at 90 °C for 60 s on a hot plate
7. expose with a contact aligner using the resonator mask for 4 s
8. postbake at 120 °C for 60 s on a hot plate
9. develop in OPD 4262 for 80 s
10. rinse with DI water for 60 s, blow dry with nitrogen
11. (optional) descum with an oxygen plasma using the RIE recipe DANDESCU for 20 s, O_2 flow 16 sccm, chamber pressure 200 mTorr, rf power 100 W

12. deposit 100 nm of aluminum at a rate of 5 – 10 Å/s using the dedicated aluminum thermal evaporator at a base pressure of $\approx 5 - 10 \times 10^{-7}$ Torr
13. lift-off the resist and metalization layers using a hot NMP bath at 80 – 90 °C liquid temperature, approximate time is 30 min with mild agitation, after the majority of metal has lifted off transfer to a second hot NMP bath for ≈ 10 min
14. rinse with DI water for 60 s, blow dry with nitrogen
15. (optional) clean the wafer with isopropyl alcohol solvent rinse for 60 s, blow dry with nitrogen

Alignment layer lithography

1. (optional) clean the wafer with an oxygen plasma using the RIE recipe DANDESCU for 30 s, O_2 flow 16 sccm, chamber pressure 200 mTorr, rf power 100 W
2. puddle LOR-5A on the wafer and spin at 4000 RPM for 60 s, produces a ≈ 0.5 μm thick resist film
3. prebake at 180 °C for 60 s on a hot plate
4. puddle OiR 906-10 on the wafer and spin at 3500 RPM for 60 s, produces a ≈ 1.1 μm thick resist film
5. prebake at 90 °C for 60 s on a hot plate
6. expose with a contact aligner using the alignment marks mask for 4 s, align the exposure to the existing resonator layer features
7. postbake at 120 °C for 60 s on a hot plate
8. develop in OPD 4262 for 80 s
9. rinse with DI water for 60 s, blow dry with nitrogen
10. (optional) descum with an oxygen plasma using the RIE recipe DANDESCU for 20 s, O_2 flow 16 sccm, chamber pressure 200 mTorr, rf power 100 W
11. deposit 10 nm of titanium followed by 100 nm of gold, both at a rate of 5 – 10 Å/s, using the CHA cleanroom e-beam evaporator at a base pressure of 1×10^{-6} Torr

12. lift-off the resist and metalization layers using a hot NMP bath at 80 – 90 °C liquid temperature, approximate time is 30 min with mild agitation, after the majority of metal has lifted off transfer to a second hot NMP bath for ≈ 10 min
13. rinse with DI water for 60 s, blow dry with nitrogen
14. (optional) clean the wafer with isopropyl alcohol solvent rinse for 60 s, blow dry with nitrogen

A.2 CPB Fabrication Recipe

E-beam resist spin-on and dicing

1. (optional) clean the wafer with an oxygen plasma using the RIE recipe DANDESCU for 30 s, O_2 flow 16 sccm, chamber pressure 200 mTorr, rf power 100 W
2. puddle MMA(8.5)MAA EL11 on the wafer and spin at 1000 RPM for 60 s, produces a ≈ 960 nm thick resist film
3. prebake at 180 °C for 5 min on a hot plate
4. puddle ZEP520A DR 2.3 on the wafer and spin at 5000 RPM for 60 s, produces a ≈ 116 nm thick resist film
5. prebake at 180 °C for 5 min on a hot plate
6. prebake at 180 °C for 30 – 60 min in an oven
7. deposit 12 nm of aluminum anti-charging layer at a rate of ≈ 5 Å/s using the dedicated aluminum thermal evaporator at a base pressure of $\approx 5 - 10 \times 10^{-7}$ Torr
8. puddle FSC-M on the wafer and spin at 2000 RPM for 60 s, produces a ≈ 3.5 μm thick resist film
9. prebake at 120 °C for 2 min on a hot plate
10. dice the sapphire wafer using the Disco-DAD 321 dicing saw with a coarse grit resinoid diamond blade (type CX-010-325-080-H from Dicing Blade Technology) at 22,000 RPM and a feed speed of 0.75 mm/s

11. peel off and clean individual die with acetone, methanol, isopropyl alcohol solvent rinses for 60 s in each solvent, blow dry with nitrogen, note that all further processing is done on individual die

E-beam lithography and junction fabrication

1. write the CPB pattern using the JEOL 6500 SEM equipped with NPGS, the write is done at a magnification of 900x, accelerating voltage 30 kV, beam current ≈ 17 pA with typical line doses of $1-10$ nC/cm and area doses of $1-10\,\mu$C/cm^2
2. strip the aluminum anti-charging layer in OPD 4262 for 60 s
3. rinse with DI water for 60 s, blow dry with nitrogen
4. develop the ZEP520A in ZED-N50 for 3 min
5. rinse with isopropyl alcohol 60 s, blow dry with nitrogen
6. develop the MMA in IPA : H_2O 5 : 1 for ≈ 3 min, adjust the development time as needed to obtain the desired undercut
7. rinse with isopropyl alcohol 60 s, blow dry with nitrogen
8. deposit the Josephson junctions in the dedicated aluminum thermal evaporator with double-angle evaporation, base pressure $\approx 5-10\times10^{-7}$ Torr, evaporation angles $\pm15-25°$, film thicknesses 300 Å and 500 Å at a rate of $5-10$ Å/s, oxidation oxygen pressure $100-2000$ mTorr for $5-30$ min
9. lift-off the resist and metalization layers using a hot NMP bath at $80-90\,°$C liquid temperature, approximate time is 20 min with mild agitation, after the majority of metal has lifted off transfer to a second hot NMP bath for $5-10$ min
10. rinse with DI water for 60 s, blow dry with nitrogen

Bibliography

[1] Richard Feynman, "Simulating physics with computers," International Journal of Theoretical Physics **21**, 467–488 (1982), ISSN 0020-7748, http://www.springerlink.com/content/t2x8115127841630/abstract/.

[2] Roman S. Ingarden, "Quantum information theory," Reports on Mathematical Physics **10**, 43–72 (Aug. 1976), ISSN 0034-4877, http://www.sciencedirect.com/science/article/pii/0034487776900057.

[3] R P Poplavskiĭ, "Thermodynamic models of information processes," Soviet Physics Uspekhi **18**, 222–241 (Mar. 1975), ISSN 0038-5670, http://iopscience.iop.org/PU1975v018n03ABEH001955.

[4] P. W. Shor, "Algorithms for quantum computation: discrete logarithms and factoring," in *Foundations of Computer Science, IEEE Annual Symposium on* (IEEE Computer Society, Los Alamitos, CA, USA, 1994) pp. 124–134, ISBN 0-8186-6580-7.

[5] Lov K. Grover, "A fast quantum mechanical algorithm for database search," in *Proceedings of the twenty-eighth annual ACM symposium on Theory of computing*, STOC '96 (ACM, New York, NY, USA, 1996) p. 212–219, ISBN 0-89791-785-5, http://doi.acm.org/10.1145/237814.237866.

[6] C. Monroe, D. M. Meekhof, B. E. King, W. M. Itano, and D. J. Wineland, "Demonstration of a fundamental quantum logic gate," Physical Review Letters **75**, 4714–4717 (Dec. 1995), http://link.aps.org/doi/10.1103/PhysRevLett.75.4714.

[7] Neil A. Gershenfeld and Isaac L. Chuang, "Bulk spin-resonance quantum computation," Science **275**, 350–356 (Jan. 1997), ISSN 0036-8075, 1095-9203, http://www.sciencemag.org/content/275/5298/350.

[8] David G. Cory, Amr F. Fahmy, and Timothy F. Havel, "Ensemble quantum computing by NMR spectroscopy," Proceedings of the National Academy of Sciences **94**, 1634–1639 (Mar. 1997), ISSN 0027-8424, 1091-6490, http://www.pnas.org/content/94/5/1634.

[9] Andrew Steane, "Multiple-particle interference and quantum error correction," Proceedings of the Royal Society of London. Series A: Mathematical, Physical and Engineering Sciences **452**, 2551–2577 (Nov. 1996), ISSN 1364-5021, 1471-2946, http://rspa.royalsocietypublishing.org/content/452/1954/2551.

[10] Peter W. Shor, "Scheme for reducing decoherence in quantum computer memory," Physical Review A **52**, R2493–R2496 (Oct. 1995), http://link.aps.org/doi/10.1103/PhysRevA.52.R2493.

[11] Lydia L. Sohn, Leo P. Kouwenhoven, and Gerd Schön, *Mesoscopic Electron Transport* (Springer, 1997) ISBN 9780792347378.

[12] J. I. Cirac and P. Zoller, "Quantum computations with cold trapped ions," Physical Review Letters **74**, 4091–4094 (May 1995), http://link.aps.org/doi/10.1103/PhysRevLett.74.4091.

[13] Daniel Loss and David P. DiVincenzo, "Quantum computation with quantum dots," Physical Review A **57**, 120–126 (Jan. 1998), http://link.aps.org/doi/10.1103/PhysRevA.57.120.

[14] A. C. Johnson, J. R. Petta, J. M. Taylor, A. Yacoby, M. D. Lukin, C. M. Marcus, M. P. Hanson, and A. C. Gossard, "Triplet-singlet spin relaxation via nuclei in a double quantum dot," Nature **435**, 925–928 (Jun. 2005), ISSN 0028-0836, http://www.nature.com/nature/journal/v435/n7044/full/nature03815.html.

[15] Y. Nakamura, Yu. A. Pashkin, and J. S. Tsai, "Coherent control of macroscopic quantum states in a single-cooper-pair box," Nature **398**, 786–788 (Apr. 1999), ISSN 0028-0836, http://www.nature.com/nature/journal/v398/n6730/abs/398786a0.html.

[16] I. Chiorescu, P. Bertet, K. Semba, Y. Nakamura, C. J. P. M. Harmans, and J. E. Mooij, "Coherent dynamics of a flux qubit coupled to a harmonic oscillator," Nature

431, 159–162 (Sep. 2004), ISSN 0028-0836, http://www.nature.com/nature/journal/v431/n7005/abs/nature02831.html.

[17] John M. Martinis, S. Nam, J. Aumentado, and C. Urbina, "Rabi oscillations in a large josephson-junction qubit," Physical Review Letters **89**, 117901 (Aug. 2002), http://link.aps.org/doi/10.1103/PhysRevLett.89.117901.

[18] B. E. Kane, "A silicon-based nuclear spin quantum computer," Nature **393**, 133–137 (May 1998), ISSN 0028-0836, http://www.nature.com/nature/journal/v393/n6681/full/393133a0.html.

[19] F. Jelezko, T. Gaebel, I. Popa, A. Gruber, and J. Wrachtrup, "Observation of coherent oscillations in a single electron spin," Physical Review Letters **92**, 076401 (Feb. 2004), http://link.aps.org/doi/10.1103/PhysRevLett.92.076401.

[20] M. V. Gurudev Dutt, L. Childress, L. Jiang, E. Togan, J. Maze, F. Jelezko, A. S Zibrov, P. R Hemmer, and M. D Lukin, "Quantum register based on individual electronic and nuclear spin qubits in diamond," Science **316**, 1312–1316 (Jun. 2007), ISSN 0036-8075, 1095-9203, http://www.sciencemag.org/content/316/5829/1312.

[21] E. Knill, R. Laflamme, and G. J. Milburn, "A scheme for efficient quantum computation with linear optics," Nature **409**, 46–52 (Jan. 2001), ISSN 0028-0836, http://www.nature.com/nature/journal/v409/n6816/full/409046a0.html.

[22] G. Ithier, E. Collin, P. Joyez, P. J. Meeson, D. Vion, D. Esteve, F. Chiarello, A. Shnirman, Y. Makhlin, J. Schriefl, and G. Schön, "Decoherence in a superconducting quantum bit circuit," Physical Review B **72**, 134519 (Oct. 2005), http://link.aps.org/doi/10.1103/PhysRevB.72.134519.

[23] John M. Martinis, S. Nam, J. Aumentado, K. M. Lang, and C. Urbina, "Decoherence of a superconducting qubit due to bias noise," Physical Review B **67**, 094510 (Mar. 2003), http://link.aps.org/doi/10.1103/PhysRevB.67.094510.

[24] A.Yu. Kitaev, "Fault-tolerant quantum computation by anyons," Annals of Physics **303**, 2–30 (Jan. 2003), ISSN 0003-4916, http://www.sciencedirect.com/science/article/pii/S0003491602000180.

[25] Alexandre Blais, Ren-Shou Huang, Andreas Wallraff, S. M. Girvin, and R. J. Schoelkopf, "Cavity quantum electrodynamics for superconducting electrical circuits: An architecture for quantum computation," Physical Review A **69**, 062320 (Jun. 2004), http://link.aps.org/doi/10.1103/PhysRevA.69.062320.

[26] M. Hatridge, R. Vijay, D. H. Slichter, John Clarke, and I. Siddiqi, "Dispersive magnetometry with a quantum limited SQUID parametric amplifier," Physical Review B **83**, 134501 (Apr. 2011), http://link.aps.org/doi/10.1103/PhysRevB.83.134501.

[27] A. Naik, O. Buu, M. D. LaHaye, A. D. Armour, A. A. Clerk, M. P. Blencowe, and K. C. Schwab, "Cooling a nanomechanical resonator with quantum back-action," Nature **443**, 193–196 (Sep. 2006), ISSN 0028-0836, http://www.nature.com/nature/journal/v443/n7108/full/nature05027.html.

[28] Paul Gannon, *Colossus: Bletchley Park's Greatest Secret* (Atlantic Books, 2007) ISBN 9781843543312.

[29] Scott McCartney, *ENIAC, the Triumphs and Tragedies of the World's First Computer* (Walker, 1999) ISBN 9780802713483.

[30] D. Leibfried, R. Blatt, C. Monroe, and D. Wineland, "Quantum dynamics of single trapped ions," Reviews of Modern Physics **75**, 281–324 (Mar. 2003), http://link.aps.org/doi/10.1103/RevModPhys.75.281.

[31] Ron Folman, Peter Krüger, Donatella Cassettari, Björn Hessmo, Thomas Maier, and Jörg Schmiedmayer, "Controlling cold atoms using nanofabricated surfaces: Atom chips," Physical Review Letters **84**, 4749–4752 (May 2000), http://link.aps.org/doi/10.1103/PhysRevLett.84.4749.

[32] Hanhee Paik, D. I. Schuster, Lev S. Bishop, G. Kirchmair, G. Catelani, A. P. Sears, B. R. Johnson, M. J. Reagor, L. Frunzio, L. I. Glazman, S. M. Girvin, M. H. Devoret, and R. J. Schoelkopf, "Observation of high coherence in josephson junction qubits measured in a three-dimensional circuit QED architecture," Physical Review Letters **107**, 240501 (Dec. 2011), http://link.aps.org/doi/10.1103/PhysRevLett.107.240501.

[33] Michael Tinkham, *Introduction to Superconductivity* (Courier Dover Publications, 2004) ISBN 9780486435039.

[34] M. H. Devoret, "Quantum fluctuations in electrical circuits," (1997) p. 351, http://adsabs.harvard.edu/abs/1997fqqf.conf..351D.

[35] V. Bouchiat, D. Vion, P. Joyez, D. Esteve, and M. H. Devoret, "Quantum coherence with a single cooper pair," Physica Scripta Volume T **76**, 165–170 (1998), http://adsabs.harvard.edu/abs/1998PhST...76..165B.

[36] R. J. Schoelkopf, P. Wahlgren, A. A Kozhevnikov, P. Delsing, and D. E Prober, "The radio-frequency single-electron transistor (RF-SET): a fast and ultrasensitive electrometer," Science **280**, 1238–1242 (May 1998), ISSN 0036-8075, 1095-9203, http://www.sciencemag.org/content/280/5367/1238.

[37] H. Paik, F. W. Strauch, R. C. Ramos, A. J. Berkley, H. Xu, S. K. Dutta, P. R. Johnson, A. J. Dragt, J. R. Anderson, C. J. Lobb, and F. C. Wellstood, "Cooper-pair box as a variable capacitor," Applied Superconductivity, IEEE Transactions on **15**, 884 – 887 (Jun. 2005), ISSN 1051-8223.

[38] D. Vion, A. Aassime, A. Cottet, P. Joyez, H. Pothier, C. Urbina, D. Esteve, and M. H. Devoret, "Manipulating the quantum state of an electrical circuit," Science **296**, 886 –889 (May 2002), http://www.sciencemag.org/content/296/5569/886.abstract.

[39] Jens Koch, Terri M. Yu, Jay Gambetta, A. A. Houck, D. I. Schuster, J. Majer, Alexandre Blais, M. H. Devoret, S. M. Girvin, and R. J. Schoelkopf, "Charge-insensitive qubit design derived from the cooper pair box," Physical Review A **76**, 042319 (Oct. 2007), http://link.aps.org/doi/10.1103/PhysRevA.76.042319.

[40] Vladimir E. Manucharyan, Jens Koch, Leonid I. Glazman, and Michel H. Devoret, "Fluxonium: Single cooper-pair circuit free of charge offsets," Science **326**, 113–116 (Oct. 2009), ISSN 0036-8075, 1095-9203, http://www.sciencemag.org/content/326/5949/113.abstract.

[41] R. Barends, J. Wenner, M. Lenander, Y. Chen, R. C Bialczak, J. Kelly, E. Lucero, P. O'Malley, M. Mariantoni, D. Sank, H. Wang, T. C White, Y. Yin, J. Zhao,

A. N Cleland, John M Martinis, and J. J. A Baselmans, "Minimizing quasiparticle generation from stray infrared light in superconducting quantum circuits," Applied Physics Letters **99**, 113507–113507–3 (Sep. 2011), ISSN 00036951, http://apl.aip.org/resource/1/applab/v99/i11/p113507_s1.

[42] Antonio D Córcoles, Jerry M Chow, Jay M Gambetta, Chad Rigetti, J. R Rozen, George A Keefe, Mary Beth Rothwell, Mark B Ketchen, and M. Steffen, "Protecting superconducting qubits from radiation," Applied Physics Letters **99**, 181906–181906–3 (Nov. 2011), ISSN 00036951, http://apl.aip.org/resource/1/applab/v99/i18/p181906_s1.

[43] I. Siddiqi, R. Vijay, M. Metcalfe, E. Boaknin, L. Frunzio, R. J. Schoelkopf, and M. H. Devoret, "Dispersive measurements of superconducting qubit coherence with a fast latching readout," Physical Review B **73**, 054510 (Feb. 2006), http://link.aps.org/doi/10.1103/PhysRevB.73.054510.

[44] Carlton M. Caves, Kip S. Thorne, Ronald W. P. Drever, Vernon D. Sandberg, and Mark Zimmermann, "On the measurement of a weak classical force coupled to a quantum-mechanical oscillator. i. issues of principle," Reviews of Modern Physics **52**, 341–392 (Apr. 1980), http://link.aps.org/doi/10.1103/RevModPhys.52.341.

[45] Jian Li, K. Chalapat, and G. S. Paraoanu, "Measurement-induced entanglement of two superconducting qubits," Journal of Physics: Conference Series **150**, 022051 (Feb. 2009), ISSN 1742-6596, http://iopscience.iop.org/1742-6596/150/2/022051.

[46] M. D. Reed, B. R. Johnson, A. A. Houck, L. DiCarlo, J. M. Chow, D. I. Schuster, L. Frunzio, and R. J. Schoelkopf, "Fast reset and suppressing spontaneous emission of a superconducting qubit," Applied Physics Letters **96**, 203110–203110–3 (May 2010), ISSN 00036951, http://apl.aip.org/resource/1/applab/v96/i20/p203110_s1.

[47] E. M. Purcell, "Spontaneous emission probabilities at radio frequencies," in *Physical Review*, Vol. 69 (1946) p. 681, http://prola.aps.org/pdf/PR/v69/i11-12/p674_2.

[48] Max Born, Hedwig Born, and Albert Einstein, *The Born-Einstein letters: correspondence between Albert Einstein and Max and Hedwig Born from 1916 to 1955* (Macmillan, 1971).

[49] A. A. Clerk, M. H. Devoret, S. M. Girvin, Florian Marquardt, and R. J. Schoelkopf, "Introduction to quantum noise, measurement, and amplification," Reviews of Modern Physics **82**, 1155–1208 (Apr. 2010), http://link.aps.org/doi/10.1103/RevModPhys.82.1155.

[50] D. I. Schuster, A. Wallraff, A. Blais, L. Frunzio, R.-S. Huang, J. Majer, S. M. Girvin, and R. J. Schoelkopf, "AC stark shift and dephasing of a superconducting qubit strongly coupled to a cavity field," Physical Review Letters **94**, 123602 (Mar. 2005), http://link.aps.org/doi/10.1103/PhysRevLett.94.123602.

[51] Kimble Quantum Optics Group at Caltech, http://www.its.caltech.edu/~qoptics/.

[52] S. Haroche and J.-M. Raimond, *Exploring the Quantum: Atoms, Cavities and Photons* (Oxford University Press, 2006) ISBN 9780198509141.

[53] J. M. Raimond, M. Brune, and S. Haroche, "Manipulating quantum entanglement with atoms and photons in a cavity," Reviews of Modern Physics **73**, 565–582 (2001), http://link.aps.org/doi/10.1103/RevModPhys.73.565.

[54] J. Majer, J. M. Chow, J. M. Gambetta, Jens Koch, B. R. Johnson, J. A. Schreier, L. Frunzio, D. I. Schuster, A. A. Houck, A. Wallraff, A. Blais, M. H. Devoret, S. M. Girvin, and R. J. Schoelkopf, "Coupling superconducting qubits via a cavity bus," Nature **449**, 443–447 (Sep. 2007), ISSN 0028-0836, http://www.nature.com/nature/journal/v449/n7161/abs/nature06184.html.

[55] Matteo Mariantoni, H. Wang, T. Yamamoto, M. Neeley, Radoslaw C. Bialczak, Y. Chen, M. Lenander, Erik Lucero, A. D. O'Connell, D. Sank, M. Weides, J. Wenner, Y. Yin, J. Zhao, A. N. Korotkov, A. N. Cleland, and John M. Martinis, "Implementing the quantum von neumann architecture with superconducting circuits," Science **334**, 61–65 (Oct. 2011), ISSN 0036-8075, 1095-9203, http://www.sciencemag.org/content/334/6052/61.

[56] Mika A. Sillanpaa, Jae I. Park, and Raymond W. Simmonds, "Coherent quantum state storage and transfer between two phase qubits via a resonant cavity," Nature **449**, 438–442 (2007), ISSN 0028-0836, http://dx.doi.org/10.1038/nature06124.

[57] Abdufarrukh A. Abdumalikov, Oleg Astafiev, Yasunobu Nakamura, Yuri A. Pashkin, and JawShen Tsai, "Vacuum rabi splitting due to strong coupling of a flux qubit and a coplanar-waveguide resonator," Physical Review B **78**, 180502 (Nov. 2008), http://link.aps.org/doi/10.1103/PhysRevB.78.180502.

[58] K. Hennessy, A. Badolato, M. Winger, D. Gerace, M. Atatüre, S. Gulde, S. Fält, E. L. Hu, and A. Imamoğlu, "Quantum nature of a strongly coupled single quantum dot–cavity system," Nature **445**, 896–899 (Feb. 2007), ISSN 0028-0836, http://www.nature.com/nature/journal/v445/n7130/full/nature05586.html.

[59] Z. Kim, B. Suri, V. Zaretskey, S. Novikov, K. D. Osborn, A. Mizel, F. C. Wellstood, and B. S. Palmer, "Decoupling a cooper-pair box to enhance the lifetime to 0.2 ms," Physical Review Letters **106**, 120501 (Mar. 2011), http://link.aps.org/doi/10.1103/PhysRevLett.106.120501.

[60] F. C Wellstood, Z. Kim, and B. Palmer, "Spectroscopy of charge fluctuators coupled to a cooper pair box," arXiv:0805.4429(May 2008), http://arxiv.org/abs/0805.4429.

[61] Z. Kim, V. Zaretskey, Y. Yoon, J. F. Schneiderman, M. D. Shaw, P. M. Echternach, F. C. Wellstood, and B. S. Palmer, "Anomalous avoided level crossings in a cooper-pair box spectrum," Physical Review B **78**, 144506 (Oct. 2008), http://link.aps.org/doi/10.1103/PhysRevB.78.144506.

[62] J. J. Sakurai and Jim Napolitano, *Modern Quantum Mechanics* (Addison-Wesley, 2007) ISBN 9780321503367.

[63] R.C. Ramos, M.A. Gubrud, A. J. Berkley, J. R. Anderson, C.J. Lobb, and F.C. Wellstood, "Design for effective thermalization of junctions for quantum coherence," IEEE Transactions on Applied Superconductivity **11**, 998–1001 (2001), ISSN 1051-8223.

[64] Audrey Cottet, *Implementation of a quantum bit in a superconducting circuit*, Doctoral dissertation, Université Paris 6 (2002).

[65] David M. Pozar, *Microwave engineering* (Wiley, 1997) ISBN 9780471170969.

[66] K. C. Gupta, *Microstrip Lines and Slotlines* (Artech House, 1996) ISBN 9780890067666.

[67] A. A. Houck, J. A. Schreier, B. R. Johnson, J. M. Chow, Jens Koch, J. M. Gambetta, D. I. Schuster, L. Frunzio, M. H. Devoret, S. M. Girvin, and R. J. Schoelkopf, "Controlling the spontaneous emission of a superconducting transmon qubit," Physical Review Letters **101**, 080502 (2008), http://link.aps.org/doi/10.1103/PhysRevLett.101.080502.

[68] AWR Corporation Microwave Office, http://web.awrcorp.com/Usa/Products/Microwave-Office/.

[69] Sadri Hassani, *Mathematical Physics: A Modern Introduction to Its Foundations* (Springer, 1999) ISBN 9780387985794.

[70] B. S. Palmer (personal communication, June 2012).

[71] Zaeill Kim, *Dissipative and Dispersive Measurements of a Cooper Pair Box*, Doctoral dissertation, University of Maryland, College Park (2010).

[72] D. F. Walls and Gerard J. Milburn, *Quantum Optics* (Springer, 2008) ISBN 9783540285731.

[73] Christopher C. Gerry and Peter L. Knight, *Introductory Quantum Optics* (Cambridge University Press, 2005) ISBN 9780521527354.

[74] David Isaac Schuster, *Circuit Quantum Electrodynamics*, Doctoral dissertation, Yale University (2007).

[75] L. Bishop, *Circuit quantum electrodynamics*, Doctoral dissertation, Yale University (2010).

[76] A. Wallraff, D. I. Schuster, A. Blais, L. Frunzio, R.-S. Huang, J. Majer, S. Kumar, S. M. Girvin, and R. J. Schoelkopf, "Strong coupling of a single photon to a superconducting qubit using circuit quantum electrodynamics," Nature **431**, 162–167 (Sep.

2004), ISSN 0028-0836, http://www.nature.com.proxy-um.researchport.umd.edu/nature/journal/v431/n7005/abs/nature02851.html.

[77] Vladimir B. Braginsky, Vladimir Borisovich Braginskiĭ, Farid Ya Khalili, and Kip S. Thorne, *Quantum Measurement* (Cambridge University Press, 1995) ISBN 9780521484138.

[78] D. I. Schuster, A. A. Houck, J. A. Schreier, A. Wallraff, J. M. Gambetta, A. Blais, L. Frunzio, J. Majer, B. Johnson, M. H. Devoret, S. M. Girvin, and R. J. Schoelkopf, "Resolving photon number states in a superconducting circuit," Nature **445**, 515–518 (Feb. 2007), ISSN 0028-0836, http://www.nature.com/nature/journal/v445/n7127/full/nature05461.html.

[79] Jay Gambetta, W. A. Braff, A. Wallraff, S. M. Girvin, and R. J. Schoelkopf, "Protocols for optimal readout of qubits using a continuous quantum nondemolition measurement," Physical Review A **76**, 012325 (Jul. 2007), http://link.aps.org/doi/10.1103/PhysRevA.76.012325.

[80] Jay Gambetta, Alexandre Blais, D. I. Schuster, A. Wallraff, L. Frunzio, J. Majer, M. H. Devoret, S. M. Girvin, and R. J. Schoelkopf, "Qubit-photon interactions in a cavity: Measurement-induced dephasing and number splitting," Physical Review A **74**, 042318 (Oct. 2006), http://link.aps.org/doi/10.1103/PhysRevA.74.042318.

[81] A. Wallraff, D. I. Schuster, A. Blais, L. Frunzio, J. Majer, M. H. Devoret, S. M. Girvin, and R. J. Schoelkopf, "Approaching unit visibility for control of a superconducting qubit with dispersive readout," Physical Review Letters **95**, 060501 (2005), http://link.aps.org/doi/10.1103/PhysRevLett.95.060501.

[82] R. J. Schoelkopf, A. A. Clerk, S. M. Girvin, K. W. Lehnert, and M. H. Devoret, "Qubits as spectrometers of quantum noise," arXiv:cond-mat/0210247(Oct. 2002), http://arxiv.org/abs/cond-mat/0210247.

[83] John David Jackson, *Classical electrodynamics* (Wiley, 1999) ISBN 9780471309321.

[84] M. Brune, P. Nussenzveig, F. Schmidt-Kaler, F. Bernardot, A. Maali, J. M. Raimond, and S. Haroche, "From lamb shift to light shifts: Vacuum and subphoton cav-

ity fields measured by atomic phase sensitive detection," Physical Review Letters **72**, 3339–3342 (May 1994), http://link.aps.org/doi/10.1103/PhysRevLett.72.3339.

[85] D. J. Heinzen and M. S. Feld, "Vacuum radiative level shift and spontaneous-emission linewidth of an atom in an optical resonator," Physical Review Letters **59**, 2623–2626 (Dec. 1987), http://link.aps.org/doi/10.1103/PhysRevLett.59.2623.

[86] H. A. Bethe, "The electromagnetic shift of energy levels," Physical Review **72**, 339–341 (1947), http://link.aps.org/doi/10.1103/PhysRev.72.339.

[87] Willis E. Lamb and Robert C. Retherford, "Fine structure of the hydrogen atom by a microwave method," Physical Review **72**, 241–243 (1947), http://link.aps.org/doi/10.1103/PhysRev.72.241.

[88] Frederick Reif, *Fundamentals of Statistical and Thermal Physics* (Waveland Press, 2008) ISBN 9781577666127.

[89] J. M. Chow, J. M. Gambetta, L. Tornberg, Jens Koch, Lev S. Bishop, A. A. Houck, B. R. Johnson, L. Frunzio, S. M. Girvin, and R. J. Schoelkopf, "Randomized benchmarking and process tomography for gate errors in a solid-state qubit," Physical Review Letters **102**, 090502 (Mar. 2009), http://link.aps.org/doi/10.1103/PhysRevLett.102.090502.

[90] F. Bloch, "Nuclear induction," Physical Review **70**, 460–474 (Oct. 1946), http://link.aps.org/doi/10.1103/PhysRev.70.460.

[91] D. Vion, A. Aassime, A. Cottet, P. Joyez, H. Pothier, C. Urbina, D. Esteve, and M. H. Devoret, "Ramsey fringe measurement of decoherence in a novel superconducting quantum bit based on the cooper pair box," Physica Scripta **T102**, 162 (2002), ISSN 0031-8949, http://iopscience.iop.org/Physica.Topical.102a00162.

[92] Michael N. Leuenberger, "The generalized rotating frame," Journal of Magnetism and Magnetic Materials **272–276, Part 3**, 1974–1975 (May 2004), ISSN 0304-8853, http://www.sciencedirect.com/science/article/pii/S0304885303021218.

[93] Mitchel Weissbluth, *Photon-atom interactions* (Academic Press, 1989) ISBN 9780127436609.

[94] F. Bloch, "Generalized theory of relaxation," Physical Review **105**, 1206–1222 (Feb. 1957), http://link.aps.org/doi/10.1103/PhysRev.105.1206.

[95] R. K. Wangsness and F. Bloch, "The dynamical theory of nuclear induction," Physical Review **89**, 728–739 (Feb. 1953), http://link.aps.org/doi/10.1103/PhysRev.89.728.

[96] Yu. Makhlin and A. Shnirman, "Dephasing of qubits by transverse low-frequency noise," JETP Letters **78**, 497–501 (2003), ISSN 0021-3640, http://www.springerlink.com/content/y1241kv0311p8112/abstract/.

[97] A. Abragam, *The Principles of Nuclear Magnetism* (Oxford University Press, 1961) ISBN 9780198520146.

[98] John M. Martinis, K. B. Cooper, R. McDermott, Matthias Steffen, Markus Ansmann, K. D. Osborn, K. Cicak, Seongshik Oh, D. P. Pappas, R. W. Simmonds, and Clare C. Yu, "Decoherence in josephson qubits from dielectric loss," Physical Review Letters **95**, 210503 (Nov. 2005), http://link.aps.org/doi/10.1103/PhysRevLett.95.210503.

[99] G. Catelani, J. Koch, L. Frunzio, R. J. Schoelkopf, M. H. Devoret, and L. I. Glazman, "Quasiparticle relaxation of superconducting qubits in the presence of flux," Physical Review Letters **106**, 077002 (Feb. 2011), http://link.aps.org/doi/10.1103/PhysRevLett.106.077002.

[100] G. Catelani, R. J. Schoelkopf, M. H. Devoret, and L. I. Glazman, "Relaxation and frequency shifts induced by quasiparticles in superconducting qubits," Physical Review B **84**, 064517 (2011), http://link.aps.org/doi/10.1103/PhysRevB.84.064517.

[101] M. Metcalfe, E. Boaknin, V. Manucharyan, R. Vijay, I. Siddiqi, C. Rigetti, L. Frunzio, R. J. Schoelkopf, and M. H. Devoret, "Measuring the decoherence of a quantronium qubit with the cavity bifurcation amplifier," Physical Review B **76**, 174516 (Nov. 2007), http://link.aps.org/doi/10.1103/PhysRevB.76.174516.

[102] Hendrik Bluhm, Julie A. Bert, Nicholas C. Koshnick, Martin E. Huber, and Kathryn A. Moler, "Spinlike susceptibility of metallic and insulating thin films at low temperature," Physical Review Letters **103**, 026805 (Jul. 2009), http://link.aps.org/doi/10.1103/PhysRevLett.103.026805.

[103] Frederick C. Wellstood, Cristian Urbina, and John Clarke, "Low-frequency noise in dc superconducting quantum interference devices below 1 k," Applied Physics Letters **50**, 772–774 (Mar. 1987), ISSN 00036951, http://apl.aip.org/resource/1/applab/v50/i12/p772_s1.

[104] K. Kakuyanagi, T. Meno, S. Saito, H. Nakano, K. Semba, H. Takayanagi, F. Deppe, and A. Shnirman, "Dephasing of a superconducting flux qubit," Physical Review Letters **98**, 047004 (Jan. 2007), http://link.aps.org/doi/10.1103/PhysRevLett.98.047004.

[105] F. Yoshihara, K. Harrabi, A. O. Niskanen, Y. Nakamura, and J. S. Tsai, "Decoherence of flux qubits due to 1/f flux noise," Physical Review Letters **97**, 167001 (Oct. 2006), http://link.aps.org/doi/10.1103/PhysRevLett.97.167001.

[106] Sheldon M. Ross, *A first course in probability* (Pearson Prentice Hall, 2010) ISBN 9780136033134.

[107] Gregoire Ithier, *Manipulation,readout and analysis of the decoherence of a superconducting quantum bit*, Doctoral dissertation, Université Paris 6 (2005).

[108] G. Falci, A. D'Arrigo, A. Mastellone, and E. Paladino, "Dynamical suppression of telegraph and 1/f noise due to quantum bistable fluctuators," Physical Review A **70**, 040101 (Oct. 2004), http://link.aps.org/doi/10.1103/PhysRevA.70.040101.

[109] Yuriy Makhlin and Alexander Shnirman, "Dephasing of solid-state qubits at optimal points," Physical Review Letters **92**, 178301 (Apr. 2004), http://link.aps.org/doi/10.1103/PhysRevLett.92.178301.

[110] K. Rabenstein, V. Sverdlov, and D. Averin, "Qubit decoherence by gaussian low-frequency noise," JETP Letters **79**, 646–649 (2004), ISSN 0021-3640, http://www.springerlink.com/content/1663623472517873/abstract/.

[111] E. L. Hahn, "Spin echoes," Physical Review **80**, 580–594 (Nov. 1950), http://link.aps.org/doi/10.1103/PhysRev.80.580.

[112] Y. Nakamura, Yu. A. Pashkin, T. Yamamoto, and J. S. Tsai, "Charge echo in a cooper-pair box," Physical Review Letters **88**, 047901 (Jan. 2002), http://link.aps.org/doi/10.1103/PhysRevLett.88.047901.

[113] Lorenza Viola, Emanuel Knill, and Seth Lloyd, "Dynamical decoupling of open quantum systems," Physical Review Letters **82**, 2417–2421 (Mar. 1999), http://link.aps.org/doi/10.1103/PhysRevLett.82.2417.

[114] Josef Schriefl, *Decoherence in Josephson Qubits*, Doctoral dissertation, Ecole Normale Supérieure de Lyon (2005).

[115] Eitan Geva, Ronnie Kosloff, and J. L. Skinner, "On the relaxation of a two-level system driven by a strong electromagnetic field," The Journal of Chemical Physics **102**, 8541–8561 (Jun. 1995), ISSN 00219606, http://jcp.aip.org/resource/1/jcpsa6/v102/i21/p8541_s1.

[116] J. A. Schreier, A. A. Houck, Jens Koch, D. I. Schuster, B. R. Johnson, J. M. Chow, J. M. Gambetta, J. Majer, L. Frunzio, M. H. Devoret, S. M. Girvin, and R. J. Schoelkopf, "Suppressing charge noise decoherence in superconducting charge qubits," Physical Review B **77**, 180502 (May 2008), http://link.aps.org/doi/10.1103/PhysRevB.77.180502.

[117] B. Suri, S. Novikov, V. Zaretskey, B. S. Palmer, and F. C. Wellstood, "Transmon qubit coupled to a quasi-lumped element resonator," in *Bulletin of the American Physical Society*, Vol. Volume 57, Number 1 (American Physical Society, 2012) http://meetings.aps.org/link/BAPS.2012.MAR.Q30.9.

[118] Stephen A. Campbell, *The Science and Engineering of Microelectronic Fabrication* (Oxford University Press, 2001) ISBN 9780195136050.

[119] Zheng Cui, *Micro-Nanofabrication: Technologies and Applications* (Springer, 2010) ISBN 9783642066979.

[120] Marc J. Madou, *Fundamentals of Microfabrication: The Science of Miniaturization* (CRC Press, 2002) ISBN 9780849308260.

[121] H. Iwai, "Roadmap for 22 nm and beyond," Microelectronic Engineering **86**, 1520–1528 (Jul. 2009), ISSN 0167-9317, http://www.sciencedirect.com/science/article/pii/S0167931709002950.

[122] Tanner EDA L-Edit Pro, http://tannereda.com/l-edit-pro.

[123] Microtronics, http://microtronicsinc.com/.

[124] Futurrex, http://futurrex.com/en/products/negative-photoresists/negative-lift-off-resists.html.

[125] Fujifilm, http://www.fujifilmusa.com/products/semiconductor_materials/photoresists/index.html.

[126] MicroChem, http://www.microchem.com/Prod-PMGI_LOR.htm.

[127] Dow Electronic Materials, http://www.dow.com/products/market/electronics-and-communications/.

[128] R. E. Howard and D. E. Prober, "Nanometer-scale fabrication techniques," in *VLSI Electronics: Microstructure Science*, Vol. 5, edited by N. G. Einspruch (Academic Press, 1982).

[129] A. N. Broers, "Resolution limits for electron-beam lithography," IBM Journal of Research and Development **32**, 502 –513 (Jul. 1988), ISSN 0018-8646, http://ieeexplore.ieee.org/xpls/abs_all.jsp?arnumber=5390017.

[130] Alec N. Broers, "Resolution limits of PMMA resist for exposure with 50 kV electrons," Journal of The Electrochemical Society **128**, 166–170 (Jan. 1981), ISSN 0013-4651, 1945-7111, http://jes.ecsdl.org/content/128/1/166.

[131] R. E. Howard, E. L. Hu, L. D. Jackel, P. Grabbe, and D. M. Tennant, "400-å linewidth e-beam lithography on thick silicon substrates," Applied Physics Letters **36**, 592–594 (Apr. 1980), ISSN 00036951, http://apl.aip.org/resource/1/applab/v36/i7/p592_s1.

[132] P. Rai-Choudhury, *Handbook of Microlithography, Micromachining, and Microfabrication* (IET, 1997) ISBN 9780852969069.

[133] JEOL Scanning Electron Microscopes, http://www.jeol.com/default.aspx?tabid=92.

[134] Nanometer Pattern Generation System, http://www.jcnabity.com/.

[135] Zeon Chemicals, http://www.zeonchemicals.com/ElectronicMaterials/.

[136] G. J. Dolan, "Offset masks for lift-off photoprocessing," Applied Physics Letters **31**, 337–339 (Sep. 1977), ISSN 00036951, http://apl.aip.org/resource/1/applab/v31/i5/p337_s1.

[137] J. Niemeyer and V. Kose, "Observation of large dc supercurrents at nonzero voltages in josephson tunnel junctions," Applied Physics Letters **29**, 380–382 (Sep. 1976), ISSN 00036951, http://apl.aip.org/resource/1/applab/v29/i6/p380_s1.

[138] A.W. Kleinsasser, R.E. Miller, and W.H. Mallison, "Dependence of critical current density on oxygen exposure in nb-AlOx-Nb tunnel junctions," IEEE Transactions on Applied Superconductivity **5**, 26 –30 (Mar. 1995), ISSN 1051-8223.

[139] W.H. Mallison, R.E. Miller, and A.W. Kleinsasser, "Effect of growth conditions on the electrical properties of Nb/Al-oxide/Nb tunnel junctions," IEEE Transactions on Applied Superconductivity **5**, 2330 – 2333 (Jun. 1995), ISSN 1051-8223.

[140] Hans Lüth, *Solid Surfaces, Interfaces and Thin Films* (Springer, 2010) ISBN 9783642135910.

[141] O. A. E. Cherney and J. Shewchun, "Enhancement of superconductivity in thin aluminium films," Canadian Journal of Physics **47**, 1101–1106 (May 1969), ISSN 0008-4204, 1208-6045, http://www.nrcresearchpress.com/doi/abs/10.1139/p69-138.

[142] Roger W. Cohen and B. Abeles, "Superconductivity in granular aluminum films," Physical Review **168**, 444–450 (Apr. 1968), http://link.aps.org/doi/10.1103/PhysRev.168.444.

[143] J. J. Hauser, "Enhancement of superconductivity in aluminum films," Physical Review B **3**, 1611–1616 (Mar. 1971), http://link.aps.org/doi/10.1103/PhysRevB.3.1611.

[144] P. Santhanam, S. Wind, and D. E. Prober, "Localization, superconducting fluctuations, and superconductivity in thin films and narrow wires of aluminum," Physical Review B **35**, 3188–3206 (Mar. 1987), http://link.aps.org/doi/10.1103/PhysRevB.35.3188.

[145] Frank Pobell, *Matter and Methods at Low Temperatures* (Springer, 1996) ISBN 9783540585725.

[146] Guy Kendall White and Philip J. Meeson, *Experimental Techniques in Low-Temperature Physics* (Clarendon, 2002) ISBN 9780198514282.

[147] D. Vion, P. F. Orfila, P. Joyez, D. Esteve, and M. H. Devoret, "Miniature electrical filters for single electron devices," Journal of Applied Physics **77**, 2519–2524 (Mar. 1995), ISSN 00218979, http://jap.aip.org/resource/1/japiau/v77/i6/p2519_s1.

[148] Midwest Microwave, https://emersonconnectivity.com/OA_HTML/xxemr_ibeCCtpSctDspRte.jsp?section=10220.

[149] Aeroflex, http://www.aeroflex.com/.

[150] Mini-Circuits, http://www.minicircuits.com/.

[151] PAMTECH, http://pamtechinc.com/.

[152] Weinreb (Caltech) Radiometer Group, http://radiometer.caltech.edu/.

[153] Richard E. Matick, *Transmission Lines and Communication Networks: An Introduction to Transmission Lines, High-frequency and High-speed Pulse Characteristics and Applications* (Wiley, 2000) ISBN 9780780360433.

[154] K. Bladh, D. Gunnarsson, E. Hürfeld, S. Devi, C. Kristoffersson, B. Smålander, S. Pehrson, T. Claeson, P. Delsing, and M. Taslakov, "Comparison of cryogenic filters for use in single electronics experiments," Review of Scientific Instruments **74**, 1323–1327 (Mar. 2003), ISSN 00346748, http://rsi.aip.org/resource/1/rsinak/v74/i3/p1323_s1.

[155] A. B. Zorin, "The thermocoax cable as the microwave frequency filter for single electron circuits," Review of Scientific Instruments **66**, 4296–4300 (Aug. 1995), ISSN 00346748, http://rsi.aip.org/resource/1/rsinak/v66/i8/p4296_s1.

[156] A. Fukushima, A. Sato, A. Iwasa, Y. Nakamura, T. Komatsuzaki, and Y. Sakamoto, "Attenuation of microwave filters for single-electron tunneling experiments," IEEE Transactions on Instrumentation and Measurement **46**, 289 –293 (Apr. 1997), ISSN 0018-9456, http://ieeexplore.ieee.org/xpls/abs_all.jsp?arnumber=571834.

[157] F. P. Milliken, J. R. Rozen, G. A. Keefe, and R. H. Koch, "50 ohm characteristic impedance low-pass metal powder filters," Review of Scientific Instruments **78**, 024701–024701–5 (Feb. 2007), ISSN 00346748, http://rsi.aip.org/resource/1/rsinak/v78/i2/p024701_s1.

[158] COAX CO., http://www.coax.co.jp/english/main.html.

[159] Spectrum Control, http://www.spectrumcontrol.com/.

[160] Anritsu, http://www.anritsu.com/en-US/Products-Solutions/Products/K102F-R.aspx.

[161] M.M. Elsbury, C.J. Burroughs, P.D. Dresselhaus, Z.B. Popovic, and S.P. Benz, "Microwave packaging for voltage standard applications," IEEE Transactions on Applied Superconductivity **19**, 1012 –1015 (Jun. 2009), ISSN 1051-8223, http://ieeexplore.ieee.org/xpls/abs_all.jsp?arnumber=5129608.

[162] Toshihisa Kamei, Yozo Utsumi, Nguyen Quoc Dinh, and Nguyen Thanh, "Wide-band coaxial-to-coplanar transition," IEICE TRANSACTIONS on Electronics **E90-C**, 2030–2036 (Oct. 2007), ISSN 1745-1353, 0916-8516, http://search.ieice.org/bin/summary.php?id=e90-c_10_2030&category=C&year=2007&lang=E&abst=.

[163] Tektronix, http://www.tek.com/datasheet/arbitrary-function-generators-0.

[164] Martinis Group at UCSB, http://web.physics.ucsb.edu/~martinisgroup/electronics.shtml.

[165] Sergey Novikov, V. Zaretskey, B. Suri, Z. Kim, B. S. Palmer, and F. C. Wellstood, "Quantum state tomography of a cooper-pair box," in *Bulletin of the American Physical Society*, Vol. Volume 56, Number 1 (American Physical Society, 2011) http://meetings.aps.org/link/BAPS.2011.MAR.B27.14.

[166] High Speed Circuit Consultants, http://www.hscc.biz/.

[167] Picosecond Pulse Labs, http://www.picosecond.com/product/category.asp?pd_id=4.

[168] Herman J. Blinchikoff and Anatol I. Zverev, *Filtering in the time and frequency domains* (Noble Pub., 2001) ISBN 9781884932175.

[169] Marki Microwave, http://www.markimicrowave.com/2791/IQ_Mixers_-_Quadrature_IF.aspx.

[170] Agilent Technologies, http://www.agilent.com/.

[171] Stanford Research Systems, http://www.thinksrs.com/products/FS725.htm.

[172] J. G. Baldwin and D. F. Dubbert, "Quadrature mixer LO leakage suppression through quadrature DC bias," NASA STI/Recon Technical Report N **03**, 01677 (May 2002), http://adsabs.harvard.edu/abs/2002STIN...0301677B.

[173] Taub, *Principles Of Communication Systems* (McGraw-Hill Education (India) Pvt Ltd, 2008) ISBN 9780070648111.

[174] John R. Miller and John M. Pierce, "A high frequency heterodyne Lock-In amplifier," Review of Scientific Instruments **43**, 1721–1723 (Nov. 1972), ISSN 00346748, http://rsi.aip.org/resource/1/rsinak/v43/i11/p1721_s1.

[175] MAC Technology, http://www.mactechnology.com/.

[176] Pasternack Enterprises, http://www.pasternack.com/sma-female-standard-stub-terminal-connector-pe4001-p.aspx.

[177] MITEQ, http://www.miteq.com/.

[178] M. S. Khalil, M. J. A. Stoutimore, F. C. Wellstood, and K. D. Osborn, "An analysis method for asymmetric resonator transmission applied to superconducting

devices," Journal of Applied Physics **111**, 054510–054510–6 (Mar. 2012), ISSN 00218979, http://jap.aip.org/resource/1/japiau/v111/i5/p054510_s1.

[179] Jonas Bylander, Simon Gustavsson, Fei Yan, Fumiki Yoshihara, Khalil Harrabi, George Fitch, David G. Cory, Yasunobu Nakamura, Jaw-Shen Tsai, and William D. Oliver, "Noise spectroscopy through dynamical decoupling with a superconducting flux qubit," Nature Physics **7**, 565–570 (May 2011), ISSN 1745-2473, http://www.nature.com/nphys/journal/v7/n7/full/nphys1994.html.

[180] Łukasz Cywiński, Roman M. Lutchyn, Cody P. Nave, and S. Das Sarma, "How to enhance dephasing time in superconducting qubits," Physical Review B **77**, 174509 (May 2008), http://link.aps.org/doi/10.1103/PhysRevB.77.174509.

[181] O. Astafiev, Yu. A. Pashkin, Y. Nakamura, T. Yamamoto, and J. S. Tsai, "Quantum noise in the josephson charge qubit," Physical Review Letters **93**, 267007 (Dec. 2004), http://link.aps.org/doi/10.1103/PhysRevLett.93.267007.

[182] P. Dutta and P. M. Horn, "Low-frequency fluctuations in solids: 1/f noise," Reviews of Modern Physics **53**, 497–516 (Jul. 1981), http://link.aps.org/doi/10.1103/RevModPhys.53.497.

[183] M. Kenyon, C. J. Lobb, and F. C. Wellstood, "Temperature dependence of low-frequency noise in Al–Al2O3–Al single-electron transistors," Journal of Applied Physics **88**, 6536–6540 (Dec. 2000), ISSN 00218979, http://jap.aip.org/resource/1/japiau/v88/i11/p6536_s1.

[184] Sh Kogan, *Electronic Noise and Fluctuations in Solids* (Cambridge University Press, 2008) ISBN 9780521070195.

[185] Li-Chung Ku and Clare C. Yu, "Decoherence of a josephson qubit due to coupling to two-level systems," Physical Review B **72**, 024526 (Jul. 2005), http://link.aps.org/doi/10.1103/PhysRevB.72.024526.

[186] W A Phillips, "Two-level states in glasses," Reports on Progress in Physics **50**, 1657–1708 (Dec. 1987), ISSN 0034-4885, 1361-6633, http://iopscience.iop.org/0034-4885/50/12/003.

[187] W. A. Phillips, "Tunneling states in amorphous solids," Journal of Low Temperature Physics **7**, 351–360 (1972), ISSN 0022-2291, http://www.springerlink.com/content/t35554757106224k/abstract/.

[188] Alexander Shnirman, Gerd Schön, Ivar Martin, and Yuriy Makhlin, "Low- and high-frequency noise from coherent two-level systems," Physical Review Letters **94**, 127002 (Apr. 2005), http://link.aps.org/doi/10.1103/PhysRevLett.94.127002.

[189] M. Von Schickfus and S. Hunklinger, "Saturation of the dielectric absorption of vitreous silica at low temperatures," Physics Letters A **64**, 144–146 (Nov. 1977), ISSN 0375-9601, http://www.sciencedirect.com/science/article/pii/0375960177905588.

[190] L. S. Levitov, "Delocalization of vibrational modes caused by electric dipole interaction," Physical Review Letters **64**, 547–550 (Jan. 1990), http://link.aps.org/doi/10.1103/PhysRevLett.64.547.

[191] Alexander L. Burin, "Dipole gap effects in low energy excitation spectrum of amorphous solids. theory for dielectric relaxation," Journal of Low Temperature Physics **100**, 309–337 (Aug. 1995), ISSN 0022-2291, 1573-7357, http://link.springer.com/article/10.1007/BF00751512.

[192] J. L. Black and B. I. Halperin, "Spectral diffusion, phonon echoes, and saturation recovery in glasses at low temperatures," Physical Review B **16**, 2879–2895 (Sep. 1977), http://link.aps.org/doi/10.1103/PhysRevB.16.2879.

[193] S. Sendelbach, D. Hover, A. Kittel, M. Mück, John M. Martinis, and R. McDermott, "Magnetism in SQUIDs at millikelvin temperatures," Physical Review Letters **100**, 227006 (Jun. 2008), http://link.aps.org/doi/10.1103/PhysRevLett.100.227006.

[194] R. McDermott, "Materials origins of decoherence in superconducting qubits," IEEE Transactions on Applied Superconductivity **19**, 2 –13 (Feb. 2009), ISSN 1051-8223.

[195] Roger H. Koch, David P. DiVincenzo, and John Clarke, "Model for 1/f flux noise

in SQUIDs and qubits," Physical Review Letters **98**, 267003 (Jun. 2007), http://link.aps.org/doi/10.1103/PhysRevLett.98.267003.

[196] Magdalena Constantin and Clare C. Yu, "Microscopic model of critical current noise in josephson junctions," Physical Review Letters **99**, 207001 (Nov. 2007), http://link.aps.org/doi/10.1103/PhysRevLett.99.207001.

[197] Hanhee Paik and Kevin D Osborn, "Reducing quantum-regime dielectric loss of silicon nitride for superconducting quantum circuits," Applied Physics Letters **96**, 072505–072505–3 (Feb. 2010), ISSN 00036951, http://apl.aip.org/resource/1/applab/v96/i7/p072505_s1.

[198] D. J. Van Harlingen, T. L. Robertson, B. L. T. Plourde, P. A. Reichardt, T. A. Crane, and John Clarke, "Decoherence in josephson-junction qubits due to critical-current fluctuations," Physical Review B **70**, 064517 (Aug. 2004), http://link.aps.org/doi/10.1103/PhysRevB.70.064517.

[199] John Clarke, "SQUID fundamentals," in *Squid Sensors: Fundamentals, Fabrication, and Applications*, edited by Harold Weinstock (Springer, 1996) ISBN 9780792343509.

[200] Bonaventura Savo, Frederick C. Wellstood, and John Clarke, "Low-frequency excess noise in Nb-Al2O3-Nb josephson tunnel junctions," Applied Physics Letters **50**, 1757–1759 (Jun. 1987), ISSN 00036951, http://apl.aip.org/resource/1/applab/v50/i24/p1757_s1.

[201] R. T. Wakai and D. J. Van Harlingen, "Low-frequency noise and discrete charge trapping in small-area tunnel junction dc SQUID's," Applied Physics Letters **49**, 593–595 (Sep. 1986), ISSN 00036951, http://apl.aip.org/resource/1/applab/v49/i10/p593_s1.

[202] Rogério de Sousa, K. Birgitta Whaley, Theresa Hecht, Jan von Delft, and Frank K. Wilhelm, "Microscopic model of critical current noise in josephson-junction qubits: Subgap resonances and andreev bound states," Physical Review B **80**, 094515 (2009), http://link.aps.org/doi/10.1103/PhysRevB.80.094515.

[203] Lara Faoro and Lev B. Ioffe, "Microscopic origin of critical current fluctuations in large, small, and ultra-small area josephson junctions," Physical Review B **75**, 132505 (Apr. 2007), http://link.aps.org/doi/10.1103/PhysRevB.75.132505.

[204] F. Deppe, M. Mariantoni, E. P. Menzel, S. Saito, K. Kakuyanagi, H. Tanaka, T. Meno, K. Semba, H. Takayanagi, and R. Gross, "Phase coherent dynamics of a superconducting flux qubit with capacitive bias readout," Physical Review B **76**, 214503 (Dec. 2007), http://link.aps.org/doi/10.1103/PhysRevB.76.214503.

[205] B. L. T. Plourde, T. L. Robertson, P. A. Reichardt, T. Hime, S. Linzen, C.-E. Wu, and John Clarke, "Flux qubits and readout device with two independent flux lines," Physical Review B **72**, 060506 (2005), http://link.aps.org/doi/10.1103/PhysRevB.72.060506.

[206] R. W. Simmonds, K. M. Lang, D. A. Hite, S. Nam, D. P. Pappas, and John M. Martinis, "Decoherence in josephson phase qubits from junction resonators," Physical Review Letters **93**, 077003 (2004), http://link.aps.org/doi/10.1103/PhysRevLett.93.077003.

[207] L. Tian and R. W. Simmonds, "Josephson junction microscope for low-frequency fluctuators," Physical Review Letters **99**, 137002 (2007), http://link.aps.org/doi/10.1103/PhysRevLett.99.137002.

[208] K. B. Cooper, Matthias Steffen, R. McDermott, R. W. Simmonds, Seongshik Oh, D. A. Hite, D. P. Pappas, and John M. Martinis, "Observation of quantum oscillations between a josephson phase qubit and a microscopic resonator using fast readout," Physical Review Letters **93**, 180401 (Oct. 2004), http://link.aps.org/doi/10.1103/PhysRevLett.93.180401.

[209] T. A. Palomaki, S. K. Dutta, R. M. Lewis, A. J. Przybysz, Hanhee Paik, B. K. Cooper, H. Kwon, J. R. Anderson, C. J. Lobb, F. C. Wellstood, and E. Tiesinga, "Multilevel spectroscopy of two-level systems coupled to a dc SQUID phase qubit," Physical Review B **81**, 144503 (Apr. 2010), http://link.aps.org/doi/10.1103/PhysRevB.81.144503.

[210] Matthias Steffen, M. Ansmann, R. McDermott, N. Katz, Radoslaw C. Bialczak,

Erik Lucero, Matthew Neeley, E. M. Weig, A. N. Cleland, and John M. Martinis, "State tomography of capacitively shunted phase qubits with high fidelity," Physical Review Letters **97**, 050502 (2006), http://link.aps.org/doi/10.1103/PhysRevLett.97.050502.

[211] Jeffrey S Kline, Haohua Wang, Seongshik Oh, John M Martinis, and David P Pappas, "Josephson phase qubit circuit for the evaluation of advanced tunnel barrier materials," Superconductor Science and Technology **22**, 015004 (Jan. 2009), ISSN 0953-2048, 1361-6668, http://iopscience.iop.org/0953-2048/22/1/015004.

[212] Seongshik Oh, Katarina Cicak, Jeffrey S. Kline, Mika A. Sillanpää, Kevin D. Osborn, Jed D. Whittaker, Raymond W. Simmonds, and David P. Pappas, "Elimination of two level fluctuators in superconducting quantum bits by an epitaxial tunnel barrier," Physical Review B **74**, 100502 (2006), http://link.aps.org/doi/10.1103/PhysRevB.74.100502.

[213] S. Ashhab, J.R. Johansson, and Franco Nori, "Decoherence dynamics of a qubit coupled to a quantum two-level system," Physica C: Superconductivity **444**, 45–52 (Sep. 2006), ISSN 0921-4534, http://www.sciencedirect.com/science/article/pii/S0921453406005776.

[214] A. M. Zagoskin, S. Ashhab, J. R. Johansson, and Franco Nori, "Quantum two-level systems in josephson junctions as naturally formed qubits," Physical Review Letters **97**, 077001 (Aug. 2006), http://link.aps.org/doi/10.1103/PhysRevLett.97.077001.

[215] Matthew Neeley, M. Ansmann, Radoslaw C. Bialczak, M. Hofheinz, N. Katz, Erik Lucero, A. O'Connell, H. Wang, A. N. Cleland, and John M. Martinis, "Process tomography of quantum memory in a josephson-phase qubit coupled to a two-level state," Nat Phys **4**, 523–526 (Jul. 2008), ISSN 1745-2473, http://dx.doi.org/10.1038/nphys972.

[216] A. Lupaşcu, P. Bertet, E. F. C. Driessen, C. J. P. M. Harmans, and J. E. Mooij, "One- and two-photon spectroscopy of a flux qubit coupled to a microscopic defect," Physical Review B **80**, 172506 (Nov. 2009), http://link.aps.org/doi/10.1103/PhysRevB.80.172506.

[217] Yoni Shalibo, Ya'ara Rofe, David Shwa, Felix Zeides, Matthew Neeley, John M. Martinis, and Nadav Katz, "Lifetime and coherence of two-level defects in a josephson junction," Physical Review Letters **105**, 177001 (Oct. 2010), http://link.aps.org/doi/10.1103/PhysRevLett.105.177001.

[218] Zhen-Tao Zhang and Yang Yu, "Coupling mechanism between microscopic two-level system and superconducting qubits," Physical Review A **84**, 064301 (Dec. 2011), http://link.aps.org/doi/10.1103/PhysRevA.84.064301.

[219] J. Eroms, L. C. van Schaarenburg, E. F. C. Driessen, J. H. Plantenberg, C. M. Huizinga, R. N. Schouten, A. H. Verbruggen, C. J. P. M. Harmans, and J. E. Mooij, "Low-frequency noise in josephson junctions for superconducting qubits," Applied Physics Letters **89**, 122516–122516–3 (Sep. 2006), ISSN 00036951, http://apl.aip.org/resource/1/applab/v89/i12/p122516_s1.

[220] L. S. Dorneles, D. M. Schaefer, M. Carara, and L. F. Schelp, "The use of simmons' equation to quantify the insulating barrier parameters in Al/AlOx/Al tunnel junctions," Applied Physics Letters **82**, 2832–2834 (Apr. 2003), ISSN 00036951, http://apl.aip.org/resource/1/applab/v82/i17/p2832_s1.

[221] W. A. Phillips, *Amorphous solids: low-temperature properties* (Springer, 1981) ISBN 9783540103301.

[222] Ning Dong, Guozhu Sun, Yiwen Wang, Junyu Cao, Yang Yu, Jian Chen, Lin Kang, Weiwei Xu, Siyuan Han, and Peiheng Wu, "Critical current fluctuation in a microwave-driven josephson junction," Superconductor Science and Technology **20**, S441–S444 (Nov. 2007), ISSN 0953-2048, 1361-6668, http://iopscience.iop.org/0953-2048/20/11/S27.

[223] Chad Rigetti, Jay M. Gambetta, Stefano Poletto, B. L. T. Plourde, Jerry M. Chow, A. D. Córcoles, John A. Smolin, Seth T. Merkel, J. R. Rozen, George A. Keefe, Mary B. Rothwell, Mark B. Ketchen, and M. Steffen, "Superconducting qubit in a waveguide cavity with a coherence time approaching 0.1 ms," Physical Review B **86**, 100506 (Sep. 2012), http://link.aps.org/doi/10.1103/PhysRevB.86.100506.

[224] Vladimir E. Manucharyan, Nicholas A. Masluk, Archana Kamal, Jens Koch, Leonid I. Glazman, and Michel H. Devoret, "Evidence for coherent quantum phase

slips across a josephson junction array," Physical Review B **85**, 024521 (Jan. 2012), http://link.aps.org/doi/10.1103/PhysRevB.85.024521.